



University
of Glasgow

Ainslie-McLaren, Gillian (2012) *Assessment of somatostatin image quantification with SPET and SPET-CT to aid characterisation of disease.*

PhD thesis.

<http://theses.gla.ac.uk/3179/>

Copyright and moral rights for this thesis are retained by the author

A copy can be downloaded for personal non-commercial research or study, without prior permission or charge

This thesis cannot be reproduced or quoted extensively from without first obtaining permission in writing from the Author

The content must not be changed in any way or sold commercially in any format or medium without the formal permission of the Author

When referring to this work, full bibliographic details including the author, title, awarding institution and date of the thesis must be given

**Assessment of somatostatin image quantification
with SPET and SPET-CT to aid characterisation of
disease**

**Gillian Ainslie-McLaren
BSc. (Hons), MSc (Med Sci)**

**Submitted in fulfilment of the requirements for the
Degree of Doctor of Philosophy**

**Department of Clinical Physics and Bioengineering
College of Medical, Veterinary and Life Sciences
Graduate School
University of Glasgow**

October 2011

Abstract

Work was undertaken in this thesis to assess the use of somatostatin image quantification with SPET and SPET-CT to aid the characterisation of disease within the body. Two radionuclide somatostatin analogues were used for this assessment, the first was NeoSPECT and the second, OctreoScan.

The primary aim of work in this thesis was to assess the role of NeoSPECT imaging in the characterisation of disease within the lungs, that is, to differentiate benign from malignant disease. Two forms of image quantification were used in the NeoSPECT assessment, a tumour to background ratio (T:B) and a value of tumour percentage uptake (% uptake).

Values of T:B and % uptake were calculated from SPET images acquired 2 hours post injection. T:B results from the benign group (n = 8) demonstrated a median T:B of 2.21, whilst the malignant group (n = 28) demonstrated a median T:B of 2.01. The differences between the groups were tested statistically via a Mann-Whitney test, which showed there to be no statistical difference between the groups (p=0.90, 95.4% CI of (-0.5598, 0.5498)).

To undertake the calculation of % uptake a non-patient acquisition (a standard acquisition) was also required, unfortunately not all of the patient cohort used for the T:B assessment had this additional acquisition. As a result of this numbers were low for the % uptake assessment in patients with a benign histology (n = 2), therefore statistical analysis could not be performed. However, review of the range of values for each histology within the malignant group proved useful as no differences were demonstrated between the ranges of values which could help to differentiate between the histologies.

Quantification of dual time point imaging was also assessed to determine if there were any variations in values calculated that could also help differentiate the different histologies. For this assessment patients were imaged at 2 and 4 hours post injection. Results from the Wilcoxon Signed Rank test of the T:B assessment found there to be no statistically significant difference between values of T:B calculated at 2 and 4 hours that was characteristic of tumour type (p=1.0 and

$p=0.14$). The difference in % uptake between 2 and 4 hours was also assessed via a Wilcoxon Signed Rank test, this test also concluded there to be no significant difference value of % uptake between the two acquisitions of the malignant group ($p = 0.73$).

An attempt was also made to quantify 'other' uptake within the mediastinum, however, a lack of anatomical information made correlation with histology impossible and as a result no firm conclusions relating image quantification to histology could be drawn from this work.

Work from this thesis concluded no quantitative difference between tissue histology could be demonstrated using NeoSPECT, either from single or dual time point imaging.

As a result of the NeoSPECT work a number of factors which limited the accuracy and reproducibility of SPET image quantification were identified. Towards the end of the NeoSPECT work hybrid imaging (SPET-CT) became available within the department at Glasgow Royal Infirmary. It was believed that hybrid imaging could resolve some of the limitations and subsequently improve the accuracy of SPET image quantification. However, NeoSPECT was removed from the market for a short period of time and therefore a similar somatostatin analogue, OctreoScan, was used to investigate if the accuracy of somatostatin image quantification could be improved as a result of SPET-CT and its associated reconstruction algorithms including a CT based attenuation correction.

Firstly, a qualitative assessment of image quality using the new hybrid reconstructions techniques was undertaken via an observer study. Images were reconstructed with the existing reconstruction techniques, as used for the NeoSPECT work, and with the new hybrid imaging techniques. Four experienced observers blinded to reconstruction technique were asked to score images in terms of their overall image quality. A Friedman test was performed on the scores for each observer, three of the four observers demonstrated a statistically significant difference in their scores between the existing and new hybrid technique ($p = 0.00$, $p = 0.003$, $p = 0.00$), with the new hybrid technique being assigned the highest scores in terms of image quality.

Images were also assessed semi-quantitatively via profile analysis which also demonstrated a clear differentiation between the existing and new hybrid techniques with increased image quality being demonstrated in the hybrid data set.

The quantitative accuracy of hybrid imaging was also assessed using phantom data. For ^{111}In the difference of the value of absolute activity calculated and that measured varied by 35% but this improved to 21 % when scatter and CT-attenuation based corrections were applied. For $^{99\text{m}}\text{Tc}$ a much more notable difference between the existing techniques used in chapter 2 and those available from the use of hybrid imaging was demonstrated, the difference in the value of absolute activity calculated and that measured improved from 67% to 0.04%, respectively.

Work in this thesis clearly demonstrated an improvement in image quality and accuracy in SPET quantification as a result of hybrid imaging techniques.

Table of Contents

Abstract	2
Table of Contents.....	5
List of Tables	9
List of Figures	11
Acknowledgements.....	13
Author's Declaration	14
Chapter 1 - Introduction	15
1.1 Current Radiopharmaceuticals used in imaging of cancer.....	16
1.1.1 ^{99m} Tc - Methylene Diphosphonate - Radiopharmaceutical Properties	17
1.1.2 Somatostatin Receptor Imaging	22
1.1.2.1 Lung Cancer and NeoSPECT Radiopharmaceutical Properties.	26
1.1.2.2 Neuroendocrine Tumours and OctreoScan Radiopharmaceutical Properties	27
1.2 Past and current imaging techniques	30
1.2.1 Gamma Camera Technology	30
1.2.2 SPET Image Reconstruction	31
1.2.2.1 Filtered Back Projection, FBP.....	32
1.2.2.2 Ordered Subset Expectation Maximisation, OSEM.....	37
1.2.2.3 Attenuation Correction	41
1.2.2.4 Image Registration.....	43
1.3 Role of image quantification.....	45
1.4 Aim of this thesis	47
Chapter 2 - NeoSPECT	48
2.1 Literature Review	50
2.2 Pan Glasgow Study - Depreotide Imaging	52
2.2.1 Aim	53
2.3 Optimisation of reconstruction techniques and reproducibility using NeoSPECT Phantom Acquisitions	55

2.3.1	Optimisation of NeoSPECT Standard Acquisition and Reconstruction Parameters	58
2.3.1.1	Methods for Investigation 1 - Reproducibility of 3 Sec STD Acquisition	59
2.3.1.2	Results for Investigation 1 - Reproducibility of 3 sec STD Acquisition	61
2.3.1.3	Methods for Investigation 2 - Influence of Attenuation Correction on STD Reconstructed Data	63
2.3.1.4	Results for Investigation 2 - Influence of Attenuation Correction on STD Reconstructed data	65
2.3.1.5	Discussion	67
2.3.2	Determining reproducibility and accuracy of quantification of 2 versus 4 hour imaging.....	68
2.3.2.1	Methods	69
2.3.2.2	Results 1 - Assessment of tumour to background ratio T:B, reproducibility	71
2.3.2.3	Results 2 - Evaluation of uptake calculation and assessment of washout reproducibility.....	72
2.3.2.4	Discussion and Conclusion	77
2.3.3	Assessment of updated reconstruction parameters	79
2.3.3.1	Methods	79
2.3.3.2	Results.....	80
2.3.3.3	Discussion and Conclusion	82
2.4	Patient Acquisitions & Image Quantification	83
2.4.1	Tumour to Background Ratio	84
2.4.1.1	Methods for Investigations 1 - 4	84
2.4.1.2	Investigation 1 Results - Iterative (IT) versus Filtered Back Projection (FBP) reconstruction of data acquired at 2 Hours .	90
2.4.1.3	Investigation 2 Results - 2Hr Iterative (IT) Tumour to background ratio T:B versus Histology.....	94
2.4.1.4	Investigation 3 Results - 2Hr and 4Hr tumour to background ratios T:B versus Histology.	98
2.4.1.5	Investigation 4 Results - Tumour to background ratio T:B in the mediastinum versus Histology.....	105
2.4.2	Tracer percentage Uptake	109
2.4.2.1	Methods for Investigations 5 - 6	109
2.4.2.2	Results for Investigation 5 - Correlation of 2Hr % Uptake with Histology	111
2.4.2.3	Results for Investigation 6 - % Uptake Washout Versus Histology	114
2.5	NeoSPECT Discussion and Conclusion	118
Chapter 3 - Hybrid Imaging		127
3.1	SIEMENS Symbia T.....	127
3.1.1	CT Technology	129
3.1.2	New SPET Reconstruction Algorithms	131
3.1.2.1	Scatter and CT attenuation Corrections.....	132

3.2	Influence on Bone Imaging	138
3.2.1	Characterisation of indeterminate Bone Scan Findings.....	138
3.2.2	Incidental Findings	139
3.3	Customised Phantoms for SPET-CT.....	142
3.3.1	Requirements	143
3.3.2	Phantom Design	144
3.3.2.1	Bone Substance	147
3.3.2.2	Identification of correct bone solution concentration	148
Chapter 4 - OctreoScan Imaging		152
4.1	Introduction	152
4.2	Literature Review	153
4.3	Patient Acquisition Data.....	157
4.3.1	Pilot Review of Flash3D Reconstruction	160
4.3.2	Methods - Corrected Versus Uncorrected.....	162
4.3.2.1	Investigation 1: Qualitative Assessment.....	165
4.3.2.2	Investigation 2: Semi-Quantitative Assessment	167
4.3.3	Results - Corrected Versus Uncorrected	169
4.3.3.1	Investigation 1: Qualitative Assessment Results	171
4.3.3.2	Investigation 2: Semi-Quantitative Analysis Results	174
4.3.4	Discussion and Conclusion.....	181
4.4	¹¹¹ In Phantom Acquisition Data	183
4.4.1	Investigation 1 - Optimisation of post reconstruction filter	183
4.4.1.1	Methods for Investigation 1 - Optimisation of post reconstruction filter.....	183
4.4.2	Investigation 2 - Accuracy of hybrid imaging quantification techniques.....	189
4.4.2.1	Methods for Investigation 2 - Accuracy of hybrid imaging quantification techniques	190
4.4.2.2	Results for Investigation 2 - Accuracy of hybrid imaging quantification techniques	193
4.4.3	Discussion/Conclusion - ¹¹¹ In Phantom Data Acquisition	195
4.5	^{99m} Tc Phantom Acquisition Data.....	197
4.5.1	Methods - ^{99m} Tc Phantom Acquisition Corrected Versus Uncorrected	197
4.5.2	Results - ^{99m} Tc Phantom Acquisition Corrected Versus Uncorrected ..	200
4.5.3	Discussion and Conclusion - ^{99m} Tc Phantom Acquisition Corrected Versus Uncorrected	205
4.6	Discussion and Conclusion	207
Chapter 5 - Thesis Conclusion and Discussion		211

Appendices	216
Appendix A - NeoSPECT LREC Approval.....	217
Appendix B - NeoSPECT Imaging Proforma.....	219
Appendix C - OctreoScan Observer Score Record	220
Appendix D - Reproducibility results for each observer.....	221
References	225

List of Tables

Table 1 - Annual Frequency of Nuclear Medicine Investigations Worldwide	15
Table 2 - Radiopharmaceuticals licensed in UK for Imaging	17
Table 3 - Affinity of SSTR expression	24
Table 4 - Somatostatin Based Imaging Agents.....	25
Table 5 - NeoSPECT Administration Details.....	27
Table 6 - Neuroendocrine tumour types	28
Table 7 - OctreoScan Administration Details	28
Table 8 - Analytical versus Iterative	41
Table 9 - Acquisition Parameters	60
Table 10 - Reconstruction Parameters	61
Table 11 - Repeatability of 3 sec Acquisition	62
Table 12 - Difference in Total Counts	66
Table 13 - Phantom Activities	69
Table 14 - T:B per transverse slice	72
Table 15 - Non-AC Recon Data.....	73
Table 16 - AC Recon Data	73
Table 17 - Sensitivities	74
Table 18 - Phantom Count Data	75
Table 19 - Activities: Actual Versus Calculated.....	76
Table 20 - Reconstruction Parameters	80
Table 21 - Comparison of Reconstruction Parameters	81
Table 22 - Acquisition Parameters	87
Table 23 - Iterative Reconstruction Parameters	88
Table 24 - Reconstruction Parameters	91
Table 25 - Summary of NeoSPECT patient's pathology details	99
Table 26 - Correlation of CT & NeoSPECT findings	100
Table 27 - T:B _s at 2 & 4Hours	101
Table 28 - Mediastinal Uptake.....	106
Table 29 - Injected Activities.....	111
Table 30 - % Uptake calculated at 2 hours.....	112
Table 31 - Total tumour counts per patient.....	115
Table 32 - Predicted Versus actual uptake at 4 hours	116
Table 33 - Typical Hounsfield Units.....	129
Table 34 - Bone Scan Performed January 08 - December 2008	148
Table 35 - Patient Trabecular Bone Values and Phantom Values	149
Table 36 - OctreoScan Whole Body Acquisition Parameters	158
Table 37 - OctreoScan SPET Acquisition Parameters	158
Table 38 - OctreoScan OSEM Reconstruction Parametes	160
Table 39 - OctreoScan Patient Demographics	163
Table 40 - Scan versus Disease Outcome.....	170
Table 41 - Entire Volume Reconstruction Technique Score	171
Table 42 - 'Entire' Volume Friedman Test Results	172
Table 43 - Lung Volume Reconstruction Technique Score.....	172
Table 44 - 'Lung' Volume Friedman Test Results	173
Table 45 - 'Entire' Volume Wilcoxon Signed Ranks Test Results	174
Table 46 - 'Lung' Volume Wilcoxon Signed Ranks Test	174
Table 47 - OctreoScan Acquisition Parameters	184
Table 48 - OctreoScan Reconstruction Parameters.....	185
Table 49 - Optimised Display Parameters.....	185

Table 50 - Settings for In111 filled phantom	188
Table 51 - Setting for Tc99m filled phantom.....	188
Table 52 - SPET-CT Phantom Activities and Acquisition Times	190
Table 53 - SPET-CT STD Activities and Acquisition Times	191
Table 54 - Sensitivities	193
Table 55 - Total Counts for Each Reconstruction Technique.....	193
Table 56 - Activities Calculated	194
Table 57 - Phantom Activities and Acquisition Times.....	197
Table 58 - STD Activity and Acquisition Times	197
Table 59 - Sensitivities	201
Table 60 - Total Counts and Sensitivity for Each Reconstruction Technique	201
Table 61 - Activities Calculated	201

List of Figures

Figure 1 - ^{99m}Tc MDP Bone Scan (Sclerotic Metastases)	19
Figure 2 - Example CT Lytic & Sclerotic Bone Lesion	20
Figure 3 - ^{99m}Tc MDP Bone Scan (Bone metastases sclerotic and lytic in name) .	21
Figure 4 - Anatomy: Hypothalamus and Pituitary Gland	22
Figure 5 - Anatomy: Stomach, Pancreas and Intestines.....	23
Figure 6 - Somatostatin Receptor and Sub-Groups	25
Figure 7 - Basic Anatomy of the Lungs	26
Figure 8 - Series Projections/Frames.....	32
Figure 9 - Sinogram generation.....	33
Figure 10 - Ramp Filter	34
Figure 11 - Butterworth Filter	35
Figure 12 - FBP Simplified.....	36
Figure 13 - Iterative approaches to image reconstruction	37
Figure 14 - OSEM Reconstruction Process.....	38
Figure 15 - Changs Attenuation Correction	42
Figure 16 - Anthropomorphic Thoracic Phantom.....	55
Figure 17 - In-house designed Phantom	56
Figure 18 - Planar view of a typical standard acquisition	60
Figure 19 - Transverse Slice of STD ROIs	61
Figure 20 - Graph of Variation in Total Cts per Acquisition	63
Figure 21 - Attenuation Circumference Delineations	64
Figure 22 - Graph of Influence of Attenuation Correction.....	65
Figure 23 - In-house Phantom Filled	69
Figure 24 - Phantom Transverse Slices 0Hr versus 2Hr.....	70
Figure 25 - ROIs for Uptake Analysis.....	71
Figure 26 - Graph of Relative Error in Activity Calculation	76
Figure 27 - Qualitative Comparison of transverse slices	81
Figure 28 - NEOSPECT Uptake in Abnormal Patient	84
Figure 29 - Patient Head and Arm Rest	86
Figure 30 - Detector Set - Up Configuration.....	87
Figure 31 - Colour Schemes	89
Figure 32 - Lung ROIs	90
Figure 33 - Graph of Variation in Total Counts.....	91
Figure 34 - Graph of 2Hr Max T:B (Total Counts)	92
Figure 35 - Qualitative Comparison	93
Figure 36 - Graph of Malignant Versus Benign Disease.....	95
Figure 37 - Lesion Type	96
Figure 38 - Graph of Characterisation of NSCLC Sub Type	97
Figure 39 - Graph of 2Hr Versus 4Hr T:B	102
Figure 40 - Graph of Pre versus Post Histology T:B Results	103
Figure 41 - Graph of Difference in Total versus Max Counts in ROI	104
Figure 42 - Graph of T:B Mediastinal Nodes	106
Figure 43 - Graph of Tumour Vs Lymph Tissue Uptake Over Time	108
Figure 44 - Graph of % Uptake @ 2Hrs.....	113
Figure 45 - Graph of Uptake @ 4Hrs Predicted Versus Actual.....	116
Figure 46 - Spot the difference.....	122
Figure 47 - Symbia T	128
Figure 48 - Loss in resolution with increasing distance	132
Figure 49 - Symbia SPET Example of Scatter Windows, DEW	134

Figure 50 - Symbia MU Map	135
Figure 51 - Bilinear Response,	137
Figure 52 - Benign Versus Malignant	138
Figure 53 - SPET CT; Invasion of Spinal Cord	139
Figure 54 - Calcified Fibroid	140
Figure 55 - Guide to compartment distribution within phantom	144
Figure 56 - Schematic of Phantom (including actual dimensions)	145
Figure 57 - In-house manufactured SPET-CT Phantom	146
Figure 58 - Standard ROI for Patient CT	149
Figure 59 - SPET CT Phantom ROIs	150
Figure 60 - Standard Images Acquired	157
Figure 61 - Peak and Scatter Windows	159
Figure 62 - Anonymised Data Format	164
Figure 63 - Example of Varying Quality of SPET Images	166
Figure 64 - OSEM Versus Flash 3D SAC	168
Figure 65 - CT Boundary Delineation	169
Figure 66 - Graph of Entire OctreoScan Volume Observer Score	171
Figure 67 - Graph of Lung OctreoScan Volume Observer Score	173
Figure 68 - SPET-CT Liver (Flash3D SAC) with profiles	175
Figure 69 - Liver Vertical profile	176
Figure 70 - Liver Vertical profile; patient arms across chest	177
Figure 71 - CT of Liver Vertical Profile	178
Figure 72 - Graph of Lung profiles	179
Figure 73 - SPET-CT Lung (CT, OSEM & F3D SAC)	180
Figure 74 - In111 Filled Phantom	184
Figure 75 - ROI's defined by structure & radioactive contents	187
Figure 76 - SPET-CT Acquisition of Hybrid Phantom	191
Figure 77 - In-111 SPET-CT ROIs	192
Figure 78 - Graph of Calculated Versus Actual Activity (MBq) In111 SPET-CT phantom	194
Figure 79 - SPET-CT Acquisition of Lung Phantom and STD	198
Figure 80 - Lung Phantom and STD ROIs	200
Figure 81 - Graph of Calculated Versus Actual Activity (MBq) Tc99m Lung Phantom	202
Figure 82 - Qualitative Differences Demonstrated	203
Figure 83 - Vertical Profiles; HOSEM Versus F3D SAC	204

Acknowledgements

The work carried out in this thesis was undertaken in the department of Nuclear Medicine at Glasgow Royal Infirmary and was supervised Dr Alison Bolster, Head of Nuclear Medicine.

I would like to thank all my colleagues in nuclear medicine at both Glasgow Royal Infirmary and Stobhill Ambulatory Care Hospital for their help and support throughout the years that it has taken the work in this thesis to be submitted. In particular I would like to say a special thank you to Mrs Carol Norwood for sourcing and retrieving patient case notes. Mrs Anne French and Mr Douglas Wright who took NeoSPECT patient acquisition set up notes and performed standard acquisitions when I was not available to do so.

I would like to thank my colleagues Dr John Shand, Dr Sai Han, Dr FW Poon, and Dr Alison Bolster who all kindly gave their own time to review images as part of the observer study for the OctreoScan work. I would also like to thank Ms Clare McKeown, who anonymised the OctreScan patient data.

I would like to thank my advisor of studies Prof Alex T Elliott who provided advice and encouragement throughout my PhD and write up period.

I would like to say a very special thank you to my supervisor Dr Alison Bolster who has provided invaluable advice, encouragement and support throughout my PhD, whilst also giving up her own time to provide comments and advice during the thesis write up period.

I would like to thank my family and friends. My parents, James and Sylvia, and my sister, Julie, who have always been encouraging and supportive of my academic choices. My grandparents, Sylvia, Eddie, Maureen and James who reminded me that life isn't easy and to show 'a bit of grit and determination', they knew the real meaning of this - Thank You!

Finally, my husband David who also sacrificed his evenings and weekends yet despite this always remained patient and supportive, and always knew when a beer was required - Cheers!

Author's Declaration

I declare that this thesis represents my own work except where referenced to others.

I declare that this thesis does not include work forming part of a thesis presented successfully for another degree.

A handwritten signature in black ink, reading "Gillian Ainslie-McLaren". The signature is written in a cursive style with a large initial 'G'.

Gillian Ainslie-McLaren

October 2011.

Chapter 1 - Introduction

Nuclear medicine imaging (now also often referred to as molecular imaging) is known for its truly functional nature which, in part, offsets the lack of spatial resolution when compared to other imaging modalities. In particular, tomographic nuclear medicine imaging with a resolution of 8mm at best, compares somewhat unfavourably to CT or MRI which can have sub 1-mm resolution. Despite this limitation, nuclear medicine imaging provides valuable physiological information which is unobtainable by CT or MRI. As a result, molecular imaging has a long and well established role in the diagnosis and management of patients with cancer and is successfully used worldwide (see **Table 1**) in imaging a number of cancers such as those involving the thyroid and other neuroendocrine tumours, liver and brain.

Country	Annual frequency of nuclear medicine procedures (per thousand population)
Canada	65
Germany	34
USA	32
Netherlands	16
Australia	12
UK	11
New Zealand	8
Portugal	4

Table 1 - Annual Frequency of Nuclear Medicine Investigations Worldwide (Gemmel, 2008)

Confidence in the effectiveness of nuclear medicine's role in managing patients with cancer has been demonstrated by the inclusion of nuclear medicine imaging procedures into UK's National Institute of Health and Clinical Excellence guidelines (NICE Clinical Guideline). NICE is an independent organisation within the UK which provides national guidelines to promote good health and also to prevent, treat and manage ill health, NICE recommends nuclear medicine imaging in their guidelines for the management of many of the main cancer groups, most notably prostate and breast cancer. In Scotland a similar body produces Scottish Intercollegiate Guidelines Network guidelines (SIGN).

1.1 Current Radiopharmaceuticals used in imaging of cancer

There are a number of radioisotopes currently used in imaging, all of which possess at least two of the following characteristics which are ideal for diagnostic imaging purposes:

- Half -life, this must be long enough to image and assess the metabolic process of organs of interest, whilst it must also be short enough to minimise the radiation dose to the patient and others.
- Decay process is also important, isomeric transition being the most desirable as this mechanism emits gamma rays and low energy electrons only, that is, no beta emissions. In this way the radiation dose to the patient can be kept low and imaging can be achieved.
- Energy of the emitted gamma rays; radioisotopes which emit low energy gamma rays (<250keV but > 80keV) are ideal as they can easily escape the human body and can be detected by a gamma camera. Again this allows the radiation dose to the patient to be minimised.
- The chemistry of the radioisotope is also important to allow binding to a suitable pharmaceutical.

The main radioisotope used currently in nuclear medicine in the UK is Tc-99m but In-111, I-123 and Ga-67 are also used. Technetium (Tc-99m) is heavily used mainly because of its flexible chemistry which allows it to be bound to many different pharmaceuticals. It also has a six hour half life and emits low (140 keV) energy gamma rays. Some typical radiopharmaceuticals which are licensed and marketed for imaging in the UK to investigate various cancers are shown in **Table 2**, (UKRG Radiopharmacy Handbook):

Radiopharmaceutical	Area of Interest
^{99m} Tc Methylidiphosphonate (MDP)	Bone malignancy and metastasis
¹²³ I Iodide or ²⁰¹ Tl Chloride or ¹³¹ I Iodide	For thyroid tumours
¹²³ I Iodide or ²⁰¹ Tl Chloride	For thyroid metastases
^{99m} Tc (V) Dimercaptosuccinic acid (DMSAV)	Medullary carcinoma of thyroid
¹²³ I metaiodobenzylguanidine (mIBG)	Neuroendocrine tumours
¹¹¹ In Pentetreotide	Somatostatin producing tumours
^{99m} Tc Depreotide	Lung malignancy
^{99m} Tc Colloid	Sentinel node localisation in breast & melanomas
²⁰¹ Tl Chloride	Active brain tumours
⁶⁷ Ga Citrate	Lymphoma (recurrence, restaging & management)
^{99m} Tc Sestamibi	Parathyroid adenoma imaging.

Table 2 - Radiopharmaceuticals licensed in UK for Imaging (UKRG, 2002)

Not all of the radiopharmaceuticals on this list are included in NICE guidelines but the products listed are being currently used to either diagnose or to aid in the diagnosis of some cancers.

1.1.1 ^{99m}Tc – Methylene Diphosphonate – Radiopharmaceutical Properties

Radionuclide bone imaging was first demonstrated in 1961 using Strontium - 85, ⁸⁵Sr. During the next 10 years there were a number of redevelopments of bone imaging radiopharmaceuticals, all of which were found to be somewhat limited either in terms of their physical or physiological characteristics. In 1971, Technetium - 99m was labelled to a number of phosphate compounds (polyphosphates, pyrophosphates and diphosphonates) all of which demonstrated a good target to background ratio. However, it was found that both the poly - and pyro - phosphates were susceptible to in vivo breakdown by tissue phosphatases, a characteristic which the diphosphonates did not share. This inability of the diphosphonates to breakdown down under tissue phosphatases along with their ability to bind to bone surface meant that this radiopharmaceutical had no loss in uptake over the time required to image a patient. At present ^{99m}Tc diphosphonates are the gold standard for imaging bone. In the UK ^{99m}Tc methylene diphosphonate (MDP) is used and in the UK and

elsewhere (for example Europe) ^{99m}Tc hydroxymethylene diphosphonate (HDP) is used (McKillop and Fogleman, 1991).

Glasgow makes use extensively of ^{99m}Tc MDP which is useful in demonstrating bone disease because the mechanism of uptake is due to bone turnover, that is, osteoblastic activity. This means that areas of high osteoblastic activity will demonstrate high uptake of diphosphonates; there are a number instances in which the body will produce an increased osteoblastic response:

- Growth (Babies, children and young adults)
- Trauma
- Infection (Osteomyelitis)
- Metabolic bone disease (Paget's disease)
- Malignancy (Primary bone tumours, metastases from prostate, breast and lung cancer)

The most common use of a ^{99m}Tc MDP bone scan today is in imaging of bone metastases. The bone scan can be used as part of the initial diagnosis and staging of the disease but may also be used to monitor disease progression or response to treatment and an example of an abnormal bone scan is shown in **Figure 1**.

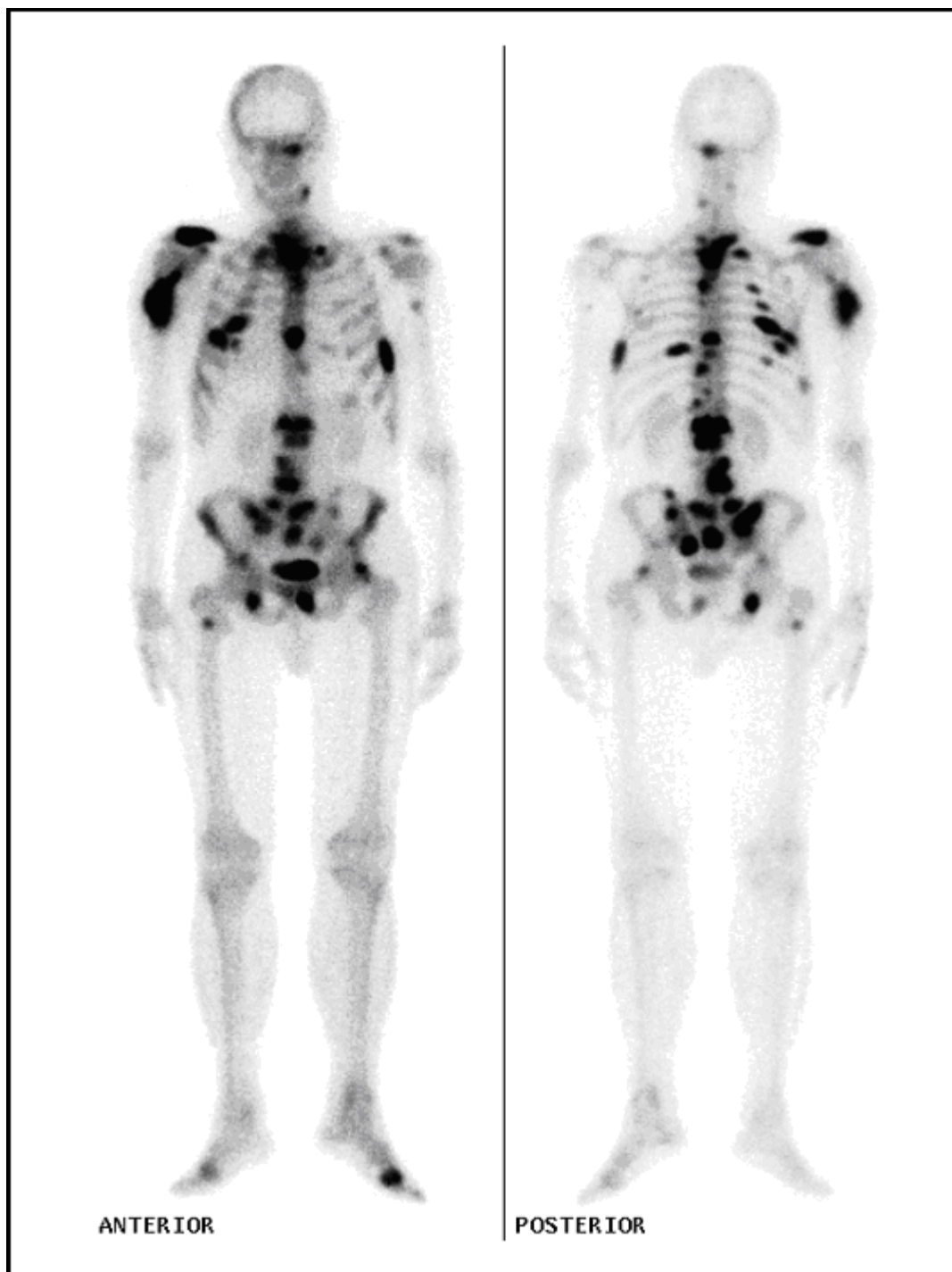


Figure 1 - ^{99m}Tc MDP Bone Scan (Sclerotic Metastases)
Images shown are whole body planar images, these images demonstrate multiple areas of increased ^{99m}Tc MDP uptake in keeping with sclerotic bone metastases.

In addition to an increase in osteoblastic response, that is sclerotic deposits, there are a number of bone diseases which result in reduced or no osteoblastic activity. These often produce lytic lesions and are usually demonstrated by x-ray and CT. **Figure 2** shows an example of a lytic and a sclerotic lesion as demonstrated by CT.

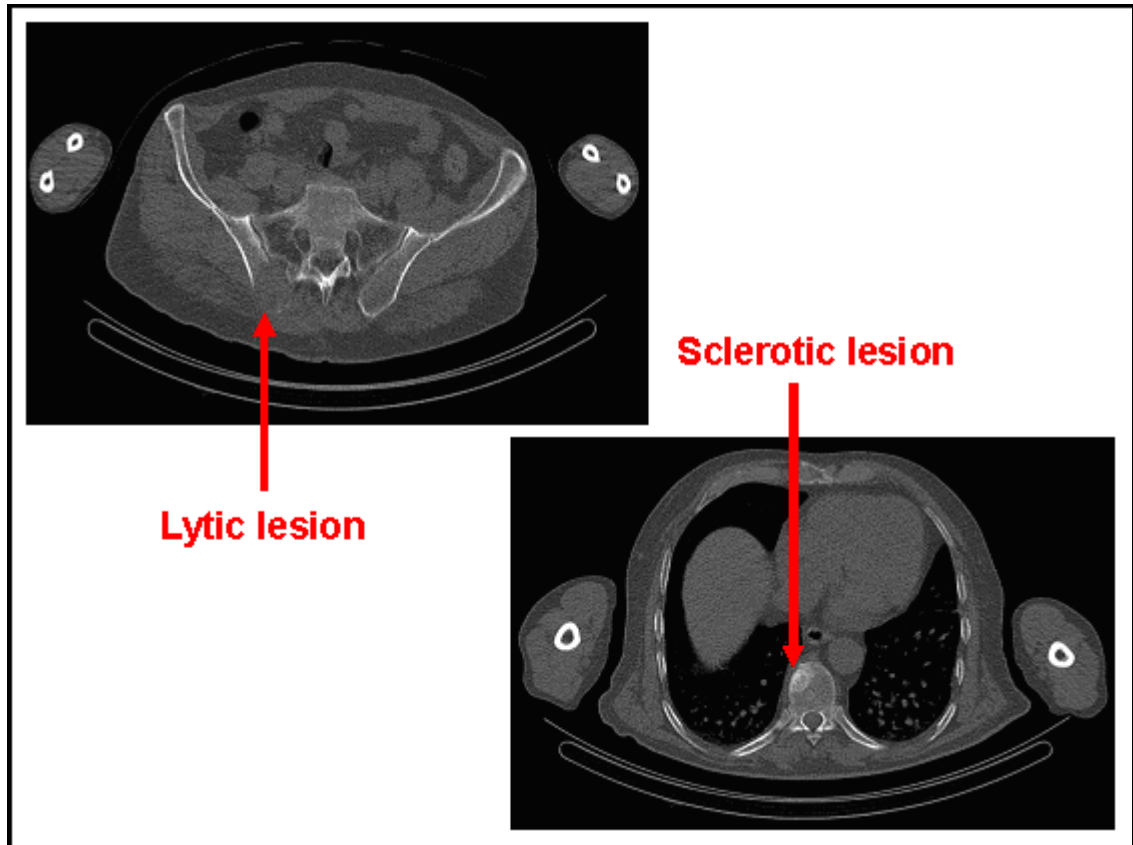


Figure 2 - Example CT Lytic & Sclerotic Bone Lesion

Images show transverse CT slices through the pelvis (upper left image) which demonstrates a lytic area of the bone and a transverse CT slice through the thorax (bottom right image) which demonstrates an area of sclerosis in one of the vertebrae.

The sclerotic lesion demonstrated in **Figure 2**, will be easily identified on the bone scan in a similar manner to the increased uptake demonstrated in **Figure 1**. The lytic lesion, however, may not be identified on the bone scan. There may be instances, however, when a bone scan is able to identify a lytic lesion. This usually only occurs when either the lytic lesion has become so large that it appears as a photopenic area or when there is an osteoblastic response in the area surrounding a lytic lesion, an example of which is shown in **Figure 3**.

Myeloma is a bone disease that produces lytic lesions and the bone scan's ability to detect these lesions lies solely in the extent of the osteoblastic reactive response to the damage evoked by the lytic component. The extent of reactive osteoblastic activity is variable and therefore the bone scan is not the ideal tool for imaging myeloma as there is a risk of missing a lesion.

Prostate cancer metastases in the bone are usually sclerotic lesions whilst breast and lung cancer metastases in the bone may have both a lytic and sclerotic component (Hayat, 2008). Depending on the primary source of cancer the bone metastases can be sclerotic or lytic or both as in **Figure 3** .

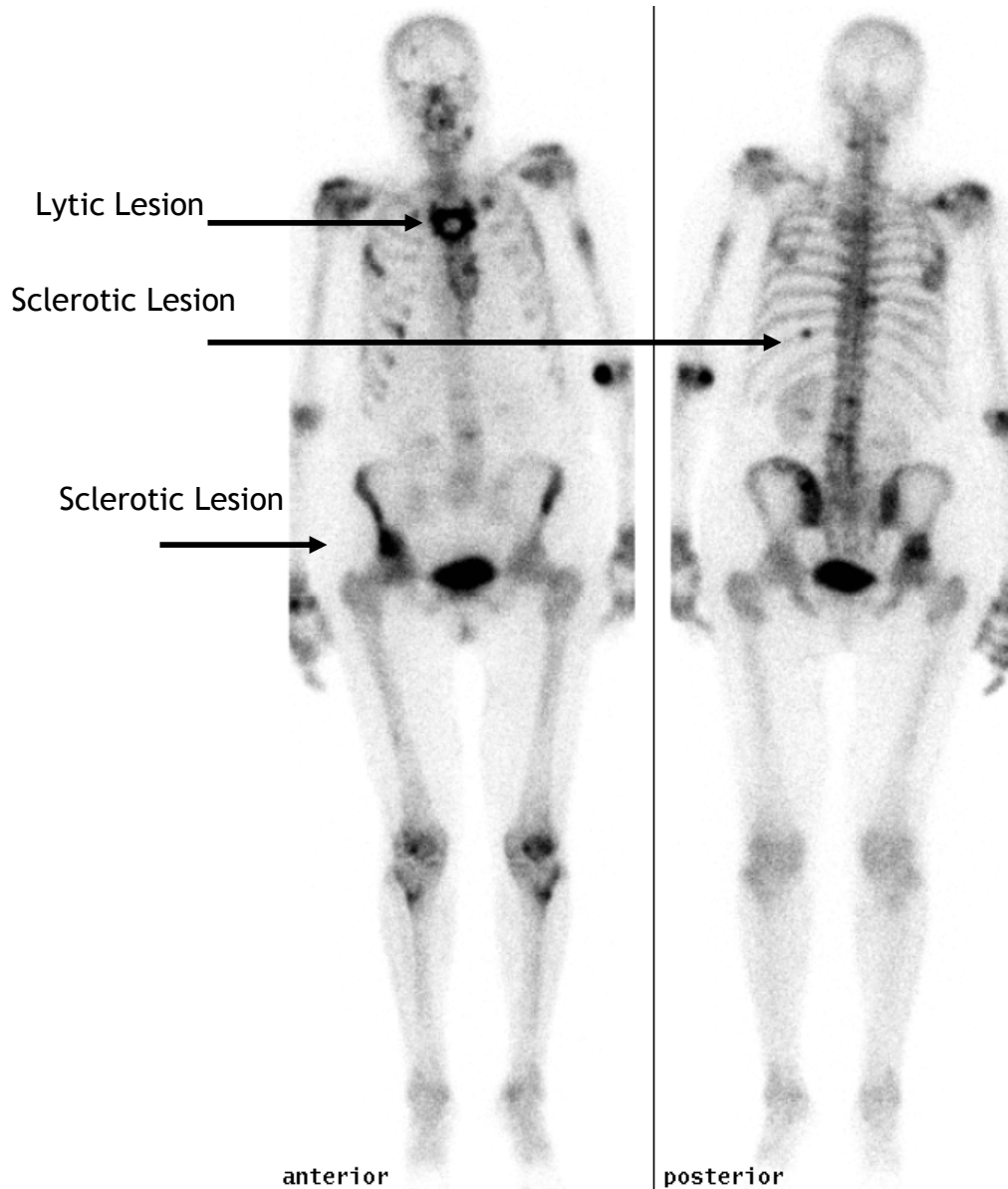


Figure 3 - ^{99m}Tc MDP Bone Scan (Bone metastases sclerotic and lytic)
Images shown are whole body planar images, the image demonstrates areas of reduced uptake along with areas of increased ^{99m}Tc MDP uptake, as indicated by the arrows and in keeping with both lytic and sclerotic lesions.

Figure 3 is a bone scan from a breast cancer patient who has bone metastases that are both sclerotic and lytic in nature.

More recently the positron emitter ^{18}F fluoride (PET-CT) has been reconsidered as a bone imaging agent. Despite this imaging technique being very effective it is also very expensive and its availability throughout the UK remains limited in some areas, whilst $\text{Tc}^{99\text{m}}$ MDP bone imaging remains a low cost, readily available and effective imaging agent.

1.1.2 Somatostatin Receptor Imaging

One of the major steps forward in molecular imaging of tumours and in particular neuroendocrine type tumours came with the introduction of several agents which allowed somatostatin receptor imaging.

Somatostatin (SST) is a Growth Hormone - Inhibiting Hormone (GH-IH), and is present on one of two forms; SST - 14 (consisting of 14 amino acids) and SST - 28 (consisting of 28 amino acids).

SST is produced by a number of organs in the body - most notably brain, intestines and pancreas. In the brain SST is produced in the hypothalamus and is released into the anterior pituitary gland - see **Figure 4**. The presence of SST inhibits the release of Growth Hormone and Thyroid Stimulating Hormone (de Herder, 2003).

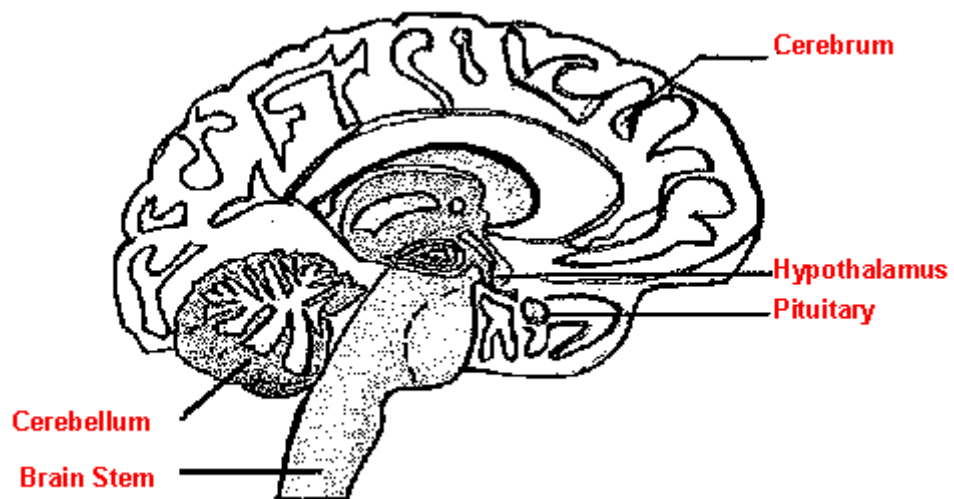


Figure 4 - Anatomy: Hypothalamus and Pituitary Gland
Image showing basic structures within the brain.

In addition to the Hypothalamus, SST is also produced in a number of locations in the gastrointestinal system (stomach, intestines and pancreas) - See **Figure 5**.



Figure 5 - Anatomy: Stomach, Pancreas and Intestines
Image showing basic structures within the abdomen (Carrieshealth).

The job of SST is to help regulate the release of hormones, as a result of which, SST has an affect on many physiological processes, most notably those which involve the gastrointestinal tract. The presence of SST in these areas inhibits the release of many gastrointestinal and pancreatic hormones, this leads to a reduction in the rate of gastric emptying whilst also reducing blood flow to the intestines and smooth muscle contractions. In addition to its hormone regulatory role, SST also controls cell proliferation in both normal and tumour tissues.

SST is able to target cells via Somatostatin Receptors (SSTR), of which there are 5 different types, SSTR 1-5. All five SSTR demonstrate a high binding affinity to both SST - 14 and SST - 28. Like SST's, SSTR's can be found throughout the central and peripheral nervous system (de Herder, 2003).

In terms of imaging, the major breakthrough came with the realization that some disease processes over expressed SSTRs. Many tumours are known to over express SSTRs, see **Table 3**. As a result of this SSTR imaging was established in the mid 1990s.

		Affinity
Neuroendocrine tumours	{Pituitary Adenomas, Carcinoids, Islet cell Ca, Paragangliomas, Pheochromocytomas, Medullary thyroid Ca, SCLC}	High
Tumours of nervous system	{Astrocytomas, Neuroblastomas, Meningiomas}	High
Lymphomas		High
Breast tumours		~50%
Ovarian Ca, Colon Ca		Low
Glioblastomas, NSCLC		No receptors
Exocrine Pancreatic Ca, Prostate Ca		No receptors

Table 3 - Affinity of SSTR expression (Reubi, 1992)

Table 3 shows non small cell lung cancer, NSCLC, using in-vitro testing, to have demonstrated no over expression of SSTR. However, further in-vivo tests found that NSCLC demonstrated uptake of some synthetic SST analogs therefore indicating that NSCLC did in fact over express SSTR. This was contradictory to the in-vitro findings and led to further investigations which concluded that NSCLC tumour tissue did not over express SSTRs however, the other pathologies associated with NSCLC did i.e. inflammatory processes surrounding the tumour such as granulomas (Blum, 2000).

Based on their affinity to bind to the various synthetic SST analogs, the five SSTRs described previously have been further divided into two subgroups, see **Figure 6**. Group 1 includes SSTR 2, 3 and 5 and these have a binding affinity with synthetic SST analogs, whilst Group 2 is comprised of SSTR1 and 4 which have an extremely poor binding affinity with synthetic SST analogs (Srikant, 2004).

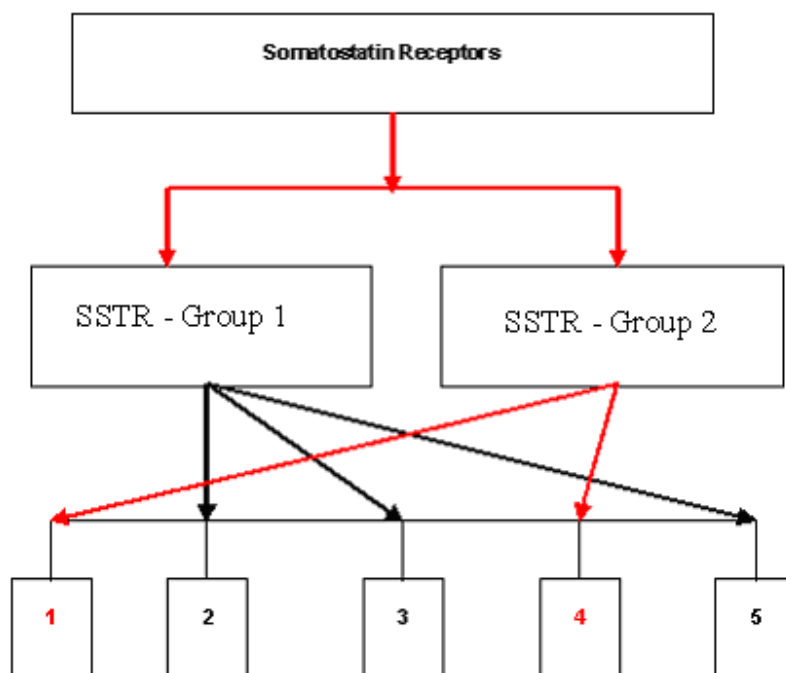


Figure 6 - Somatostatin Receptor and Sub-Groups

Chart categorising somatostatin receptors subgroups based on their affinity to bind with synthetic SST analogs. Group 1 - are receptors with high affinity indicated by black arrows and Group 2 - are receptors with low affinity indicated by the red arrows.

An overview of some of the more successful peptides available or investigated over the years are detailed in **Table 4**.

Radioligand	Availability	Receptor binding data
^{123}I -octreotide	No longer in use	Not studied
^{123}I - Tyr ³ -octreotide	No longer in use	hSSTR2, 5
^{111}In -DTPA-D-Phe ¹ -octreotide (pentetreotide)	Commercially available	hSSTR2, 5
^{111}In -DOTA-Tyr ³ -octreotide	May be prepared in house	hSSTR2, 5
^{111}In -DOTA-lantreotide (MAURITIUS)	In house	hSSTR2-5
$^{99\text{m}}\text{Tc}$ -HYNIC- octreotide	In house	Not studied
$^{99\text{m}}\text{Tc}$ -depreotide	Commercially available	hSSTR2, 3, 5
^{123}I -VIP	In house	hSSTR 3, VIPR1, 2

Table 4 - Somatostatin Based Imaging Agents (Baert and Sartor, 2006)

In 2004, of those described in **Table 4** only 2 radiopharmaceuticals were considered effective in imaging tumours which over expressed somatostatin receptors in: these had the trade names of OctreoScan (^{111}In pentetreotide) and NeoSPECT ($^{99\text{m}}\text{Tc}$ depreotide).

1.1.2.1 Lung Cancer and NeoSPECT Radiopharmaceutical Properties

Lung cancer remains one of the leading causes of mortality within the world. It can be subclassified into various types with the two major sub-types of primary lung cancer being Small Cell (SCLC) and Non-Small Cell (NSCLC). These are defined by how the tumour cells look under a microscope.

Lung cancer of a small cell nature is responsible for 1 in 5 lung cancers and is usually as a direct result of smoking. This form of lung cancer is usually treated with chemotherapy and radiotherapy, whilst NSCLC can be treated using surgery, chemotherapy and radiotherapy (MacMillan-Lung, 2011).

Around 80% of lung cancers are of the NSCLC type. NSCLC are prone to spread and distant metastasis can be found. Around 7% - 10% of patients are asymptomatic and disease in these patients is found incidentally. The NSCLC types are divided into a further three subsets, squamous cell carcinomas, adenocarcinomas and large cell carcinomas.

Squamous cell carcinoma is the commonest of the NSCLC group and is often as a direct result of smoking. These types of tumours usually form around the centre of the lung, near the large airways, the bronchi - see **Figure 7**.

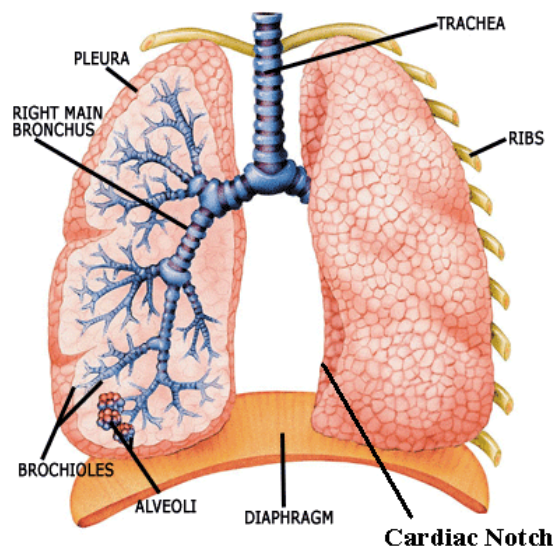


Figure 7 - Anatomy of the Lungs
Image showing basic structures within the lungs (W-Healthy, 2011)

Most peripheral tumours are of the adenocarcinoma type and these are most often associated with non-smokers (CancerResearchUK-Lung, 2011). Unlike squamous cell and adenocarcinomas, tumours of a large cell type can occur in any part of the lung and are rapidly growing tumours.

As discussed in **section 1.1.2**, disease and processes surrounding the disease associated with both small and non small lung cancer (SCLC and NSCLC) have been found to over express somatostatin receptors relative to normal tissue. ^{99m}Tc -labelled Depreotide, commercially known as ^{99m}Tc -labeled NeoSPECT, is a Technetium, ^{99m}Tc , labeled, 10 amino acid, synthetic peptide that contains a SSTR-binding domain. Details of NeoSPECT administration to patients are detailed in **Table 5**.

Activity Administered (MBq):	600
Volume Administered (ml):	5
Route:	Intravenously
Effective Dose (mSv):	12
Preparation of Patient:	No special preparation
Imaging Time:	2 hours post injection

Table 5 - NeoSPECT Administration Details (NeoSPECT™, 2001)

Of the 5-SSTR subgroups demonstrated in **Figure 6**, depreotide binds to three of these; SSTR2, 3, and 5 with a high affinity. Not only do SST peptide analogs bind to SSTRs but they also clear rapidly from the circulation.

1.1.2.2 Neuroendocrine Tumours and OctreoScan Radiopharmaceutical Properties

The terms Neuroendocrine tumour (NET) covers a large family of tumours that originate from the neuroendocrine system since neuroendocrine cells are found all over the body. However, most NET's fall into one of the two main groups; Pancreatic Neuroendocrine Tumours (PNT) and Carcinoid Tumours. **Table 6** details some of the various forms of the PNT along with organs where carcinoid tumours may originate.

Pancreatic Neuroendocrine Tumours	Carcinoid Tumours
Insulinoma	Small Bowel
Gastrinoma	Large Bowel
Glucagonoma	Pancreas
Somatostatinoma	Lung
VIPoma	Ovaries

Table 6 - Neuroendocrine tumour types (Baert and Sartor 2006) (MacMillan-NET, 2011)

It is the carcinoid group which are usually imaged with OctreoScan as the PNT group contains tumours for which Octreoscan is not as sensitive, this is because this group of tumours may or may not overexpress SSTR and in particular SSTR2, or 5 (Baert and Sartor, 2006).

Around 85% of carcinoid tumours occur in the digestive system (CancerResearchUK-NET, 2011) but can be found in other organs as described in **Table 6**. These types of tumours are, however, rare and can be difficult to diagnose, with currently only 1500 people in the UK being diagnosed each year (MacMillan-NET). OctreoScan is most commonly used to identify and localize carcinoid tumours and their metastases.

¹¹¹In-labelled Pentetreotide, commercially known as ¹¹¹In-labeled OctreoScan, is an Indium, ¹¹¹In, labeled, synthetic peptide that contains a SSTR-binding domain pharmaceutical called pentetreotide. Details of OctreoSCAN administration to patients are detailed in **Table 7**.

Activity Administered (MBq):	220
Volume Administered (ml):	2
Route:	Intravenously
Effective Dose (mSv):	17
Preparation of Patient:	Bowel Prep evening before imaging and information regarding Sandostatin therapy should be obtained.
Imaging Time:	2 hours post injection

Table 7 - OctreoScan Administration Details

OctreoScan is similar to NeoSPECT in that it is also a somatostatin analogue but it binds to a fewer SSTRs. Of the 5-SSTR subgroups demonstrated in **Figure 6**, pentetreotide binds to two of these; SSTR2, and 5 with a high affinity. It should be noted that this uptake may be inhibited if the patient is undergoing

Sandostatin therapy therefore it is important that this information is known prior to imaging (OctreoScan®).

Physiological uptake of OctreoScan is demonstrated in the pituitary gland, thyroid, liver, spleen and bowel. Also, since almost all of the tracer is eliminated from the body via the renal system, uptake is demonstrated in the kidneys, ureters and urinary bladder (OctreoScan®).

1.2 Past and current imaging techniques

The gamma camera was first designed by Hal Anger in the 1960s. Since then although there have been major technological advances, the basic concepts proposed by Anger still form the basis of today's gamma cameras.

1.2.1 Gamma Camera Technology

The gamma camera makes use of the scintillation properties of the NaI(Tl) crystal. Using a lead collimator to minimise scattered radiation, gamma rays incident on the crystal produce light which is detected using an array of photomultiplier tubes.

In 1960, Anger's first camera had a circular field of view, since then improvements in crystal growing and manufacture mean that most modern cameras are rectangular in shape and of significant size (540mm x 400mm). In the original systems a single camera head was used, nowadays multi-headed systems are the norm. Improvements in mechanics and electronics have made it possible to move from images where the camera remained static throughout the study to those where the camera moves with respect to the bed to allow wholebody imaging. This was followed by the use of the camera being rotated through 360° to obtain projections around the patient's body. Major advances in computing power within the last 20 years then meant that these projections could be reconstructed to allow tomographic images which could be manipulated in three dimensions. In a general department which undertakes mainly wholebody and tomographic studies it is usual to have a double headed camera with the heads mounted 180° opposed.

Gamma Cameras now utilise analogue to digital converters (ADC's) on each photomultiplier tube (PMT) allowing for on-the-fly corrections and microprocessor driven calculations of the x, y and z signals to be made, moving away from the inherent problems of Anger arithmetic. (Farr & Allisy-Roberts, 1998).

Most recently, technology has allowed hybrid type cameras to become a reality, and the SPET-CT and PET-CT systems are now the norm. These usually use a doubled headed gamma camera with an X-Ray CT tube bolted on. The latest systems on the market include a SPET gantry and CT gantry which are able to be used independently. The SPET-CT images then allow the registered SPET and CT data to be interpreted together using a fused image, and separately. This has been a huge step forward in the use of nuclear medicine imaging renowned for the poor spatial resolution inherent in Anger's design. These hybrid systems allow maximum use of molecular imaging's high sensitivity, functional nature and contrast, displaying these along with the high spatial resolution and anatomical information of the CT image.

SPET MRI systems are now being planned which will need to dispense with the Anger type camera and replace the nuclear medicine component with a solid state type detector.

The move to tomographic imaging has been welcomed by the professions within nuclear medicine but much of the published work looks at qualitative image quality. Little literature has looked specifically at quantifiable quantities within patient data which would allow more use of nuclear medicine when considering treatment response to, for example, chemotherapy agents. Part of the work of this thesis aims to investigate one small area of this tomographic quantification and its reproducibility.

1.2.2 SPET Image Reconstruction

SPET data are a series of planar images taken at various angles around the patient/object - see Figure 8. The problem with the raw image data acquired is that they are not a true representation of the distribution of radioactivity within the patient. The photons emitted from the organ or tissue are attenuated by various structures within the body before reaching the detector. In addition the 3D image is generated from a series of 2D acquisition.

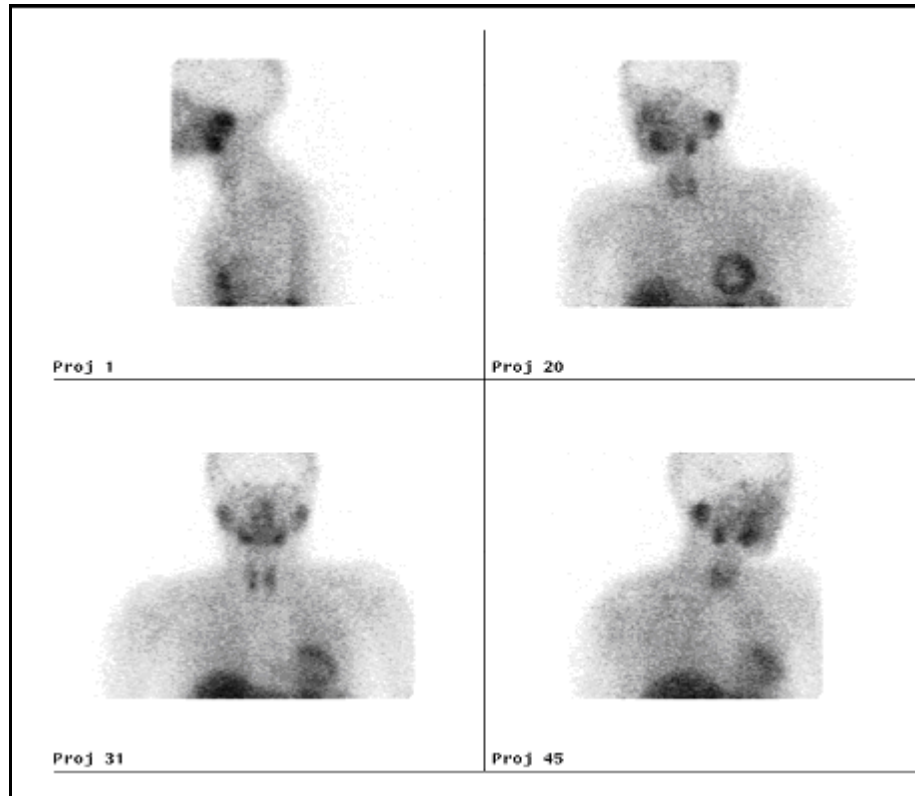


Figure 8 - Series Projections/Frames

Image showing four randomly selected projections from a complete SPET acquisition of the upper body, neck and head.

Reconstruction of these images can be handled in one of two ways; Analytical via Filtered Back Projection techniques or Iteratively (Bruyant, 2002).

1.2.2.1 Filtered Back Projection, FBP

Filtered Back Projection (FBP) has long been the traditional reconstruction method for tomographic data reconstruction and not only in Nuclear Medicine. As discussed, tomographic data consist of a series of planar images acquired at various angles also known as projections. The first step in the FBP reconstruction process is to create a sinogram from the acquired data. For each transverse slice a sinogram is simply a series of projections which represent the distribution of a tracer in the body at every angle. An example of a sinogram is shown in **Figure 9**.

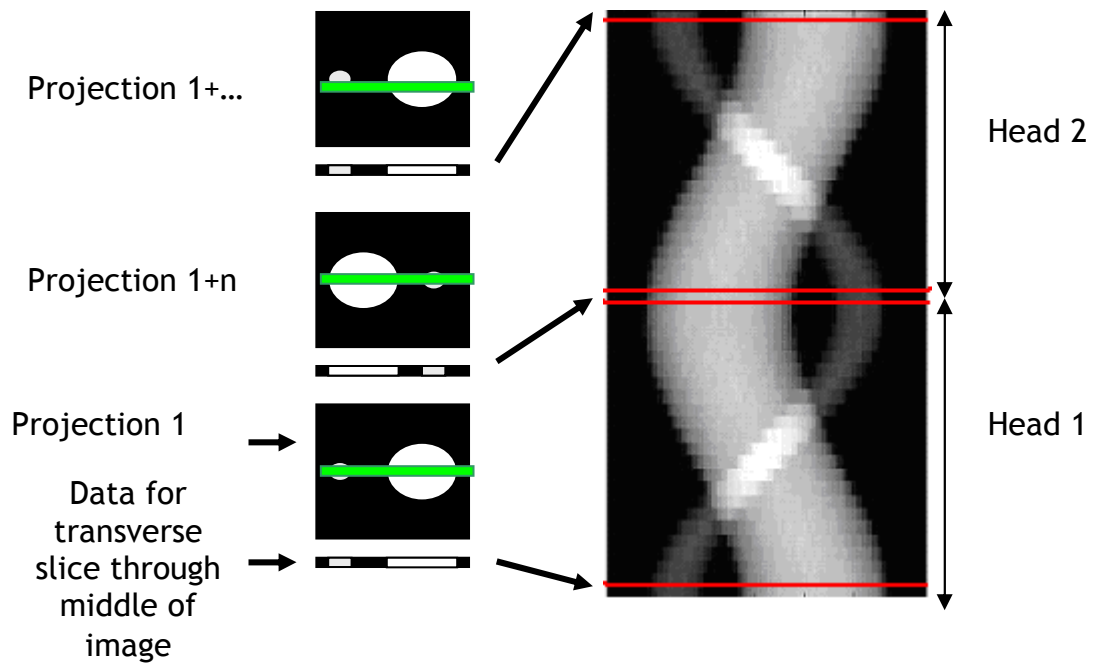


Figure 9 - Sinogram generation
Image showing three example projection images (on the left) along with the resultant sinogram (on the right) for the transverse slice shown in green.

The sinogram created is used to reconstruct the data, but to reconstruct the data at this stage would produce poor quality images. In particular an artifact known as the star artifact would be introduced. This star artifact is a bi-product of back projection and can be best seen on the reconstruction of a point source which in fact looks like a star because of the projection lines which radiate centrally from the reconstructed image. This is characteristic $1/r$ blurring, so named because the density of the artifact diminishes by $1/r$ with distance r from the point. If the whole image is considered, each point has this associated blurring meaning that the image quality is very poor. In order to remove this blurring a filter step is required and the entire process becomes **filtered** back projection. To filter the data in the spatial domain is computationally intensive, however, by converting the data into the frequency domain the same results can be achieved by simply applying a weighting factor to the data. The sinogram is converted into the frequency domain by performing a Fourier Transform on the data.

Once in the frequency domain a high pass filter is used to remove this $1/r$ blurring. The type of filter used, known as a ramp filter, works by multiplying the image data, at each frequency by a weighting factor that increases linearly with increasing frequencies - see **Figure 10** .

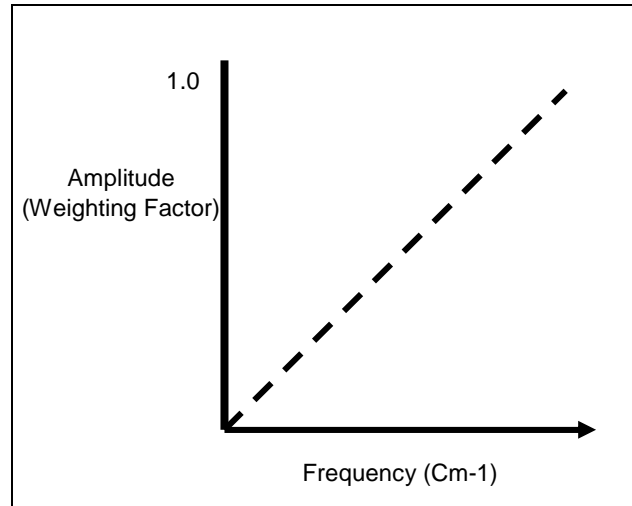


Figure 10 - Ramp Filter
Image showing the linear characteristics of a ramp filter used in FBP.

Despite being able to remove some of the low to mid frequency components from the data the ramp filter has the disadvantage of amplifying the statistical noise (which is high frequency) present in the data and this also degrades the image.

High frequency noise components can be removed using a low-pass filters which has the effect of smoothing the image. There are various low-pass filters available; Hamming, Butterworth, Shepp-Logan, Metz, Wiener, each of which has different curve characteristics in the frequency domain. The degree of high frequency components removed is dependent upon the cut-off frequency (the frequency above which all other frequencies are removed). However, depending on the filter, further characteristics of the curve may be altered. An example of this type of filter is the butterworth, this filter has an additional factor to consider known as the order (gradient of the curve) - see **Figure 11**.

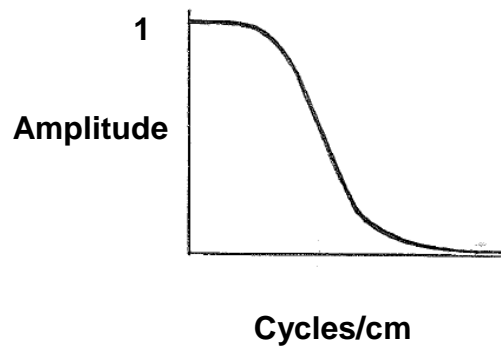


Figure 11 - Butterworth Filter
Image showing the curve characteristics of a butterworth filter which can be used in FBP.

The difficulty with any filtering of this type is that it in addition to removing the high frequency noise within the data, the fine detail of the image which is also high frequency can be lost as the filter cannot distinguish between the high frequency components. The cut-off value of the filter is therefore important so that image quality can be optimised. Too much smoothing and the image becomes blurred.

In FBP a combined ramp and low-pass filter are used pre back projection (reconstruction), therefore 2D filtering is performed. Once filtered the sinogram is converted back into the spatial domain and the data back projected (Delebeke and Israel, 2010; Bruyant, 2002). The Back Projection reconstruction technique can be described using a simple 3x3 pixel array [A]. Each 3x3 array represents a single projection through the patient i.e. P1-4 [A]. Contained in each cell is the value for the number of photons detected in that voxel [B] - refer to **Figure 12**.

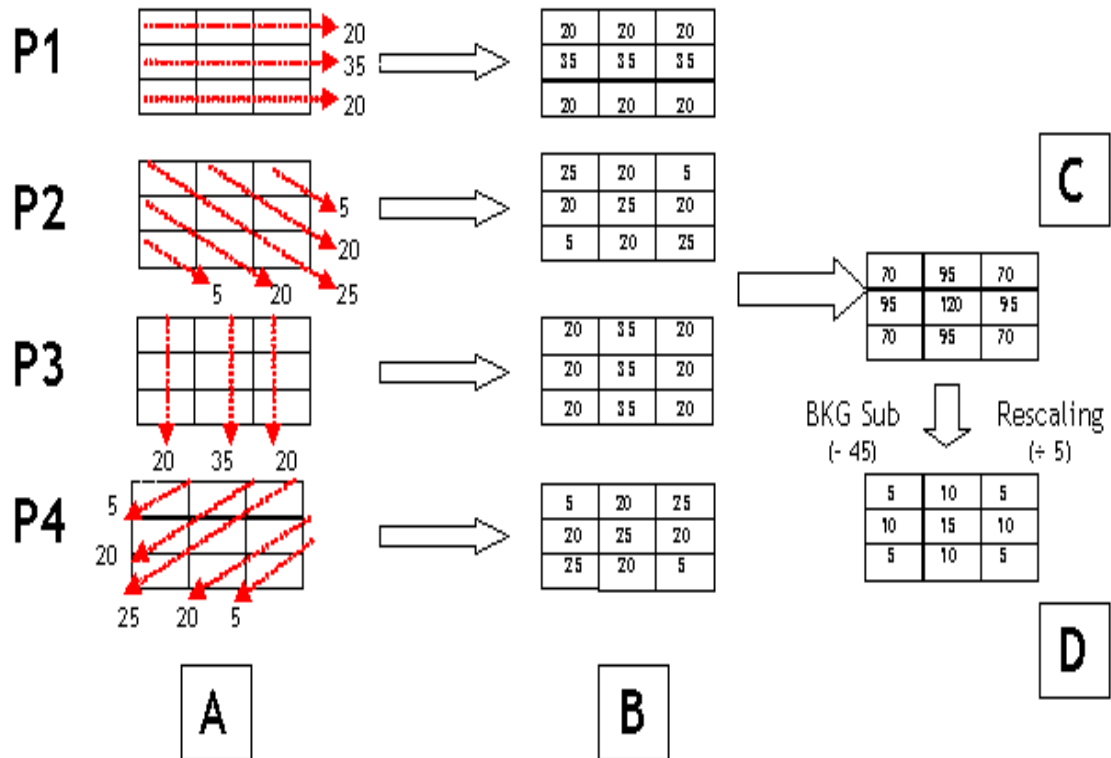


Figure 12 - FBP Simplified

Image showing a post filtered 3x3 projection matrix and a simplified reconstruction process achieved via FBP (Farr & Allisy-Roberts, 1998).

The 3x3 array in [B] are summed together and the result is [C]. A background subtraction is then applied i.e. in this case a global background value of 45 is subtracted from each voxel in the array. The values are then rescaled or normalised. In this example this is achieved by dividing each cell by 5 and the result given in array [D]. **Figure 12** provides a simplified explanation, in reality in order to minimise any artefacts as a result of attenuation from the patient for example attenuation artefact¹, opposing projections are added pixel by pixel.

In recent years for most reconstructions filtered back projection (FBP) has been replaced/superseded by forms of Expected Maximisation algorithms which previously were only really used in CT reconstruction.

¹ This is when the image appears less intense in the centre, the intensity of counts gradually increases as you move away from the centre towards the edge of the patient or object which has been nearer the camera.

1.2.2.2 Ordered Subset Expectation Maximisation, OSEM

OSEM reconstruction is an iterative reconstruction technique unlike FBP which is an analytical technique. **Figure 13** illustrates just some of the many different approaches to iterative image reconstruction. Iterative reconstruction techniques can be split into two very discreet branches; ‘Algebraic’ and ‘Statistical’. The main difference between these two branches is in how the measured projection and the estimated projection are compared, corrected and updated through the reconstruction process (Vandenberghe, 2001).

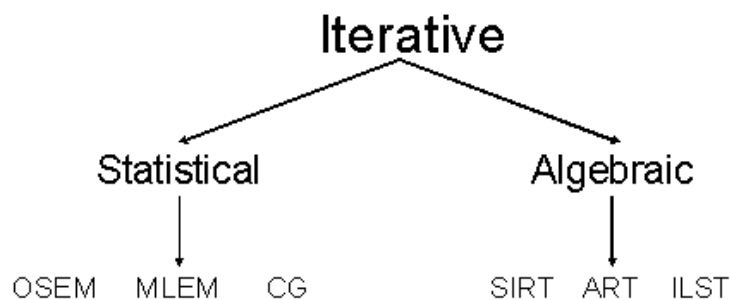


Figure 13 - Iterative approaches to image reconstruction

Chart categorising iterative reconstruction techniques into statistical (OSEM, Ordered Subset Expectation Maximisation; MLEM, Maximum Likelihood Expectation Maximisation; CG, Conjugate Gradient) and algebraic (SIRT - Simultaneous Iterative Reconstruction Technique; ART - Algebraic Reconstruction Technique; ILST - Iterative Least-Squares Technique) approaches (Vandenberghe, 2001).

OSEM falls into the likelihood category as the basis of this technique is formed by the Expectation - Maximisation, E-M, algorithm. The E-M algorithm is used to find a solution when there is an unknown variable in the measured data set. The algorithm has two basic components; an Expectation and a Maximisation Step.

The very first stage in this ‘*Expectation*’ process is to create an estimated slice, an arbitrary estimate. To do this, the first slice of the raw data is taken and from it’s projection an estimated slice is created, this is usually a homogenous slice whose values can be derived from an average of the projection values (Step 1 of **Figure 14**).

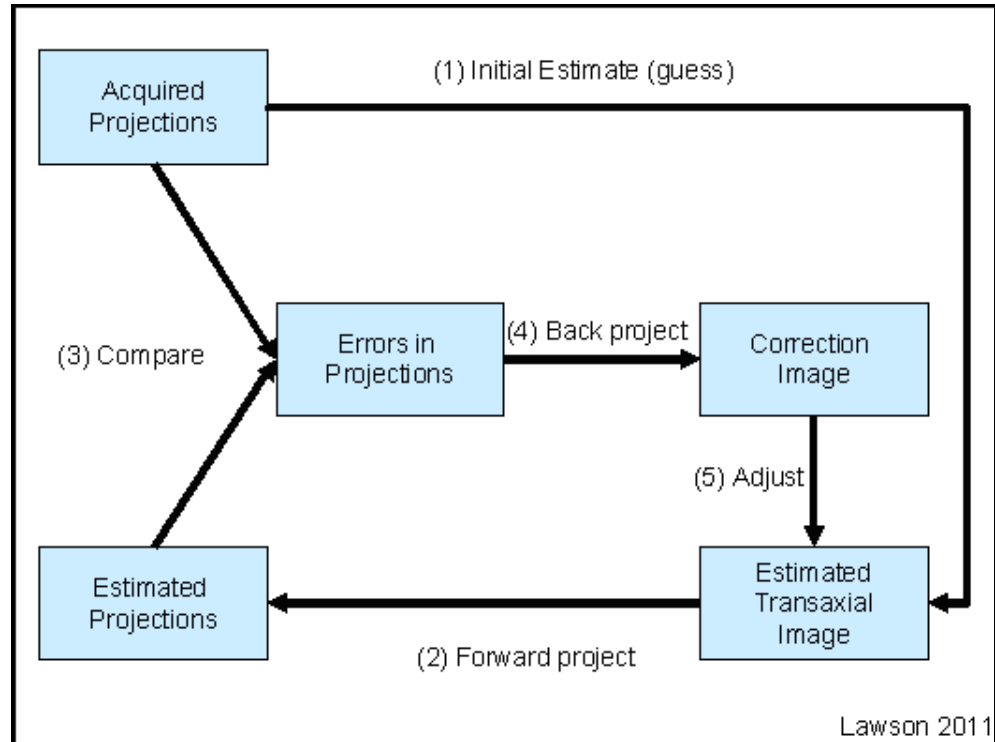


Figure 14 - OSEM Reconstruction Process

Image showing a non-mathematical representation of the OSEM reconstruction algorithm (Lawson, 2011).

The estimated transaxial image is then forward projected (Step 2 of **Figure 14**). A comparison is then made between the projection of the estimated slice and the projection of the measured slice (i.e. the raw data), (Step 3 of **Figure 14**).

The measured slice projection is then amended to match the expected - this is known as the '**Maximisation**' step (Step 5 of **Figure 14**). This whole process is then repeated until the difference between the actual and the estimated / expected reaches convergence in other words approaches zero or when the number of iterations which has been set is reached.

It is at stages 2 and 4 of **Figure 14** that corrections such as resolution recovery, attenuation and scatter should be applied to the estimated forward projection data and the back projected data.

This process is repeated for each slice measured (for every frame acquired). However, the homogenous slice used as the estimate for the first slice is now replaced by the resultant image created from the first slice data. The estimate

image for slice 3 is therefore the resultant image created from slice 2 and so on and so forth until the last slice.

This sequential approach means that reconstructing with EM algorithms requires a significant amount of computer processing and until recent years the limitations in computer processing hardware dictated the limited use of these commercially. Only in recent years has the development of more powerful computer processors and subsequent reduction in price allowed a number of forms of EM to be viable commercially (Bruyant, 2002).

The Ordered Subset Expectation Maximisation, OSEM, algorithm has found an application in Nuclear Medicine. This algorithm essentially produces the same quality reconstructed data as an EM algorithm but it is able to perform the reconstruction at a much faster rate, therefore making it more clinically suitable and commercially viable (Hudson, 1994). The OSEM reconstruction technique is able to achieve faster reconstruction rates as it is a more general form of EM. It processes the data in sequential subsets (group's frames) which is ideal since the data is acquired sequentially.

The number of subsets influences how quickly the data can be reconstructed. Increasing the number of subsets reduces the overall reconstruction time. The number subsets can be between 1 and 16, however this value is dictated by the number of projections acquired and there should be at least 4 projections per subset.

The outcome of the first subset is used to define the outcome of the second subset and therefore the 2nd subset will be used to define the outcome of the 3rd and so on and so forth.

It should be noted that the number of iterations will influence factors such as resolution, contrast and noise. Increasing the number of effective OSEM iterations will increase the noise, the effective OSEM iterations is defined in **Equation 1:**

$$\text{Effective_OSEM_Iterations} = S_n \times I_n$$

Equation 1

where S_n is the number of subsets and I_n is the number of iterations. It should be noted that in cases where the number of effective OSEM Iterations is greater than 20, a post reconstruction filter is required (Hermes, 2008). Also, if resolution recovery is used then the number of iterations should also be increased.

Resolution recovery is when information about the acquisition system, collimator parameters and resolution of the crystal are used to ‘inform’ the subsequent iterations and in theory produce a more accurate reconstructed image.

It is also possible to ‘inform’ the iterative process about other known information in particular if an attenuation map is available, say from a CT image then this information can be used during the iterations again in theory producing a more accurate reconstructed volume.

Once the data are reconstructed they can also be filtered to achieve a smoother image, this is undertaken by removing any high frequency components. Low pass filters available for use with OSEM reconstruction at GRI are the Butterworth, Low Pass, Hamming, Metz and Gaussian. Unlike FBP, since this filtering is performed on the reconstructed data it is referred to 3D image filtering (whereas FBP uses 2D filtering).

As always there are a number of “Pro’s and Con’s” for both the analytical and iterative techniques, some of which have been summarized in **Table 8**.

Analytical Reconstruction Techniques (Filtered Back Projection)		Iterative Techniques (Optimised Subset Expectation Maximisation)	
PROs Fast Recon Rate	CONs Correcting data for scatter etc can be difficult	PROs Discreteness of data included in model	CONs Number of iterations should be optimized for good image quality
Direct Inversion of Projection Formula	Data requires pre and post recon filtering Quantitation unreliable	Projection noise can better estimated and corrected Correct for collimator geometry, scatter and attenuation. Able to Quantify	Slow Recon Rates
	Amplification of noise requiring more filtering	Reduced image noise	

Table 8 - The “Pros’s and Con’s” of Analytical versus Iterative reconstruction techniques (Bruyant, 2002; Vandenberghe, 2001).

The tomographic acquired data are not a direct measurement of the distribution of radioactivity within the patient but are a measure of the distribution of emission events which will include scatter events and background radiation, when applying FBP technique to reconstructions, the reconstruction will include all this additional ‘dirty data’ (noisy data). In addition to higher noise content FBP can also introduce a streaking affect because of the back projection lines. When compared with the traditional FBP reconstruction techniques, EM algorithms are shown to demonstrate a reduction in overall image noise whilst also removing the streaking affect which is a common characteristic of FBP (OSEM Technologies, 2006; Bruyant, 2002). Elimination of the streaking effect and noise can be achieved because the data reconstruction process does not rely on the fact that the emission events lie anywhere on a line.

1.2.2.3 Attenuation Correction

Nuclear medicine images have always had a major issue because of the inherent attenuation from within the patient. Several mathematical corrections have been used over the years to correct for this. Although attenuation is present in all nuclear medicine imaging, it becomes more apparent in SPET imaging where the central parts of the transverse slices are significantly reduced in counts with respect to the outer edges.

Until the last few years the most acceptable way of correcting for this has been to apply a uniform attenuation correction. This means defining the outer edge of the body and assuming that all tissue within this body has a uniform attenuation

co-efficient, usually taken to be that of water. Chang's algorithm is the most commonly used uniform attenuation correction algorithm (Prekeges, 2011).

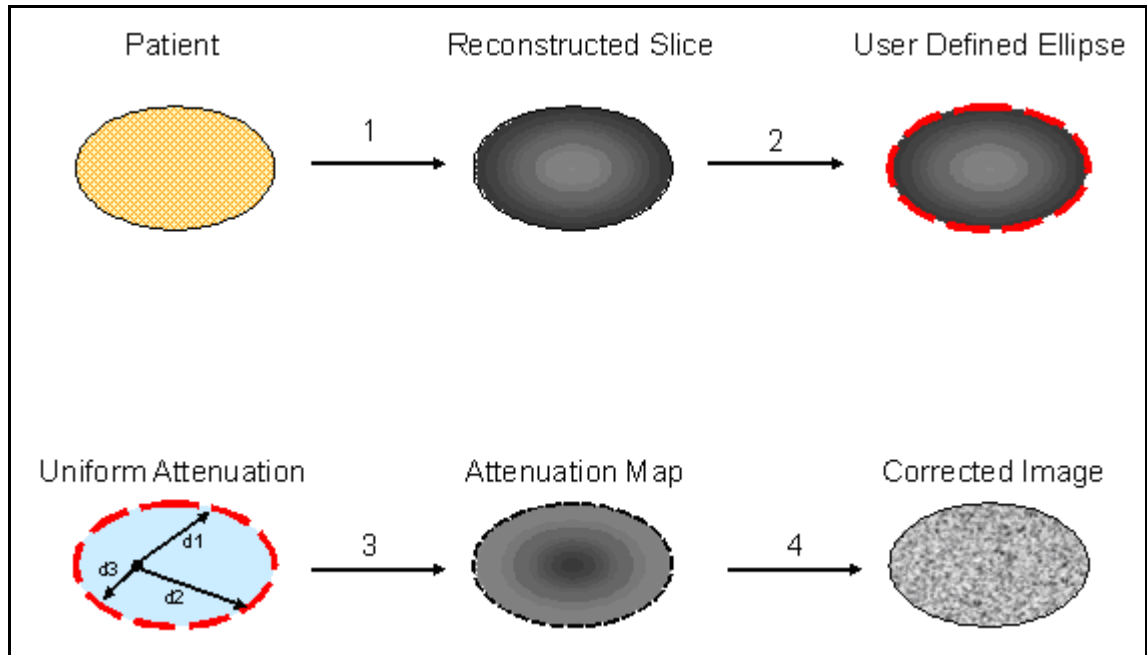


Figure 15 - Changs Attenuation Correction

Image shows a basic pictorial representation of Chang's attenuation correction process.

To perform a Chang's type correction, the patients body habitus has to be defined (Step 2 **Figure 15**), that is the circumference of the patient. This is achieved by drawing either a circle or ellipse, whichever fits best around the patient's body shape on the reconstructed transverse slices.

The next step in creating the MU map is to generate a uniform attenuation map which matches the user defined circumference for each slice. For each pixel on the uniform attenuation map a correction coefficient is calculated at each projection / angle based on its distance from the circumference boundary (d_1 , d_2 , d_3 are shown as examples of this in **Figure 15**). An average is taken of these values and applied to the pixel, see **Equation 2**.

$$CC = \frac{1}{\left(\sum_n e^{\mu d_n} \right) \div n}$$

Equation 2

where μ is the attenuation coefficient of water, d_n is the distance a photon will travel between any given pixel within the circumference and any given point on the edge of the circumference (see **Figure 15**) and n is the number of projections / angles

Thus a new non uniform map is produced (Step 3 **Figure 15**). The corresponding transverse slice is then multiplied by this MU map and the corrected slice/image created (Step 4 **Figure 15**) (Hutton, 2002).

Patients, however, are not made up entirely of water but are comprised of bone (which is dense) and lungs (which are full of air) both of which are at either end of the spectrum in terms of attenuation. Therefore this technique can provide either an under or over estimate of the counts in each pixel depending on the part of the body being imaged.

SPET CT has allowed the use of a CT attenuation map to permit actual measured values of attenuation coefficient for each patient to be used. In addition, the increased use of iterative type reconstruction algorithms means that these can be informed with the information about attenuation leading to what in theory should be a much better image representation of the patient, see **Chapter 3 section 3.1.2.1**.

1.2.2.4 Image Registration

Image registration is a very useful tool in enabling the comparison of two volumes on a slice by slice basis. This is an optional processing step and is performed using the reconstructed data.

This technique can be used to compare, for example, two reconstructed SPET volumes, or a CT with a SPET volume. The image registration process simply transforms one volume to match another.

All image processing and review at Glasgow Royal Infirmary, is performed on the Hermes system. The Hermes system uses two approaches to image registration:

1. Automated

2. Manual

The automated approach employs a 'multi-resolution technique'. This technique essentially blurs the image i.e. reduces image resolution. It then tries to look for similar small volumes that are of a similar shape and size within the main volume and calculates the difference between them. The technique then adjusts this second volume to match the first (1 iteration). A number of iterations are performed each time increasing the overall image resolution and therefore fine tuning the technique.

The manual approach allows the user to identify and define specific landmarks on one volume via crosshairs and co-locate these landmarks on the corresponding slice on the second volume, again via the placement of crosshairs. The second volume will therefore be shifted to match the first by matching the position of the crosshairs.

1.3 Role of image quantification

There are several important areas where specific quantification of an image is vital. Usually these are related to treatment response or treatment planning.

Historically, image quantification has been used in the planning for thyroid iodine treatment, and for treatment planning and response to for example mIBG. This has been used extensively in planar images for many years. This technique is reproducible and easy to perform in a general nuclear medicine department.

At present cardiac imaging is the only investigation which relies on quantification from SPET reconstructed images and this quantification forms an integral part of many Nuclear Cardiology reports. There are a number of factors which can be quantified from cardiac perfusion studies; including regional myocardial perfusion, perfusion defects and left ventricular size and function. All of these are assessed via relative differences in perfusion distribution of the myocardium between end-diastole and end-systole or between rest and stress states. (Hesse, 2005). However, quantification of uptake from other SPET investigations, and in particular, in the form of an absolute value of activity, has not been extensively used. Filtered back projection data is inherently noisy making quantification unreliable and this is probably the reason that more data are not available investigating SPET quantification. Only the advent of commercially available iterative reconstruction algorithms has led to the possibility of accurate image quantification. In addition, as mentioned previously, the ability to use SPET CT data to allow non-uniform attenuation correction has meant that systems are now available which in theory should provide a suitable reconstructed data set for quantification.

The usefulness and the role of SPET quantification has not been fully exploited and therefore has, as yet, to be clearly defined. Very little has been published looking at SPET quantification in terms of treatment planning or response.

The purpose of this work was to investigate the role of SPET image quantification in the diagnosis and subsequent management of patients. Work has been undertaken on image data from patients with suspected Non Small Cell

Lung Cancer. During the timescale of the work detailed in this thesis, hybrid systems (SPET -CT Units) became widely available for the first time which led to one of these units being installed in the site where this investigation was carried out in 2007. SPET - CT units have since had a significant impact on the way in which patients are imaged in Nuclear Medicine in terms of additional anatomical information and also the promise of improved image quality with respect to tomographic imaging via the use of CT attenuation correction and other corrections available in the software. This therefore prompted questions as to the extent to which the reconstructed image quality could be improved and what, if any, impact this would have on the accuracy of tomographic image quantification.

The data set of non-small cell cancer patients which formed the basis for the first part of work within this thesis was complete prior to the installation of the SPET CT unit. However many of the questions raised by these data suggested that attenuation correction using non-uniform attenuation maps generated from CT might improve the data. In an effort to try and answer some of these questions it was necessary to find data which could be used for this. It was reasonable to assess such factors using OctreoScan patients since these patients have SPET imaging performed of the pelvis and abdomen, as standard, whilst some patients have further imaging taken of the chest. In addition the agent used for these patients was very similar to that used for the lung cancer patients, albeit targeting a different cancer set.

1.4 Aim of this thesis

The initial aim of this study was to investigate the ability to use quantitative values from SPET images to determine whether these could be used to aid definitive diagnosis and predict or measure response to any intervention. There has been no significant published work looking specifically at SPET image quantification in this context.

Unfortunately, midway through the original work, the license for NeoSPECT, the radiopharmaceutical being used was bought over by another company. As a result NeoSPECT was removed from the market for a substantial period of time. As a result the original number of 50 patients anticipated for the study was not achieved.

In addition, during the period of time when NeoSPECT was unavailable a SPET-CT system was introduced within Glasgow Royal Infirmary. Along side the introduction of image capture on computer, the introduction of SPET-CT has been the most major advance in the nuclear medicine technology field since Anger's original work in the 1960s. Many of the drawbacks associated with nuclear medicine images are theoretically addressed by the use of hybrid imaging and it was important for a thesis on this subject to consider these and determine whether the use of a hybrid system was able to address some of the inadequacies.

Due to SPET-CT's infancy an opportunity was realised that allowed some of the postulated solutions to the pitfalls identified from the original SPET quantification work to be investigated further and comparison to be drawn between quantification of SPET with a SPET-CT data set.

To this end, the work presented in this thesis attempts to investigate quantification of both SPET alone, and SPET-CT images, in the diagnostic use of somatostatin receptor imaging.

Chapter 2 - NeoSPECT

Currently, patients who have resectable lung cancer, that is, lung cancer that may be treatable by surgery, will undergo surgical staging by mediastinoscopy before definitive resection. In the past 10 years, many more therapies have become available to treat disease both in the lung and more specifically within the mediastinum. There is, therefore, an increased need to determine whether these new treatments are effective in individual cases. Nuclear medicine imaging is functional, and it would seem reasonable to use functional imaging such as SPET (Single Photon Emission Tomography) or Positron Emission Tomography (PET) to determine disease progress and to predict therapy efficacy since anatomical imaging will miss any subtle changes in function.

PET imaging using ^{18}F Fluro-deoxy-glocose (FDG) has been shown to offer benefits over CT (which is an anatomical imaging modality) in terms of nodal staging of bronchial carcinoma. In a meta-analysis by Dwamena *et al.* (1999), the mean sensitivity and specificity were reported as 79% and 91% for PET and 60 and 77% for CT. When the work for this thesis began, there were only six PET scanners in the UK. These scanners were often used primarily for research and had significant running costs. Due to a large NHS capital injection, the number of PET scanners has risen dramatically within NHS departments in the last few years but there are still major restrictions placed on those patients who can have a PET scan because of limited availability. The cost of these scans remains relatively high when compared with SPET. In 2011, the typical cost of a PET-CT scan performed by Greater Glasgow and Clyde NHS health board was in the region of sixteen hundred pounds whilst a SPET-CT can range between five to seven hundred pounds (Dr J Dennis & Dr A Bolster, personal communication).

A widely available, inexpensive, non-invasive tool to accurately stage patients with lung cancer is required to benefit both the patients and also from a health economic point of view to best target therapy. $^{99\text{m}}\text{Tc}$ labelled Depreotide imaging (NeoSPECT), may offer such a tool. The radiopharmaceutical marketed as NeoSPECT is presently licensed only for the assessment of solitary pulmonary nodules. Images for this purpose are obtained using a gamma camera and can be

used to measure tissue uptake of the depreotide. Depreotide, as described in Chapter 1, is a 10 amino acid peptide that binds with high affinity to certain subtypes of somatostatin receptors (SSR's). Several malignant processes (including small and non-small cell lung cancer) and some benign processes hyper-express varying subtypes of the SSR's. NeoSPECT has been shown to have high sensitivity (96.6%) and reasonable specificity (73.1%) in detecting malignant pulmonary nodules (Blum, 2000). There is conflicting evidence, however, as to its use in assessing potential hilar and mediastinal nodal involvement. Despite small studies showing sensitivities of 81-100% and specificities of 80-86% (Berkowitz, 2001; Waxman, 2002), there is no available convincing data on which to base clinical decisions. In addition, there is no standard technique available which has good reproducibility and accuracy and can be used to quantify and measure changes in these types of functional images.

2.1 Literature Review

To date, the literature is supportive of the use of ^{99m}Tc labelled depreotide as a non-invasive diagnostic tool in the differentiation of benign disease from malignant solitary pulmonary nodules (SPN).

Dwamena *et al.* (1999) demonstrated that functional imaging using FDG PET was significantly more accurate than CT for the characterisation of mediastinal nodes in patient with Non Small Cell Lung Cancer, NSCLC.

Blum *et al.* (2000) performed ^{99m}Tc labelled Depreotide SPET acquisitions on 114 patients with solitary pulmonary nodules of less than or equal to 6cm as seen on a chest x-ray. These patients had demonstrated an absence of any benign pattern of calcification on CT and also showed no demonstrable radiographic stability during the 2 years prior to the study. All of the 114 patients had a NeoSPECT scan (^{99m}Tc -Depreotide SPET Scan) performed and subsequently underwent histological examination. The SPET images were reported by 3 nuclear medicine specialists who were blinded to the histological findings and gave each scan a positive or negative scoring based on the presence or absence of a region of intense tracer uptake in an area corresponding to the SPN region shown on the chest x-ray. The final score allocated to each patient was taken as being the majority score between observers, this was then compared with the histological findings.

Histological findings showed that of the 114 patients involved, 88 were found to have a histological result compatible with malignant neoplasm. Of the 88 patients the NeoSPECT images correctly identified 85 with 3 false-negative determinations when comparison was made with the histology report. 7 false positive determinations were demonstrated of which 6 were granulomas and one hamartoma. The NeoSPECT scan correctly excluded malignancy in 19 of the 26 patients who had benign histological findings. These finding gave a sensitivity of 96.6% with a specificity of 73.1%.

Blum *et al.* (2000) concluded that ^{99m}Tc -Depreotide SPET scanning was a safe and useful method in the non-invasive investigation of solitary pulmonary

nodules with sensitivity comparable to fluorine-18 fluorodeoxyglucose (FDG) positron emission tomography (PET).

Work presented by Berkowitz *et al.* (2001) showed that for SPN the sensitivity of NeoSPECT was 94% and specificity of 78%. These investigators also quoted sensitivity and specificity of NeoSPECT for hilar and mediastinal disease to be 100% and 80% respectively.

Waxman *et al.* (2002) concluded NeoSPECT to be a sensitive agent for the detection of lymph node metastasis in the hilum and mediastinum, with specificity by site which was clinically acceptable.

Recent research within nuclear medicine has been heavily driven towards PET imaging and the use of F-18 FDG and other agents in tumour localisation and quantification. Research has demonstrated PET imaging to be extremely effective in tumour localisation and is now considered by many to be the gold standard imaging tool in the detection and staging of many cancers. Availability of PET imaging facilities is, however, very limited in Britain, in fact up until 2008 Scotland did not have a clinically run PET service and whilst England had some PET centres, access to such facilities was dependant upon a patient's geographical location and was subject to large waiting lists.

Kernstein *et al.* (2001) presented work comparing PET imaging of the mediastinum with SPET imaging and found SPET to be just as effective at differentiating between benign and malignant disease in terms of sensitivity and specificity. This is good news for patients who require such a service, as most general nuclear medicine departments are capable of performing SPET imaging.

2.2 Pan Glasgow Study - Depreotide Imaging

The work of this section of thesis focussed on a pan-Glasgow study which was undertaken to investigate the role of NeoSPECT (depreotide) imaging in the staging of lung cancer by means of a prospective, multicentre trial based within the West of Scotland. A copy of the local research ethics committee at GRI approval notice can be found in **Appendix A**. Two groups of patient were included in the trial;

Group 1 - Patients who required mediastinoscopy² to determine if lung cancer had spread to the lymph glands.

Group 2 - Patients with lung cancer going forward for surgery to remove the lung or part thereof. These patients had samples of lymph glands taken during their operation as part of routine clinical care to make sure the cancer had not spread to the lymph glands.

Patients were identified at multidisciplinary lung cancer meetings held throughout the West of Scotland. Patients eligible to take part in the study were those identified as having potentially curable lung cancer and/or patients with equivocal mediastinal lymphadenopathy, requiring further classification.

Patients who were not considered eligible for the study were those who had undergone cardiothoracic surgery in the preceding 2 months, had previous radiotherapy to the thorax or previous surgery for lung cancer or tuberculosis, previous antituberculous chemotherapy (in the last 2yrs), previous systemic chemotherapy for intra-thoracic malignancy, pregnancy, known contrast allergy, lung lesions greater than 1cm in diameter or those already taking part in any other clinical trials.

The consultant in charge of the patient's care was then responsible for selecting which of their patients would be suitable to be included in the trial. Patient's suitability being paramount since the patient would be required to spend a significant amount of time being imaged. The trial involved an injection of the

² Mediastinoscopy is a surgical procedure which takes samples of the lymph glands situated in the chest behind the breast bone to determine if there is disease present.

radiopharmaceutical - NeoSPECT, see section 1.1.2.1 of Chapter 1 for details - SPET imaging of the thorax and planar images of the abdomen. Both the SPET and planar images were acquired at two discrete time points post injection namely 2 hrs and 4 hrs. Imaging at two discrete time points post injection allowed changes in the distribution of uptake over time to be identified and investigated to determine if this helped characterise the disease process.

To assess the role of NeoSPECT imaging qualitatively, the images acquired were reviewed along side the conventional CT scan images used for staging, thus allowing any additional information provided by NeoSPECT to be identified and its value determined.

2.2.1 Aim

The main aim of the study was to determine whether NeoSPECT could be used to accurately stage disease in the mediastinum. In addition, dual time point imaging was included in the protocol to determine whether this aided disease diagnosis or patient prognosis.

The most exciting aspect of this research proposal lay in the lack of published literature available both qualitatively and more specifically quantitatively. This was indicative of a need for further investigation which would hope to exploit all characteristics of the radiopharmaceutical through investigation of the imaging parameters and reconstruction techniques.

To date, none of the published literature discusses or demonstrates any reproducible technique, which could be used quantitatively to monitor the response of the mediastinum to chemotherapy treatment, or that would allow staging of disease in the mediastinum. It was therefore clear that further research was required in order to define the role of NeoSPECT imaging in the assessment of disease in the mediastinum.

This project investigated techniques to determine absolute uptake in a reproducible and useful fashion which could then be used to determine any significant changes.

For each patient SPET and planar data were acquired (discussed in more detail in **section 2.4**). In addition to the SPET data acquired for patients, each patient data set were accompanied by an acquisition of a standard source so that this could be used for quantification.

2.3 Optimisation of reconstruction techniques and reproducibility using NeoSPECT Phantom Acquisitions

Phantoms allow workers in nuclear medicine to develop acquisition and analysis procedures without the need for exposing patients to radiation. It is important to make the parameters used for the phantom acquisitions as near the clinical situation as possible.

There were 2 phantoms used to assess and validate the NeoSPECT work, the first was the RSD (Radiology Support Devices) (RSD, 2010) anthropomorphic thoracic phantom as shown in **Figure 16** and the second was an in-house designed and manufactured phantom, see **Figure 17**.

Components of the RSD anthropomorphic phantom were considered tissue equivalent in accordance with the International Commission on Radiation Units and Measurement Report No. 44. and anatomically correct; further information about this phantom can be found at www.rsdphantoms.com, supported by a number of references detailed on the website. The phantom contained a bone component to replicate thoracic skeleton including vertebrae and rib cage, and was hollow to allow fillable organs to be inserted for example lungs, heart, liver.



Figure 16 - Anthropomorphic Thoracic Phantom
Image showing the RSD anthropomorphic thoracic phantom, the phantom contained all the major organs found in the thorax (Bone, lungs, heart, and liver).

The body of the phantom was made from polyurethane, which was modified to produce a tissue equivalent material with a mass density of 1.10g cc^{-1} and a linear attenuation coefficient of 0.160cm^{-1} for $^{99\text{m}}\text{Tc}$.

RSD stated that the components used in the thoracic skeleton closely met the values of mass densities quoted in a report by the International Commission on Radiation Units and Measurement (ICRU, 1989), which are quoted for both cortical and spongiosa components of the human skeleton as 1.88g cc^{-1} and 1.16g cc^{-1} respectively, (RSD, 2010). The cortical bone component of this material demonstrated a linear attenuation coefficient of 0.280cm^{-1} for $^{99\text{m}}\text{Tc}$.

Although liver, heart and lung inserts were available, the only organs used were the lungs and heart inserts. The lungs were hollow shells that were filled with Styrofoam beads; these mimicked the air occupancy within the lungs. In addition to the Styrofoam beads these shells could also be filled with a radioactive solution which provided an overall mass density of 0.4g cc^{-1} .

The second phantom used was an in-house phantom. The design for the in-house phantom was born out of limitations in the RSD phantom in that there was no mechanism for adding/creating an abnormal area within either lung volume to mimic lung tumour tissue.



Figure 17 - In-house designed Phantom
Image showing the in-house designed lung phantom; this phantom contains two main chambers (left and right lung) which allowed additional volumes to be added to each lung chamber to simulate tumour volumes.

The in-house phantom was made from moulded perspex and contained two hollow inserts which were filled with polystyrene balls to replicate the air within the lungs. The size of the hollow inserts were based on values quoted in the “Report of the Task Group on Reference Man” (ICRP Task Group), whilst the thickness of Perspex used was based on the resolution of the gamma camera, that it is no thicker than 10mm.

To achieve and replicate an abnormality in the lung, each insert contained a small aperture on its anterior face where a small vial could be inserted (one was located in what would be the right lung apex and one in the base of the left lung). These small vials could be easily filled with known quantities of activity. The actual phantom manufactured is shown in **Figure 17**.

Phantom work was undertaken for the following reasons:

1. To optimise acquisition and reconstruction parameters of the standard volume.
2. To determine reproducibility and hence to determine the smallest significant difference which could be detected between the two time points. These differences might be due to experimental setup of the orbit, or simply because of the statistical fluctuations in the counting statistics.
3. To determine an accurate method of calculating the activity within a specific tissue or organ. This involved an acquisition of both a standard volume of known activity and an acquisition of the phantom with the components filled with known activities of radioisotope - these activities were as close to activities demonstrated in patient investigations as possible.

The following sections and subsections detail this work both in terms of image acquisition and reconstruction.

2.3.1 Optimisation of NeoSPECT Standard Acquisition and Reconstruction Parameters

For quantification of nuclear medicine images, standard acquisitions are often acquired. These are images of a known activity and volume and are usually acquired under the same conditions as the patient. A standard (STD) acquisition is essential for image quantification in order to translate counts into an appropriate value of activity which is often expressed as percentage uptake. It was also important to undertake work to ensure that the set-up, acquisition and reconstruction parameters for the 'Standard' were appropriate and close to those of the patient acquisitions since these formed the basis for the image quantification.

The patient area of interest, the thorax, is comprised of many different components including bone, muscle, soft tissue and air. Each of these components has different attenuating properties. It is important for true quantification that the STD acquisition should mimic that of the patient. However as camera time is at a premium in a busy department, it was important to determine whether a reduction in acquisition time for the STD only was possible. To simulate the attenuation of the photons within the actual patient, the STD volume was placed in a perspex phantom (see **Figure 16** of **section 2.3**) which contained bony structures and had lung inserts containing polystyrene beads to mimic the air space of lungs.

The STD volume was placed in between the two lung inserts to mimic as best as possible the attenuation of a lung lesion. The phantom includes the spine and ribs and therefore mimics this attenuation. The removable breast tissue from the phantom was not used to standardise the acquisition for both male and female.

The following acquisition and reconstruction variables were investigated:

- | | |
|------------------------|--|
| Investigation 1 | Frame time; reproducibility of 3 sec STD acquisition frame. |
| Investigation 2 | Influence of attenuation correction on STD reconstructed data. |

2.3.1.1 Methods for Investigation 1 - Reproducibility of 3 Sec STD Acquisition

Each patient had data acquired over 360 degrees using 2 gamma camera heads (180 degrees each), each frame was acquired for 30 seconds. The duration of each frame is important as this ensures that the images acquired are statistically sufficient in counts and thus produce high quality images both quantitatively and qualitatively.

A frame time of 30 seconds resulted in a total patient acquisition time of 30 minutes (excluding set up time). Whilst this was acceptable for a patient acquisition it was considered too lengthy for a non-patient acquisition in a busy patient department. Consideration had to be given to reducing the frame time to a value that would not disrupt the patient flow in a busy department but would maintain statistical stability in terms of counts and image quality. The frame time for the STD acquisition only was reduced to a tenth of the patient acquisition frame time that is from 30 second to 3 seconds. To assess whether or not 3 second frames would produce images statistically sufficient in counts the repeatability of the measurement was assessed.

The STD acquisitions were performed using a source of known activity placed in the phantom as described in **section 2.3** for this purpose the phantom was used simply to mimic the attenuation of a human thorax. A small plastic vial containing approximately 5MBq of ^{99m}Tc was used as the standard (STD) - see **Figure 18**. It should be noted that neither the lungs nor the thoracic cavity were filled with a radioactive solution. For the purpose of illustrating the edge of the phantom in **Figure 18**, a number of radioactive wraps were placed over its surface, this form of edge delineation was not used in the actual acquisitions which formed the analysis.

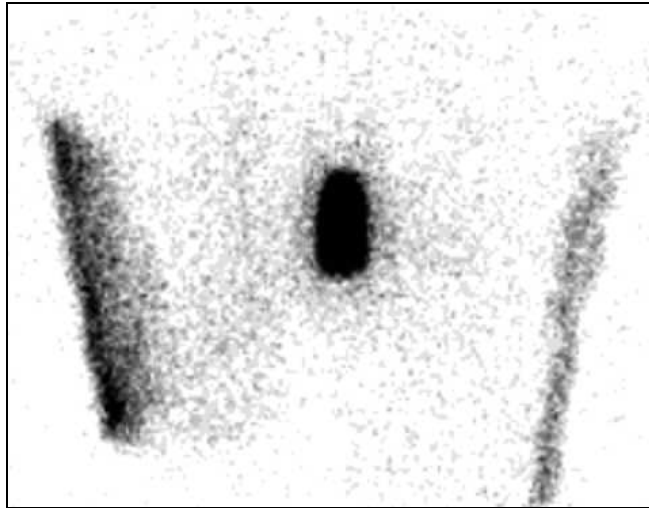


Figure 18 - Planar view of a typical standard acquisition
Image showing the standard volume placed centrally within the RSD anthropomorphic thoracic phantom, equivalent to a patient lying supine on the imaging couch.

A total of 10 consecutive acquisitions were performed - there was no repositioning of the standard between acquisitions. The acquisition parameters are described in **Table 9**. The gamma camera used for all the work within this chapter was the Philips Forte camera (previously sold by ADAC). It is a double headed large field of view gamma camera (500mm x 370mm field of view). The collimator used was the VXHR, this is a parallel hole, low energy, high resolution collimator with longer bore septa. It is designed for use with Krypton but its sensitivity and resolution compare well with other manufacturer's LEHR (low energy high resolution) collimators.

Collimator:	VXHR
Degrees of Rotation :	Non-circular, 360 degree acquisition using 2 heads (180 degrees per head)
Frame time:	3 seconds
Interval:	3 degrees
Energy Window (keV):	10% window on 140
Matrix:	128 x 128
Set Up @: 0 & 180 degrees	For the purpose of these acquisitions the heads were set round the circumference of the phantom.

Table 9 - Acquisition Parameters

Each acquisition was reconstructed using the predefined parameters described in **Table 10**.

Reconstruction Method:	Iterative HOSEM – Hermes Ordered Subset Expectation Maximisation
Protocol:	NeoSPECT
Number of slices:	16 (STD counts > BKG counts)
Start slice:	42
Filter:	Low Pass with cut-off 1.5 cycles/cm
Iterations	4
Subsets	6
Zoom:	No Zoom

Table 10 - Reconstruction Parameters

The reconstruction parameters used in the patient protocol ‘NeoSPECT’ will be described later in **Table 23** of **section 2.4.1**. To assess reproducibility, each acquisition was analysed quantitatively using region of interest analysis. Using the reconstructed data, regions were drawn on the transverse plane of the images; one around the standard and one around an appropriate area of background as shown in **Figure 19**.

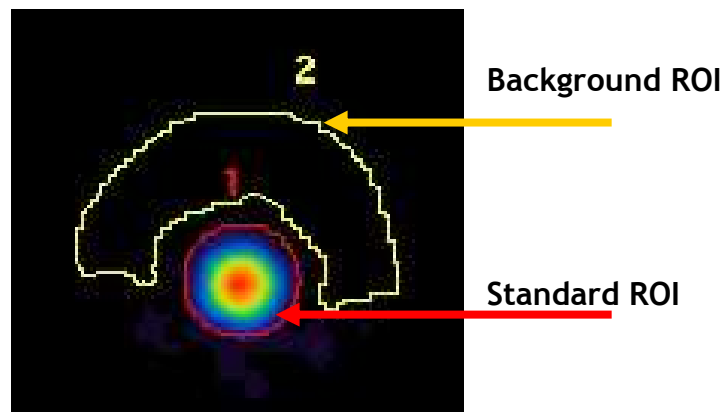


Figure 19 - Transverse Slice of STD ROIs

Image showing a reconstructed transverse slice of the standard volume with regions of interest depicted by arrows.

These regions were saved and copied onto each transverse slice in turn, throughout the total reconstructed volume. The saved regions were uploaded and applied to the remaining 9 acquisitions in a similar way to allow a comparison to be made.

2.3.1.2 Results for Investigation 1 - Reproducibility of 3 sec STD Acquisition

From the regions of interest, values of total counts and number of pixels were extracted. The standard volume was visualised on 16 slices in the transverse plane, **Table 11** details the total counts per slice per acquisition. The value of

total counts from the ‘standard ROI’ was corrected for background by applying area normalisation to the background region as described in **Equation 3**.

$$C_{Cor} = \left(C_{STD} - \frac{C_{BKG}}{A_{BKG}} \times A_{STD} \right)$$

Equation 3

where C_{Cor} is the counts corrected for background, C_{BKG} is the counts from background, A_{BKG} is the area of the background ROI, C_{STD} is the counts from the standard, A_{STD} is the area of the standard ROI.

For a more accurate comparison a decay correction was also applied to the total counts from STD acquisitions 2 -10, as described in **Equation 4** and **5**.

$$A = A_0 e^{-\lambda t} \quad \text{where} \quad \lambda = \frac{1}{T} \ln 2$$

Equation 4

Equation 5

where A is activity at the image time, A_0 is the original activity at time zero (time of measurement), t is the difference in time from the time of measurement to time of imaging, and T is the half life of the isotope which for Tc99m is 6 hours.

	STD 1	STD 2	STD 3	STD 4	STD 5	STD 6	STD 7	STD 8	STD 9	STD 10
Slice 42	865	453	498	462	498	412	561	533	423	415
Slice 43	2606	1682	1526	1823	1582	1637	1608	1648	1534	1523
Slice 44	4797	3819	3656	4136	3404	3540	3578	3177	3419	3400
Slice 45	6575	5748	5958	5774	5118	5145	5416	5037	5076	5243
Slice 46	7227	6797	6964	6521	6177	5952	6114	6544	5761	6178
Slice 47	7137	7417	7144	6935	6725	6494	6420	6738	6056	6297
Slice 48	7368	7557	7348	7008	6875	7075	6751	6473	6473	6313
Slice 49	7761	7225	7182	7031	6832	7298	6656	6729	6477	6495
Slice 50	7505	7209	6807	7126	6962	6872	6357	6685	6279	6549
Slice 51	7236	7518	7075	6923	7095	6428	6380	6258	6383	6332
Slice 52	7043	7158	7154	6504	6621	6307	6436	6202	6078	5779
Slice 53	5980	6089	6156	5900	5617	5969	5956	5847	5180	5170
Slice 54	4213	4890	4701	4725	4487	4712	4705	4466	4289	4513
Slice 55	2668	1820	3262	3314	3263	3185	3109	2892	3134	3253
Slice 56	1403	1820	1845	2048	1872	1844	1880	1653	1661	1581
Slice 57	383	650	645	859	671	781	868	682	626	506
Total	80767	79459	80849	81268	79054	80167	80573	80379	78605	80674

Table 11 - Repeatability of 3 sec Acquisition

The last row on the table is the sum of the total counts over the complete standard volume.

A mean of the sum of the total counts value was taken and the standard deviation calculated; 80179 ± 862 (2.15%). The trend in values is demonstrated in **Figure 20**.

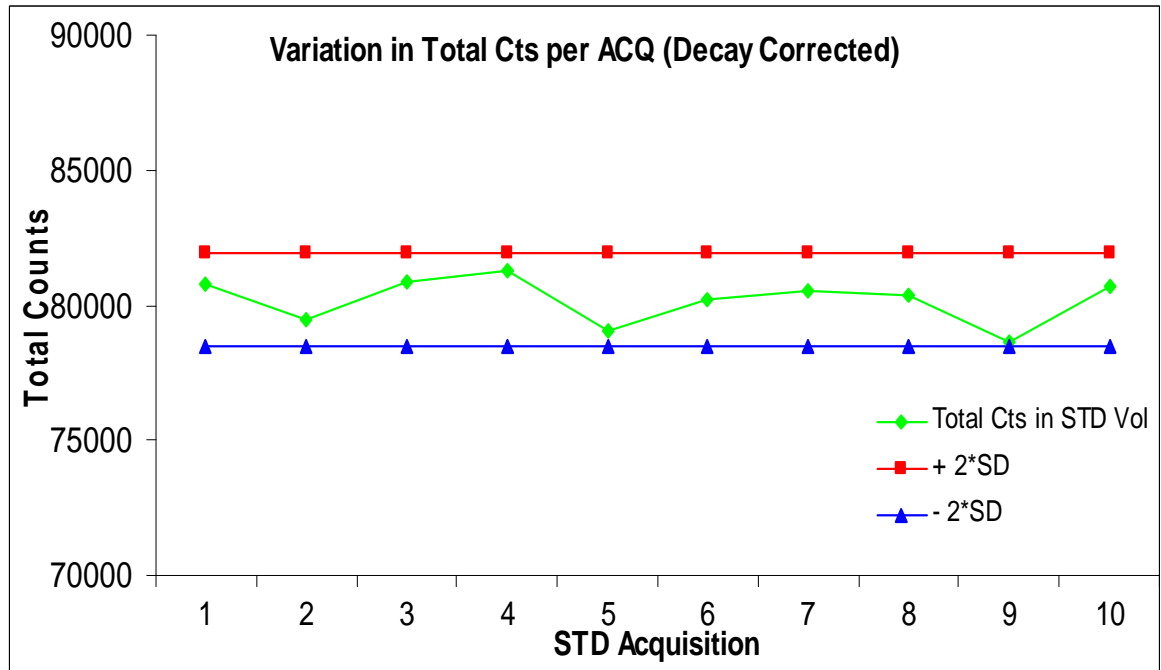


Figure 20 - Graph of Variation in Total Cts per Acquisition

The graph shows the plot of the sum of the total counts obtained from ROIs placed on the transverse slice containing the standard volume for each acquisition (green line) and the upper and lower 2x standard deviations (red and blue lines respectively).

From **Figure 20** it can be seen that the total counts for the acquisitions lie within +/- 2 standard deviations.

2.3.1.3 Methods for Investigation 2 - Influence of Attenuation Correction on STD Reconstructed Data

In addition to optimising the STD acquisition parameters, it was also important to ensure that the reconstruction parameters of the STD matched those of the patient and were appropriate. This included establishing whether or not to use a geometric attenuation correction on the STD data. A total of 18 patients had a standard acquisition i.e. an acquisition of a vial of known activity used to calculate sensitivity, performed along with their diagnostic study. The reconstruction of the patient data included the use of a geometric attenuation correction which was mapped to the circumference of the patient.

It was important to assess the influence this correction would have on the reconstructed data and what impact this would have on quantitative analysis, that is the sensitivity and the subsequent calculation of uptake. This was undertaken by using the acquisition data from the 10 consecutive STD acquisitions performed in section 2.3.1.1, this data were subsequently reconstructed with and without an attenuation correction using the parameters detailed in Table 10.

Figure 21 shows a transverse slice of the STD, the Standard volume being the most central of the hot areas on the slice.

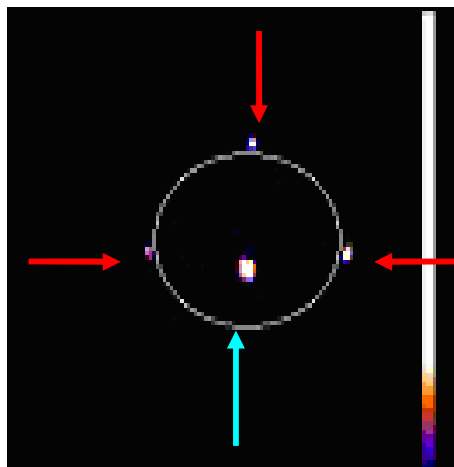


Figure 21 - Attenuation Circumference Delineations

The image shows a transverse slice of the standard volume (centrally) and the markers to define the outer edges of the phantom as shown by the red and blue arrows. required for the attenuation correction,

To identify the surface of the phantom a number of small radioactive markers were placed on the outside body of the phantom - these are indicated by the red arrows. These markers allowed the circumference of the phantom to be identified shown with the blue arrow. This allowed an ellipse to be drawn where everything inside the ellipse was corrected for attenuation using a Chang's correction - see Chapter 1 section 1.2.2.3 for details. This correction assumes uniform attenuation within the defined circumference and the attenuation coefficient for water is usually used. On the Hermes system this is set as 0.12 cm^{-1} for $^{99\text{m}}\text{Tc}$.

The ROIs are shown in **Figure 19**. ROIs were drawn on all slices on which the standard volume was identified. These regions were saved and applied to each transverse slice, throughout the total volume of the standard.

2.3.1.4 Results for Investigation 2 - Influence of Attenuation Correction on STD Reconstructed data

From the regions of interest, values of total counts and number of pixels were extracted for both reconstructed data sets and on both reconstructed volumes (with and without attenuation correction). The standard volume was visualised on 16 slices in the transverse plane. The value of total counts from the ‘standard ROI’ was corrected for background by applying area normalisation to the background region as described by **Equation 3**.

The values of total counts were then summed over the entire volume of the standard. There was a period of ninety minutes between the first and last acquisition therefore values of total counts were corrected for decay using **Equation 4** and **Equation 5** to allow a direct comparison. **Figure 22** demonstrates the influence of the application of attenuation correction on the counts in this standard volume.

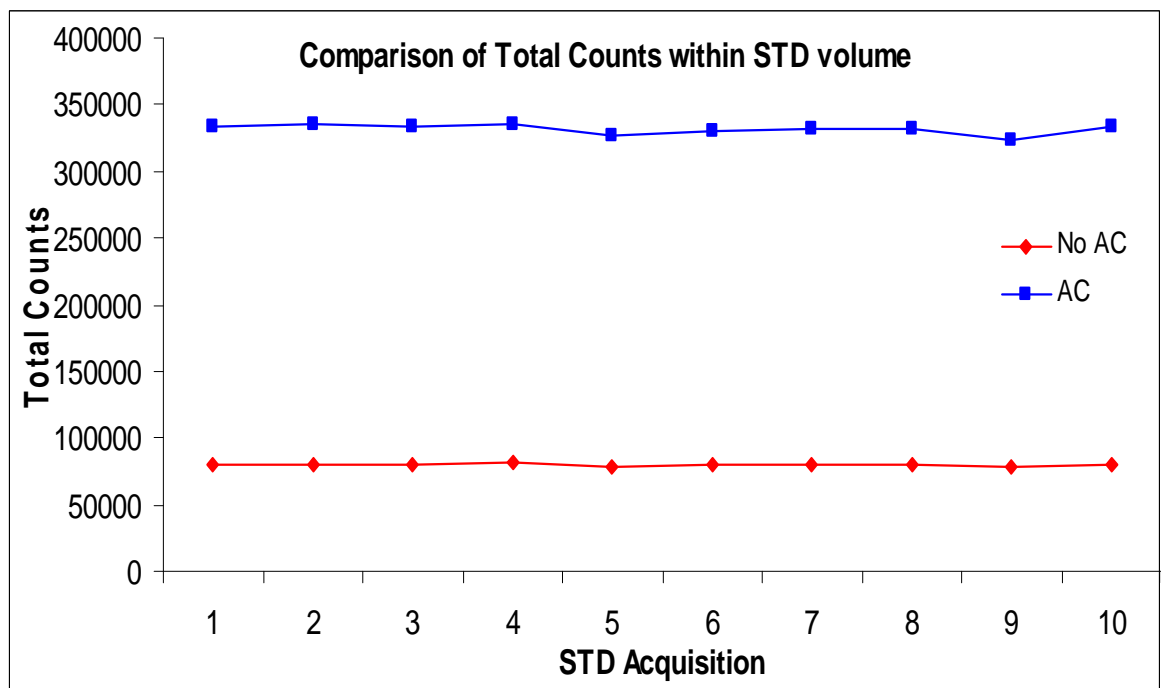


Figure 22 - Graph of Influence of Attenuation Correction

The graph shows plots of the total counts from the standard volume obtained from ROIs placed on the transverse slice for each acquisition; image data corrected for attenuation correction are shown by the blue points and trendline whilst image data with no attenuation correction applied is shown by the red points and trendline.

Whilst the trend in total counts within the ROIs was the same there was a significant difference in magnitude of the total counts, a ratio of total counts from the attenuation corrected volume to the non-attenuation corrected volume of approximately 4:1 was observed.

Differences in the value of total counts between the two reconstruction techniques are detailed further in **Table 12**.

	STD 1	STD 2	STD 3	STD 4	STD 5	STD 6	STD 7	STD 8	STD 9	STD 10
Slice 1	2764	1428	1495	1431	1469	1286	1636	1666	1332	1328
Slice 2	8246	5178	4734	5749	4926	5165	4997	5192	4825	4830
Slice 3	15129	12050	11537	13099	10699	11074	11332	10026	10712	10816
Slice 4	20753	18150	18786	18190	16072	16139	17073	15877	15994	16618
Slice 5	22727	21399	21994	20508	19479	18770	19268	20508	18195	19545
Slice 6	22474	23355	22463	21948	21284	20439	20280	21218	19123	19898
Slice 7	23295	23780	23145	22049	21635	22302	21284	20390	20408	19972
Slice 8	24390	22659	22529	22060	21413	22920	20947	21030	20314	20405
Slice 9	23532	22567	21319	22379	21833	21506	19969	21074	19650	20485
Slice 10	22679	23496	22040	21672	22115	20005	19940	19501	19890	19767
Slice 11	22033	22356	22349	20323	20627	19610	19968	19304	18909	18059
Slice 12	18572	18870	19233	18280	17423	18404	18476	18138	15961	16123
Slice 13	13040	14980	14531	14535	13790	14495	14502	13772	13165	13967
Slice 14	8271	12343	9986	10238	10016	9802	9515	8861	9594	10054
Slice 15	4359	5551	5611	6324	5736	5667	5806	4996	5105	4924
Slice 16	1280	1968	1985	2690	2072	2408	2704	2058	1945	1569
Total	253545	250131	243738	241476	230589	229994	227697	223612	215121	218363
Total (decay Cor)	253545	255288	252901	254566	247004	250336	252030	251157	245599	253300

Table 12 - Difference in Total Counts per acquisition

The number of slices over which the standard was visualised did not differ between reconstruction techniques only between acquisitions which could be accounted for by slight variations in the transverse position of the bed.

From the values of the total counts, length of acquisition and activity in the volume the system sensitivity was found. The average of this value over the 10 acquisitions was calculated as 40 cps per MBq (SD of 0.4) and 167 cps per MBq (SD of 2.0) for the non-corrected and corrected data respectively - details of the calculation of sensitivity can be found in **section 2.3.2.3 - Equation 6**.

2.3.1.5 Discussion

The data contained in the results section above is not that of the original analysis but has been corrected for a scaling factor present in some of the standard data reconstructions. It is worth mentioning that original analysis in **section 2.3.1.2** of the 10 consecutive acquisitions highlighted that in some of the standard acquisitions there seemed to be a significant difference in the total number of counts within the standard volume. This was unrelated to the natural decay of the isotope with the total counts being either doubled or halved from the expected value.

A similar anomaly was also observed when comparing the corrected versus the non-corrected count data - **section 2.3.1.4**. For a large number of the reconstructions the value of sensitivity calculated for the corrected and non-corrected were the same. Interrogation of the header file information of the reconstructed data highlighted a factor applied to some of the reconstructions which was independent to the use of an attenuation correction although the factor was seen more in the attenuation corrected volumes.

This correction factor was called an 'RPAH Scale factor' (Royal Prince Albert Hospital), on investigation it was found that this factor was a feature of OSEM reconstruction and was used when the number of counts per pixel exceeded +/- 32000. The RPAH factor essentially corrects for pixel saturation and therefore affects the count statistics which has a subsequent affect on both image contrast and on any value of sensitivity calculated. Unaffected data was assigned a scale factor of 1 whilst the value of the scale factor used ranged between 0.10 and 0.57 for the data affected. A review of all SPET data discussed in the thesis demonstrated that none of the actual reconstructed patient data required the use of the RPAH factor and that the application of this factor was restricted to the Standard acquisition data. All ROI count statistics with an RPAH scale factor were corrected and restored by dividing the counts by the RPAH scale factor.

The results demonstrate that repeated acquisitions under the same conditions gave reproducible quantitative values for counts within the standard volume. Total counts for each acquisition were all within +/- 2 standard deviations, that is $\pm 2.15\%$, which demonstrated reproducibility of measurement. Standard

acquisition frames of 3 seconds were therefore considered to be acceptable showing stability of the resultant count statistics.

The use of an attenuation correction in the reconstruction of the raw data gave on average an increase of 4:1 in the total counts demonstrated in the STD reconstructed volume of the standard.

Since the standard reconstruction was used to define the sensitivity of the system, which in turn allowed quantification of areas of uptake to be calculated, the question over the use of attenuation correction is an important one. From the results in **section 2.3.1.4** there is no way to determine whether or not the use of an attenuation correction would provide an accurate estimation of system sensitivity but instead to realise the implications of its use on the data. Using an attenuation correction produced a much larger value of system sensitivity in comparison to the non - corrected data. The use of the corrected sensitivity value could lead to an underestimation in the uptake and of course the use of the uncorrected sensitivity could lead to the over estimation of uptake. Further work with a phantom was required to determine which reconstruction technique provided the most accurate measure of system sensitivity - see **section 2.3.2.3**. The RPAH factor should also be considered when undertaking any quantification of iteratively reconstructed SPET data to ensure data are corrected or restored appropriately, particularly in the standard acquisitions where the small volume means that the image comprises only a very few pixels.

2.3.2 Determining reproducibility and accuracy of quantification of 2 versus 4 hour imaging

In order to establish how reproducible SPET imaging could be in evaluating and quantifying areas of uptake the in-house phantom was used. A retrospective review of normal NeoSPECT patient data was undertaken to try to determine typical lung to background ratios. This information along with the liquid volume of each component was used to help select appropriate activities and create radioactive solutions to fill each component.

2.3.2.1 Methods

The filled phantom along with 1 abnormality insert was placed on the imaging bed and left for an hour to allow the solution to equilibrate, see **Figure 23**.

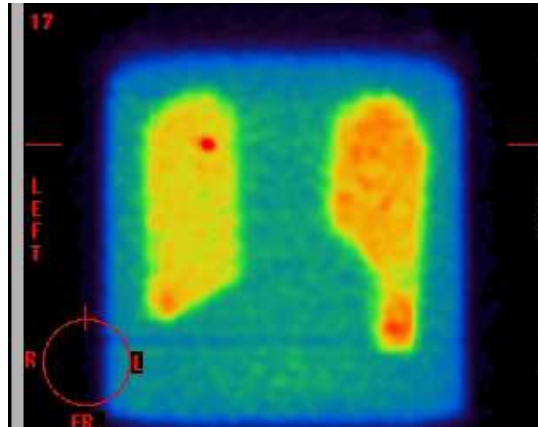


Figure 23 - In-house Phantom Filled
Image showing a coronal slice of the in-house lung phantom filled with a ^{99m}Tc solution, including an additional tumour insert placed in the apex of the right lung (left on image volume).

Table 13 details the activities in each insert/component at time of first set of imaging.

	Body	Lung (right and left)	Abnormality/vial
Activity (MBq)	458.7	176.6	0.54
Volume (ml)	14500	700 & 650	1

Table 13 - Activities and volumes used to fill the in-house phantom

The phantom set up, acquisition and reconstruction had to replicate those of a patient. These are described in **section 2.4.1** and summarised in **Table 22** and **Table 23**. The phantom was imaged twice with a 2 Hour gap between the first and second acquisition. On completion of the first acquisition, the phantom remained on the imaging couch. Since there was no change to the phantom, any variations in T:Bs (tumour to background ratio - described in more detail in **section 2.4.1**) demonstrated were a combination of statistical variations and reproducibility of the AC correction and ROI analysis technique and not reproducibility of the set-up (this was therefore the minimum difference to expect). In reality for the patient data, the patient did not remain on the bed between imaging, therefore values of bed height, detector distance etc. were all noted and used to set up the second acquisition.

Both reconstructed data sets were viewed using ‘Volume Fusion Display’ on the Hermes system, which allows both reconstructions to be displayed simultaneously and registered. The focal area of uptake representing the abnormality was identified on both sets of images, and regions of interest, ROIs, were drawn on the transverse slices. Image quantification was in the form of:

1. Tumour to background ratio, T:B
2. Absolute Uptake (MBq and expressed as % uptake)

For analysis of T:B values, ROIs were drawn around the abnormality and around an adjacent area which was representative of normal lung uptake (Background) as shown in **Figure 24**. For T:B ROI analysis the only stipulation on the placement of the background ROI was that it was consistent between the two sets of images.

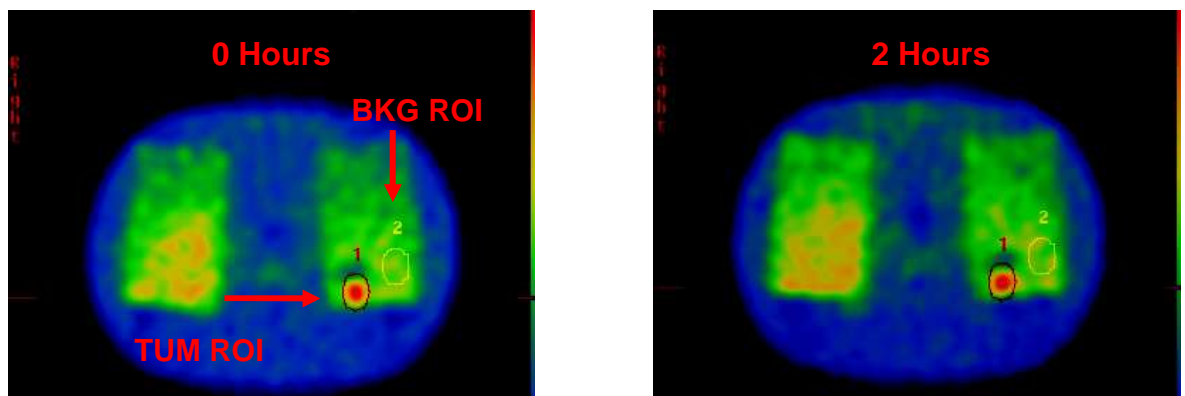


Figure 24 - Phantom Transverse Slices 0Hr versus 2Hr

Images shown are reconstructed transverse slices through the in-house lung phantom. Also shown on each slice are the background (BKG) and tumour (TUM) ROIs used to calculate the T:B. The image on the left is a reconstructed transverse from the 0Hr acquisition whilst the image on the right is the corresponding slice from an acquisition performed 2 hours later.

The use of a background correction is almost always applied to planar data since the total counts contained in a ROI usually contains a contribution of counts from adjacent and overlying organs/structures. The advantage of SPET imaging is that organs and structures in the body can be viewed without having to distinguish between uptake in an area of interest and an overlying organ. To assess the accuracy of calculating a value of absolute uptake from SPET imaging consideration had to be given to the use of a background correction. However,

since this relies on a background ROI an equally important factor was the placement of this ROI. As the main concern for SPET data arises from the contribution of counts from adjacent areas it would be more appropriate that the background ROI encompassed that of the tumour/vial as shown in **Figure 25**.

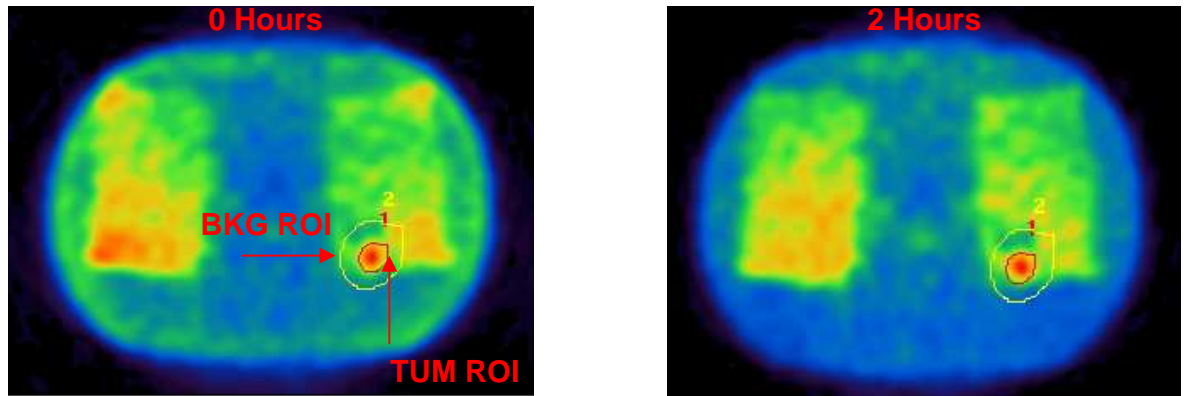


Figure 25 - ROIs for Uptake Analysis

Images shown are reconstructed transverse slices through the in-house lung phantom. Also shown on each slice are the background (BKG) and tumour (TUM) ROIs used to calculate a value of percentage uptake. The image on the left is a reconstructed transverse from the 0Hr acquisition whilst the image on the right is the corresponding slice from an acquisition performed 2 hours later.

For both assessments of quantification technique namely measurement of T:B and calculation of uptake values, values of total and maximum counts along with the number of pixels (area) were extracted from the ROIs. Data were obtained from all transverse slices which demonstrated the tumour vial.

2.3.2.2 Results 1 - Assessment of tumour to background ratio T:B, reproducibility

Tumour to background ratios, T:B_s were calculated using data from the reconstructed transverse slices. On the transverse plane the tumour/vial was identified on 3 slices on both the 0 hour acquisition and the 2 hour acquisition. **Table 14** details the values of T:B calculated over the tumour/vial volume from the transverse plane.

	Total Counts		Maximum Counts	
	0 Hour ACQ	2 Hour ACQ	0 Hour ACQ	2 Hour ACQ
Slice 55	1.15	1.13	1.61	1.42
Slice 56	1.20	1.14	1.69	1.63
Slice 57	1.07	0.95	1.35	1.28

Table 14 - T:B calculated per transverse slice at 0 and 2Hrs.

Using the values of total counts the maximum T:B calculated from the 0 hour acquisition was 1.20 and for the 2 hour acquisitions was 1.14, the maximum ratio for both acquisitions was found on slice 56.

The maximum difference in T:B demonstrated between 0 and 2 hour acquisition was 0.07. Repeated reconstruction and analysis (x10) of the 0Hr acquisition demonstrated a maximum difference of 0.19 with mean a T:B of 1.22 +/- 0.02.

Comparing the T:B calculated from maximum counts per pixel it can be seen that the maximum value of T:B calculated at 0 hours was 1.69 and at 2 hours was 1.63, whilst the maximum difference demonstrated was 0.06.

2.3.2.3 Results 2 - Evaluation of uptake calculation and assessment of washout reproducibility

To calculate a value of percentage uptake, a value of absolute activity in the area of interest/tumour must be calculated first. To assess the accuracy of this calculation with SPET data, the in-house phantom acquisitions described in **section 2.3** were used along with data from a standard acquisition. The standard acquisition being used to calculate the sensitivity of the gamma camera. The standard was reconstructed with and without an attenuation correction (AC and non-AC). ROIs were drawn on the transverse slices, one around the standard vial and one over an area of background as shown previously in **Figure 19**.

From the STD ROIs values of total counts and number of pixels were extracted. Since these ROIS differed in size the counts in the background ROI were normalised to the STD ROI as described by **Equation 3**.

Table 15 and Table 16 detail the counts demonstrated in each slice.

	Standard Counts	Background Counts	BKG Corrected Counts
Slice 44	1451	12	1439
Slice 45	3822	9	3813
Slice 46	6921	11	6909
Slice 47	8923	7	8917
Slice 48	9379	4	9375
Slice 49	9612	6	9606
Slice 50	9884	7	9878
Slice 51	9397	8	9388
Slice 52	8632	10	8621
Slice 53	8306	18	8287
Slice 54	7879	18	7861
Slice 55	6693	4	6688
Slice 56	4761	1	4760
Slice 57	2638	4	2634
Slice 58	1079	4	1075
Slice 59	279	1	278
Total	99655	126	99529

Table 15 - Non-AC Recon Data

	Standard Counts	Background Counts	BKG Corrected Counts
Slice 44	7847	49	7799
Slice 45	20647	45	20602
Slice 46	37233	43	37190
Slice 47	48071	25	48046
Slice 48	50678	4	50673
Slice 49	51720	25	51696
Slice 50	53229	52	53178
Slice 51	50774	38	50735
Slice 52	46411	61	46351
Slice 53	44559	94	44465
Slice 54	42309	84	42226
Slice 55	35957	23	35934
Slice 56	25476	15	25461
Slice 57	14144	33	14111
Slice 58	5721	28	5693
Slice 59	1468	4	1464
Total	536245	622	535624

Table 16 - AC Recon Data

Values of standard counts and background corrected counts from each transverse slice for both AC and non-AC data were summed over the entire volume of the vial. These values were then used in Equation 6 along with length of acquisition and activity contained in the vial to calculate the sensitivity.

$$Sensitivity = \frac{(C_{STD} \div T_{ACQ})}{A_{STD}}$$

Equation 6

where C_{STD} is the counts from the standard, T_{ACQ} is the sum of the length of the acquisition from each head (measured in seconds), A_{STD} is the measured activity of the standard.

The activity in the standard vial at the time of imaging was 3.64 MBq, this was measured just prior to imaging using the Capintec isotope calibrator. Each frame was 3 seconds long with 120 frames acquired meaning the total duration of the acquisition was 360 seconds. Using these values the sensitivity (counts per second per MBq) was calculated - see **Table 17**.

	No Attenuation Correction		Attenuation Correction	
	No Bkg Corr (c s ⁻¹ MBq ⁻¹)	Bkg Corr (c s ⁻¹ MBq ⁻¹)	No Bkg Corr (c s ⁻¹ MBq ⁻¹)	Bkg Corr (c s ⁻¹ MBq ⁻¹)
Sensitivity	76	76	409	409

Table 17 - Sensitivities

The background activity can essentially be considered as being negligible relative to the STD volume activity as its subtraction has no reflection on the value of sensitivity calculated as demonstrated in **Table 17**.

As with the standard data processing, the phantom was reconstructed with and without attenuation correction. The use of the background correction in calculating a value of absolute activity had to be considered and assessed.

From the ROIs, values of counts and number of pixels were extracted. These values were used in **Equation 7** to obtain a true value of background counts, the counts in the background ROI were corrected for tumour counts and then normalised to the tumour region.

$$C_{BKG} = \left(\frac{C_{BKG+T} - C_T}{A_{BKG+T}} \right) \times A_T$$

Equation 7

where C_{BKG} is the background counts, C_{BKG+T} is the counts from the ROI containing both background and tumour, A_{BKG+T} is the area of the ROI containing both background and tumour, C_T is the counts from the tumour ROI, A_T is the area of the tumour.

Values of counts from tumour and background areas are given in **Table 18**, the value of counts in each slice were summed over the volume of the vial/tumour as shown in the last row.

	No Attenuation Correction				Attenuation Correction			
	0 Hrs ACQ		2 Hrs ACQ		0 Hrs ACQ		2 Hrs ACQ	
	BKG	Tum	BKG	Tum	BKG	Tum	BKG	Tum
Slice 55	7437	14686	5819	11168	30201	61275	23424	46157
Slice 56	7320	15415	5819	11616	30198	65959	23390	48806
Slice 57	7313	12302	5428	9235	32512	56447	22237	39710
Total	22070	42403	17066	32019	92911	183681	74051	134673

Table 18 - Phantom Count Data

The activity of the vial/abnormal region demonstrated in the reconstructed images was calculated using **Equation 8**.

$$A_T = \frac{\left(C_{Total} \div T_{ACQ} \right)}{S_{STD}}$$

Equation 8

where A_T is the activity (MBq), T_{ACQ} is the sum of the length of the acquisition from each head (measured in seconds), S_{STD} is the sensitivity, C_{Total} is the total counts from the tumour ROI.

Table 19 details the values of activities at 0 hours and 2 hours calculated from the image data and the actual values corrected for decay. A background correction is almost always applied to planar data since the counts from an area of interest are usually contributed by adjacent and overlying structures.

Consideration as to whether or not a background correction was appropriate for SPET tomographic imaging was considered. To allow a comparison, an uptake was calculated using values of total counts which had been corrected for background alongside data that had not been corrected for background.

	Actual (MBq)	No Attenuation Correction (MBq)		Attenuation Correction (MBq)	
		Tum	Tum (Bkg Corrcted)	Tum	Tum (Bkg Corrcted)
0 Hrs	0.54	0.16	0.07	0.67	0.33
2 Hrs	0.42	0.12	0.05	0.49	0.24
Diff	0.12	0.04	0.02	0.18	0.09

Table 19 - Activities: Actual Versus Calculated

The difference between 0 and 2 hours was calculated for the expected difference (due to decay of the source only) and for the image derived activities. In addition to this differences between the calculated and the known at 0 and 2 hours are shown in Figure 26.

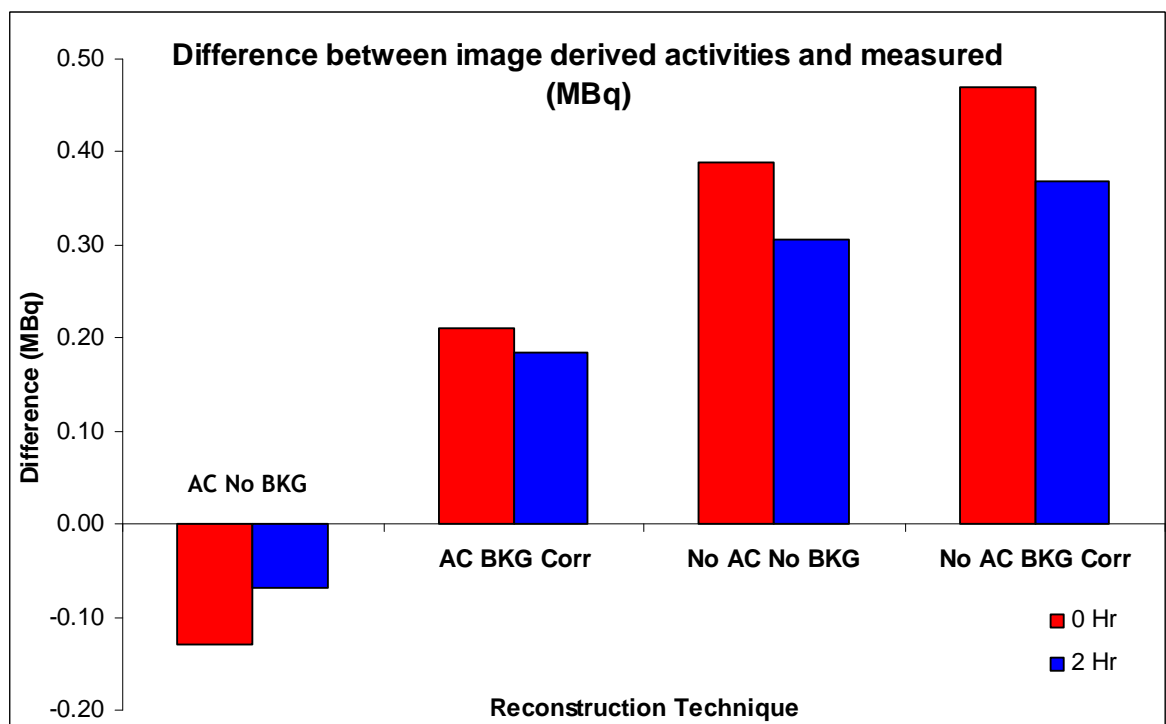


Figure 26 - Graph of Relative Error in Activity Calculation

Bar chart comparing the difference between values of absolute activities calculated from the reconstructed image data with the values measured on the radionuclide calibrator. The red bars indicate the differences observed at 0 hours and the blue at 2 hours.

The largest difference was demonstrated when no attenuation correction was applied. The smallest difference demonstrated between the calculated and measured values of activity at 0 hours was -0.13 and -0.07 at 2 hours, which were calculated using the data corrected for attenuation but not for background. From the repeated reconstruction and analysis (x10) of the 0Hr acquisition data with no background correction but with AC the maximum

difference in the range of activities calculated was 0.39MBq, the mean activity calculated was found to be 0.95MBq +/- 0.04.

Comparison with the attenuation and background corrected data demonstrated a difference of 0.21MBq and 0.18MBq at 0 and 2 hours respectively. From the repeated reconstruction and analysis (x10) of the 0Hr acquisition data with AC and background correction the maximum difference in activities calculated was 0.29MBq with a mean activity of 0.55MBq +/- 0.03.

It should also be noted that the error in isotope calibrator reading is +/- 0.02MBq.

2.3.2.4 Discussion and Conclusion

As discussed previously, it is important that the acquisition of the standard data matches closely the conditions of the patient acquisition and that the standard reconstructions match the patient data reconstructions. However, results demonstrated that the application of an attenuation correction to the reconstructed standard data grossly increased the value of sensitivity calculated. This increased sensitivity meant that the activity calculated became meaningless. This is most likely as a result of over-compensating the data for a attenuation when the medium causing the attenuation was essentially air (with very low attenuation) and not water. For this work, it was more accurate to calculate a value of sensitivity from the standard data that was not corrected for attenuation correction using Chang's technique.

This was not the case for phantom work or patient work, as both of these volumes contain water and other attenuating medium. It important to apply an attenuation correction to both patient and phantom data as the counts from the various organs/structures in the torso will be affected by attenuation.

Comparison of the attenuation corrected values with and without a background correction are described in **Table 19**. This shows that the value of activity calculated from the non-background corrected data more closely matches the value measured on the isotope calibrator. However, reproducibility measurements performed with the data from the phantom at 0Hr which included

attenuation correction demonstrated that for the non-background corrected data a mean activity of $0.95\text{MBq} \pm 0.04$ and for the data with background correction, a mean activity of $0.55\text{MBq} \pm 0.03$. This would support the use of a background correction for patient data.

2.3.3 Assessment of updated reconstruction parameters

All the image handling for this project was performed using software from Hermes Medical Solutions. The Hermes software system can be used to display and analyse various types of images including planar, dynamic, whole body and SPET. This software can also perform image reconstruction of raw 3D data using either Filtered Back Projection techniques or Iterative techniques (OSEM) - these have been described previously in **Chapter 1**. When the software was first purchased, OSEM was relatively new to the commercial market and therefore Hermes provided basic advice as to the number of subsets and iterations required to achieve good quality reconstructed images. Having no experience of iterative reconstruction techniques, the department at GRI decided to follow the advice provided by Hermes. At the time data were compared with previous data which used filtered back projection and the data quality was assessed qualitatively to be consistent. During this project however, Hermes collaborated with Prof B Hutton of UCL, who provided advice on optimising the reconstruction parameters in terms of the number of subsets and iterations. This advice only became available after all the trial NeoSPECT data had been acquired and reconstructed and so there was some concern that the reconstructed data may not have been optimised, which might affect the quantitative analysis. Since this was a major part of the project, it was decided to compare the images reconstructed from a subset of the total patient population using the original parameters with those reconstructed using the new parameters proposed.

2.3.3.1 Methods

New advice from Hermes stated that the number of subsets should be dictated by the number of projections acquired, see **Equation 9**.

$$Subsets = \frac{\# \text{ of Projections}}{4}$$

Equation 9

A total of 10 patients were selected to undertake this investigation, these being patients who took part in the NeoSPECT trial and had demonstrated abnormal uptake within the lungs on the NeoSPECT images. The data were reconstructed using the original and new suggested parameters as described in **Table 20**.

	Iterative HOSEM – Hermes Ordered Subset Expectation Maximisation	
Reconstruction Method:	Original Parameters	New Advice
Iterations:	4	4
Subsets	6	30
Zoom:	0	0
Filter	Low Pass cut-off 1.5 cycles/cm	No advice (Low Pass cut-off 1.5 cycles/cm used)
Attenuation Correction	Yes	No advice (Yes used)

Table 20 - Reconstruction Parameters

To ensure a good comparison between the existing with the new parameters the volume reconstructed was exactly the same and this was defined by the start slice and total number of slices. In addition where no advice was given with the new parameters, for example with the filter and attenuation correction, the original parameters were used.

The abnormal area was analysed quantitatively via Tumour to Background ratios (T:B). The Hermes software allows up to 3 reconstructed volumes to be loaded, viewed and analysed simultaneously. The tumour and background areas were drawn on the transverse plane. The extent of disease was assessed using the sagittal and coronal planes also, allowing the volume and extent of disease to be accurately identified on the transverse plane.

Using the original reconstruction, an ROI was drawn around the area of abnormality and an area of normal lung uptake, which were then applied to the same slice on the newly reconstructed data. The number of slices on which the abnormality/tumour was visible varied between patients but never between reconstruction techniques.

From these regions, values of total counts and total number of pixels were extracted to allow a ratio to be calculated T:B. The tumour and the background ROI were often not equal in size and therefore the BKG region was normalised to the tumour region prior to calculating the ratio.

2.3.3.2 Results

From a qualitative perspective the image quality of those reconstructed using 30 subsets appeared to contain more noise in comparison to those reconstructed using the original parameters advised- see **Figure 27**. There were, however, no

instances where the ROI defined on the original reconstruction did not encompass the tumour volume on the new reconstruction. This was also true for the number of transverse slices over which the tumour was present.

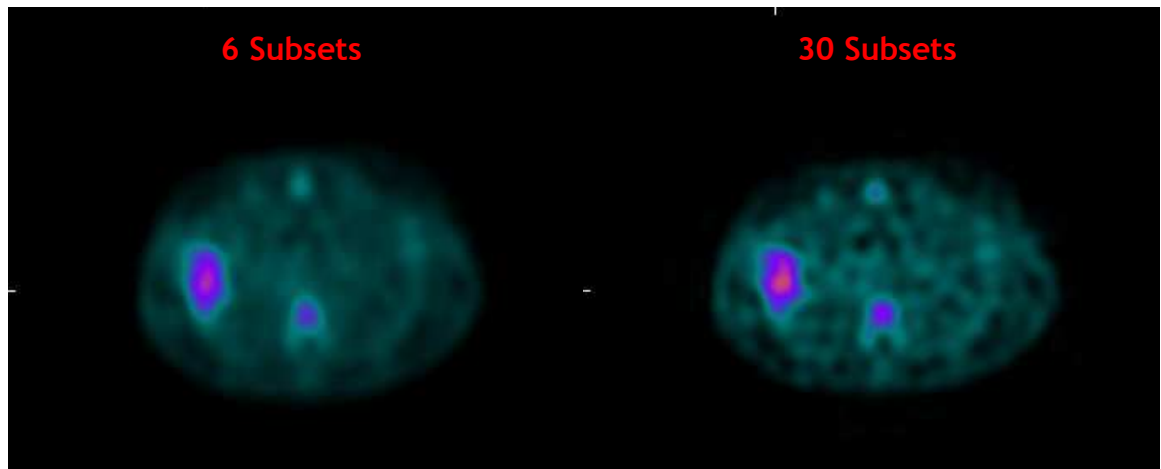


Figure 27 - Qualitative Comparison of transverse slices
Images show a transverse slice of SPET data reconstructed with 6 subsets (on the left) and with 30 subsets (on the right). The transverse slices shown are through the thorax of patient with positive NeoSPECT uptake in the right lung.

Results from the quantitative evaluation of the reconstruction techniques can be found on Table 21.

Patient	Max T:B		Absolute Differences	
	6 Sub	30 Sub	Max	Average
1	1.60	1.57	0.17	0.07
2	2.85	2.59	0.28	0.12
3	1.85	1.91	0.26	0.08
4	1.37	1.30	0.08	0.04
5	1.98	1.95	0.14	0.07
6	1.83	1.89	0.16	0.09
7	1.71	1.56	0.19	0.09
8	2.31	2.33	0.11	0.04
9	1.52	1.76	0.34	0.16
10	1.65	1.53	0.22	0.10

Table 21 - Comparison of Reconstruction Parameters via T:B

The maximum difference in ratios seen in any one volume was 0.34, whilst the mean of the maximum differences was 0.19.

2.3.3.3 Discussion and Conclusion

The difference between data reconstructed using the original Hermes settings and those using the new advice from Hermes was not considered significant as the reproducibility of the measurement assessed in **section 2.3.2.2** demonstrated differences in T:B ratios of up to 0.20, therefore it was considered unnecessary to reanalyse the previously reconstructed data using the new advice.

2.4 Patient Acquisitions & Image Quantification

The main patient data group comprised those involved in the trial (see **section 2.2**) to investigate the use of quantification to assess if dual time imaging could characterize tissue type in terms of washout rates. However, to increase sample size, data were also used from patients who had routine NeoSPECT imaging which consisted of SPET imaging at the 2 hours post injection time frame only.

In addition to the clinical data for the trial, the data allowed improvements in reconstruction software (for example the commercial advent of iterative reconstruction) to be assessed in terms of its quantitative value. This was of great value as the majority of previously published data involved quantification of data reconstructed using Filtered Back Projection techniques.

Data were used from 36 patients in total, of whom 19 had dual time imaging performed. The data were then grouped and analysed as follows:

- Investigation 1** Comparison between Filtered Back Projection and Iterative reconstruction techniques for all patients.
- Investigation 2** 2hr Acquisition Tumour to Background ratio T:B, versus histology findings.
- Investigation 3** 2hr Versus 4hr Acquisition T:B and wash out versus histology findings in the main tumour.
- Investigation 4** 2hr Versus 4hr Acquisition Mediastinal Uptake Versus histology findings
- Investigation 5** 2hr Acquisition percentage uptake versus histology findings.
- Investigation 6** 2hr Versus 4hr Acquisition percentage uptake wash out versus histology findings in the main tumour.

2.4.1 Tumour to Background Ratio

One of the most basic means of assessing the difference in uptake between two tissue types is simply a target tissue to background tissue ratio, T:B. In this context background tissue is in fact physiological uptake in equivalent non-disease tissue. The target tissue is the tissue which is known or suspected to contain disease, characterized usually by a focal area of increased radiopharmaceutical uptake. Whilst the background tissue is merely tissue preferably of the same organ that demonstrates a more diffuse and notably physiological normal level of radiopharmaceutical uptake, in other words is disease free. In terms of NEOSPECT uptake this is best demonstrated by the example study shown in **Figure 28**.

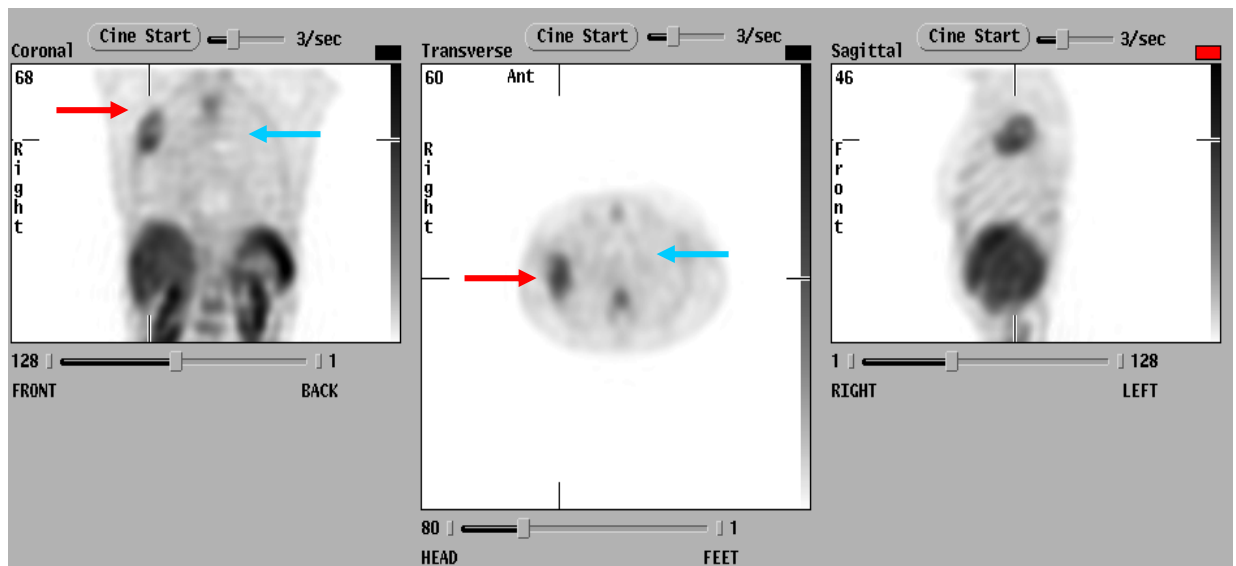


Figure 28 - NEOSPECT Uptake in Abnormal Patient

Images shown are reconstructed coronal, transverse and sagittal slices as displayed by the Hermes system. This patient demonstrated increased uptake in the upper lobe of their right lung - as shown by red arrows on the coronal and transverse planes, the blue arrow shows normal lung tissue.

In **Figure 28** the red arrow highlights the area of abnormal uptake within the lung (right apex) and the blue shows normal lung uptake in the contralateral lung.

2.4.1.1 Methods for Investigations 1 - 4

The imaging protocol for routine NeoSPECT patients (the non-study patients), required each patient to have a SPET acquisition followed by a static planar image of the chest and the pelvis. This imaging was performed 2 hours post

injection of the radiopharmaceutical. The SPET acquisition was of the thorax, including the entire lung field in the field of view (FoV) and (because of the proximity to the lungs) also including both axillae. An elliptical orbit was chosen for the SPET acquisition in order to reduce patient to detector distance and increase image quality.

This orbit of rotation was optimised further by requesting the patient (when capable) to lie with their hands and arms behind their heads for the duration of the scan thus avoiding unnecessary attenuation from the patient's arms. This helped to improve overall image quality by minimising scatter, improving sensitivity and thus improving image resolution whilst also helping to achieve good visualisation of the axillae. Aside from ensuring that the entire thorax (including the axillae) were in the FoV there was no other setup specifications.

The setup for patients who had dual time imaging was slightly more controlled in that for these patients it was important to try and replicate the set up parameters and conditions of the first acquisition during the second acquisition. To aid this, a proforma had to be completed by imaging staff- see Appendix B. This allowed the parameters associated with the setup to be documented during the first study and the operator could then ensure both data volumes acquired were similar. This also meant that variations in the count statistics caused by the orbit of rotation could be limited which was important since quantitative analysis would be performed.

The proforma contained details including that of the bed height and transverse position. Each patient was positioned on the scanning bed 'feet first', their arms and shoulders were placed in a head and arm rest - see **Figure 29** - which was always placed at the end of the scanning bed. This meant that from a translation point of view the patient's position could be replicated.



Figure 29 - Patient Head and Arm Rest

Image of the department's arm and headrest used for NeoSPECT acquisitions. This aid is designed to assist the patient in maintaining the "arm up" position during the scan. The "arms up" position allows the detectors of the gamma camera to get closer to the thorax.

The proforma also included details of the gamma camera head orbit. The elliptical orbit of rotation for the gamma camera heads was defined at four angles as shown in **Figure 30**. At these angles the heads were positioned as close as possible to the patient without being in actual contact. The detector positions at each angle were recorded. The orbit was then tested by rotating the heads around the patient to ensure clearance. Any amendments to the gamma camera head position were recorded. It was possible that the bed height could influence how close the detectors could get to the patient and the operator could vary this to aid optimisation of the orbit of rotation. The value of bed height was also recorded.

Recently manufactured gamma cameras have sensors (usually infra red) positioned on each gamma camera head to detect the patient and as a result the orbit of rotation is able to mimic that of the actual patient allowing the detectors to get even closer to the patient. However, none of the gamma cameras used for this study had this facility. The orbit was computed from the four marked points as shown in **Figure 30**.

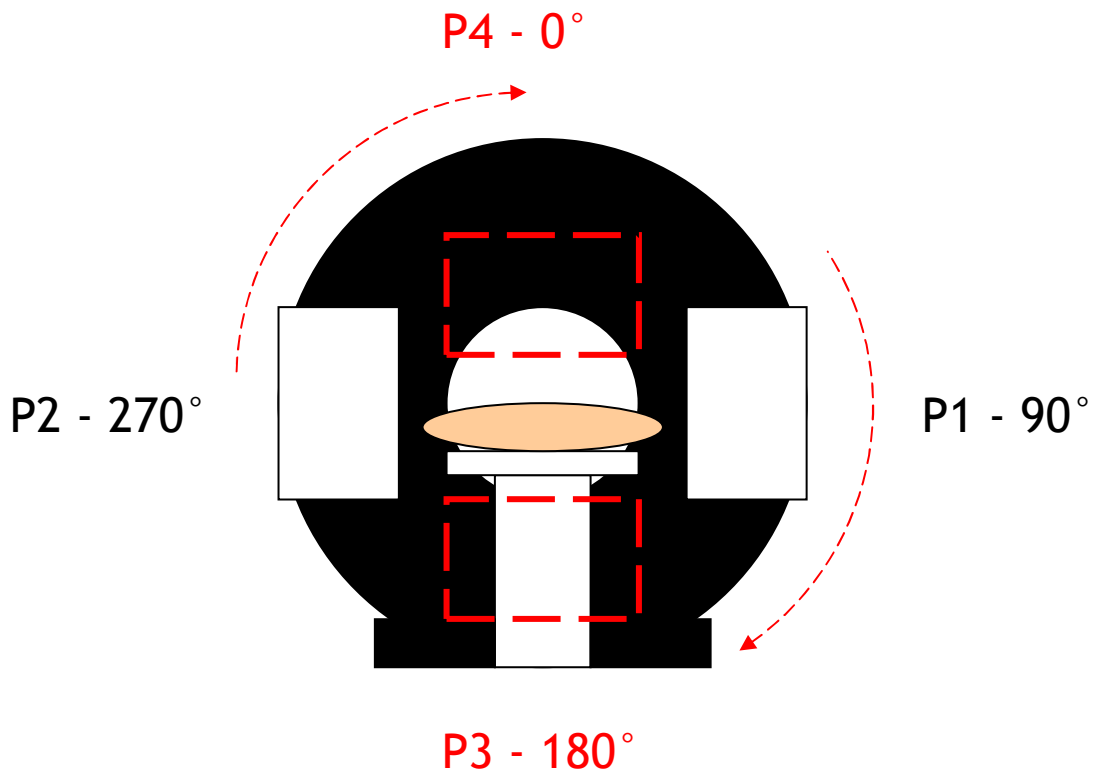


Figure 30 - Detector Set - Up Configuration

Image shown is a simplified diagram indicating the configuration of the detectors used to set the orbit of rotation for NeoSPECT acquisitions.

Limiting the positional differences at the acquisition stage meant less manipulation of the reconstructed data at later stages.

A summary of the acquisition parameters for SPET imaging can be found in **Table 22**. The camera used was the Philips Forte as was used for the STD acquisitions.

Orbit:	Elliptical
Patient Position:	Supine and Feet First
Collimators:	VXHR parallel hole, low energy, high resolution with long bore septa
Frame Time:	30s
Matrix size	128 x 128
Number of Frames:	120
Rotation:	360 (180 per head)

Table 22 - Acquisition Parameters

The raw data for each patient were reconstructed using the traditional Filtered Back Projection technique and then the Ordered Subset Expectation

Maximisation (OSEM) iterative technique³. In both cases the full FoV was reconstructed to allow accurate slice by slice comparisons to be drawn.

Reconstruction Method:	Iterative HOSEM – Hermes Ordered Subset Expectation Maximisation
Protocol:	NeoSPECT
Post Reconstruction Filter:	Low Pass 1.5
Iterations:	4
Subsets	6
Zoom:	No zoom (either on acquisition or following reconstruction)

Table 23 - Iterative Reconstruction Parameters

In the case of patients who had 2 and 4 hour imaging, despite limiting the variations in the acquisition setup, there were slight differences in the acquisition volumes. These were corrected by co-registering the reconstructed volumes using the purpose designed Hermes software.

The Hermes registration software offered both automatic and manual options. There are a number of automatic techniques used for registration, the majority of these are iterative and are based on minimization techniques to match the volumes. The Hermes system uses a ‘multi-resolution technique’. This option was considered initially to help reduce the time spent during the image processing stage. However, visual evaluation of the volumes highlighted some notable differences between the volumes indicating that the volumes had not been matched successfully via the automatic process. Therefore it was decided that the semi automated form of image registration should be used - Landmark Registration. For more details on image registration refer to **section 1.2.2.4 of Chapter 1**.

Once processing of the raw data was complete, the volume(s) were loaded into Hermes ‘Volume Fusion Display’ software, which displays the images in 24-bit colour depth (16,777,216 colours). Volume Fusion Display allowed two separate volumes to be displayed either separately or fused. ROI analysis could also be performed. Since ROI analysis was being used to try to identify any defining characteristics, in terms of tracer uptake, between various tissues, it was important that the delineation between normal and abnormal was accurate. Consideration had therefore to be given to optimizing how these volumes were

³ Refer to section 2.3 for optimisation of reconstruction parameters

being displayed. Visual assessment was undertaken and it was realized that the images were more appropriately displayed in 'absolute mode'. This means that the images were scaled to the maximum counts per pixel seen in the entire volume rather than 'relative mode' which scales a slice to the maximum counts in that particular slice. Secondly, with a wide range of colour schemes available it was important to choose a scheme that drew the eye to areas of increased uptake and could help delineate between normal and abnormal tissue.

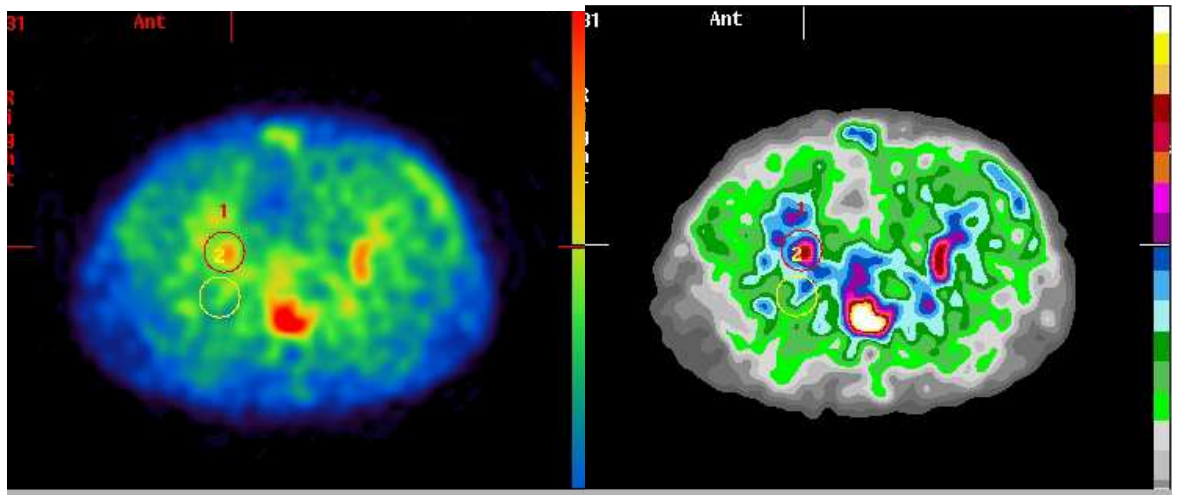


Figure 31 - Colour Schemes

Images show transverse slices through a patient's thorax with corresponding ROIs around the tumour and over an area of background. The image on the left is displayed using colour scheme 'Renal' which has 256 colours and the image on the right using the '17 point' colour scheme.

Whilst the scheme is subjective to the user, it was decided that 2 of the best schemes for viewing the data were 'Renal' shown on the left of **Figure 31** and the '17 point' scheme on the right.

For ROI analysis the '17' point scheme was chosen as there are only 17 actual colours within the colour scale. This is a discontinuous scale which unlike the 'Renal' scale (256 different colours) means that changes in the counts per pixel appear more significant than they actually are, producing more discrete boundaries.

To calculate tumour to background ratios an ROI was drawn around the area of abnormal or focal increased uptake on the transverse slice. A second ROI was then drawn around an area of normal lung uptake either in the same or the contralateral lung depending on the extent of the disease - an example is shown in **Figure 32**.

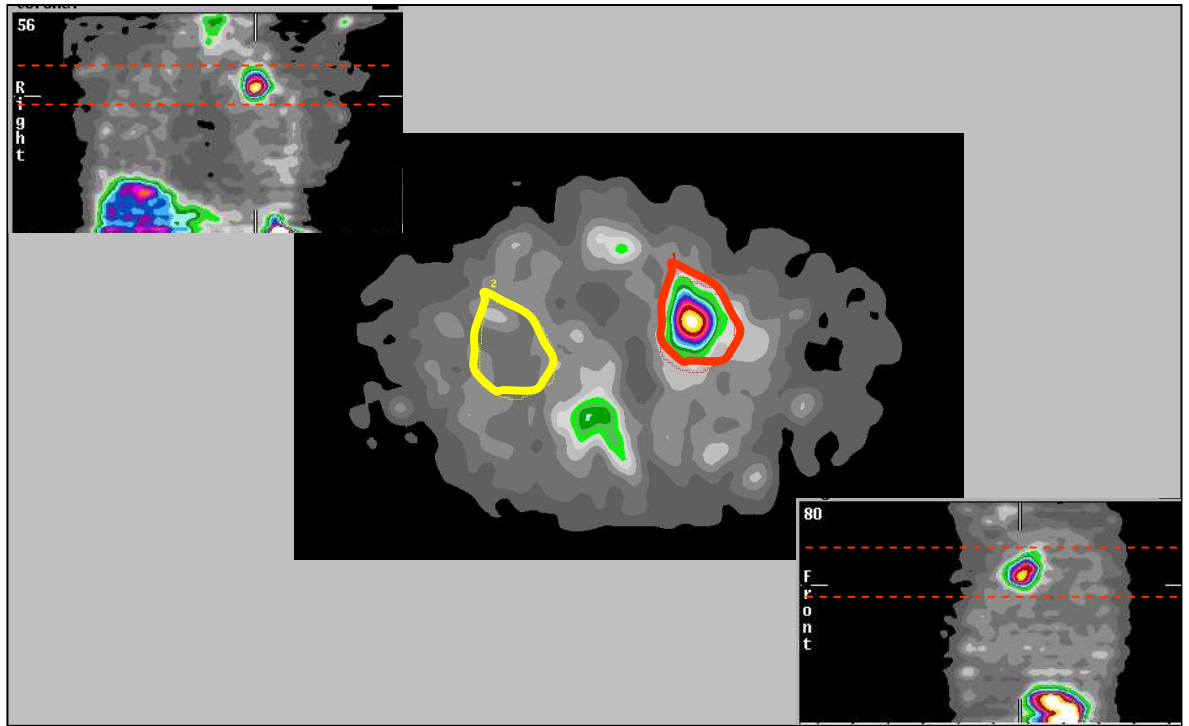


Figure 32 - Lung ROIs

Images shown are of the reconstructed coronal (top left), transverse (central) and sagittal (bottom right) slices through a NeoSPECT patient's thorax. Example background and tumours ROIs are shown on the transverse slice; yellow and red ROIs respectively. The red dashed lines on the coronal and sagittal slice define the upper and lower limits of the tumour.

From the ROIs, values were obtained of total and maximum counts. ROI sizes were also obtained. In most cases the tumour and background ROIs were equal in size, however, this was patient and specifically patient disease dependant and therefore for some patients the size of these two ROIs differed to allow appropriate tissue areas to be selected. To compare counts demonstrated in one ROI to another, the ROIs had to be either the same size or normalized to area i.e. the background ROI was normalised to the area of the tumour ROI.

2.4.1.2 Investigation 1 Results - Iterative (IT) versus Filtered Back Projection (FBP) reconstruction of data acquired at 2 Hours

Since iterative reconstruction techniques were available, one of the aims of this work was to determine if there were significant differences between the two reconstructed data sets that could affect or influence the results of image quantification. To investigate this 10 patient were selected (6 malignant and 4 benign); each of these patients had an area of increased uptake demonstrated on their planar images at 2 Hours. Each patient's tomographic data were

reconstructed using both FBP and IT reconstruction techniques. Details of the reconstruction parameters are given in **Table 24**.

Filter Back Projection	Iterative HOSEM
# of Slices - Full Field of View	# of Slices - Full Field of View
Post Recon Filter - Low Pass 0.8	Post Recon Filter - Low Pass 1.5
Iterations - NA	Iterations - 4
Subsets - NA	Subsets - 6
Zoom - 0	Zoom - 0

Table 24 - Reconstruction Parameters

Tumour and background regions of interest were drawn on the transverse slices and T:B ratios calculated. **Figure 33** charts the difference in the total counts found in each Tumour region corrected for background, it should be noted that where the size of the region differed between reconstruction techniques the regions were normalised to those of the iterative technique.

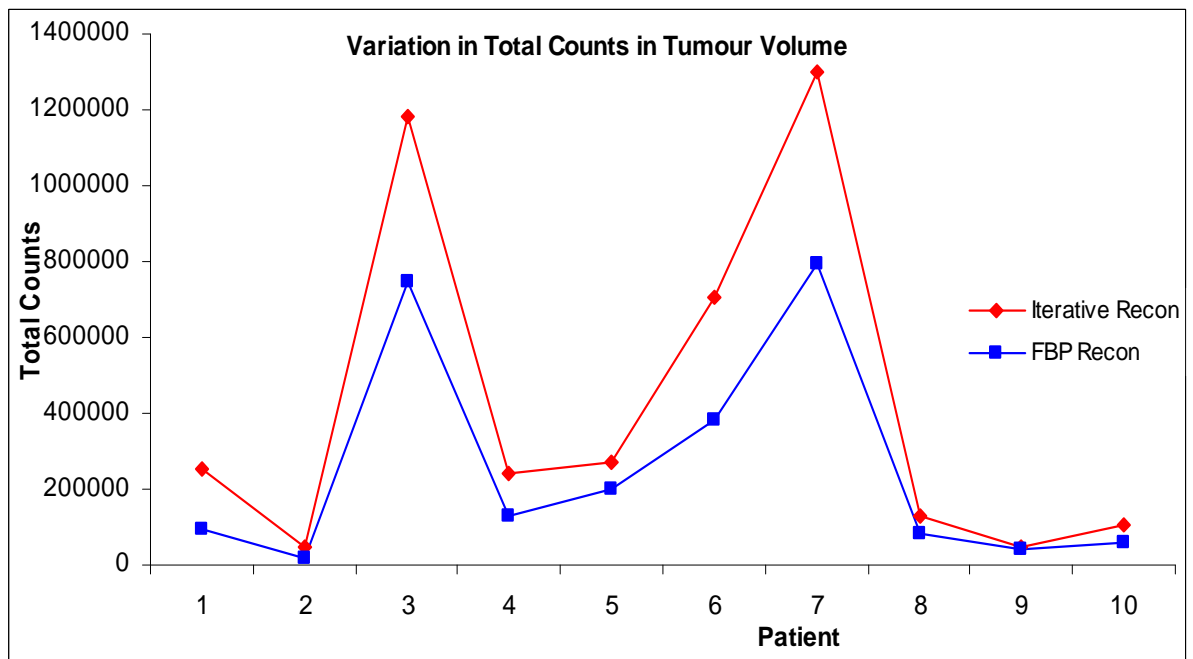


Figure 33 - Graph of Variation in Total Counts

The graph shown is a plot of the total counts demonstrated in a tumour volume for both iterative and FBP reconstruction techniques (red and blue data points and trendline respectively)

A difference in the total number of counts in each tumour volume was noted between the iterative and FBP techniques, however, in terms of the ratios calculated the differences appeared less significant, see **Figure 34**.

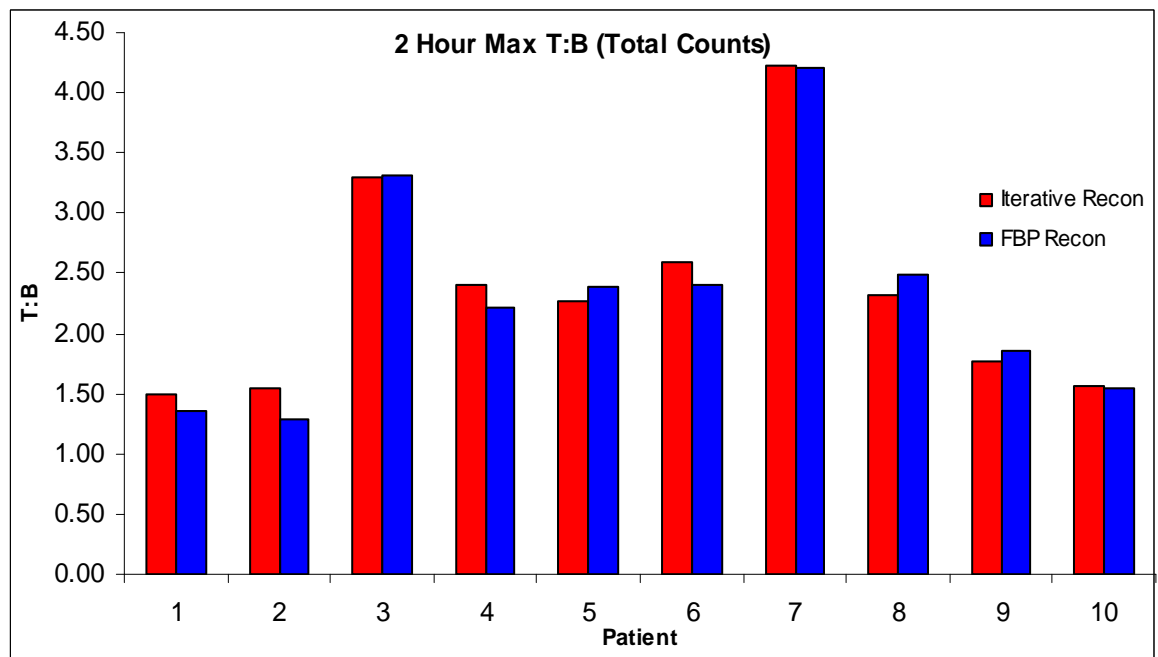


Figure 34 - Graph of 2Hr Max T:B (Total Counts)

Bar chart of the of the maximum T:B calculated using the total counts from the 2 hours acquisition only. Values calculated from data reconstructed with iterative techniques are shown in red and with FBP in blue.

The largest difference in T:B noted between the two reconstruction techniques was 0.25, the maximum difference demonstrated when assessing the reproducibility of the T:B was found to be 0.19.

To test for differences between the values from the two reconstruction techniques a wilcoxon signed rank test was performed. This test did not conclude a statistically significant difference between techniques, the p-value was $p=0.359$, estimated median of -0.04 and a 94.7 CI of $(-0.155, 0.075)$. Since there is no trend in the differences, it is likely that differences seen are within the variation expected from the reproducibility of the techniques.

From a quantitative perspective there was no significant difference between the two reconstruction techniques however it was decided that all subsequent data would be reconstructed using iterative techniques as there was a clear difference in the images from a qualitative perspective. **Figure 35** is typical of the image quality seen using each technique.

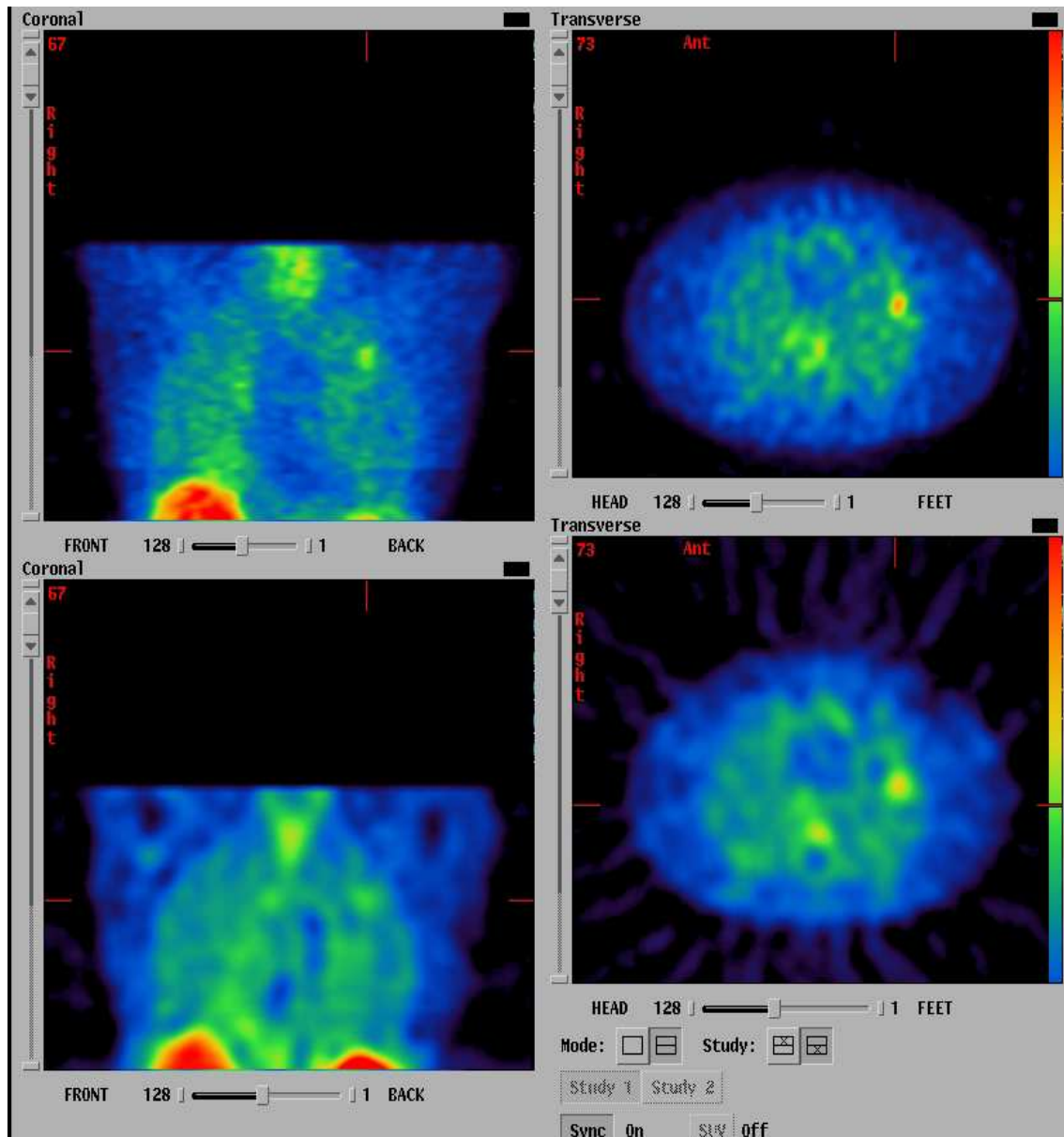


Figure 35 - Qualitative Comparison

Images shown are coronal and transverse slices through a NeoSPECT patient, the upper images are of data reconstructed using iterative techniques whilst the bottom images are from data reconstructed using FBP. This patient has positive NeoSPECT uptake in the apex of the left lung.

The upper row of **Figure 35** demonstrates a coronal and transverse slice of data reconstructed using iterative techniques whilst the lower row shows the corresponding slices reconstructed using filtered back projection. The first notable feature when comparing these images is the clearer delineation of the cardiac cavity, where the iterative reconstruction technique appears to preserve resolution rather than reduce it. Secondly, when reviewing the corresponding transverse slices, the ‘starring or streak artifact’ associated with Filtered back projection is absent from the iterative techniques and so the natural contour of the body appears to be better delineated.

Section Summary - Investigation 1

There are no significant quantitative differences seen between FBP and IT reconstructions however, it was felt that IT reconstruction provided a notable improvement qualitatively. IT reconstruction was therefore used in all subsequent sections.

2.4.1.3 Investigation 2 Results - 2Hr Iterative (IT) Tumour to background ratio T:B versus Histology

All NeoSPECT acquisitions undertaken between 2002 and 2006 at Glasgow Royal infirmary were reviewed. Areas of non-physiological uptake of NeoSPECT were identified and these classed as positive studies at 2 hours post injection. A total of 36 patients were identified as having positive NeoSPECT studies, some of whom had taken part in the pan-Glasgow trial.

Of the 36 patients, more than half were from the trial (19), the remaining 17 patients having been referred to the department for a NeoSPECT following an abnormality demonstrated on a chest x-ray. Case notes and electronic data bases (CRIS radiology system, National PACS system and the clinical portal) were all reviewed to obtain follow up details of each patient in order to determine if the disease demonstrating uptake on the NeoSPECT images was malignant or benign.

Information was obtained for all patients apart from 1 patient who had been referred from another healthcare trust and therefore details such as histology or clinical/radiographic follow up could not be obtained. This patient was excluded from the group. Of the remaining 35 patients 13 were female and 22 were male, their ages ranged between 49 years and 86 years with the group's mean age being 67.7 years.

Images were reconstructed using iterative reconstruction with the parameters described in **Table 23** in the previous section. From the 35 patients, a total of 36 lesions/hot areas were identified. Of the 36 lesions, 28 were associated with malignant disease whilst the remaining 8 were associated with benign disease.

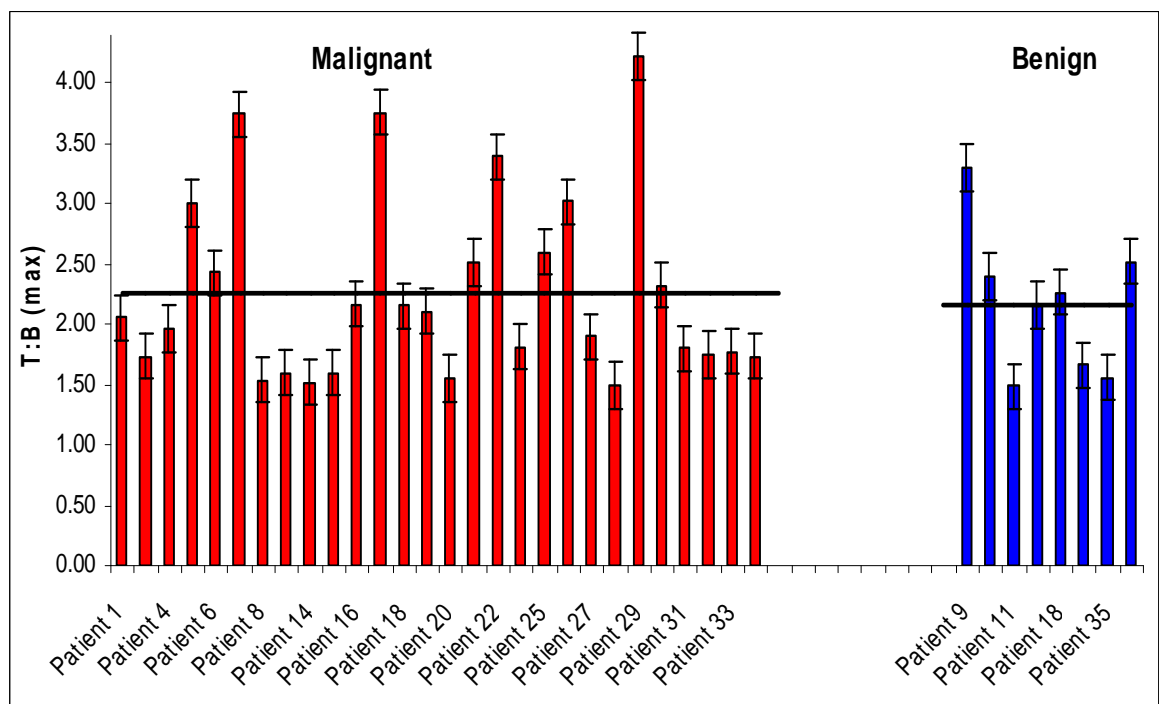


Figure 36 - Graph of Malignant Versus Benign Disease
 Bar chart showing the values of T:B calculated for each patient. The red bars show values from the malignant group and the blue bars from the benign group. The solid black line through each group is mean calculated for each group.

From **Figure 36** it can be seen that values of the maximum (max) T:B calculated ranged between 1.50 to 4.23 with a mean of 2.26 for the malignant group (the mean is shown by a solid black trendline). For the benign group values of the max T:B calculated ranged between 1.49 to 3.30 with a mean of 2.17 and again this is shown using a solid black trendline. Considering that the reproducibility of the techniques has shown a variation of 0.2, there appears to be no significant difference in terms of T:B between these two groups.

Statistical differences between the benign and malignant group were assessed using a Mann-Whitney test, results from this test giving a median for the malignant group of 2.01 and 2.21 for the benign group. The test found there to be no significant difference in the distribution of values when comparing the malignant and benign groups ($p=0.90$, 95.4% CI of (-0.5598, 0.5498)).

In the Malignant group, 23 lesions were identified histologically as Non Small Cell Lung Cancer and 1 lesion as Small Cell Lung Cancer. Histology and therefore classification was unavailable for 4 lesions but information retrieved from the

case notes and/or radiology reports detailed the lesions to be of malignant origin.

Figure 37 shows further histological breakdown of the lesion sub-types in the Non Small Cell group.

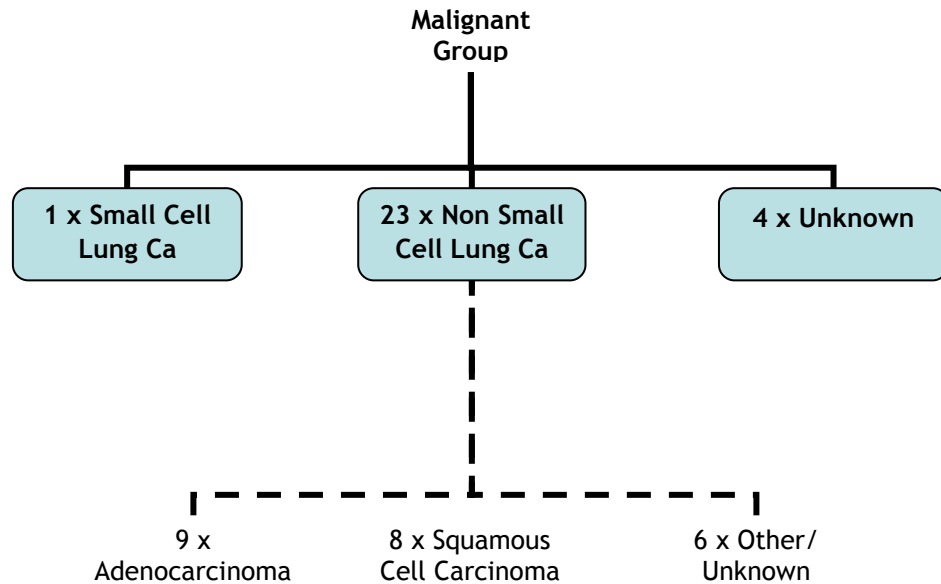


Figure 37 - Lesion Type

Image shown is the categorisation of the patient data groups based on histological findings.

From **Figure 37** it can be seen that 6 lesions fall into the ‘other/unknown’ category, of which 4 had no further information regarding the nature of their sub type histology. The distribution of T:B’s between the NSCLC sub groups can be seen in **Figure 38**, where the black bold trendline demonstrates the mean of each group.

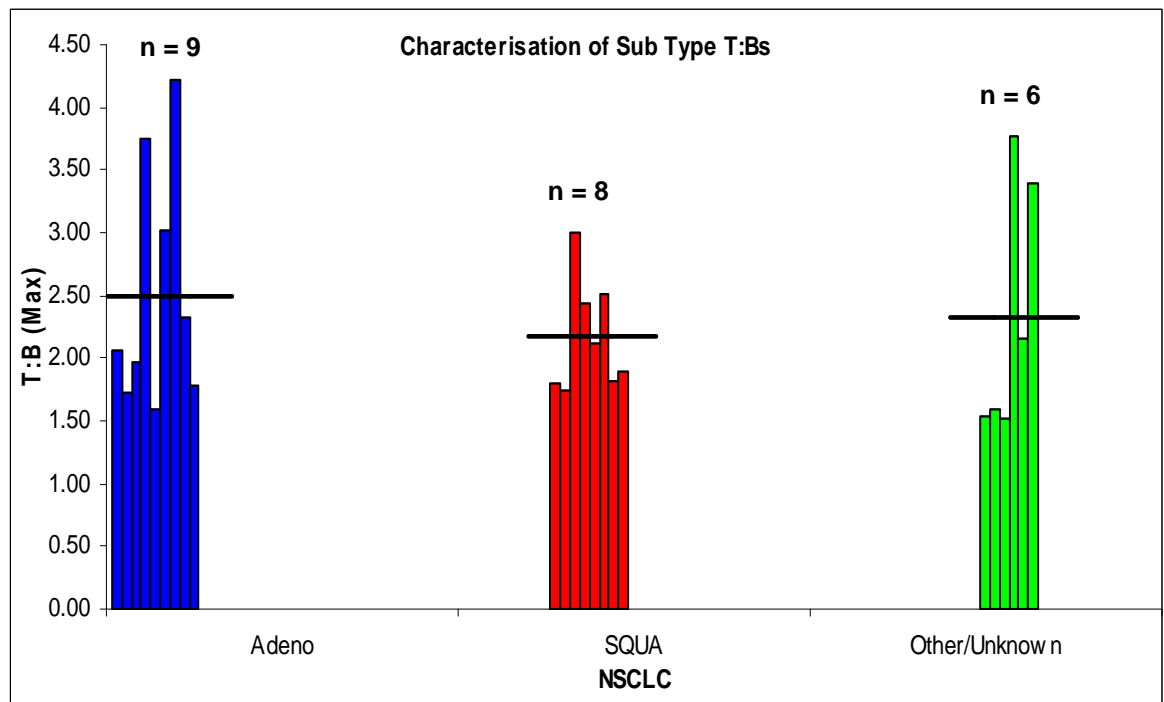


Figure 38 - Graph of Characterisation of NSCLC Sub Type

Bar chart showing the values of T:B calculated for each histological sub type of NSCLC, the blue bars represent the adenocarcinoma, the red bars the Squamous cells and the green bars the unknown. The mean is also shown for each group via a black solid trendline.

The largest group was the Adenocarcinoma group followed by the Squamous cell group and finally was the Other/Unknown group, the range of T:B's calculated for each group is given below:

Adenocarcinoma Range: 1.59 - 4.23, mean = 2.49

Squamous cell Range: 1.75 - 3.01, mean = 2.17

Other/Unknown Range: 1.52 - 3.76, mean = 2.33

The two highest values of T:B's demonstrated in the Other/Unknown group were 3.76 and 3.39 and were from patient 17 and 22 respectively. Both these patients had known histology, Patient 17 had a Pancoast tumour and Patient 22 had Large Cell Carcinoma. Whilst the majority of Pancoast tumours are Squamous Cell they can also be Adenocarcinomas or Large Cell and for this reason these have been included in the 'other/unknown' category (Guerrero, 2009).

Despite there being no clinical difference in the clinical management of patients in the different subgroups of NSCLC, statistical analysis was performed which looked for differences in the distribution of T:B_s between the Adenocarcinoma and Squamous cell group. The 'other/unknown' was excluded due to uncertainty of the nature of the tumour.

Results from a Mann-Whitney test demonstrated medians of 2.06 and 2.00 for the Adenocarcinoma and Squamous cell groups respectively. A p-value of 0.88 was calculated along with a 95.1% CI of (-0.460, 1.220) therefore there is no significant difference between the Adenocarcinoma and Squamous cell group.

Section Summary - Investigation 2

There is no significant difference demonstrated between the T:B ratio which would allow diagnosis of disease or disease sub-type.

2.4.1.4 Investigation 3 Results - 2Hr and 4Hr tumour to background ratios T:B versus Histology.

Based on the results demonstrated from **section 2.4.1.2**, analysis of the 2 v 4Hrs volumes was performed with data reconstructed using iterative techniques and not the tradition FBP methods. This group comprised 19 patients, imaged as described in previous sections. In this group, 7 were female and the remaining 12 male. At the time of imaging, their ages ranged between 49 and 81 years, with a mean of 68 years.

Pathology was obtained for 18 patients, while one patient did not have pathology performed and was diagnosed clinically based on growth of lesion over time. Of the 18 patients who had known pathology, 10 had the pathology of the lesion(s) confirmed following the NeoSPECT scan whilst the other 8 had some tissue removed from the lesion either via bronchoscopy or CT guided biopsy before the NeoSPECT image.

Table 25 summaries details of the mechanism of diagnosis of tumour type and duration between NeoSPECT scan and the pathology being determined.

NeoSPECT #	Age	Histology	Pathology Technique	# of days prior/ post NeoSPECT Scan
1	71	NSCLC - Adeno	Wedge resection	27
2	58	NSCLC - Adeno	CT Biopsy	-23
4	62	Unknown	Thoracotomy	34
5	69	NSCLC - Squa	CT Biopsy	-22
6	63	NSCLC - Squa	(Attempted Thoracotomy)	- ? ⁴
7	66	NSCLC - Unknown	CT Biopsy	-15
11	81	Negative	Wedge resection	7
12	66	Negative	Lobectomy	8
15	60	NSCLC - Unknown	Wedge resection	12
16	71	NSCLC - Unknown	No Path (Diagnosed Clinically)	78
19	76	+ve - Unknown	Thoracotomy	2
21	49	NSCLC - Unknown	Bronchial Biopsy	-21
22	72	NSCLC - Squa	Lobectomy	22
23	70	?	CT Biopsy	-36
26	65	NSCLC - Squa	Bronchial Biopsy	-11
27	76	NSCLC - Adeno	Wedge resection	31
28	74	NSCLC - Squa	No Path (Diagnosed Clinically)	NA
31	77	NSCLC - Squa	Lobectomy	52
32	66	SCLC	CT Biopsy	- ? ⁴

Table 25 - Summary of NeoSPECT patient's pathology details

The location of each area sampled was determined from the patient's CT image. Firstly, a qualitative comparison was made between the CT findings and the NeoSPECT image to determine if there was correlation of tumour location. The CT reports for all patients were obtained and the location of the tumour noted and compared to the NeoSPECT scan. These findings are detailed in **Table 26**. This table also describes any other notable uptake demonstrated on the NeoSPECT scan, which unless stated otherwise would be in keeping with lymph node uptake and is noted in terms of location.

⁴ The exact date is not known.

NeoSPECT #	CT Location of Tumour	NeoSPECT Concordance(Y/N)	NeoSPECT - Other Uptake
1	Right Mid Lung	Y	Rt Upper Lobe Rt Lower Lobe Lt Mid Lobe
2	Right Upper Lung	Y	Rt Mid Lobe Lt Mid Lobe
3	Right Mid Lung	Y	Rt Mid Lobe
4	Right Upper Lung	Y	Rt Mid Lobe Rt Lower Lobe
5	Right Lower Lung	Y	Rt Mid Lobe
6	Left Upper Lung	Y	Rt Upper Lobe Trachea Lt Mid Lobe
7	Left Upper Lung	Y	-
8	Left Lower Lung		Rt Mid Lobe Lt Mid Lobe
9	Right Upper Lung	Y	Trachea
10	Right Lower Lung	Y	-
11	Left Upper Lung	Y	Rt Mid Lobe (?Tumour) Trachea
12	Right Upper Lung	Y	-
13	Right Upper Lung	Y	Rt Upper Lobe Rt Lower Lobe Lt Upper Lobe Lt Lower Lobe
14	Right Lower Lung	Y	-
15	Left Upper Lung	Y	Trachea
16	Right Upper Lung	Y	Rt Mid Lobe
17	Left Upper Lung	Y	RT Mid Lobe Trachea
18	Left Lower Lung	Y	-
19	Right Lower Lung	Y	-

Table 26 - Correlation of CT & NeoSPECT findings

Of particular note is that none of the areas of 'Other Uptake' lay within lung tissue but rather adjacent to or within the cardiac cavity. Analysis of this data is undertaken in **section 2.4.1.5**.

Areas of abnormal uptake within the lung were identified on all 19 patients. The size of the abnormality varied between patients and was not thought to be characteristic of tumour type.

As before ROI analysis was performed on the tumour volume. T:B ratios were calculated using both the total and max counts, results are detailed in **Table 27**.

NeoSPECT #	T:B using Total Counts in ROIs			T:B using Max Count per Pixel in ROIs		
	2Hr T:B	4Hr T:B	Diff	2Hr T:B	4Hr T:B	Diff
1	2.06	2.17	0.11	3.01	3.56	0.55
2	1.73	1.69	0.04	2.07	2.07	0.00
3	1.96	2.40	0.43	2.91	3.10	0.20
4	3.01	2.80	0.20	3.65	3.52	0.13
5	2.43	2.85	0.42	2.63	2.69	0.06
6	3.74	4.94	1.20	4.38	4.62	0.24
7	1.49	2.26	0.77	1.69	2.42	0.73
8	2.16	2.37	0.21	3.78	4.28	0.50
9	1.59	1.53	0.06	1.97	1.72	0.25
10	2.17	2.18	0.01	2.16	2.70	0.54
11	2.11	2.37	0.26	3.32	3.81	0.50
12	2.52	2.55	0.03	2.51	2.59	0.08
13	3.39	3.62	0.23	3.82	3.30	0.51
14	1.81	1.75	0.06	2.72	2.29	0.43
15	3.02	3.22	0.20	4.51	3.89	0.63
16	1.90	1.86	0.04	2.27	2.00	0.27
17	1.50	1.14	0.35	2.40	2.11	0.29
18	1.80	1.79	0.01	2.16	2.03	0.13
19	1.75	1.72	0.03	2.17	2.50	0.33

Table 27 Tumour to background ratios (T:Bs) at 2 & 4Hours calculated using total and maximum counts

From the values calculated using the total counts found in each ROI, the max T:B at 2 Hrs was 3.74 and at 4Hrs was 4.94, with mean values of 2.22 and 2.38 respectively. When calculating the T:B using the maximum counts per pixel the max value at 2Hrs was 4.51 and at 4Hrs 4.62, with mean values of 2.85 and 2.90.

Figure 39 demonstrates the distribution in T:B at 2 and 4Hours for the various histology's.

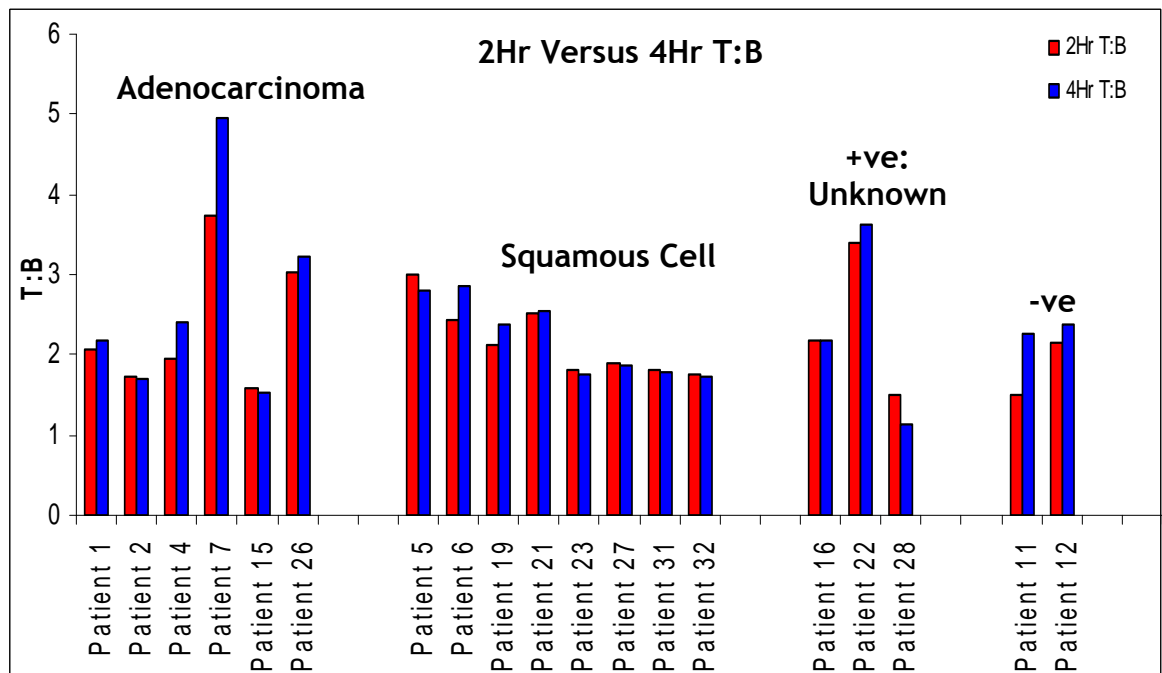


Figure 39 - Graph of 2Hr Versus 4Hr T:B
Bar chart showing the values of T:B calculated at 2 and 4 hours post injection, indicated by the red and blue bars respectively.

The maximum differences demonstrated between the 2 and 4hour T:B using the total counts was no greater than 1.2 and using the maximum counts per pixel 0.73.

Histology for these patients was attained via a number of methods as described in **Table 25**. Depending on the size of the tumour it was important to establish if sampling of the lesion before imaging had impacted on the any of the results. Of the 7 patients with pre-NeoSPECT histology, none had negative histology which indicates that the sample was taken of the true tumour site.

Figure 40 shows the data split into histology sampled prior to and after the NeoSPECT imaging.

Due to the sample size of the '+ve unknown' and '-ve' categories testing for difference between the values of T:B between 2 and 4 hours was not possible. However, a wilcoxon sign rank test could be used to asses the difference in dual time imaging for the 'Adenocarcinoma' and 'Squamous Cell' groups.

The 'Adenocarcinoma' group failed to demonstrate any statistically significant difference in the values of T:B ratios calculated at 2 and 4 hours, the p-value

calculated was 0.142, with an estimated median of -0.200 and 94.1% CI of (-0.820, 0.050). Similarly the 'Squamous Cell' also failed to demonstrate and statistically significant differences in the T:B ratios calculated between 2 and 4 hours, the p-value calculated was 1.00, with an estimated median of -0.002 and 94.1% CI of (-0.205, 0.110).

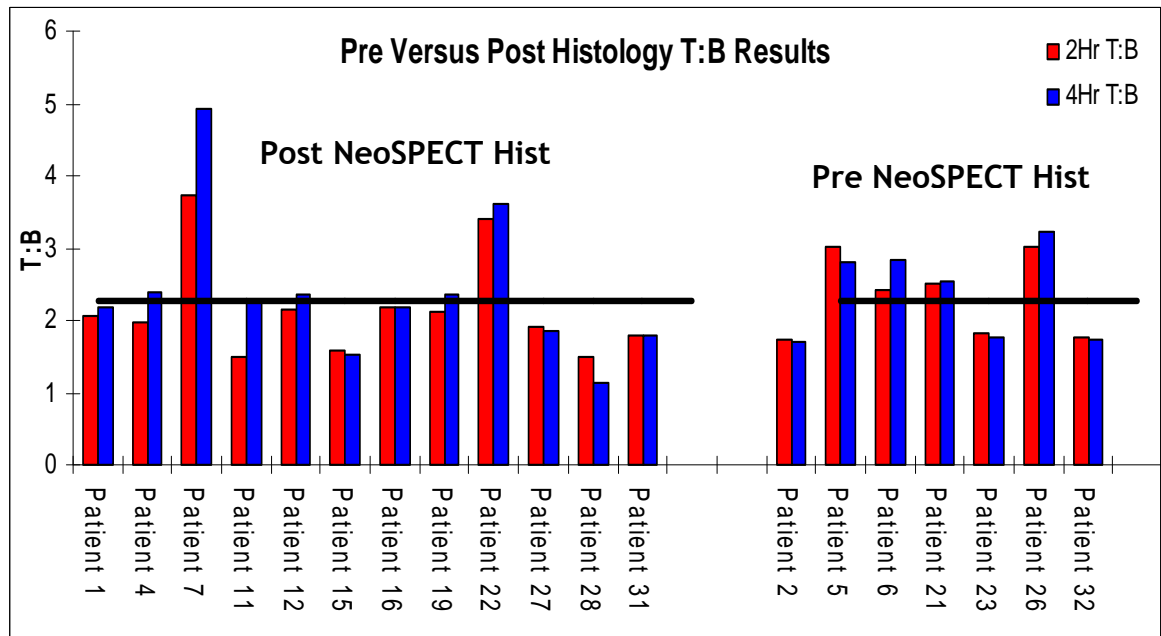


Figure 40 – Graph of Pre versus Post Histology T:B Results

Bar chart showing the values of T:B calculated at 2 and 4 hours post injection, indicated by the red and blue bars respectively. This data is grouped and presented based on whether tissue sampling was performed post or pre NeoSPECT imaging.

Of the 7 patients who had their tumours sampled prior to having the NeoSPECT imaging 4 were via CT guided biopsy, 2 by bronchoscopy and 1 patient had a failed attempt at a thoracotomy. Of this 'Pre NeoSPECT' group only 3 (43%) of these patients had T:B less than the mean (2.27) of the group who had histology sampled after NeoSPECT ('Post NeoSPECT Hist' group). In the 'Post NeoSPECT' group 6 (50 %) patient had values of T:B less than the mean.

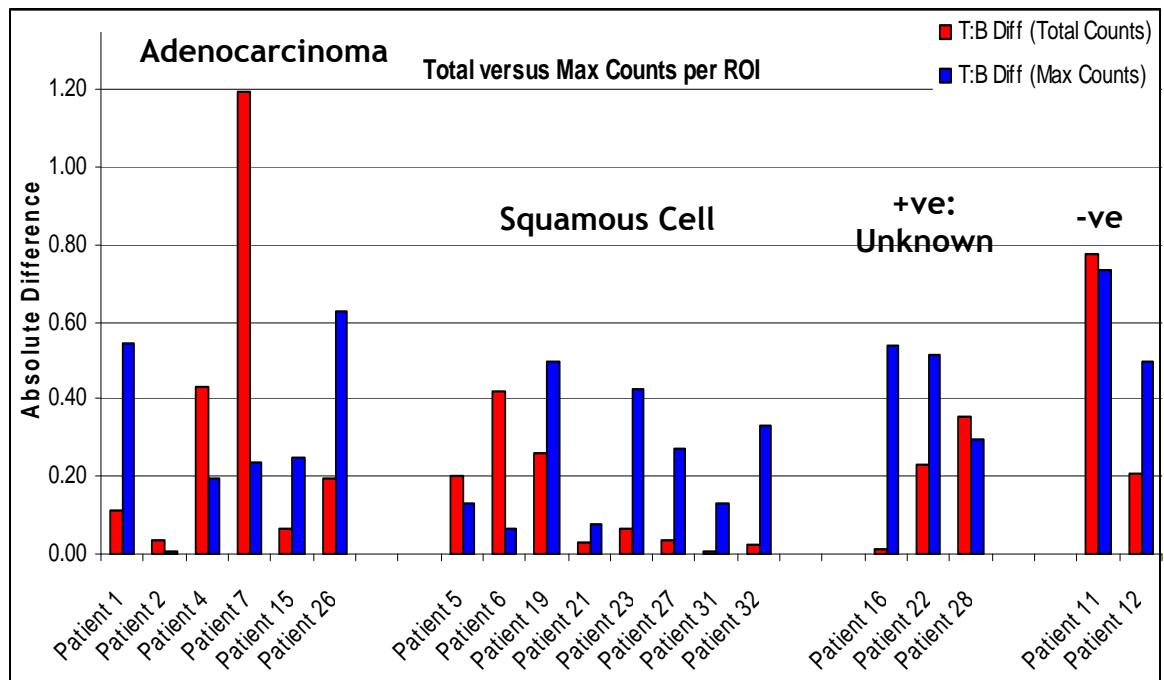


Figure 41 - Graph of Difference in Total versus Max Counts in ROI
Bar chart showing the difference in values of T:B calculated at 2 and 4 hours post injection, indicated by the red and blue bars respectively, using both the max and total counts. This data is grouped and presented based on the histological findings.

When performing image subtraction in other areas of nuclear medicine, for example parathyroid subtraction analysis, there has never been any definitive approach as to the use of either total counts or maximum counts per pixel in a ROI to calculate the contrast index (ratio) used for the subtraction (Leslie, 2002; Hindie, 2009). This is likely because the appropriateness of its use is dependent upon the distribution of the radiopharmaceutical within a given organ or ROI i.e. an area of high counts in a ROI not representative of the overall distribution within a region resulting in either an under or over estimation of the index. **Figure 41** charts the difference in T:Bs calculated between 2 and 4 Hrs using both the total ROI counts and the maximum counts per pixel to assess if the ratio of max counts per pixel is more characteristic of tumour type, these data are contained in **Table 27**.

A wilcoxon signed rank test was performed to determine if there was a difference between the T:B difference calculated at 2 and 4 hours using the total count within the ROI and the T:B difference calculated using the maximum counts per pixel from the ROI. This test found there to be no statistically significant difference between the calculation techniques, a p-value of 0.469

was calculated along with an estimated median of -0.08 and 94.9% CI of (-0.30, 0.145).

Section Summary - Investigation 3

It can be seen that there is no clear pattern and no statistically significant difference of washout from 2h to 4h images which correlates with either disease type or when biopsy was performed.

There appears to be no benefit in using two times frames for imaging with NeoSPECT.

2.4.1.5 Investigation 4 Results - Tumour to background ratio T:B in the mediastinum versus Histology

Around two thirds of patients who had dual time imaging demonstrated uptake in the mediastinum which was thought likely to represent nodal uptake. Thirteen of the nineteen patients imaged demonstrated uptake in the mediastinum. For each patient the number of nodes identified was recorded along with the site of the node. The site of the node was defined relative to the lung containing tumour as ipsilateral to the tumour ('side of Tum'), on the contralateral side from the tumour ('Opp Side') or as being either pretracheal or anterior mediastinal nodes ('Mid'). **Table 28** details the areas identified as being lymph nodes.

Patient ID	Pathology	# of Nodes	# Side of Tum	# Opp side	Mid
Patient 1	Adenocarcinoma	3	2	1	/
Patient 2		2	1	1	/
Patient 4		1	1	/	/
Patient 7		3	1	1	1
Patient 15		1	/	/	1
Patient 26		1	/	/	1
Patient 5		Sqaumous Cell	2	2	/
Patient 6	1		1	/	/
Patient 19	1		/	/	1
Patient 21	0		/	/	/
Patient 23	0		/	/	/
Patient 27	1		1	/	/
Patient 31	0		/	/	/
Patient 32	0		/	/	/
Patient 16	+ve Unknown	0	/	/	/
Patient 22		4	2	2	/
Patient 28		2	/	1	1
Patient 11	- ve	0	/	/	/
Patient 12		2	1	1	/

Table 28 - Mediastinal Uptake

T:B quantification undertaken on all lymph nodes detailed in **Table 28**. It should be noted that the patients are grouped in **Table 28** in accordance with their associated main tumour histology as in **Figure 39** and **Figure 41**.

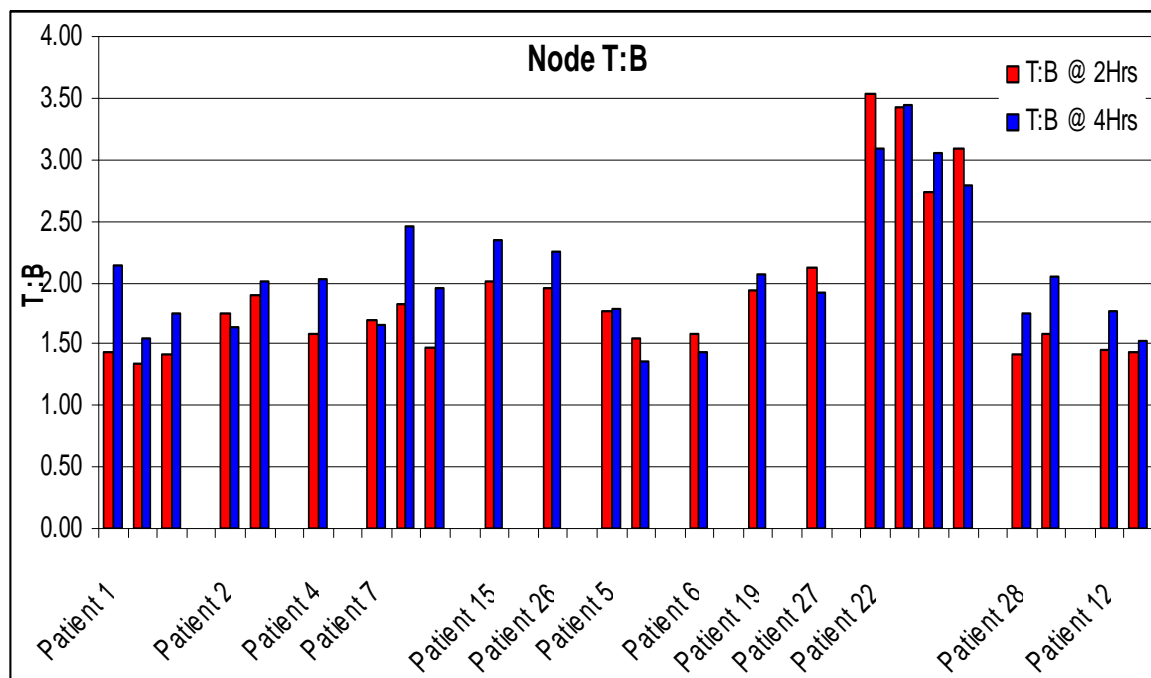


Figure 42 - Graph of T:B Mediastinal Nodes
Bar chart showing the values of T:B calculated from sites considered to lymph nodes at 2 and 4 hours post injection, indicated by the red and blue bars respectively.

At 2 hours the range of T:Bs calculated in the mediastinal nodes for all patients shown in **Figure 42** was between 1.34 and 3.54, with a mean of 1.96. At 4 hours this range was 1.35 -3.43, with a mean of 2.07. The maximum absolute difference between nodes at 2 and 4 Hours was 0.72.

Figure 42 demonstrates the difference in lymph node uptake between 2 and 4 hours for patient with both positive and negative histology. Due to the difficulties in correlating nodes demonstrated using NeoSPECT imaging with those sampled histologically, differences between 2 and 4 hours could only be assessed by grouping the patients based on the primary tumour histology and not node histology. Due to sample size statistical analysis was only performed on the group of patients who had a positive primary tumour, a Wilcoxon signed rank test was performed to assess for differences in T:B between 2 and 4 hours. Results from this test concluded that there were no statistically significant difference between the difference in T:B ratio measured at the two time points, p-value was 0.108, with an estimated median of -0.130 and an 95% CI of (-0.295, 0.030).

To investigate the trend in Depreotide uptake between tumour and lymph node tissue and how these both changed over time, the T:B were assigned a score of 1 and -1. A score of 1 was assigned if the T:B at 4Hr was greater than that at 2Hr, and -1 was assigned if the T:B at 2Hr was greater than 4Hr. It should be noted that when the difference in T:B between 2 and 4Hrs was less than 0.1 a score of 0 was assigned. This value was based on the previously measured differences during analysis of reproducibility - see **Figure 43**.

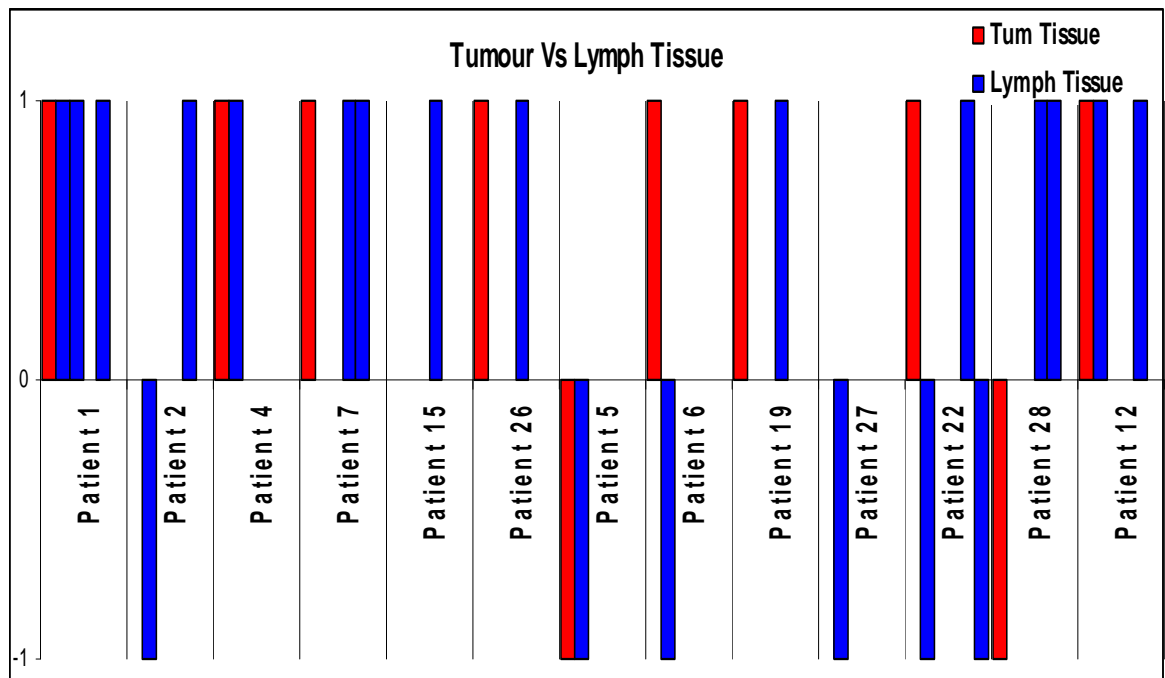


Figure 43 - Graph of Tumour Vs Lymph Tissue Uptake Over Time
Bar chart indicating changes in tumour and lymph tissue uptake during dual time imagine, tumour is tissue is indicated by the red bars and lymph tissue by the blue bars.

In the Adenocarcinoma group all 6 patients demonstrated nodal uptake compared with 4/8 patient in the Squamous cell group, 2/3 in the positive unknown group and 1/2 for the negative group. Three patients had their tumour ratio scored 0 (Patient 2, 15 and 27). Of the remaining patients, 7 demonstrated an increase in T:B values in both tumour and related lymph tissue between 2 and 4 hours, whilst 1 patient demonstrated a reduction in T:B values between 2 and 4 hours in both tumour and lymph tissue. Discordance in T:B values between the tumour and lymph tissue was seen in 2 patients (patient 6 and 28). In the case of patient 28 the lymph nodes were located on the contralateral lung to the tumour whilst for patient 6 the node was ipsilateral to the tumour.

Section Summary - Investigation 4

Images showed mediastinal nodal uptake, however again there seemed no clear trend in the washout rate based on changes to T:B ratio with respect to disease type.

There was a slight trend to changes in tumour and lymph nodes over time to be similar in individual patients, however this was not completely the case.

NeoSPECT imaging has clearly demonstrated nodal uptake, however, the nature of those nodes demonstrating cannot be assessed easily. This is because correlation between imaging and histological findings was impossible due to the lack of exact anatomical information available from the NeoSPECT imaging.

2.4.2 Tracer percentage Uptake

As discussed in the previous section an estimate of the amount of tracer within a tumour volume relative to normal tissue can be calculated using ratios. However, an alternative to this is to calculate the absolute uptake, in other words the proportion of the radiopharmaceutical injected which is subsequently absorbed/taken up by an area or organ of interest, in this case the suspected tumour. Unlike T:B ratios this method of quantification takes into account tumour size and therefore may provide a more information with respect tumour burden and how this changes over time.

This technique has been used successfully in planar imaging over the years and is used regularly for example for thyroid gland function. The technique's accuracy in SPET imaging and its value with regard to NeoSPECT is not clear. Its use in differentiating benign from malignant disease, is not known and would require investigation. It is therefore important to establish if there is a role for the uptake calculation in the characterization of tumour/tissue type and also if the uptake value can identify differences between 2 and 4 hour imaging.

2.4.2.1 Methods for Investigations 5 - 6

The majority of patients who had NeoSPECT (Depreotide) imaging performed between January 2004 and February 2006 at Glasgow Royal Infirmary had a standard volume study also acquired. This allowed an absolute measurement of activity to be calculated. A total of 19 patients had a standard study volume acquired, of whom 12 were from the trial and therefore also had dual time imaging acquired.

For all patients the standard study acquisition was acquired following either the 2 or 4 Hr acquisition. This allowed for the setup conditions including detector

distance and bed height used during the patient acquisition to be reproduced for the standard study.

The standard volume consisted of a 5ml vial, which was filled with residual NeoSPECT and made up to 5ml using saline. The value of activity contained was measured using a radionuclide calibrator and was noted in MBq. This solution was then mixed thoroughly. The vial was then placed inside the phantom - see **Figure 16** - between the lung inserts and secured to the vertebral column with tape. The standard acquisition data were reconstructed using the same parameters as the patient reconstructions but without the use of an attenuation correction for reasons investigated and detailed in **section 2.3.2.3**

The reconstructed standard images were loaded into 'Volume Fusion Display' and ROIs were drawn around the standard and the background as described previously. Values of total counts and number of pixels were extracted from these and tabulated. The counts in each slice were area normalised and background corrected as described **Equation 3**.

The total counts from each slice were then summed together and, since the standard was contained in a small volume, its activity was able to be measured prior to and after acquisition using the Capintec® well type radionuclide calibrator. Therefore the value of total counts, activity and acquisition length were used in **Equation 6** to calculate the sensitivity of the system.

The original ROI analysis used for the phantom analysis in section 2.3.2.1 illustrated a ROI background region which encompassed the tumour volume. This technique was not used in the patient population as there was no discrete edges to the tumour volume and there was concern that the background region could encompass some low grade disease and therefore not be a true representation of normal lung. Therefore the ROIs employed for the patient data set were more in keeping with those illustrated in **Figure 32**.

The patient ROI data were handled in a similar manner to the phantom data, the number of counts found in each tumour region being corrected for normalised background counts as described in **Equation 3**. The tumour counts were summed

over the depreotide avid tumour volume and used along with the value of sensitivity to calculate the activity in the tumour using **Equation 8**.

2.4.2.2 Results for Investigation 5 - Correlation of 2Hr % Uptake with Histology

The Administration of Radioactive Substance Advisory Committee (ARSAC) sets a diagnostic reference level (DRL) of 600MBq for NeoSPECT administrations, however, in the case of over or underweight patients the activity administered to the patient may be altered in order to optimise both the dose received and quality of the image (ARSAC, 2006). The activity injected into the patient was calculated from a measurement of syringe activity prior to injection and the residual activity in the syringe following injection. These were measured using a calibrated radionuclide calibrator. **Table 29** details the activities injected; for patients 13 and 16 there was no residual activity recorded.

Patient ID	Syringe Activity (MBq)	Residual Activity (MBq)	Injected Activity (MBq)	Patient Activity @ 2Hrs (MBq)	Patient Activity @ 4Hrs (MBq)
Patient 1	622	35	587	452	347
Patient 2	592	30	562	436	350
Patient 3	603	85	518	389	-
Patient 4	601	143	458	361	288
Patient 5	626	29	597	471	367
Patient 6	639	30	609	471	-
Patient 7	555	74	481	354	-
Patient 8	594	32	562	436	345
Patient 9	579	50	529	408	324
Patient 10	658	48	610	460	-
Patient 11	486	32	454	330	-
Patient 12	560	46	514	391	319
Patient 13	526	-	526	397	-
Patient 14	578	113	465	365	292
Patient 15	608	35	573	402	346
Patient 16	620	-	620	474	377
Patient 17	610	126	484	353	291
Patient 18	438	18	420	311	251
Patient 19	666	165	501	364	-

Table 29 - Injected NeoSPECT Activities (MBq)

The mean of the activities injected was 528MBq and ranged between 420 - 610MBq. Using **Equation 4** and **5** along with the values of 'injected activity' in

column 4 of **Table 29**, values of decay corrected activity at the time of imaging were calculated.

With the exception of Patient 7, values of % uptake were calculated for all patients; Patient 7 did not demonstrate any abnormal uptake. Details of values of uptake calculated at 2 hours can be found in **Table 30**.

Patient ID	Histology	Activity	Total Counts	Activity in Tumour	% Uptake
Patient 1	NSCLC - Adeno	452	38306	0.48	0.11%
Patient 2	NSCLC - Adeno	436	35187	0.22	0.05%
Patient 3	Unknown	389	221619	1.76	0.45%
Patient 4	NSCLC - Squa	361	379717	2.54	0.70%
Patient 5	NSCLC - Squa	471	173696	0.85	0.18%
Patient 6	NSCLC - Unknown	471	46131	0.36	0.08%
Patient 8	Negative	436	27192	0.25	0.06%
Patient 9	Negative	408	217103	1.47	0.36%
Patient 10	NSCLC - Unknown	460	387019	3.07	0.67%
Patient 11	NSCLC - Unknown	330	79151	0.27	0.08%
Patient 12	+ve - Unknown	391	104627	0.81	0.21%
Patient 13	NSCLC - Unknown	397	511204	7.89	1.99%
Patient 14	NSCLC - Squa	365	21156	0.39	0.11%
(Rt)	NSCLC - (unknown)	365	133058	2.48	0.68%
Patient 15	NSCLC - Squa	402	275783	3.92	0.98%
Patient 16	NSCLC - Adeno	474	249740	1.69	0.36%
Patient 17	NSCLC - Squa	353	92951	0.59	0.17%
Patient 18	NSCLC - Squa	311	66610	0.42	0.14%
Patient 19	SCLC	364	556257	4.29	1.18%

Table 30 - % Uptake calculated at 2 hours

Table Key: NSCLC - Adeno: Non Small Cell Lung Cancer - Adenocarcinoma, NSCLC - Squa: Non Small Cell Lung Cancer - Squamous Cell, SCLC: Small Cell Lung Cancer, +ve: positive for lung cancer but no details regarding type available i.e. differentiation between NSCLC or SCLC.

The range of activities found in areas associated with tumours ranged between 0.22 and 7.79MBq with a mean of 1.78MBq (SD of 1.96).

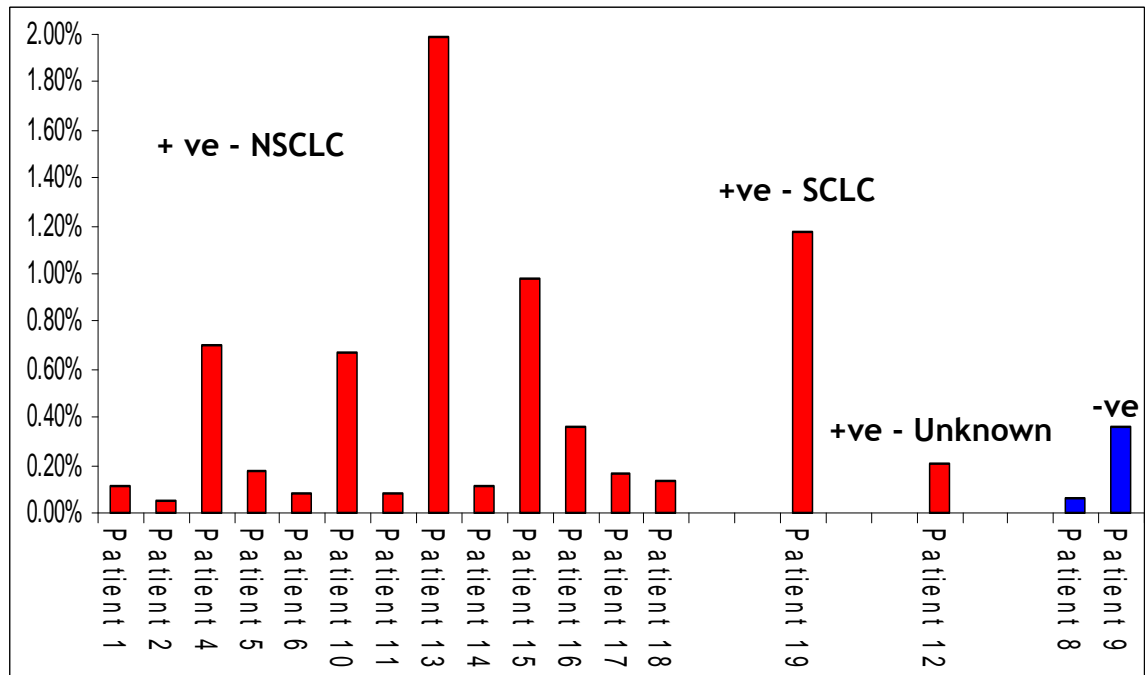


Figure 44 - Graph of % Uptake @ 2Hrs
 Bar chart showing the values of % uptake calculated at 2 hours post injection, red bars indicate malignant group and blue bars benign group.

The trend of % uptake values is shown in **Figure 44**; as with previous results the patients were grouped by their histological findings. Of the eighteen patients shown in **Figure 44**, 2 were found to have negative histology i.e. these were patients that were recruited to the study who were believed to have malignant disease. The uptake demonstrated in the 2 patients with negative histology ranged between 0.06 - 0.36%. Of the fifteen patients with positive histology, nine demonstrated uptake within this range, one patient demonstrated uptake less than this range and five patients demonstrated uptake that was greater than this range.

The NSCLC group was categorised further by histology subtypes comprising of three patients with Adenocarcinoma, six patients with Squamous cell carcinoma and 4 patients whose case notes did not detail any information regarding histology subtype. The range of uptakes calculated for the subtypes are given:

Adenocarcinoma: 0.05 - 0.36%, mean = 0.17% ± 0.002

Squamous Cell Carcinoma: 0.14 - 0.98 %, mean = 0.38% ± 0.004

No subtype: 0.08 - 1.99 %, mean = 0.71% ± 0.009

There were no differences found in the values of percentage uptake which could differentiate between the histological subtypes in the NSCLC group. Incidentally, the value of percentage uptake for the SCLC was 1.18%. The sample size did not allow statistical analysis to be undertaken.

Section Summary - Investigation 5

Similar to the results found with T:B ratios , no clear difference between groups can be measured using absolute percentage uptake.

2.4.2.3 Results for Investigation 6 - % Uptake Washout Versus Histology

It is well known that different tissue types can washout radiopharmaceuticals at differing rates to adjacent tissues and this has been exploited in parathyroid imaging where the rate of washout is used to help differentiate parathyroid from thyroid tissue. It was considered important, therefore, to establish whether or not the tumour tissue had a different washout rate of NeoSPECT when compared with normal lung tissue and tissue from other disease processes.

Of the 17 patients whose data were used to calculate percentage uptake in **section 2.4.2.2** only 12 patients had dual time imaging along with a standard acquisition. Of these patients, 13 lesions were identified on NeoSPECT imaging with histological characterisation. If the tumour tissue had a different washout rate in comparison to normal tissue (background) then either a rise or fall in the uptake calculated at between 2 and 4 hours would be expected. If there was no change in either it would be expected that the uptake would remain constant over the two time periods. Therefore based on the 2Hr results the 4Hr results could be predicted for no change and these could then be compared to the actual 4 hour results. **Table 31** details these results.

Patient ID	2Hr Total Counts	4Hr Predicted Counts	4Hr Total Counts	Difference
Patient 1	38306	29424	33853	-4429
Patient 2	35187	28198	38093	-9895
Patient 4	379717	303127	318571	-15443
Patient 5	173696	135234	119595	15639
Patient 8	27192	21541	24589	-3048
Patient 9	217103	172647	175242	-2595
Patient 12	104627	85476	73934	11542
Patient 14(i)	21156	16889	19461	-2573
Patient 14(ii)	133058	106220	109531	-3311
Patient 15	275783	237325	195975	41350
Patient 16	249740	198601	187197	11404
Patient 17	92951	76671	71359	5312
Patient 18	66610	53896	50701	3195

Table 31 - Total tumour counts per patient at 2 and 4Hrs

From section 2.3.2.3, for dual time acquisitions the phantom results demonstrated a minimum difference of 11428 in counts between the predicted and measured (13.46%). From Table 31 the percentage difference between predicted and actual at 4 hours ranged between 1.50% and 35.0%. Of the 13 lesions only 5 demonstrated a difference greater than 13.5% but the phantom was acquired under absolute ideal conditions and so other factors such as reproducibility of the set-up and the use of attenuation correction for the patient may account for this. Figure 45 plots how the calculated values of uptake compare with the predicted value.

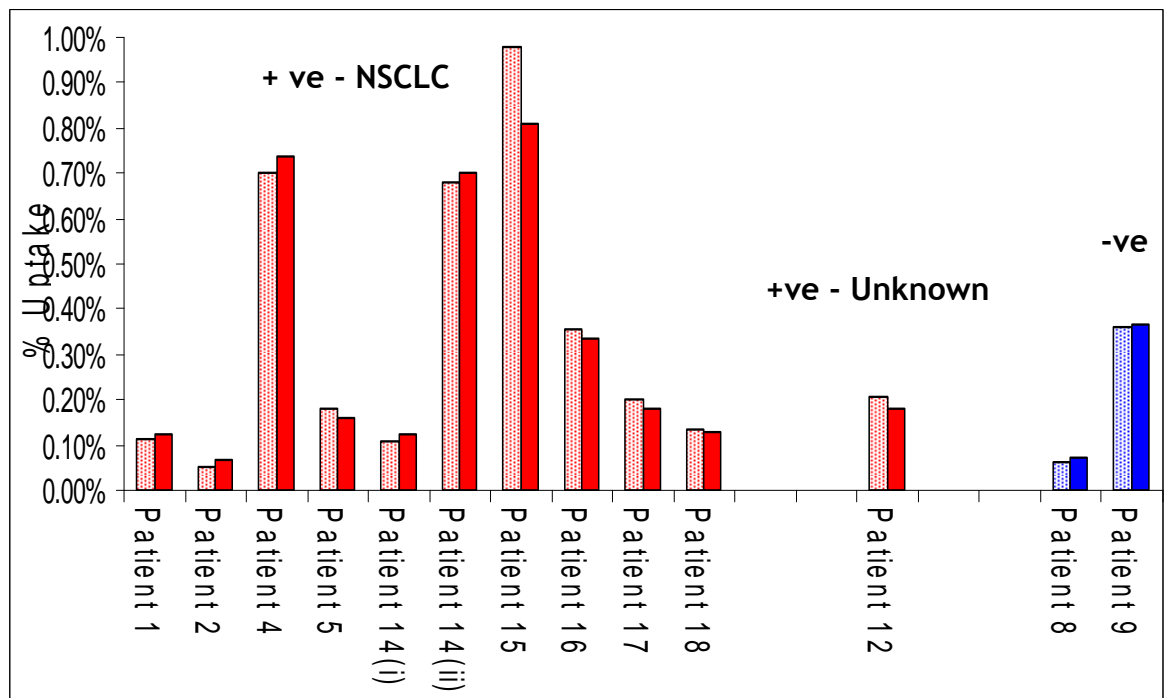


Figure 45 - Graph of Uptake @ 4Hrs Predicted Versus Actual
Bar chart showing the values of % uptake calculated from the 4 hours SPET images (shown by solid coloured bars) versus the predicted values of % uptake (shown by the dashed bars). Red bars indicate malignant group and blue bars the benign group.

The solid red bars denotes % uptake calculated for the patients with positive histology and the solid blue bars are the patients with negative histology whilst their associated shaded bars represent the predicted values of % uptake calculated. Despite some large differences noticed in the total counts this did not translate to into large differences in value of % uptake, Table 32 detail further the difference in % uptake demonstrated.

Patient ID	Histology	4Hr Predicted % Uptake	4Hr Actual % Uptake	Difference
Patient 1	NSCLC (Adeno)	0.11%	0.12%	-0.01%
Patient 2	NSCLC (Adeno)	0.05%	0.07%	-0.02%
Patient 4	NSCLC (SQUA)	0.70%	0.74%	-0.04%
Patient 5	NSCLC (SQUA)	0.18%	0.16%	0.02%
Patient 8	NEGATIVE	0.06%	0.07%	-0.01%
Patient 9	NEGATIVE	0.36%	0.37%	-0.01%
Patient 12	POSITIVE (?)	0.21%	0.18%	0.03%
Patient 14 (i)	NSCLC (SQUA)	0.11%	0.12%	-0.02%
Patient 14(ii)	NSCLC	0.68%	0.70%	-0.02%
Patient 15	NSCLC (SQUA)	0.98%	0.81%	0.17%
Patient 16	NSCLC (Adeno)	0.36%	0.34%	0.02%
Patient 17	NSCLC (SQUA)	0.20%	0.18%	0.02%
Patient 18	NSCLC (SQUA)	0.14%	0.13%	0.01%

Table 32 - Predicted Versus actual uptake at 4 hours

Review of the imaging proforma and referral cards completed at the time of imaging drew a correlation between some of the more notable differences seen (Pat 4, 12, 15), these patients were noted as being non-compliant patients. These patients experienced difficulties with compliance as a result of physical condition, such as spondylitis, which caused difficulties in reproducing the positional set-up at acquisition for the second SPET acquisition. In addition to this some patients complained of 'other' conditions with associated pain, often resulting in movement during the acquisition.

The differences between the 'predicted' and 'actual' values of % uptake at 4 hours were assessed statistically via a Wilcoxon signed rank test which concluded there to be no significant difference between the 'actual' and 'predicted' values; p-value was 0.727, the estimated median was 0.005 and the 95% CI of (-0.015, 0.020).

The findings of no significant difference between the 'predicted' and 'actual' values of % uptake at 4 hours indicates that there was no significant change in the distribution and uptake of NeoSPECT between 2 and 4 hours.

Section Summary - Investigation 6

No significant difference in percentage uptake was demonstrated over the potential 2 hour washout time period which could be related to disease type. Whilst the T:B ratio data also demonstrated there to be no significant difference, this technique did not take into account variations in the extent of NeoSPECT distribution and tumour burden over time. The calculation of percentage uptake includes information from the whole tumour volume unlike the measure of T:B which only provides a measure from the maximum slice from the tumour volume. Therefore it was important for completeness to consider and assess all possible factors which could describe variations in tracer distribution over time.

2.5 NeoSPECT Discussion and Conclusion

The numbers originally anticipated for the study were not achieved. When the pan-Glasgow NeoSPECT trial was first proposed, Nycomed Amersham agreed to fund fifty NeoSPECT doses resulting in dual time data for 50 patients i.e. 100 SPET acquisitions. However, at the beginning of 2006 and halfway through the trial, Nycomed Amersham sold the NeoSPECT brand and product to IBA Molecular. At this stage only 19 of the intended 50 patients had been recruited. NeoSPECT was taken out of production until its re-launch in 2008 and thus, in addition to the lower than anticipated study numbers, the number of patients who would have had a routine NeoSPECT scan also dropped. This has meant that the data presented here is not as powerful as would have been expected had the trial recruitment reached completion. In an attempt to address this for at least some of the investigations, routine patient data was added. The data which looked at the two time points are therefore limited in the statistical significance which could be attached to it because of the small sample size.

At the time of the study all the published data using NeoSPECT quantification involved data reconstruction using FBP reconstruction technique. One of the advantages of iterative reconstruction is that it may produce reconstructed images whose pixel data are a more accurate representation of the true image. The data presented here have allowed work to be undertaken to identify whether or not iterative reconstruction could improve the ability to firstly characterize the tumour and secondly quantitate tumour uptake. It was therefore important to re-evaluate the role of NeoSPECT Image quantification in light of the availability of better reconstruction algorithms.

Comparison of the reconstruction data demonstrated a range of T:B ratios from 1.49 - 4.32 for the iteratively reconstructed data and a range of 1.29 - 4.21 for the FBP reconstructions, with medians of 2.32 and 2.39 respectively. Since the data were not normally distributed, non-parametric analysis was undertaken in the form of a Wilcoxon Signed rank Test which demonstrated a p-value of 0.359, estimated median of -0.04 and a 94.7% CI of (-0.155, 0.075), indicating no difference between the groups in terms of the max T:B value calculated in each volume. Despite there being no proven statistical difference between

reconstructions there was a significant difference qualitatively in that the FBP images were of a lower image quality. It was therefore considered appropriate to continue to analyse the data with only iterative reconstruction as there was concern that FBP reconstruction compromised accurate delineation of the tumour volume which in turn could result in an underestimation or overestimation of the total counts in the tumour volume. This is an important factor when considering percentage uptake values.

In terms of the T:B ratios, review of the data qualitatively would have estimated the T:B ratio to be at least 2:1, however, these qualitative expectations did not translate quantitatively. The range in T:B ratios calculated lay between 1.50 to 4.23 for the malignant group and 1.49 to 3.30 for benign group. The counts in the tumour regions of those patients who had lower than anticipated T:B ratios were not considered to be unusually low. However, the presence of active benign lung disease could have led to some low grade uptake, which would have caused a slight elevation of the counts in the background region. This would have resulted in the lower than anticipated values of T:B. Despite attempts to minimise this effect, by placement of the background ROI on the contralateral lung, it remained impossible to determine a difference between widespread active benign lung disease and low grade tumour uptake. A possible solution to identifying the presence of active benign lung disease may be achieved by grading lung uptake against another organ such as the liver i.e. measuring a Lung to Liver ratio.

A Mann-Whitney test was undertaken to determine if there was any statistically significant differences between the benign and malignant group. This test gave a p-value of 0.90 and 95.4% CI of (-0.5598, 0.5498), concluding there to be no statistically significant difference in the T:B ratios calculated at 2 hours between the malignant and the benign group. A Mann-Whitney was performed to try and determine if the malignant group could be characterised further by determining if there were any differences between the diseases process within the malignant. This test found there to be no statistically significant differences between the larger of the groups, Adenocarcinoma and Squamous cell group (p-value 0.88).

The T:B ratios were assessed further by trying to establish if there was a difference between values calculated at 2 hours to those calculated at 4 hours in the malignant group. Statistical comparison between the 2Hr and 4Hr group was achieved by a Wilcoxon signed rank test. The outcome of this demonstrated no significant difference in T:B ratio between 2 and 4 hours between the Adenocarcinoma and Squamous cell groups (p-value 0.142 and 1.00 respectively).

As demonstrated, the T:B ratio form of quantification failed to identify any difference between the benign and malignant groups. This technique, however, may be inhibited by the presence of benign lung disease and particularly so when both lungs are involved. Calculating a percentage uptake, however, should be a more sensitive form of characterisation for dual time imaging, as this doesn't rely on the use of a background correction and takes into account factors such as tumour size.

The first assessment of the percentage uptake values tried to determine whether or not the percentage uptake demonstrated at 2 hours was typical of the tumour histology. Due to the small sample numbers between the groups no statistical analysis could be undertaken, however, comparison of the ranges of values between histologies proved useful. Two of the eighteen patients found to have negative histology demonstrated uptake which ranged between 0.06 - 0.36%. Of the remaining patients with a positive histology, nine demonstrated uptake within this range, one patient demonstrated uptake less than this range and five patients demonstrated uptake that was greater than this range.

The NSCLC group was categorised further by histology subtypes comprising of three patients with Adenocarcinoma, six patients with Squamous cell carcinoma and 4 patients whose case notes did not detail any information regarding histology subtype. No differences were found between the ranges of values of percentage uptake which could help to differentiate between the histological subtypes in the NSCLC group.

Finally, the difference in percentage uptake calculated between 2 and 4 hours was assessed via a Wilcoxon signed rank test. This test concluded there to be no significant difference in uptake between the two acquisitions for the malignant group; p-value was 0.727, the estimated median was 0.005 and the 95% CI of (-0.015, 0.020).

The ability to reproduce the set-up conditions of the first acquisition proved more challenging for those patients who demonstrated a large BMI. These patients were often less compliant with the procedure and there was more variation with regards to the orbit of rotation. Increased orbits of rotation and/or scatter and attenuation within the patient compromised the ability to resolve and delineate the tumour volume accurately. To try to reduce the effects of attenuation, a Changs attenuation correction was applied. This form of attenuation correction, however, transforms the data linearly across its volume independent of the material that the photon traverses through which depending on the sex and BMI of the patient could be breast/fatty tissue or simply lung. Therefore counts in the lungs are over-corrected, which would have contributed to increased uptake in lung background regions. With this in mind, where accuracy is important, this form of attenuation correction may not be the best tool when considering image quantification.

Work with the in-house designed and manufactured phantom was undertaken to validate the results and characterise changes but the phantom is a static geometric volume with components that have discrete boundaries and is acquired under ideal conditions including no repositioning. These factors should be taken into consideration when comparing the patient data to the phantom as the patient volume is a dynamic volume as a result of breathing, it often has non-discreet tumour boundaries, none of which the phantom could replicate. However, what the phantom work does provide is a threshold for the minimum differences able to be measured.

Quantification in the mediastinum was subject to the same drawbacks demonstrated by tumour quantification. However, in addition to this on the SPET imaging, nodes could only be characterized purely based on their size and shape which could not be confirmed. This combined with a lack of anatomical

information meant that comparison with any histology could not be undertaken accurately.

Due to Depreotide's high binding affinity to NSCLC tumours, consideration has been given to its use as an agent for radionuclide targeted therapy. The top row of **Figure 46** demonstrates an area of focal uptake in the right lung with proven positive histology whilst the bottom row is from a patient who also demonstrates focal uptake in the left lung which is similar in size and shape but whose histology demonstrated benign disease.

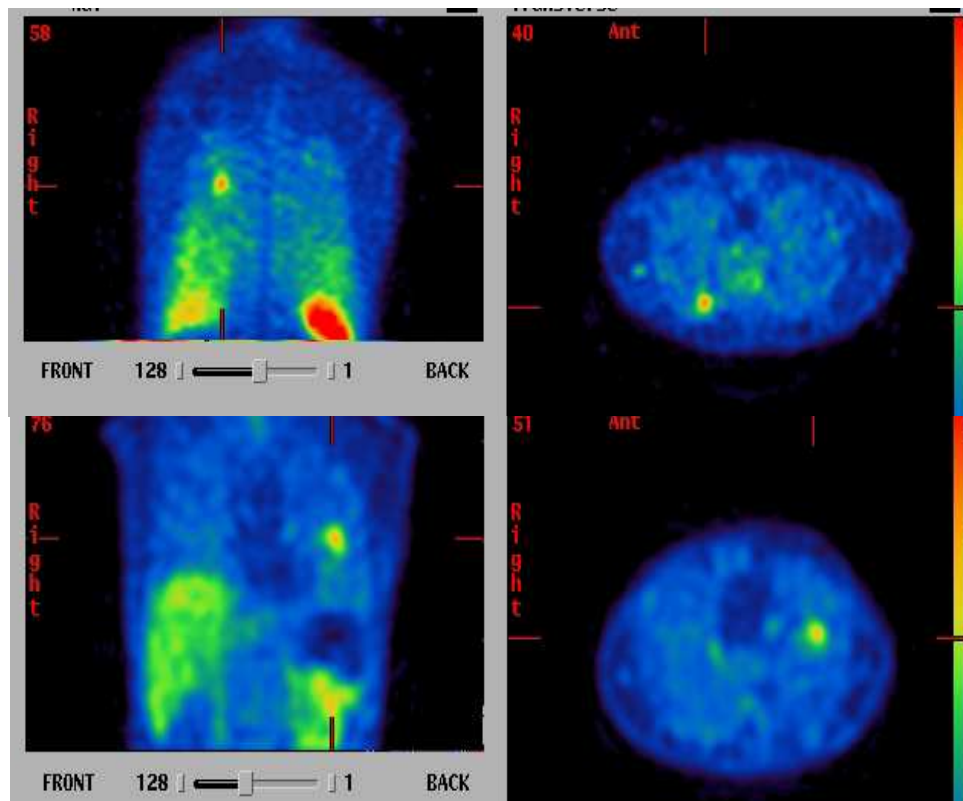


Figure 46 - Spot the difference

Image showing a coronal and transverse slice from a patient with positive NeoSPECT uptake with histologically proven malignancy - top row. The coronal and transverse slices on the bottom row are from a patient who has histologically proven benign disease.

Although NeoSPECT imaging was unable to differentiate between benign and malignant groups, work undertaken in **section 2.4** does provide a quantitative indication of this binding affinity. Results demonstrated lower than anticipated T:B ratios which may be partly due to difficulties in identification of true background lung tissue as many patients also had uptake which was related to benign processes in addition to the tumour. If characterisation of the tumour tissue could be achieved by some other method and Depreotide was to be used

as a targeted therapy agent then identification of additional benign processes in the lungs must be considered as there is the potential to damage non-malignant tissue and therefore reduce capacity and function. The fact that significant uptake exists in benign disease make it unlikely that a therapy agent based on NeoSPECT would be of any value.

In addition to there being no significant difference between the malignant and benign groups using T:B ratios from both standard and dual time imaging, there was also a failure to successfully calculate uptake from SPET data. A major reason for the failure of SPET to calculate uptake accurately lay with the accuracy of the sensitivity measurement and the use of an attenuation correction. The accuracy was dependent upon replicating the attenuating conditions of the patient acquisition in the standard acquisition as these conditions influenced the value of sensitivity calculated. This is easily achieved in some other forms of image quantification, namely thyroid uptake measurements, as the amount of attenuating tissue is limited by the anatomical position of the thyroid gland, where the average amount of attenuating tissue is easily estimated and incorporated into a standard phantom providing a more accurate measure of sensitivity. However, depth is a factor when considering uptake within the thorax as the depth of the tumour between patients varied, a factor which is compounded further by BMI and breast tissue therefore the amount of attenuation was difficult to estimate and standardise for the purpose of the standard acquisition.

The standard acquisition was not the only difficulty realised. There were a number of issues that impacted on the quality of the data. These included patient compliance and movement, repositioning, patient size and sex which had an obvious impact on the amount of attenuating and scatter material and its position within the patient volume.

Recent advances in Gamma Camera hardware and software may help to eliminate some of the problems experienced. Firstly, there were a number of physical difficulties which simply could not be overcome such as the patient's flexibility and general compliance. These often led to large orbits of rotation i.e. large distance between the detector and the thorax of the patient. This led to subsequent degradation in image quality in other words resolution. It then

became difficult to accurately delineate the tumour boundaries. For the patients detailed, the orbit of rotation was limited by the gamma camera system itself as the heads were only capable of undertaking a circular or elliptical orbit with a fixed maximum radius. However, nowadays almost all gamma cameras are able to closely contour the patient's diameter via motion sensors and are also able to correct for increased patient to detector distance by storing information about the orbit of rotation in the acquisition header files and by the use of resolution recovery. Another change to the way images are acquired is the addition of a scatter window, which allows the peak window data to be corrected for a contribution due to scatter during the reconstruction process.

Probably the biggest advance in gamma camera technology which could potentially have a massive impact on the data presented is the advent of Hybrid Imaging. SPET-CT systems are now widely available and are simply a double headed gamma camera with a CT unit bolted onto the gantry. These systems allow a SPET acquisition to be performed followed by a low dose CT which in turn is used to create an attenuation map for the patient. The attenuation map allows for a truer attenuation correction to be performed. If this correction could be used to provide a more accurate calculation of percentage uptake then it may be that this value would prove useful in optimizing the dose of NeoSPECT for target therapy. **Chapter 4 - Octreotide**, details further investigation of the influence and effect of an attenuation correction on SSR images.

All of these new features could have potentially impacted on the quality of the data and results both qualitatively and quantitatively, in particular the estimation of sensitivity derived from the standard acquisition. If the attenuation and scatter in the patient could be accounted and corrected for, it raises the question of whether or not the standard acquisition requires to mimic that of the patient in terms of its attenuation and depth characteristics. The standard acquisition could simply be the acquisition of a vial of known activity and volume and therefore a more accurate measure and calculation of sensitivity. This would have to be investigated further, see **Chapter 4**.

In terms of its localisation ability, SPET-CT would have no doubt proved a powerful tool in the identification of tumour volume. Correlative imaging could have allowed for the tumour ROI volume to be defined on the CT images and the

ROIs copied to the SPET volume which could have simplified the ROI analysis process and reduced any delineation inaccuracies caused by the partial volume effect and scatter in the SPET image. Review of some of the patients' CT data showed tumour volumes that were very discrete on the CT images but on the SPET data demonstrated multiple focal areas rather than one large diffuse volume. This additional anatomical information could also have helped improve the identification of normal/disease free lung required as part of the T:B analysis.

When assessing uptake in the mediastinum, one of the other major difficulties with the SPET only data was the characterisation of this uptake, as uptake was considered to be nodal based on its size, shape and location. The actual source of this type of uptake could not be confirmed and therefore SPET-CT would have helped identify whether the uptake corresponded to that of a lymph node. Another equally difficult problem was in identifying which nodes actually had uptake and these suspected areas of nodal uptake could only be regionalized in terms of their gross location in the thorax. This made correlation with the histological findings and/or any other imaging difficult if not impossible. Again SPET-CT could have provided the additional localisation information required, and confirmed if uptake demonstrated was that of a lymph node or not. In addition SPET-Ct would have improved the confidence in the identification of any potential additional nodes with low grade uptake.

The quantitative results detailed in the thesis did not discover any statistically significant differences between the benign and malignant group. "Neo SPET-CT" could possibly lead to a clearer differentiation between the groups through its ability to identify and compare large differences in the tumour volume based on the CT and compare these with the SPET distribution. This imaging technique could also potentially help indicate early infiltration of disease to surrounding tissue, allowing disease progression or response to treatment to be monitored more accurately. This could also be true for lymph node involvement.

Whilst it could be argued that a diagnostic CT data would be obtained for these patients the reality is that there is often a notable time difference between both forms of imaging during which time there could be disease progression in the malignant group or regression of disease in the benign group therefore volumes

defined using previous CT imaging may not prove to be reliable. In addition breath hold diagnostic CT images are often very different from the SPET studies where a breath hold image would be impossible.

In spite of the small sample sizes, the data show no clear message that NeoSPECT could be used to differentially diagnose malignant from benign disease, or to sub-categorise tumour type. The image data however does demonstrate clearly that these images can show disease tissue both in the main lung tumour sites and uptake in lymph nodes within the mediastinum. Although this had been previously reported by Waxman, 2002, this had not been previously quantified. Quantitative work undertaken in this thesis failed to provide any additional value to previous findings as a result of being unable to successfully correlate the lymph node uptake with the node sampled histologically.

Further work

In order to determine whether or not “NeoSPECT-CT” could have improved the quality of image data significantly enough to lead to an improvement in the sensitivity of the quantification measurements the natural step would be to assess future NeoSPECT and SPET studies with SPET-CT. Unfortunately timing made this impossible but in order to investigate this work will be presented in chapter 4 looking at the use of SPET-CT with another type of SSR imaging agent, octreotide.

Chapter 3 - Hybrid Imaging

3.1 SIEMENS Symbia T

The first SPET-CT unit was developed during the 1980s and 1990s at the University College of San Francisco. The development of this type of system stemmed from a desire to add anatomical information to the excellent functional imaging of nuclear medicine. In addition the CT component could be used to correct for image degradation caused by soft tissue absorption (attenuation) which is a problem with all nuclear medicine imaging.

The first commercial system using a CT tube became available in 1999 and was manufactured by GE Healthcare as the GE Millennium VG Hawkeye™. This comprised a standard double headed VG gamma camera and a CT component. The CT component of the Hawkeye system was designed with cardiac imaging and attenuation correction specifically in mind and, because of this, was designed specifically to produce low dose, single slice CT images. The CT tube was designed for slow tube rotation - this was a considered and deliberate feature of the design in an attempt to produce a CT image that better matched the nuclear medicine component in terms of patient movement, caused primarily by patient breathing.

During 2006, Glasgow Royal Infirmary (GRI) were inviting manufacturers to complete a tender application for a SPET CT system. At this time there were three major manufactures of SPET-CT units involved; GE Healthcare, Phillips Medical Systems and Siemens Medical Systems. In January 2007, following the tendering process, GRI installed and commissioned a Siemens Symbia T SPET-CT unit as shown in **Figure 47**.

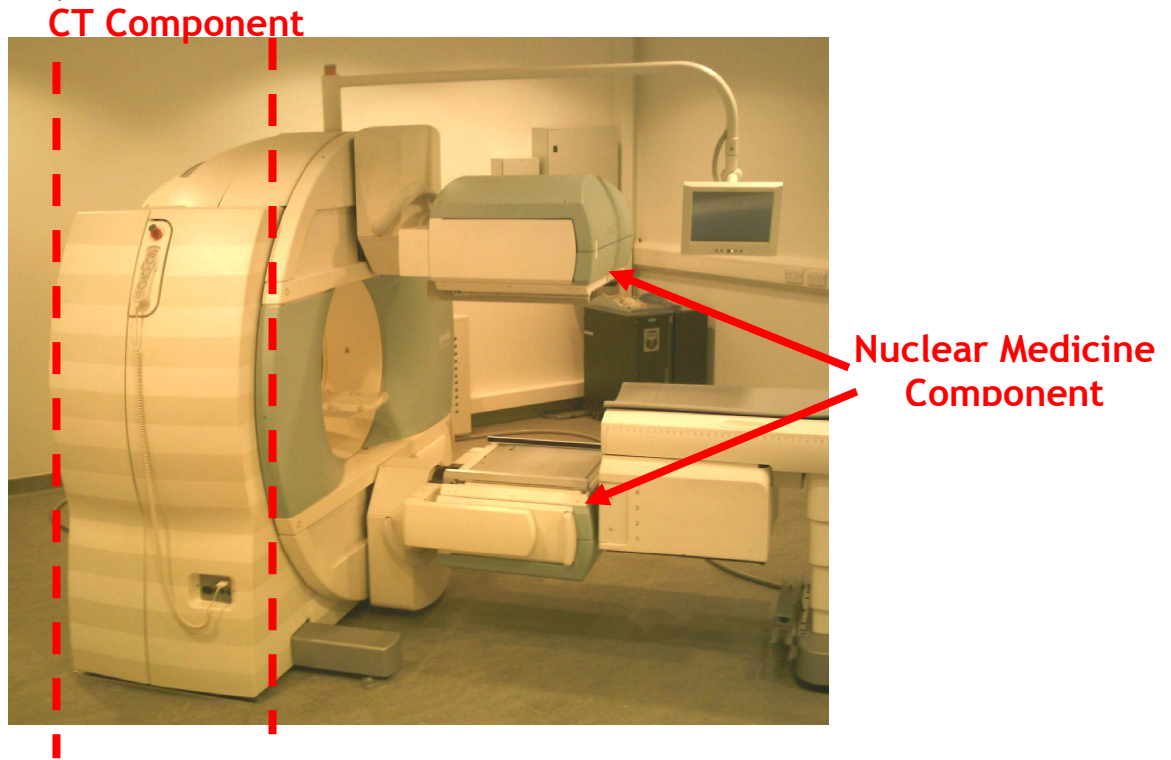


Figure 47 - Symbia T
Image of the Symbia T Hybrid Imager at GRI.

There were a number of small differences between these units, most of which were subtle and software based, but the largest and most important (to GRI) difference between these units was the CT component. The Siemens Symbia T offered a fully diagnostic 2 slice tube optimized to produce low dose CT images meaning the functionality and image parameters were limited only by preprogrammed software rather than hardware. Since the CT tube was a diagnostic tube, images could be acquired at a much faster rate, leading to less movement artifact in the CT image and thus, when compared to the GE unit, a better quality CT dataset. The software however limited this tube to work at low dose. The Phillips Medical system incorporated a high dose fully diagnostic 6 slice CT tube which made the unit very expensive and as our tender and requirement for imaging was primarily for the SPET component of the machine, the Phillips system was not considered as a result of cost and the high CT dose.

3.1.1 CT Technology

The first ever commercial CT scanner was the EMI scanner, which was installed in 1970 at the Atkinson Morley Hospital in Wimbledon, England. This was as a result of work undertaken by Godfrey Hounsfield, a British Electrical Engineer who was working for EMI Central Research laboratories in England.

In 1979 both Hounsfield and a South African born American Physicist Allan McLeod Cormack shared the Nobel Prize in Medicine. Both scientists had worked independently of one another, Cormack being recognised for developing the associated mathematical theory and Hounsfield for applying this theory and creating the first ever CT scanner, (Wiki-CT, 2011).

Of the two scientists, Hounsfield is probably the more recognisable as his name was given to the unit used to quantify the radiodensity of structures. The Hounsfield Unit, HU, is defined in **Equation 10**.

$$HU = 1000 * \frac{\mu_{material} - \mu_{water}}{\mu_{water}}$$

Equation 10
(Delbeke & Israel, 2010)

where μ is the linear attenuation coefficient and HU the hounsfield unit. Typical values of HU for common substances are given in **Table 33**.

Substance	Hounsfield Unit, HU
Air	- 1000
Fat	- 120
Water	0
Muscle	+ 40
Contrast	+ 130
Bone	+ 400 or more

Table 33 - Typical Hounsfield Units
(Wiki-Hounsfield, 2011)

In terms of its hardware, the CT component of the Symbia T comprises a diagnostic tube and two rows of detectors (known as slices). These are optimised via the system's software to acquire only low dose CT volumes.

Despite the Symbia having a diagnostic tube the images, in comparison with current day CT scanners, are considered of low quality and 'non-diagnostic'. This is due to the acquisition properties including lower mAs (tube current) although the image quality is also related to the system's default smoothing kernel used to reconstruct the raw CT data (Siemens, 2005).

In a bid to optimise the resolution of CT images acquired, the size of the acquisition matrix was considered. Although this parameter could be modified it could only be achieved through a very indirect manner. The matrix of the Symbia T's CT is dictated by the matrix size of the SPET acquisition, that is the matrix size of the CT will always be double the matrix size of the SPET acquisition. Typically, SPET acquisitions are acquired using a 128x128 matrix to achieve good count statistics per pixel, which would result in a CT with a 256x256 matrix. Careful consideration was given to what size of SPET acquisition matrix would produce the best possible resolution of the CT without compromising the SPET image quality. Within the limitations, the preference was to produce a CT with 512 x 512 matrix from a SPET acquisition acquired using a 256 x 256 matrix. However, software on the Symbia allowed for rebinning of the raw SPET acquisition data following the CT acquisition which meant that the raw SPET data could be folded back down to a 128 x 128 matrix. All SPET-CT's were undertaken by acquiring 256 x256 SPET with a 512 x512 CT.

The Symbia's default smoothing kernel used for reconstruction is the B08s which must be applied if the CT is to be used to perform an attenuation correction. However the Symbia T offers 3 smoothing kernels to reconstruct the raw data; B08s, B30s and B60s, B08s being the lowest in terms of resolution, because it has the highest smoothing and the B60s the highest resolution (less smoothing). Whilst B08s must be used when performing attenuation correction, the senior radiologist decided that the B60s was the most suitable smoothing kernel for CT images as part of SPET-CT localisation as this kernel produced sharper images.

In addition to the aforementioned parameters, the Symbia software also has the option of working in 'CareDose4D' mode which is used to ensure the lowest dose to the patient. The 'CareDose4D' mode uses Automatic Exposure Control, AEC, techniques and is achieved by firstly acquiring a topogram/scout view. This 2D acquisition is able to determine the radiographic density of the patient. The

density profile, along with a fixed tube voltage of 130kV_p, is used to modify other CT parameters according to the patient's size. In this way, the system ensures that the parameters for a thin patient are not equal to those of heavier patients (Siemens, 2006).

The dose is therefore optimised on a patient by patient basis. If a patient is larger than average, the dose modulation system adjusts the acquisition parameters to ensure the best image quality with a specifically set reference mAs. The system employed at GRI aims for a reference current of 17mAs.

3.1.2 New SPET Reconstruction Algorithms

Section 1.2.2 of Chapter 1 details two very different approaches to tomographic image reconstruction. As discussed, originally tomographic reconstruction took an analytical (FBP) approach but has since moved onto an iterative approach in the form of OSEM algorithms, as used for the reconstruction of the NeoSPECT patient data. These algorithms have been improved further by the addition of resolution recovery.

The Symbia T software, Syngo, provides both analytical and iterative techniques for SPET data reconstruction. Of the iterative reconstructions, there were 2 techniques available; the standard 2D OSEM as described in previous chapters and Flash 3D.

Flash 3D reconstruction is a Siemens OSEM algorithm with resolution recovery. The resolution recovery component of the algorithm compensates for degradation to image resolution caused by the increased distance placed between the source, in this case the organ within the patient, and the detector. There are two main causes for increased source to detector distance:

1. Collimator depth.
2. Radius of rotation, which is dictated by patient circumference and/or tolerance to the camera heads being close to the patient surface.

Loss of resolution with increasing distance is illustrated in **Figure 48**. The ‘True’ line for collection of projection data is shown along with the ‘reality’ which has been shown as a fan beam for the purpose of illustration. This means that the area of acceptance for gamma rays increases with distance from the detector therefore gamma rays from outside the ‘True’ projection will be accepted by the detector and this causes blurring of the projection image.

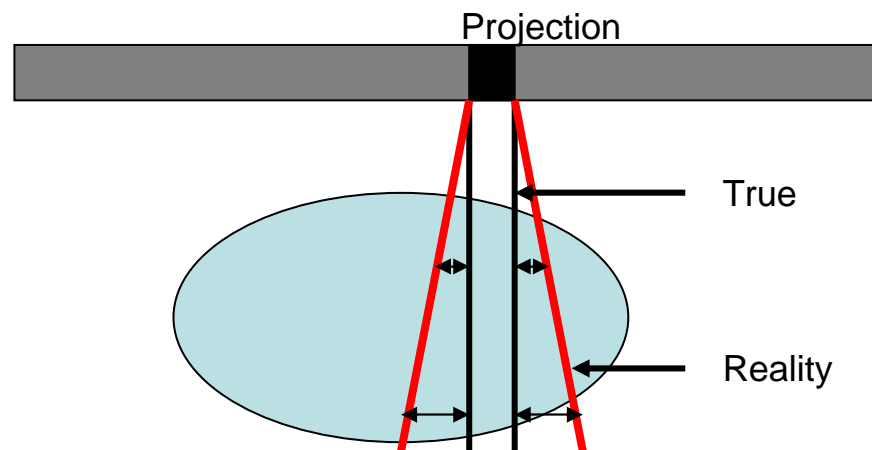


Figure 48 - Loss in resolution with increasing distance
Image demonstrating the loss in resolution with depth, the blue circle represents a focus of activity and the long grey rectangle, the detector.

The fan beam model can be incorporated into the OSEM algorithm and on the Symbia this is known as OSEM 2D reconstruction but resolution recovery is a 3D problem and therefore a cone beam provides a true representation of the collection of gamma rays out with the ‘True’ projection. The Siemens Flash 3D algorithm uses a cone beam model and is therefore able to correct for the acceptance of gamma rays out with the true projection in 3 dimensions. Siemens use detailed information of the collimator and orbit of rotation to model this effect and include this correction to the iterative reconstruction (Lawson, 2011)

3.1.2.1 Scatter and CT attenuation Corrections

All Nuclear Medicine imaging is susceptible to the effects of attenuation and the scatter of gamma rays within the body. Image degradation due to scatter occurs when gamma rays from elsewhere in the body are deflected from their original path (true projection), during this process they lose only a small quantity of their energy, and are subsequently detected in the photo-peak of another

projection. It is the summation of all of these reduced energy gamma rays which broaden the base of the photo-peak when detected and cause image degradation by image blurring.

In addition to reducing image quality, the inclusion of scattered gamma rays within the photo peak will also have an impact on any image quantification undertaken.

It is important to attempt to correct the images for these scattered photons and there are two methods that can be used. The first method involves measuring the scatter, which is achieved via either Dual Energy Windows (DEW, ^{99m}Tc acquisitions) or Triple Energy Windows (TEW, ^{111}In acquisitions). Alternatively, the scatter correction can be corrected for by modeling the scatter using, for example, Monte Carlo Modeling.

Siemens Flash3D corrects for scatter using the DEW or TEW method by directly measuring the scatter windows. This estimated measure of scatter is applied to the estimated slice created in the 'expectation' stage of the OSEM algorithm and to back projection of the raw data. **Figure 49** is a screen capture from a SPET acquisition performed on the Symbia T. It shows two energy windows which are preset by Siemens for Tc99m scatter correction. Window A is the photo-peak and window B is the scatter window.

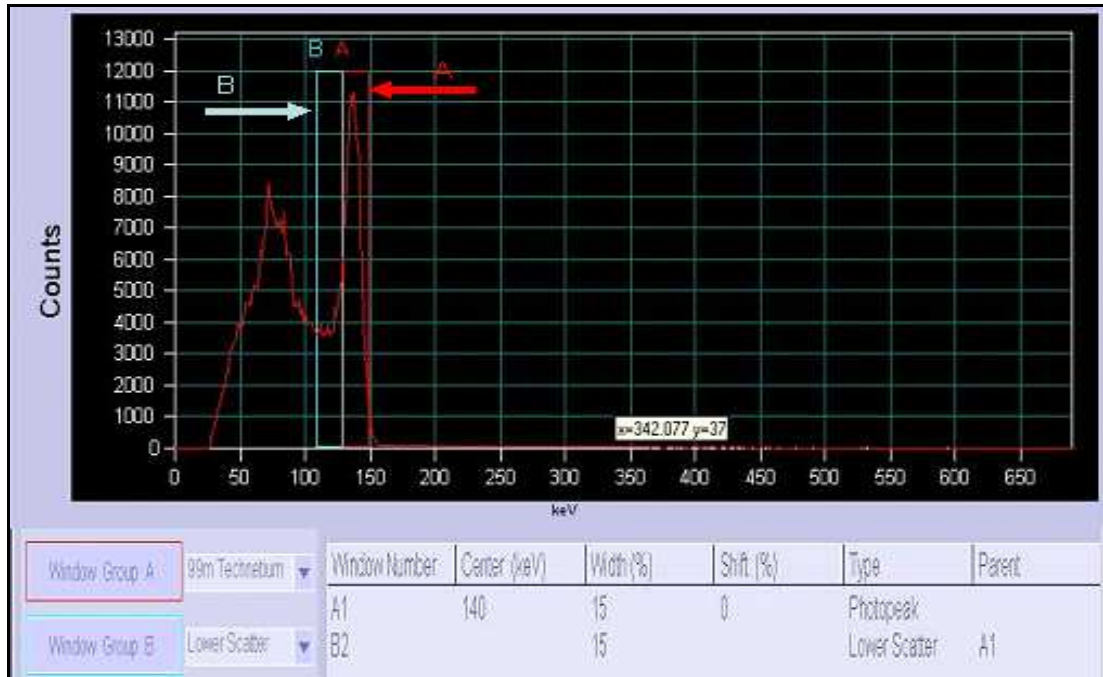


Figure 49 - Symbia SPET Example of Scatter Windows, DEW

Image showing a screen capture of the energy spectrum taken from the Symbia of a Tc99m SPET acquisition. The dual energy windows A and B are shown, Window A (in red) is the main Tc99m photopeak centred on 140keV and Window B (in blue) is the scatter window used.

In addition to being able to correct for scatter, both the Siemens Flash3D and OSEM2D algorithms also allow for an attenuation correction to be applied.

In **Chapter 2**, attenuation was corrected for by using a uniform geometric technique. The Symbia T, however, utilises the data from the low dose CT to convert HU's into attenuation coefficients (MU) and is therefore able to produce a map of these, an MU map. An example of an MU map is shown in **Figure 50**.

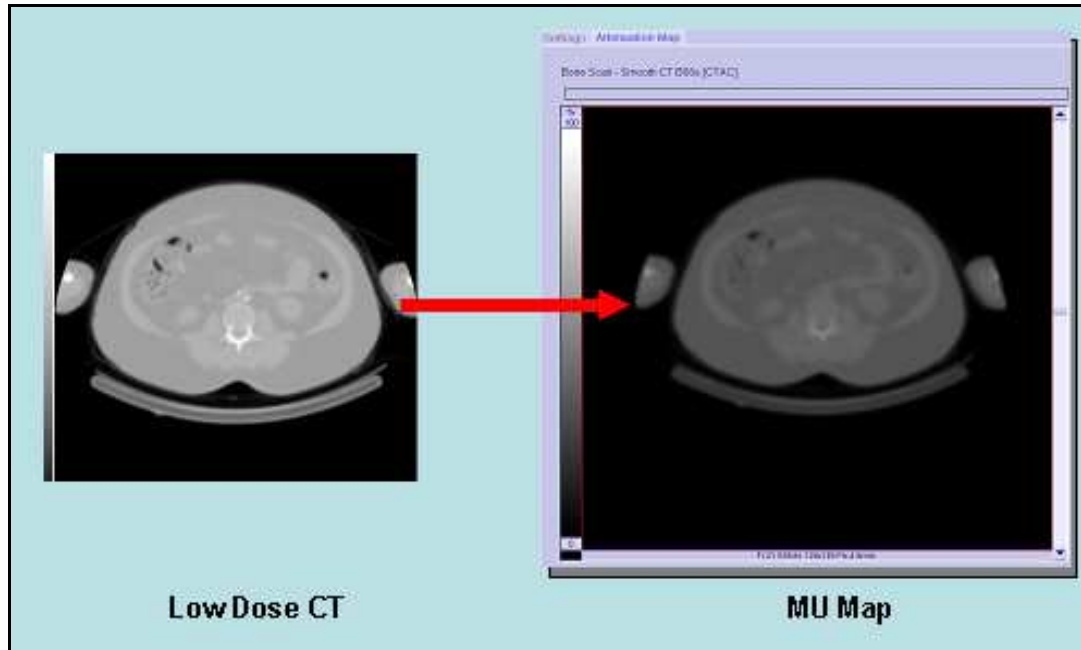


Figure 50 - Symbia MU Map

Images show a low dose CT transverse slice through a patients abdomen (Image to the left) and the corresponding screen capture from the Symbia of the MU Map (Image to the right).

The standard conversion from CT HU to MU is usually in the form of a ‘piece-wise’ bilinear fit model as firstly described by Blankespoor et al in 1996 (Brown, 2008). The bilinear model makes a distinction between materials which are comprised of air-water and water-bone. Therefore there are two HU dependant equations that must be used to perform the conversion. The first equation is used for HU values less than 0, refer to **Equation 11**.

$$\mu_{material@140keV} = \frac{HU * (\mu_{water@140keV} - \mu_{air@140keV})}{1000}$$

Equation 11
(Delebeke & Israel, 2010)

The second equation is used for HU values greater than 0, refer to **Equation 12**.

$$\mu_{material@140keV} = \mu_{water@140keV} + \frac{HU * (\mu_{bone@140keV} - \mu_{water@140keV})}{1000 * (\mu_{bone@CTkeV_{eff}} - \mu_{water@CTkeV_{eff}})}$$

Equation 12
(Delebeke & Israel, 2010)

Recent work undertaken by Brown et al (Brown, 2008) described an adaptation of this model which aimed to provide a simpler approach in that instead of using two equations to perform the conversion a single equation could be used, as described using **Equation 13**.

$$\mu = y_0 + (a \times HU)$$

Equation 13

where μ is the attenuation coefficient, y_0 is the attenuation coefficient of water (when $HU = 0$), a is a material scaling factor and HU is the Hounsfield unit.

However, to maintain the bilinear model approach a scaling factor, a , was introduced which differentiated between the two distinct types of material used, with $HU < 0$ and $HU \geq 0$. To convert HU into attenuation coefficients using a 120 kV_p CT and for a radionuclide with energy of 140 keV the following values should be inserted into **Equation 13**:

1. $y_0 = 0.149\text{cm}^{-1}$.
2. For HU values less than 0, $a = 0.15 \times 10^{-3}$.
3. For HU values greater than or equal to 0, $a = 0.14 \times 10^{-3}$.

Using these values the conversion can be calculated and is shown as in **Figure 51**.

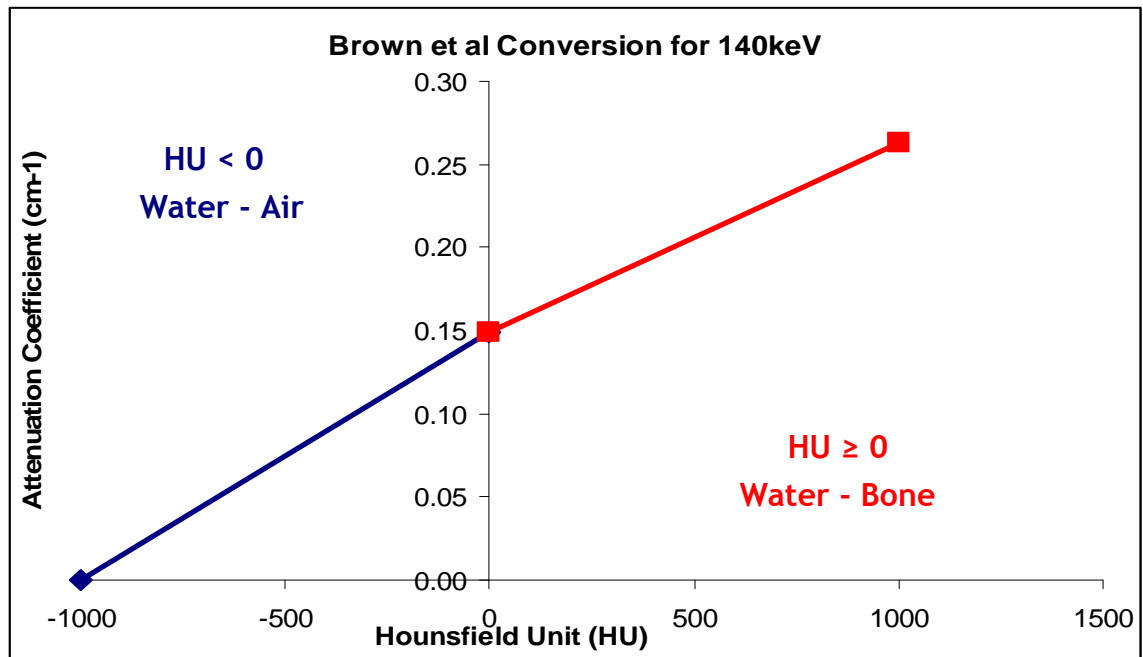


Figure 51 - Bilinear Response

The relationship between the attenuation coefficient and the Hounsfield unit for a 140keV x-ray as described by Brown *et al.* 2008.

The various values of MU's for specific radioisotopes along with values of effective energy of the CT are stored in 'look up' tables within the reconstruction algorithm. Despite information regarding the exact method employed by Siemens being unavailable, the conversion will take the form of a bilinear model and will be accessed via lookup tables.

Similar to the treatment of scatter, the OSEM algorithm applies these factors to both the estimated and measured data sets. However, it is important to note that the relationship described by Brown *et al* assumes a narrow beam, meaning data which have been corrected for scatter.

3.2 Influence on Bone Imaging

Since its installation, the department at GRI has undertaken over 2500 SPET CT acquisitions, a large proportion of these having been undertaken following review of the planar whole body bone images. The added CT information has been particularly useful in differentiating between benign or traumatic disease and that which is malignant in origin.

3.2.1 Characterisation of indeterminate Bone Scan Findings

Figure 52 highlights the importance of the SPET-CT's ability to differentiate between benign and malignant processes.

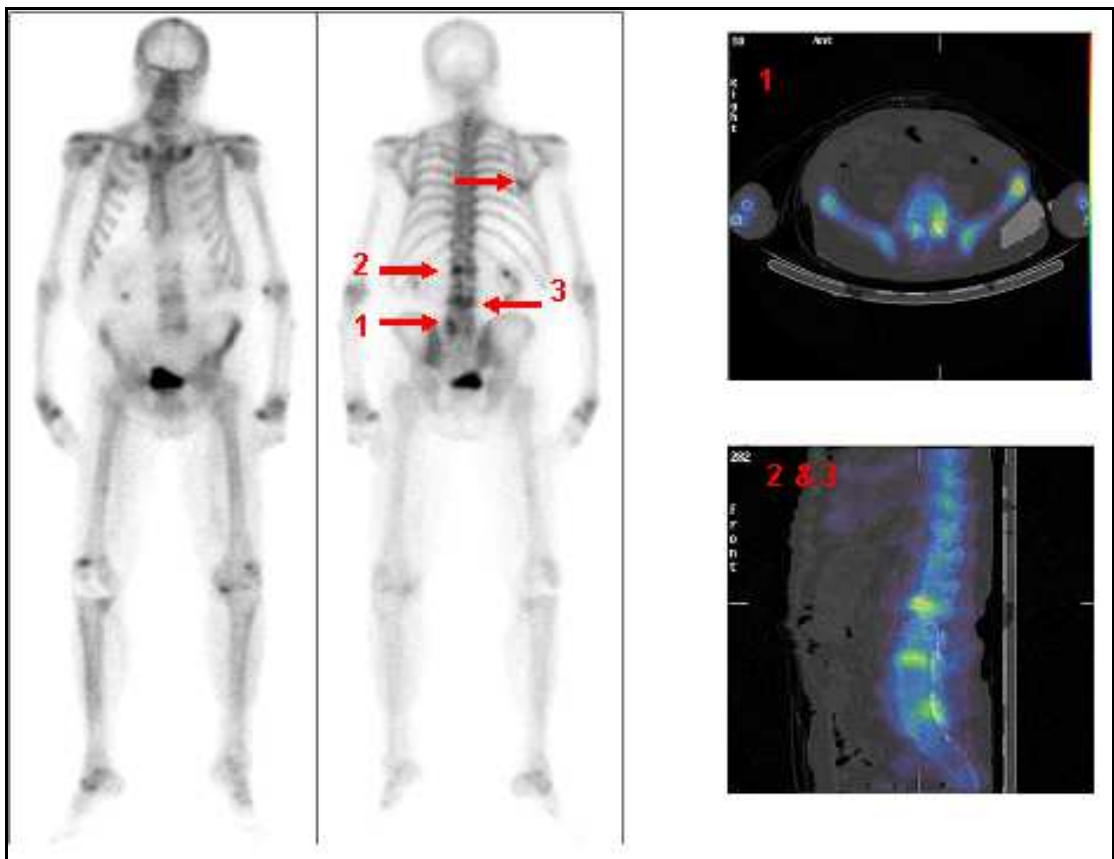


Figure 52 - Benign Versus Malignant
Images shown are of a whole body planar bone scan with several areas of increased Tc99m-MDP uptake, indicated by red arrows. The corresponding transverse and sagittal slices from fused SPET-CT demonstrating benign bone disease are shown on the right.

The whole body planar image is from a patient with known prostate cancer with a general deterioration in overall health and left sided leg weakness. The appearances seen on the bone scan were in keeping with the patient's symptoms and raised the suspicion of bone metastases. SPET-CT of these areas, however, demonstrated degenerative disease with no evidence of bone metastases.

3.2.2 Incidental Findings

In addition to improving the diagnostic accuracy (Han 2010) of the bone scan, the CT component of the acquisition has also been useful in displaying other incidental findings.

A whole body bone scan was performed on a 63 year old woman who was newly diagnosed with breast cancer and complained of back pain. A whole body scan was undertaken to stage the disease before the appropriate management could be decided. The bone scan showed multiple areas of increased uptake which, although suspicious of metastases, could also have represented degenerative (benign disease). This patient went on to have SPET-CT of the mid thoracic spine.

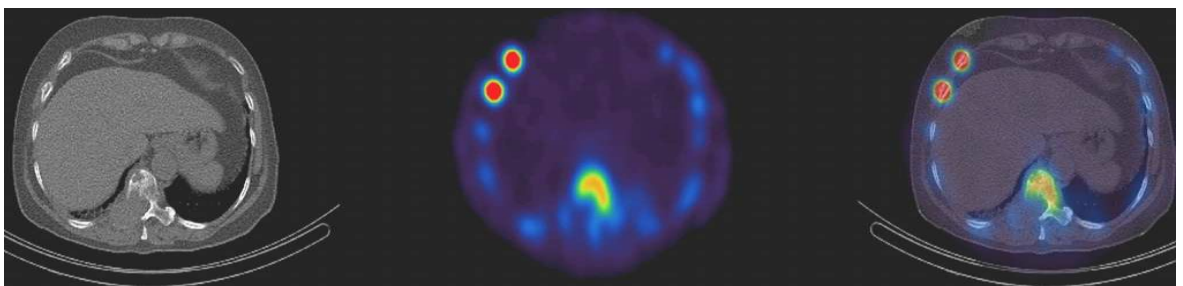


Figure 53 - SPET CT; Invasion of Spinal Cord

Image shown are transverse slices of a patient with spinal cord invasion; CT image on the left, Tc99m MDP bone SPET image centrally and the fused SPET-CT images on the right.

The SPET CT confirmed the multiple areas of increased uptake to be metastatic disease caused by multiple sclerotic lesions. In addition to these the scan also demonstrated a large destructive lesion in the T10 vertebra which was invading the spinal canal and therefore had the potential to compromise the integrity of the spinal cord as shown in **Figure 53**. As a direct result from the SPET CT, the

patient went on to have an urgent MRI of the thoracic spine and was treated with radiotherapy for impending cord compression.

Figure 54 demonstrates another example of a suspicious area of uptake, this time the area of abnormality appears to involve the right side of sacrum as shown by the red arrows.

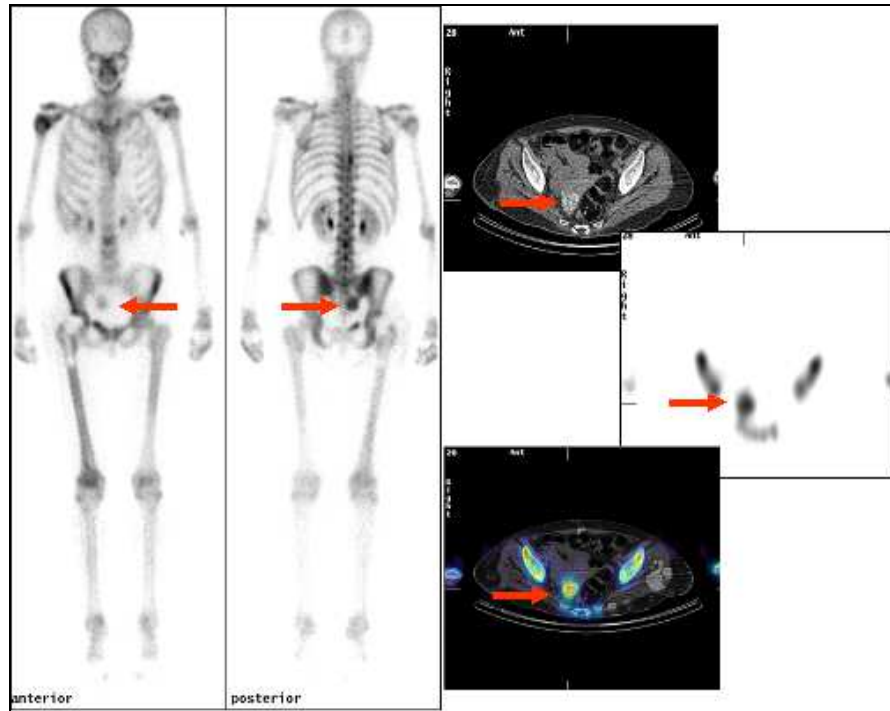


Figure 54 - Calcified Fibroid

Images shown are of a whole body planar bone scan with an area of increased Tc99m-MDP uptake overlying the right side of sacrum, indicated by red arrows. The corresponding transverse CT, SPECT and SPECT-CT Fused slices, on the right, demonstrated a calcified fibroid.

As can be seen in **Figure 54** the area of abnormality did not actually lie within the bone but out with. Without SPET CT imaging, the reporter would have had to rely on either interval bone imaging or imaging using another modality to confirm or exclude bone metastases as the diagnosis.

In the department at Glasgow Royal Infirmary, it has certainly been the case that SPET-CT has demonstrated a large reduction in the number of indeterminate bone scan reports being issued and subsequently reduced the number of patients for whom in the past a repeat bone scan after a reasonable period of time may have been required. It has also reduced the number of patients who have had to be referred to other imaging modalities in order to

form a definitive diagnosis (Han et al, 2011). However, despite aiding the diagnostic value of planar whole body bone scans, when the unit was installed there was very little published information regarding the use of SPET- CT in quantitative imaging other than in the area of cardiac imaging. Work undertaken in the remaining and following chapters was undertaken to investigate whether or not the accuracy of NeoSPECT quantification could have been improved with the use of SPET CT imaging. This involved careful assessment of the associated reconstruction algorithms and an evaluation of the qualitative differences in uptake in the abdomen, pelvis and (to a lesser extent) the chest demonstrated between the existing and new SPET imaging techniques.

3.3 Customised Phantoms for SPET-CT

The size, shape and function of individual organs can vary greatly between patients, leading to variations in the distribution of radiopharmaceutical within the patient. Identification and understanding of normal, abnormal and physiological uptake of the radiopharmaceutical is paramount in assessing the parameters for the reconstruction technique. In order to allow the accuracy of the image processing to be measured and to achieve a more in depth understanding of the reconstruction processes in particular the processing involved in the CT attenuation correction, a phantom was essential. Phantoms allow a known activity and distribution of radiopharmaceutical to be imaged in idealised circumstances and this means that the reconstructed data set and any measured parameters can be compared with this known distribution.

There are few anthropomorphic phantoms currently available commercially which are suitable for nuclear medicine purposes. There are even fewer that are suitable for new hybrid nuclear medicine SPET-CT units.

To overcome this problem, a bespoke phantom that met the needs of the research project and that could be designed and manufactured in-house was required. This phantom had to mimic a patient and therefore had to contain components which represented bone, lung and liver, the properties of which had to be applicable to both the Nuclear Medicine and the CT aspects of imaging.

Designing a phantom with known dimensions of vessels and compartments, also allowed the accuracy of SPET quantification to be assessed. This is achievable as known activities of radiopharmaceuticals can be introduced to the individual compartments of the phantom allowing a comparison of calculated activity to be made with actual activity. This also allowed the phantom to be used to determine the effect of both reconstruction techniques and filter parameters.

3.3.1 Requirements

The main purpose of the phantom was to mimic some of the different attenuating volumes and structures found within the thorax of a patient. It had to include therefore a volume representative of lung, bone, liver and general tissue. The design brief for this phantom raised the following questions:

1. ***What is the purpose of the phantom?*** - The phantom will be used to assess the accuracy of reconstruction techniques and post processing activities.
2. ***Physical Size?*** - Approximate dimensions, in mm, 250-300 diameter x 300 high.
3. ***Weight?*** - As light as possible for easy handling, when filled with liquid.
4. ***Materials?*** - Mainly perspex and no metals.
5. ***Compartment Contents?*** - Saline solution, water, polystyrene beads to represent air in the lungs, and liquid bone solution.
6. ***Adaptability?*** - If designed to include bone, liver, lung and tumour compartments this should cover any future requirements.

A number of features had to be considered for this phantom. Firstly, the volume had to be large enough to house additional smaller volumes within it. Two of these volumes would have to simulate lung compartments. These compartments would contain both polystyrene beads and liquid solution (radioactive). The polystyrene beads to simulate an air component to the compartment in keeping with the actual lung. This is the same approach used by RDS phantoms for their lung component in their anthropomorphic phantom (RSD Phantom). Additional objects may be placed inside either or both of the lung compartments to mimic tumour volume. These compartments must be easy to fill and evacuate.

The liver compartment required to be a simple volume not requiring any additional components. This compartment should simply be capable of being

liquid filled (not necessarily radioactive) and must be filled and evacuated easily.

The spinal cord compartment, surrounded by material mimicking bone, also required to be filled and evacuated easily with liquid (radioactive solution).

The distribution of the compartments within the main compartment of the phantom should mirror the distribution of organs and structures normally found within the thorax; refer to **Figure 55**.

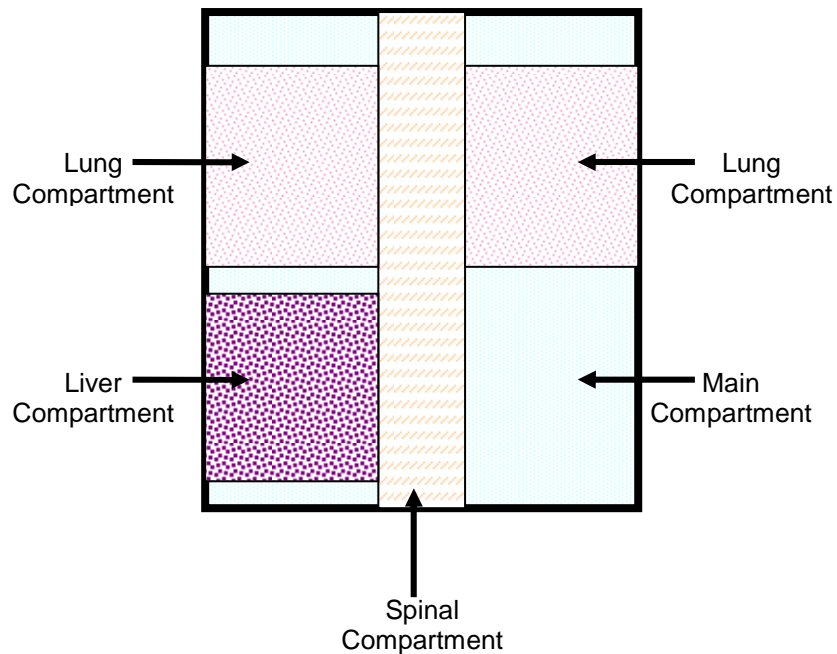


Figure 55 - Guide to compartment distribution within phantom
Image showing the basic distribution of compartments required for the SPET-CT phantom.

All compartments including the main vessel required a system which allows the phantom to be filled and vented easily to avoid air bubbles.

3.3.2 Phantom Design

Throughout the manufacturing process of the phantom, the design went through a number of transformations to accommodate the limitations of the materials used and to keep the size and weight of the phantom to a minimum.

Firstly, the overall size of the phantom had to be reconsidered, as the weight of the phantom when filled with liquid solution made it too heavy to transfer and therefore impractical. In addition to this, the weight of the phantom when filled with liquid was stressing the joins/joints, compromising the water seal and long term durability of the phantom.

A compromise had to be achieved that would allow the phantom to be filled with liquid whilst still being able to meet the requirements described in Section 3.3.1. This was achieved by removing one of the lung components, therefore reducing the overall radius of the main body of the phantom - see Figure 56.

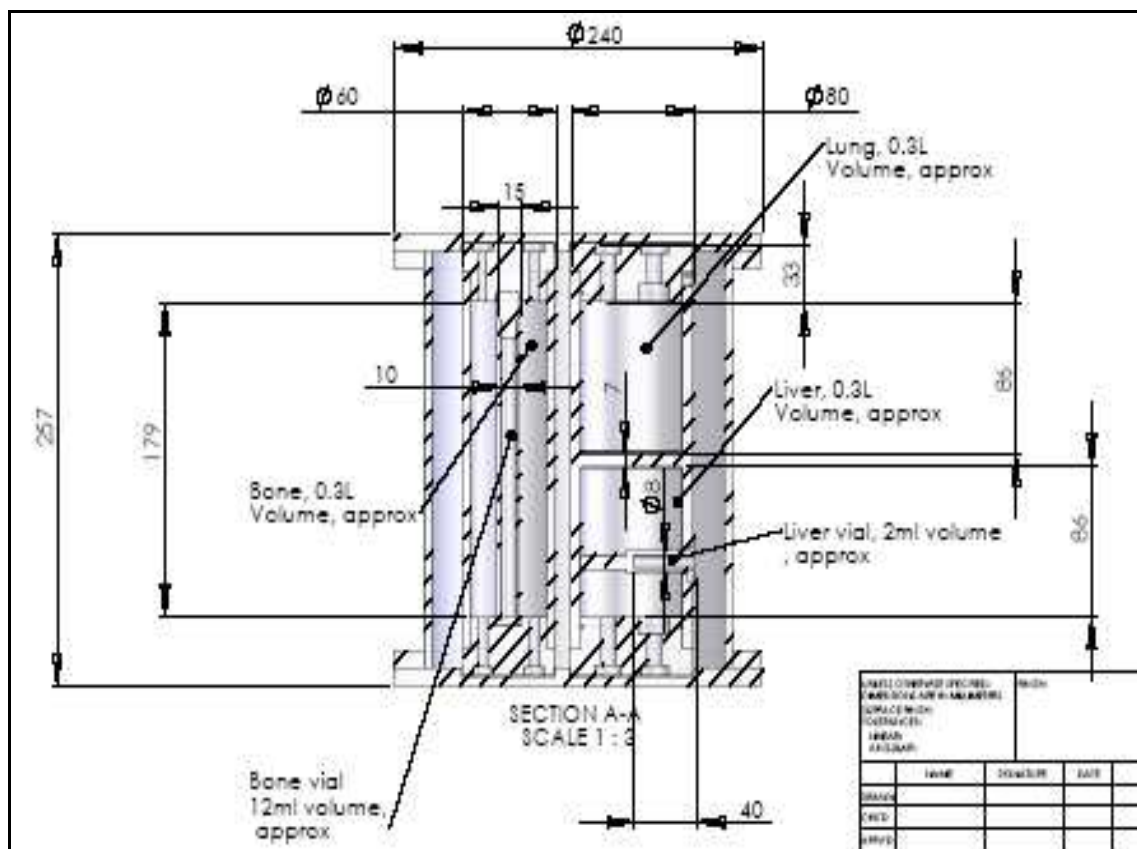


Figure 56 - Schematic of Phantom (including actual dimensions)
Image showing the detailed design schematic of the SPET-CT phantom produced in-house by the mechanical workshop.

Figure 56 is the actual schematic that was approved for in-house manufacture. This schematic shows a bone, lung and a liver component with a tumour volume within it.

The main body of the phantom was made from perspex moulded into a cylindrical shape. The base and lid of the main volume were then fixed to the moulded cylinder via an adhesive.

In order to create two separate compartments that lay one directly above the other, i.e. to emulate the anatomical distribution of liver and lung, a solid cylinder of perspex had to be drilled out. Two cavities were therefore created that were separated by a small layer of perspex. The bone compartment was fashioned in a similar manner to the lung/liver components and this cylindrical compartment contained another cylindrical compartment that would essentially act as the spinal cord. The spinal compartment was the only volume within the main body of the phantom that extended over the entire inside length of the phantom. The final in-house manufactured phantom is shown in **Figure 57**.

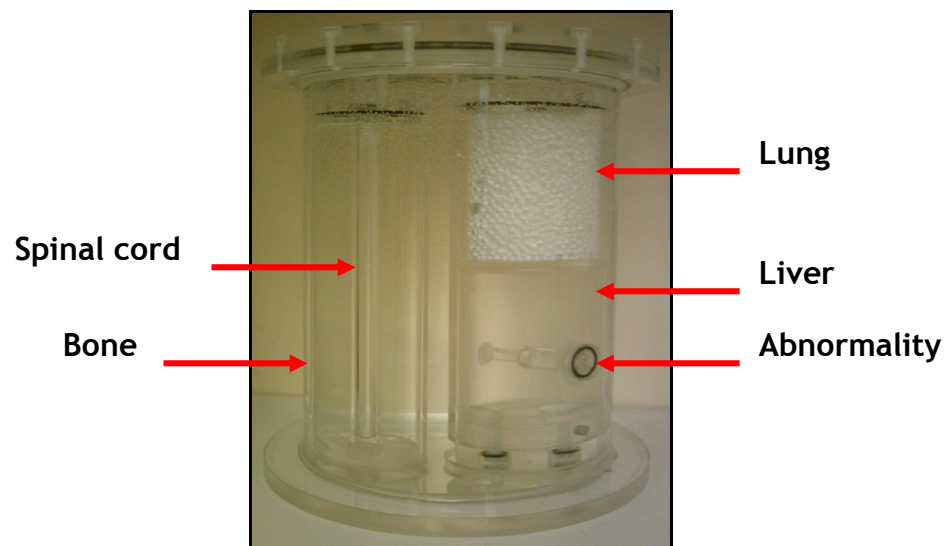


Figure 57 - In-house manufactured SPET-CT Phantom
Image of the actual phantom produced by the in-house mechanical workshop. The red arrows indicating the compartments included in the original basic design.

In terms of the thickness of perspex, either drilled or moulded, there was only one real specification and that was for it to be as thin as practicable but no thicker than 10mm as nuclear medicine imaging is unable to resolve structures less than approximately 10mm. The most challenging aspect of the phantom was the bone component, as this compartment was required to have similar properties to bone in terms of electron density.

3.3.2.1 Bone Substance

Bone is composed of 2 discrete components: cortical and trabecular bone, the abundance of these components being dependent on the type of bone. There are 5 bone types in the human body each of which have varying densities (Stalheim-Smith, 1993):

1. Long Bones - These are bones which are longer than they are wide. They have a strong layer of cortical bone encapsulating trabecular bone (examples include the femur and humerus).
2. Short Bones - These are bone that are as wide as they are long. They are comprised of a thin layer of cortical bone encapsulating trabecular bone, (examples include the wrists and ankle bones).
3. Flat Bones - 2 thin parallel layers of cortical bone surrounding a thin layer of trabecular bone (examples include the skull).
4. Irregular Bones - mixture of thin layers of cortical bone surrounding trabecular bone (example include the spine and hips).
5. Sesamoid Bones - mostly cortical bone (examples include the patella).

The bone component of the phantom needed to simulate bone within the thorax and abdomen. A material/substance similar to vertebral bone, in other words irregular bone, was required. Sourcing such a solid material proved difficult and equally any materials found were expensive and the ease of the subsequent in-house manufacturing process was difficult to assess.

An alternative approach to a solid piece of material was to consider a liquid solution that could emulate vertebral bone. This option provided the phantom with a greater degree of flexibility in terms of its use i.e. if a bone component was not required it could easily be removed, it also gave rise to the possibility of varying the concentration of bone solution depending on which type of bone was being considered.

The use of liquid solution to emulate bone has been used in the past (Hosie, 1993), by dissolving various weights of Potassium Hydrophosphate (K_2HPO_4) in water to achieve varying concentrations that could mimic different bone types i.e. liquid bone. It was decided that a K_2HPO_4 solution was ideal for use in the phantom as it could be sourced in-house, was relatively inexpensive and varying concentrations could be made up to meet the requirements of use.

3.3.2.2 Identification of correct bone solution concentration

From Hosie's paper, a concentration 150mg/ml was deemed an appropriate K_2HPO_4 solution. However, this had to be tested therefore the solution was added to the long bone cylinder as shown in **Figure 57**. To assess the appropriateness of the solution, it was necessary to establish whether it mimicked true trabecular vertebral bone in terms of its electron density. To determine this, region of interest analysis was performed on a number of patient CT's. **Table 34** details typical demographics of bone scan patients seen in the department.

	Total Number	Average Age (Years), Standard Deviation
All	2051	65.1 Yrs, 14.3
Female	1132	63.3 Yrs, 14.5
Male	919	67.3 Yrs, 13.8

Table 34 - Bone Scan Performed January 08 - December 2008

In total 10 patients were selected at random, whose age ranged between 62 - 89 years; 6 patient were female and 4 male. Two of the 10 patients were known to have osteoporosis.



Figure 58 - Standard ROI for Patient CT
Image of a CT sagittal slice from a patient through the lower abdomen and pelvis, including an example of ROI placements within the vertebrae.

In each case, the vertebrae selected demonstrated no visual abnormalities and ROI analysis was performed over 10 slices on both the coronal and sagittal planes. From the ROI's, values of Hounsfield Units (max) were obtained. **Figure 58** demonstrates the standard ROI used to obtain values.

An average was taken and over the 10 slices for each plane, these are given in **Table 35**. ROI analysis was also performed on the phantom - as shown in **Figure 59** and average values are also given in **Table 35**.

Patient	Average HU from Coronal Slices	Average HU from Sagittal Slices
Patient 1	186	182
Patient 2	259	252
Patient 3	350	313
Patient 4	241	237
Patient 5	360	320
Patient 6	284	247
Patient 7	289	263
Patient 8	165	137
Patient 9	237	210
Patient 10	244	239
Phantom	234	243

Table 35 - Patient Trabecular Bone Values and Phantom Values

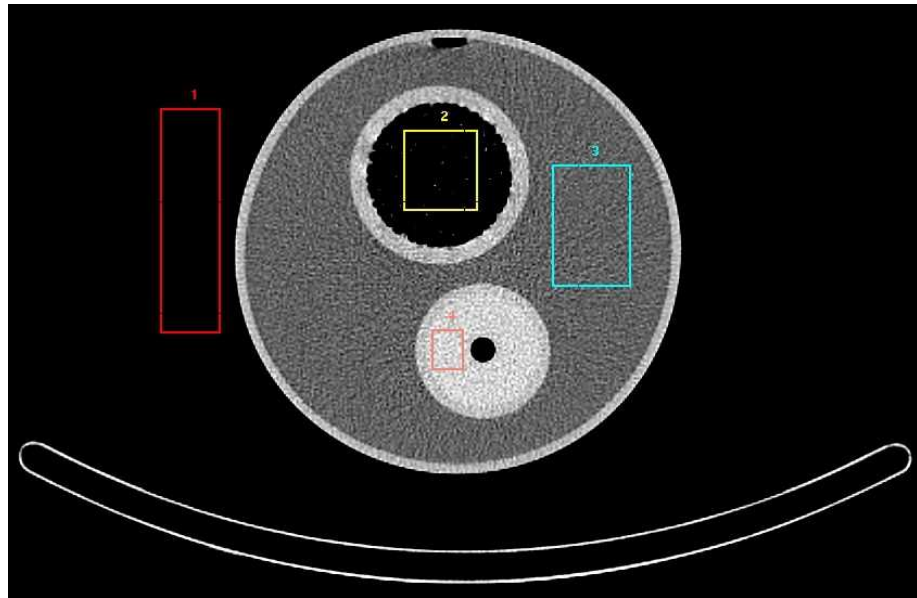


Figure 59 - SPET CT Phantom ROIs

Image shown is a transverse CT slice through the in-house SPET-CT phantom and the placement of the ROIS used to measure the Hounsfield units.

Hounsfield Units for patient data of normal trabecular bone ranged between 137HU and 360HU with a mean of 250, the phantom gave an average value of 238 HU which lies within the patient range. The bone component solution concentration was thus considered a suitable solution to mimic trabecular bone found in the normal vertebrae.

Summary/Conclusion:

Production of the phantom proved to be a lengthy process; this was principally due to the continuously evolving design of the phantom as a direct result of material and manufacturing limitations. In addition to this, the correct identification, suitability, and sourcing of a material which could mimic trabecular vertebral bone in terms of its electron density proved challenging. For the most part, the 150mg/ml K_2HPO_4 solution provided HU values that were comparable to those demonstrated in actual patient CTs with normal bone, therefore this concentration of solution was used to fill the bone component for work undertaken in the remaining thesis.

The manufacture of this phantom including the bone component allowed accurate quantification to be undertaken using SPET-CT imaging including reconstructions with non-uniform attenuation corrections. Quantifications in chapter 2 showed that there were often inaccuracies in the measurement of acquired activity and it would seem reasonable to suppose that the application of attenuation correction (and to some degree scatter correction and resolution recovery) should improve these values. Work using this phantom to calculate measured activity will be discussed in **Chapter 4**.

Chapter 4 - OctreoScan Imaging

4.1 Introduction

The work undertaken in **Chapter 2** raised two specific questions of whether or not hybrid imaging could improve firstly, the accuracy of the quantification achieved from SPET data as a result of using resolution recovery, scatter and CT - attenuation correction and, secondly, improve tumour delineation with the addition of anatomical information to the NeoSPECT data.

As the Symbia-T SPET-CT was not installed until 2007, there was no scope to investigate these inferences with NeoSPECT as the department was no longer using this agent by then. However, another commonly used radiopharmaceutical which shares many properties with NeoSPECT is OctreoScan. Like NeoSPECT, OctreoScan is a somatostatin analogue, pentetreotide, which when labeled with In-111 is used to locate neuroendocrine tumours (NET) - see **section 1.1.2.2** of **Chapter 1** for more details.

Since the mechanism of uptake for OctreoScan is thought to be similar to that of NeoSPECT, it was considered appropriate to undertake a retrospective review of 32 patients who had an OctreoScan scan with SPET-CT as part of their normal management, and to assess and compare the corrections available with SPET-CT and the influence of the additional information on image quality.

4.2 Literature Review

A literature review of SPET-CT OctreoScan was undertaken prior to the start of this study, but it was found that, as a result of the infancy of SPET-CT and resolution recovery reconstructions, there was a lack of published information available. This work stands on its own as there is little published work looking at OctreoScan specifically or even data specifically relating to indium-111. In addition to this, in the absence of data being available with depreotide, it allowed postulation of any improvements which might have been possible had SPET-CT been available. The work in this chapter sets out to investigate the claims set out in Chapter 2 relating to improvements which might have been possible while also aiming to establish if SPET-CT OctreoScan improved the detection of NET. In addition it was possible to use this data to investigate if the current standard imaging protocols should be amended in response to the availability of hybrid imaging.

Since its installation at Glasgow Royal Infirmary, and following the time frame in which this work was carried out there has been an increase in the availability of SPET-CT systems throughout the UK and Europe. As a result there is now more work being published using these systems, including work using their commercially available reconstruction algorithms that allow factors such as scatter, non-linear attenuation and resolution recovery to be considered and corrected for.

A comprehensive review of the clinical uses of SPET-CT was published in 2010 (Mariani, 2010). This review identified a number of nuclear medicine investigations where SPET-CT imaging improved the overall specificity of the study in comparison with traditional planar or SPET only imaging.

In terms of OctreoScan, in 2008 a study was carried out by Perri *et al.* (2008) looking specifically at whether or not the accuracy of detection and localisation of suspected NET (neuroendocrine tumour) in OctreoSCAN imaging could be improved with SPET-CT in comparison to SPET only imaging. A total of 81 patients with known or suspected neuroendocrine tumours had SPET-CT performed. The SPET and SPET-CT images were interpreted separately, the

nature of lesions identified were validated with either histopathology or clinical/imaging follow up. In terms of patients, 92.6% were correctly classified using SPET-CT in comparison to 79% using SPET alone. Improvement in the localisation of lesions using SPET-CT was also demonstrated, 94.7% in comparison 45.6% for SPET alone.

The main motivation for the application of SPET image quantification is treatment dosimetry and monitoring treatment response. Cremonesi *et al.* (2006) identified OctreoSCAN as a suitable imaging substitute for mapping the bio-distribution of ^{90}Y , which can be labeled to a number of somatostatin analogues to be used as a form of treatment for somatostatin receptor positive neuroendocrine tumours.

In a recent review of some of the literature available for absolute quantification in SPET published by Ritt *et al.* (2011), it was concluded that absolute quantification of activity using low energy radionuclides was achievable within a 10% error.

The review discussed the key elements affecting absolute quantification in SPET, such as attenuation, scatter and partial volume. There were a total of eight publications which specifically investigated absolute quantification using hybrid systems. Of note were in-vitro (phantom) work carried out by Shcherbinin *et al.* (2008) and in-vivo work by DaSilva *et al.* (2001), Willowson *et al.* (2008) and Zeintl *et al.* (2010).

Shcherbinin *et al.* (2008) assessed the accuracy of absolute uptake of a number of radioisotopes ($^{99\text{m}}\text{Tc}$, ^{111}In , ^{123}I and ^{131}I) using an anthropometric thorax phantom and a hybrid system. Results from which demonstrated activity estimations with errors which lay between 3% and 5% for all isotopes.

All of the in-vivo work undertaken by DaSilva *et al.* (2001), Willowson *et al.* (2008) and Zeintl *et al.* (2010) were performed using hybrid systems and not independent CT system. DaSilva *et al.* (2001) investigated the accuracy of absolute quantification by quantifying uptake in the myocardium of adult pigs. Each pig was administered with $^{99\text{m}}\text{Tc}$ -Sestimibi, the animals were then killed after a short period of time and subsequently imaged with SPET-CT. Following

imaging the heart was removed and activity within the myocardium measured. DaSilva *et al.* (2001) were able to demonstrate quantitative errors in the order of 10% regarding absolute quantification between the measured activity and that calculated from the SPET images.

Quantitative accuracy of absolute uptake was assessed by Willowson *et al.* (2008) in lung V/Q SPET-CT imaging; quantification was undertaken of the perfusion phase (Q) of the study. This was not a dual isotope study, both the ventilation and perfusion were performed with ^{99m}Tc , therefore the perfusion scan was corrected for background ventilation agent before quantification. This study demonstrated a difference between the measured activity injected and that calculated to fall between -7.4% to 2.1%, with an average error calculated at 2.6%.

Zeintl *et al.* (2010), quantified the activity present in the bladder from patients undergoing ^{99m}Tc -diphosponate bone imaging. Urine was collected from the patient following SPET-CT imaging and activity measured using a well counter. Corrections were applied that accounted for the changes in concentration of activity within the bladder between the acquisition start time and the time at which the urine was collected. This investigation demonstrated errors which ranged between -7.8% and 16.9% with an average error of 6.5% in the estimation of activity.

Of the validation studies reviewed by Ritt *et al.* (2011), either in-vivo (phantom) or in-vitro, the majority were performed using ^{99m}Tc and there remains few published data on other isotopes, in particular ^{111}In . One recently published study by Assie *et al.* (2010), not included in Ritt *et al.* (2011) review, investigated the accuracy of ^{111}In quantification via phantom and monte carlo simulation data. SPET data was corrected for factors affecting image quality such as scatter, attenuation and partial volume effects. This work was not performed using a hybrid imaging system but a separate CT was acquired on independent system and used for non-uniform attenuation correction. VOI analysis was undertaken, where the VOIs were delineated by the CT. Assie *et al.* (2010) concluded accurate absolute quantification of ^{111}In from SPET acquisitions was possible using OSEM reconstructions algorithms that incorporated scatter, non-uniform attenuation and partial volume corrections. A less than 20% error

was achieved in estimating activities of organs and tumours that were greater than 20mm in diameter.

Despite a maximum error in estimating activity of 10% for ^{99m}Tc , Ritt *et al.* (2011) acknowledged that the techniques to perform SPET-CT quantification requires strict reproducible patient set-up conditions along with the appropriate application of various corrections incorporated into the iterative reconstruction techniques. Based on the lack of autonomy in the patient set-up and image processing Ritt *et al.* (2011) described the techniques used to date not entirely suitable for the clinical environment due to large time constraints required.

4.3 Patient Acquisition Data

Patients attending Nuclear Medicine at Glasgow Royal Infirmary for diagnostic procedures are always asked to consent to the use of their images/data for teaching purposes and/or clinical audit. In addition to this the department was issued with a letter from the local research ethics committee, LREC, which stated that the use of SPET-CT could be considered as a service development and therefore ethics was not needed. Hence no application to LREC was required for this section of work.

The standard activity of OctreoScan administered is 220MBq of Indium-111 labelled octreotide in 2ml, it is administered intravenously. OctreoScan studies include a whole body image and a SPET-CT image of abdomen/pelvis at 24 hours post injection.

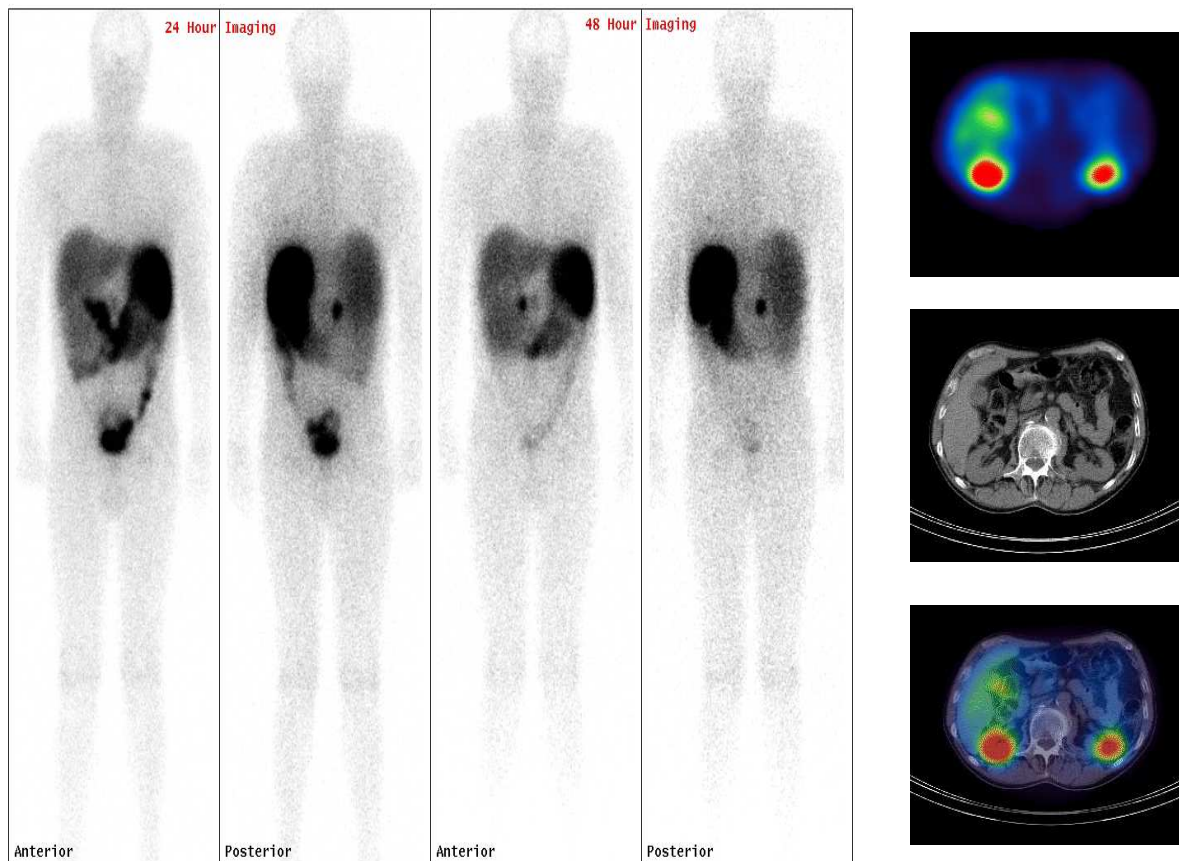


Figure 60 - Standard Images Acquired

Images shown are of standard whole body planar OctreoSCAN images acquired at 24 and 48 hours post injection (on the left) and transverse SPET, CT and Fused SPET-CT (on the right) of an area over the abdomen performed at 24 hours.

24 hour imaging is followed by a whole body image at 48 hours post injection +/- a SPET-CT of any additional areas of interest if these have not been previously included in the 24 hour SPET field of view - see **Figure 60**.

Acquisition parameters for the whole body images are detailed in **Table 36**.

Collimator:	MELP
Frame time:	10 cm / min
Energy Windows (keV):	10% window on 172 and 10% window on 247
Matrix:	1024 x 256
Orbit:	Auto Body Contour

Table 36 - OctreoScan Whole Body Acquisition Parameters

In 2010 the European Association of Nuclear Medicine, EANM, published guidelines on OctreoScan imaging procedures, (Bombardieri, 2010). These guidelines suggest whole body imaging is undertaken at 3cm/min, however, our institution acquires whole body images using 10cm/min.

For SPET imaging these guidelines suggest 45s per angle, whereas, the standard practice at our institution is 30s per angle. These guidelines also stipulated a 64x64 matrix to be used for the SPET acquisition. Our institution performs SPET-CT imaging, on the Symbia-T system and the quality of the CT images acquired are influenced by the SPET acquisition parameters. To produce a high quality CT the SPET data is acquired in a 256x256 matrix. The SPET 256x256 data is then binned down to 128x128 for reconstruction and display as discussed previously. Acquisition parameters of the SPET component are detailed in **Table 37**.

Collimator:	MELP
Degrees of Rotation:	360 degrees (180 each head)
Frame time:	30 seconds
Interval:	3 degrees
Energy Windows:	5 Windows; 2 x Peak, 3x Scatter
Matrix:	256 x 256
Orbit:	Auto Contour

Table 37 - OctreoScan SPET Acquisition Parameters

From **Table 37** it can be seen that aside from the peak data acquired for In-111, additional energy windows were also acquired. The Symbia T software was able to acquire SPET studies with or without scatter windows. Auto-contouring is also

used as opposed to a fixed orbit of rotation as this ensures the orbit is as close to the patient as possible.

Despite the fact that the application of a scatter correction had never been investigated locally, all SPET acquisitions acquired on the Symbia T were acquired with both peak and scatter energy windows. This approach was taken to allow data to be reviewed retrospectively and make a decision based on the data if the correction was deemed appropriate at a later stage.

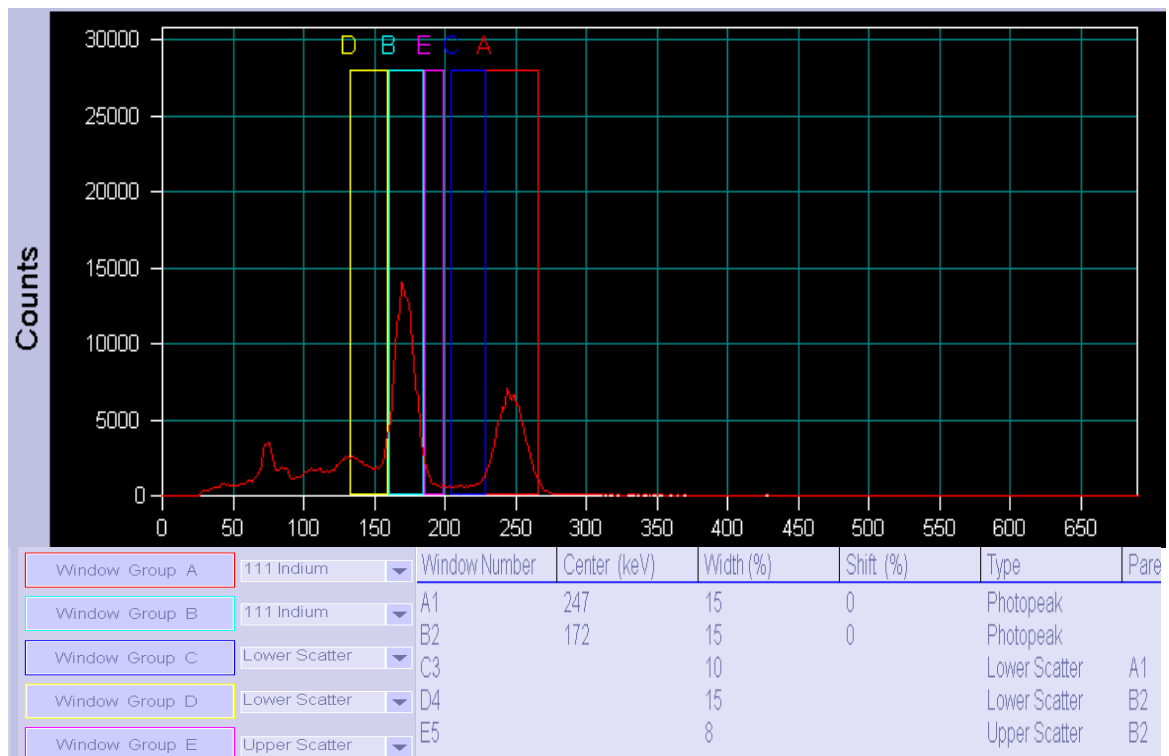


Figure 61 - Peak and Scatter Windows

Image showing a screen capture taken of the energy spectrum from the Symbia of an In111 SPET acquisition, the various peak and scatter windows acquired are shown. Windows A and B are the photopeak energies for In¹¹¹ while windows C, D and E are the relevant scatter windows.

For In-111, scatter data was acquired below and above the first peak, and a scatter window was acquired below the second peak as illustrated in **Figure 61**. Prior to the Symbia-T's installation reconstructions of OctreoScan SPET studies were undertaken on the Hermes system. These reconstructions did not include any scatter corrections. The software on the Symbia-T was capable of performing 3 different reconstruction techniques for SPET:

1. Filtered Back Projection
2. OSEM2D- Siemens version of the Hermes OSEM (HOSEM).
3. Flash3D - This is an Iterative Reconstruction algorithm with Resolution Recovery which has the option of employing scatter and CT-attenuation corrections (SAC).

The details of each technique have been discussed in previous chapters.

Reconstruction Method:	OSEM – Ordered Subset Expectation Maximisation
Subsets:	4
Iterations:	8
Number of slices:	Full Field of View
Low Pass Filter Setting:	Gaussian FWHM 8.4mm (default settings)
Zoom:	No Zoom

Table 38 - OctreoScan OSEM Reconstruction Parameters

To allow a direct comparison, the standard OSEM reconstruction parameters for OctreoScan studies used on the Hermes system were translated to the Symbia T, these are given in **Table 38**. The post filter applied on the Hermes system for Octreotide studies was a Butterworth filter with cut-off 0.8 cycles/cm and order 5. The shape of a Butterworth filter is shown in Figure 11. On the Symbia T the post filter applied was a Gaussian. Although the shape of this filter is different from that of a Butterworth (as its name implies it is shaped like a Gaussian), the effect on the image is similar. This Gaussian filter is described by its full width at half maximum (FWHM) and on applying Siemens default setting (FWHM 8.4mm) to the data, the reconstructions were judged by the clinicians at Glasgow Royal Infirmary to be comparable to those reconstructions from the legacy Hermes system. For a Gaussian filter as the FWHM increases so does the amount of smoothing.

4.3.1 Pilot Review of Flash3D Reconstruction

Siemens heavily promote the use of resolution recovery, Flash3D, in all SPET image reconstruction. Prior to undertaking any major comparative work to assess

differences between the standard reconstruction (OSEM 2D) and the new reconstruction technique (Flash 3D with and without corrections), it was important to become familiar visually with the basic Flash3D technique that is with no corrections, and to establish if there were any qualitative differences in image quality between the standard reconstruction and the basic Flash 3D technique.

SPET acquisition data from 15 patients were selected at random. Since the data acquired were in a 256x256 matrix the data had to be binned down into a 128x128 matrix prior to reconstruction. The data were reconstructed using both the OSEM 2D and the basic Flash 3D techniques, the parameters described in **Table 38** for the OSEM2D were replicated for the basic Flash3D reconstruction.

Both reconstructed SPET volumes were visually interpreted simultaneously using Hermes Multi-Modality Display protocol, this protocol allowed a slice by slice comparison of each technique. Two experienced observers recorded which organs were demonstrated and if any areas of increased focal uptake were demonstrated.

Flash 3D did not identify any new lesions when compared with OSEM2D, however, in 2 of 15 patients the lesions appeared more resolved. In terms of the OSEM, 3 out of the 15 patients demonstrated additional lesions in the OSEM reconstruction that were apparently not seen using Flash 3D. This would therefore suggest that the Flash 3D method of image reconstruction possibly removed lesions when compared with the OSEM 2D method. However, further review of the SPET volumes with the associated CT demonstrated the discordant areas to be part of an existing lesion which was demonstrated on the Flash 3D volume but which appeared over a smaller number of slices. Of the 3 volumes all the discordant areas were located in the abdomen and within areas of very low counts, therefore these very subtle differences are most likely an indication of improved image resolution as a direct result of using Flash 3D.

It was clear from this pilot review of the images that there were no major differences in terms of clinical diagnosis when adding Flash 3D to the reconstruction algorithm but that there was a difference in the image quality and because of this there was a potential for a difference in the quantification

as a result of the improved resolution. It was therefore decided that it was worthwhile to proceed to a more in-depth analysis of this using the larger patient data set.

4.3.2 Methods - Corrected Versus Uncorrected

Until hybrid imaging was introduced to the department at GRI, OctreoScan SPET studies had always been reconstructed using standard OSEM techniques. Whilst, for the most part, this reconstruction was deemed suitable, there were instances where confidence was low in terms of the true nature of the origin of uptake. This was either because the area of uptake lay within an area of low counts or in an area of bowel where there remained increased physiological uptake despite the use of a bowel preparation prior to imaging.

Hybrid imaging proposed a solution to the identification of low grade uptake within these areas via the various corrections which could be included in the reconstruction algorithm. In addition the anatomical information provided by the CT volume allowed better localisation of these areas and some characterisation. To investigate fully whether or not the corrections and additional anatomical information might lead to an improvement in image quality and accuracy of NET lesion detection an assessment using a comparison of the standard reconstruction with the new reconstruction techniques was undertaken.

For this investigation 32 OctreoScan consecutive patients were selected from the department's image archive. These patients all had routine imaging performed between April 2007 and May 2010. The anonymised demographics of the patients selected are detailed in **Table 39**, this table also details the clinical question.

OctreoScan #:	Age	Sex	Query
Oct Pat 1	80	F	? Active avid SSTR Tumour
Oct Pat 2	53	F	Pancreatic Carcinoma, staging scan
Oct Pat 3	67	M	Wegners granulomatosis, pre-treatment scan
Oct Pat 4	71	M	Liver Mets. ? Site of primary
Oct Pat 5	44	M	Kidney Carcinoma. ? Mets
Oct Pat 6	84	F	RUQ mass ?Carcinoid
Oct Pat 7	65	M	Liver Mets. ? Primary
Oct Pat 8	58	M	? Malignant ascites
Oct Pat 9	44	F	Mass ? NET (Gastrinoma)
Oct Pat 10	83	M	Mass ? NET
Oct Pat 11	83	F	Gastrinoma, ?Mets
Oct Pat 12	77	F	? Recurrent carcinoid tumour
Oct Pat 13	64	M	Large left side abdominal mass. ? NET
Oct Pat 14	63	F	? Carcinoid mets
Oct Pat 15	77	M	? Gastrinoma
Oct Pat 16	41	F	Known carcinoid tumour. ? Mets
Oct Pat 17	64	M	Pancreatic mass. ? NET
Oct Pat 18	62	F	Metastatic carcinoid lymph node. ? Primary
Oct Pat 19	51	M	Duodenal polyp carcinoid. ? Mets
Oct Pat 20	74	M	Carcinoid syndrome. ? Primary
Oct Pat 21	53	F	Mass pancreatic tail. ? NET
Oct Pat 22	61	M	NET Lung. ? Mets
Oct Pat 23	40	M	Resection of primary carcinoid tumour. ? residual disease
Oct Pat 24	38	F	? Mesenteric carcinoid mass
Oct Pat 25	60	F	NET Liver. ? Mets, staging scan
Oct Pat 26	56	M	Carcinoid prostate ? Mets
Oct Pat 27	41	M	? Gastrointestinal carcinoid tumour
Oct Pat 28	49	M	Metastatic carcinoid tumour bowel? Extent
Oct Pat 29	57	M	Mass head of pancreas. ?NET
Oct Pat 30	69	F	Mass body of pancreas. ? NET
Oct Pat 31	65	F	? Recurrent carcinoid.
Oct Pat 32	39	F	Carcinoid tumour appendix. ?Mets

Table 39 - OctreoScan Patient Demographics

Each of the patients detailed above had the following SPET reconstructions performed on the Symbia-T:

1. Reconstruction 1 - OSEM basic (O2D)
2. Reconstruction 2 - Flash3D basic (F3D)
3. Reconstruction 3 - Flash3D with Corrections (F3D SAC)

The parameters outlined previously in **Table 38** were used for all 3 reconstructions, however, as suggested, reconstruction 3 also included a scatter and CT-attenuation correction.

All reconstructions were registered to their associated CT. There were 2 reconstructed CT volumes available, the first used a smooth kernel (B08s) to reconstruct. The B08s CT was used for attenuation correction and was of limited diagnostic use. The second CT was reconstructed using a sharp CT kernel (B60s), this reconstructed CT was higher in resolution in comparison to the B08s and was better for localisation and characterisation of organs and lesions, all SPET data was therefore registered with B60s CT.

To ensure the observers were blinded to the reconstruction technique and the patient, the data was anonymised. To do this each registered SPET reconstruction and CT were selected together and assigned new demographics. It should be noted that this process did not overwrite any of the original patient demographics but simply created duplicate image files, only the header files of the duplicate images were amended. Each file took the format shown in **Figure 62**.

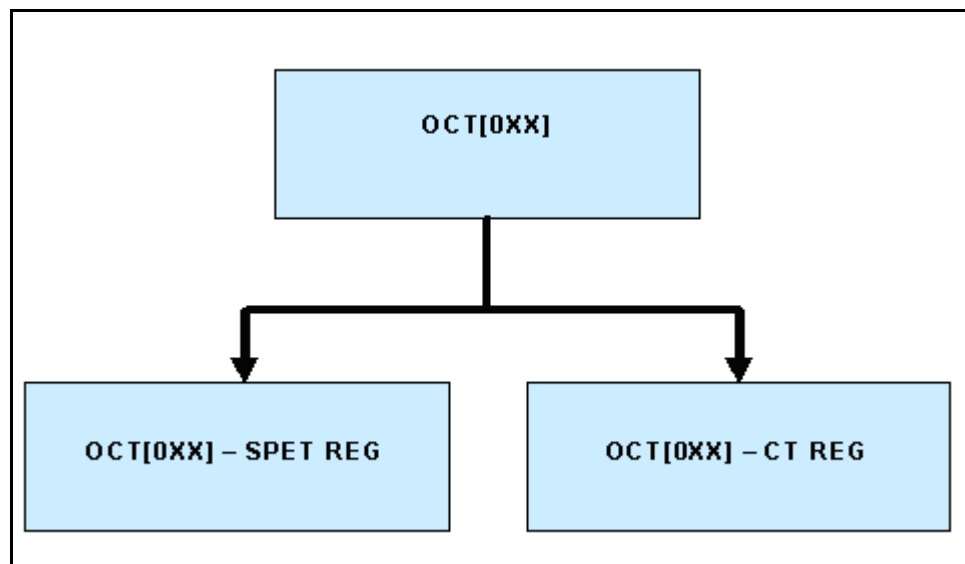


Figure 62 - Anonymised Data Format
Image showing how the patient data was anonymised.

Each anonymised data set contained only 1 SPET and 1 CT volume. This meant that each patient had a minimum of 3 anonymised data sets, each of which had

a different number assigned. The process of anonymising data was randomised to avoid assigning numbers in successive order to the data sets. To allow ease in accessing these files a separate folder in the database was created to store the files in, this was called “Pentetreotide Study”. In addition, to estimate intra-observer reproducibility multiple copies of several images were included within the randomisation.

4.3.2.1 Investigation 1: Qualitative Assessment

Four observers were chosen to score the images, each observer was experienced in the interpretation and/or reporting of OctreoScan studies. Observers were asked to review each data set using the Hybrid Imaging Viewer on the Hermes system.

The observers were asked to score each SPET volume in terms of image quality and assign each volume a score between 1 and 5; 1 being the poorest and 5 best. When assigning a score the observers were asked to consider the following points:

1. Delineation of patient habitus or in other words does the edge of the patient on the SPET image match that seen on the CT or is there scatter outside the patient’s body.
2. Delineation of the lungs as air.
3. Uniformity of uptake across solid organs e.g. liver, spleen, kidneys, bladder.
4. Delineation of any abnormalities and/or loops of gut.

Each observer was asked to score the total SPET volume, this was usually the abdomen. Where the lungs were included in the FoV the observers were asked to score this separately in addition to a score for the entire volume. This was in an attempt to determine improvements which would have been made to the NeoSPECT data had SPET-CT been available.

The purpose of the CT was to act as a reference for the SPET data and allowed the observer to ensure areas of uptake demonstrated on the SPET images corresponded to areas of abnormality or areas of expected physiological uptake. The CT was also important when assessing the distribution of the uptake within an organ for example, the liver, as it was important to exclude the presence of disease processes which would result in a non-uniform distribution of uptake. **Figure 63** provides some example cases. Observers were informed that when disease or other abnormality was present this should not be reflected in a poorer score, that is the quality of the distribution of uptake in the SPET data should not be scored low as a result of an existing process for example liver metastases.

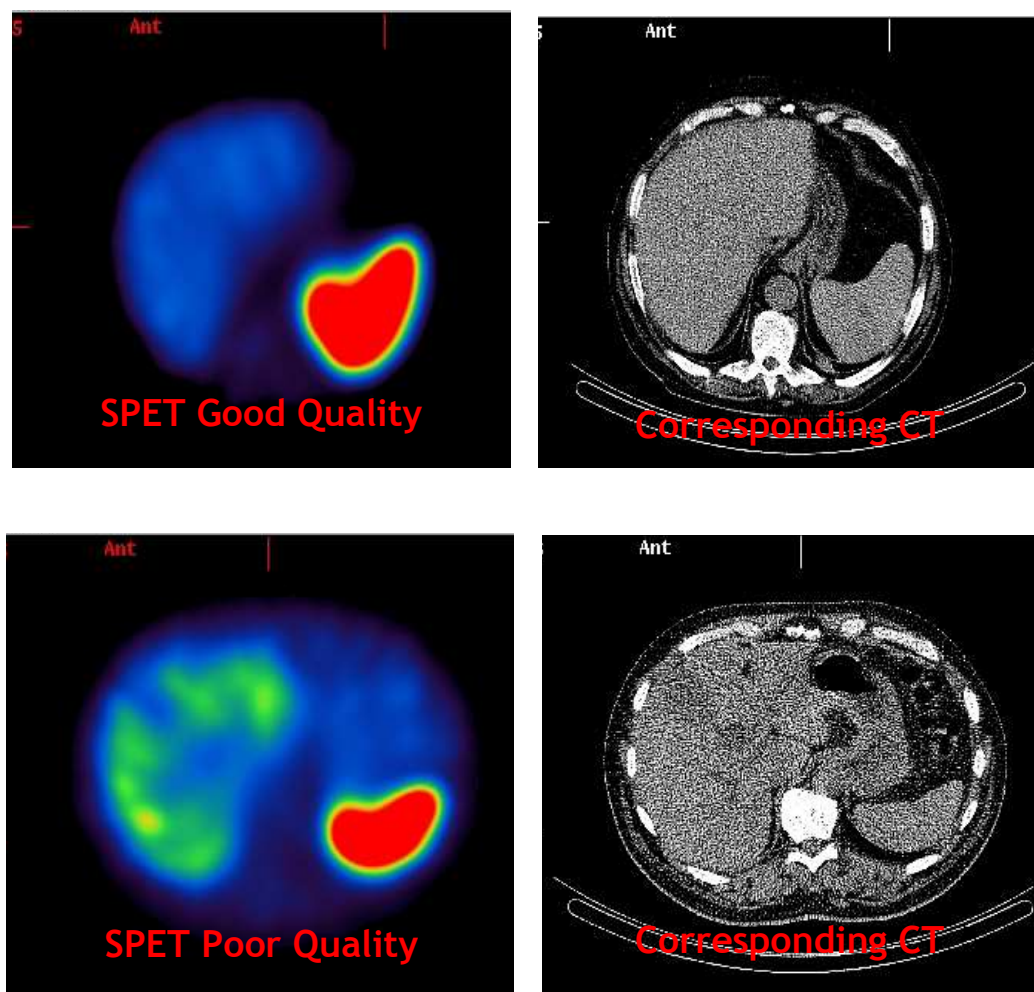


Figure 63 - Example of Varying Quality of SPET Images

Images shown are SPET and CT transverse slices of two patients showing upper abdomen and highlighting the difference in distribution across the liver. The top row images demonstrate a liver with uniform distribution on the SPET (image on the left) and the corresponding CT (image on the right). The bottom row images demonstrate a liver with non-uniform distribution on the SPET (image on the left) and the corresponding CT (image on the right).

The top row in **Figure 63** demonstrates uptake that was uniformly distributed across the liver whilst the bottom row demonstrates how disease processes could affect the distribution of uptake across an organ. Review of the diseased liver in isolation of the CT may have resulted in a poorer score being assigned. A copy of the score sheet issued can be found in **Appendix C** -.

In addition to image quality, the reproducibility of each observer was also assessed. This was achieved by incorporating 10 duplicate images. These were also anonymised and included in the randomisation.

4.3.2.2 Investigation 2: Semi-Quantitative Assessment

Of the 32 patients detailed in **Table 39** 27 were selected at random for profile analysis. The object of the profile analysis was to determine if differences between the reconstruction techniques could be identified in terms of image resolution or count distribution.

Profile analysis was undertaken using the Multi-Modality Display protocol on the Hermes System. This protocol allowed the three registered SPET volumes to be displayed interchangeably allowing two studies to be displayed at any one time with the option of interchanging the second with the third and vice versa when required. This allowed profiles defined on the first volume to be superimposed onto the same pixel y-position on the other 2 volumes.

Horizontal and vertical profiles were applied to the transverse slice where an organ was demonstrated, **Figure 64** shows an example of a horizontal profile applied through the liver and spleen. A profile width of 5 pixels was selected for use in all analysis performed. Pixel count information along the profiles was saved and imported into Excel to allow comparison of the distribution of counts across the profiles between the reconstruction techniques.

The profile analysis allowed characteristics of the distribution of tracer through each organ, for example the liver and kidneys (when seen), to be compared as shown in **Figure 64**.

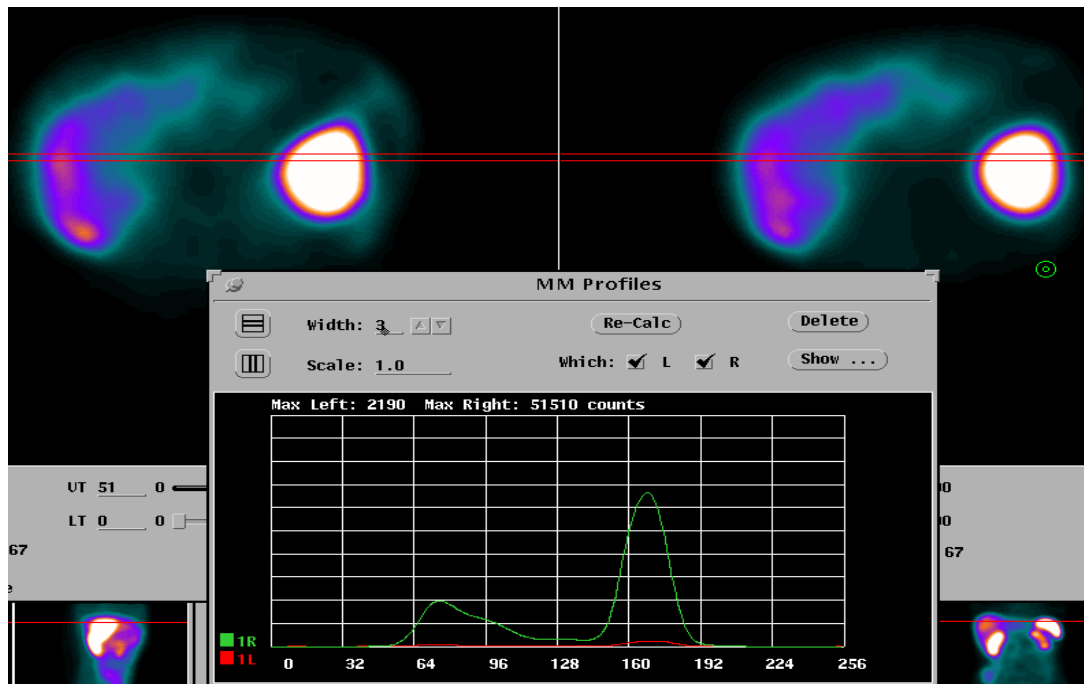


Figure 64 - OSEM Versus Flash 3D SAC

Image shown are of a screen capture from the Hermes system demonstrating profile analysis. The transverse slice on the left is from a volume reconstructed with OSEM and the volume on the right is reconstructed with Flash 3D SAC. The box placed centrally illustrates the profiles obtained through the liver and spleen; the green profile is from the Flash 3D with SAC and the red profile hidden along the x-axis is from the OSEM reconstruction.

From the horizontal profile analysis the first significant feature was the increase in counts demonstrated in the Flash 3D SAC volume, as shown in **Figure 64** (the green distribution in counts represents the F3D and the red the O2D). In the slice shown, the counts from the Flash 3D SAC reconstruction are approximately 20 times that of the OSEM reconstruction therefore the characteristics of the OSEM profile are hidden along the x-axis. To allow a comparison of the characteristics of each profile the data for each reconstruction were normalised to its own maximum counts.

Since the Hermes terminal was dual screen, one of the registered SPET and CT could be displayed using the Multi-Modality Display protocol on a second screen. This allowed a slice by slice profile comparison of the SPET studies with the CT, see **Figure 65**.

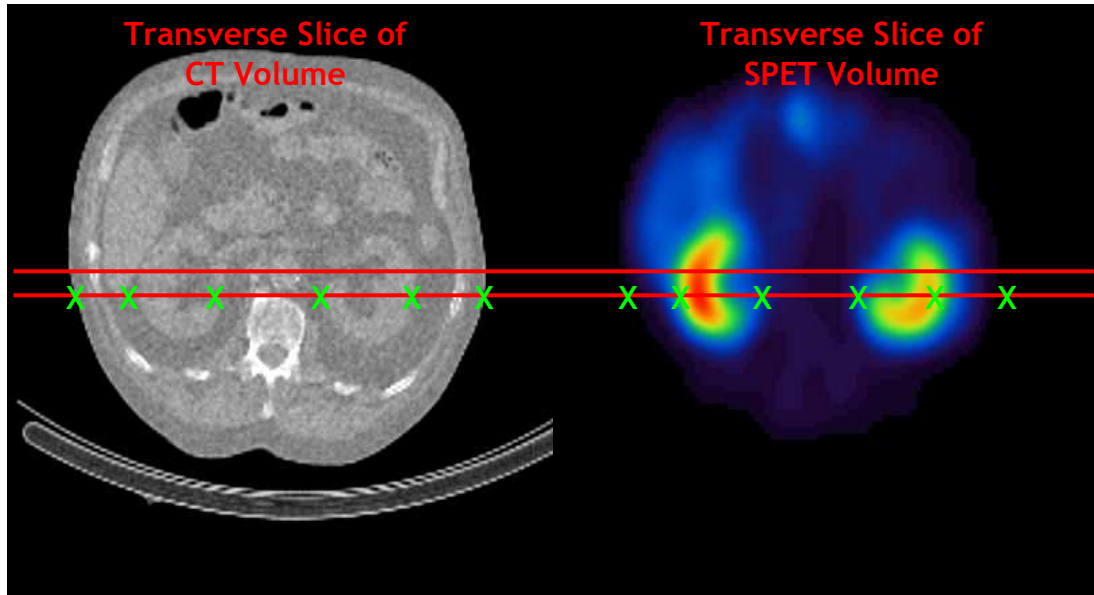


Figure 65 - CT Boundary Delineation

Images shown are transverse CT (on the left) and SPET (on the right) slices which contain the kidneys. The red lines illustrate the placement of the profile for analysis and the green crosses indicate the markers used to delineate the CT and SPET organ boundaries.

The use of the CT image allowed a measure of the true patient and organ boundary to be compared with that defined in the SPET image. Using the CT image the boundaries of the organs and or abnormalities were marked along the profile length (shown by green crosshairs in **Figure 65**). The corresponding organ edge on the SPET volume was identified and marked.

4.3.3 Results - Corrected Versus Uncorrected

Of the 32 patients 15 were females and 17 were males. The average age of this group was 60 years (38 - 84 years).

OctreoScan #	Age	Activity Administered (MBq)	Scan Outcome
Oct Pat 1	80	156	Negative Study
Oct Pat 2	53	200	Positive Study (Liver and Pancreas)
Oct Pat 3	67	220	Negative Study
Oct Pat 4	71	185	Negative Study
Oct Pat 5	44	200	Positive Study (Lymph nodes)
Oct Pat 6	84	200	Negative Study
Oct Pat 7	65	152	Positive Study (mass pancreas)
Oct Pat 8	58	181	Negative Study
Oct Pat 9	44	200	Negative Study
Oct Pat 10	83	120	Negative Study
Oct Pat 11	83	199	Negative Study
Oct Pat 12	77	199	Negative Study
Oct Pat 13	64	212	Negative Study
Oct Pat 14	63	217	Positive Study (2 nd part of duodenum)
Oct Pat 15	77	200	Negative Study
Oct Pat 16	41	197	Negative Study
Oct Pat 17	64	200	Positive Study (mass pancreas)
Oct Pat 18	62	182	Negative Study
Oct Pat 19	51	220	Negative Study
Oct Pat 20	74	214	Positive Study (mesenteric nodule)
Oct Pat 21	53	208	Positive Study (mass pancreas)
Oct Pat 22	61	202	Positive Study (Rt femur and greater trochanter)
Oct Pat 23	40	154	Negative Study
Oct Pat 24	38	218	Positive Study (Mesenteric mass)
Oct Pat 25	60	217	Positive Study (Liver)
Oct Pat 26	56	155	Positive Study (gastric fundas)
Oct Pat 27	41	191	Negative Study
Oct Pat 28	49	201	Positive Study (ascending, transverse & descending colon)
Oct Pat 29	57	121	Positive Study (mass pancreas)
Oct Pat 30	69	157	Positive Study (mass pancreas)
Oct Pat 31	65	200	Negative Study
Oct Pat 32	39	196	Negative Study

Table 40 - Scan versus Disease Outcome

Mean activity administered 186MBq +/- 40. Of the 32 patients, 27 patients generated 3 reconstructed volumes for review with CT, whilst 5 patients had 2 SPET-CT volumes acquired and in these instances both volumes were reconstructed with each technique outlined in **Section 4.3.2**. A total of 111 volumes were created for assessment. Added to this the 10 duplicate volumes used to assess observer reproducibility and there was a total of 121 REG SPET-CT's which were assessed.

4.3.3.1 Investigation 1: Qualitative Assessment Results

The scores assigned by each observer for each patient and volume were grouped by reconstruction type and the total score for each reconstruction technique was calculated. This total was then normalised to the 'maximum total' for the set to allow ease of score comparison between observers. Details of the total score observed for the 'Entire Volume' are given in **Table 41** and illustrated in **Figure 66** for all observers.

	Entire Volume Score (Including duplicates)		
	O2D	F3D	F3D SAC
Observer 1	0.92	1.00	0.96
Observer 2	0.74	0.96	1.00
Observer 3	0.73	0.93	1.00
Observer 4	0.39	0.88	1.00

Table 41 - Entire Volume Reconstruction Technique Score

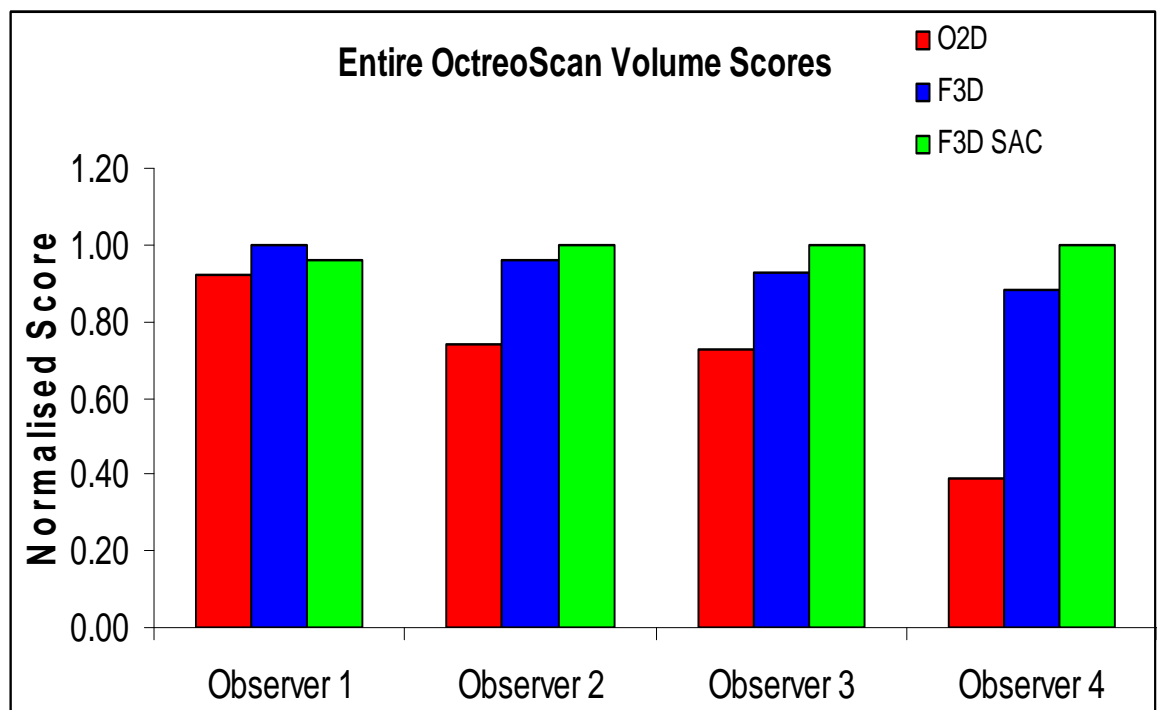


Figure 66 - Graph of Entire OctreoScan Volume Observer Score
Bar chart showing the scores allocated by each observer for each reconstruction technique. The red bars indicate the scores given for the OSEM reconstruction, the blue bars for the Flash 3D with no corrections and the green bars for Flash 3D with corrections.

From the results, it can be seen that 3 out of the 4 observers allocated the F3D SAC the largest score, second to this was F3D and lastly all 4 observers allocated

the O2D the lowest score. To assess more closely for statistically significant differences between the scores allocated to each reconstruction technique for each observer the un-normalised data was used and a Friedman test was performed, see **Table 42** for the results.

	Entire OctreoScan Volume Score (Including duplicates)						
	P-Score	O2D		F3D		F3D SAC	
		Est. Median	Sum of Ranks	Est. Median	Sum of Ranks	Est. Median	Sum of Ranks
Observer 1	0.374	3.00	90.0	3.00	103.5	3.00	94.5
Observer 2	0.000	2.17	65.6	3.00	105.0	3.08	117.5
Observer 3	0.003	3.00	78.0	4.00	98.5	4.00	111.5
Observer 4	0.00	1.00	58.0	3.00	107.0	3.00	122.5

Table 42 - 'Entire' Volume Friedman Test Results

For the entire volume set of data only one of the four observers failed to provide scores that were statistically significantly different between reconstruction techniques. Of the remaining three observers, all three allocated scores which ranked the 'O2D' reconstruction with the lowest score and ranked 'F3D SAC' as the reconstruction with the highest score.

The 'Lung Volume' scores for all observers are given in **Table 43** and results illustrated in **Figure 67**.

	Lung Volume Score (Including duplicates)		
	O2D	F3D	F3D SAC
Observer 1	0.74	0.92	1.00
Observer 2	0.87	0.90	1.00
Observer 3	0.78	1.00	0.99
Observer 4	0.41	0.84	1.00

Table 43 - Lung Volume Reconstruction Technique Score

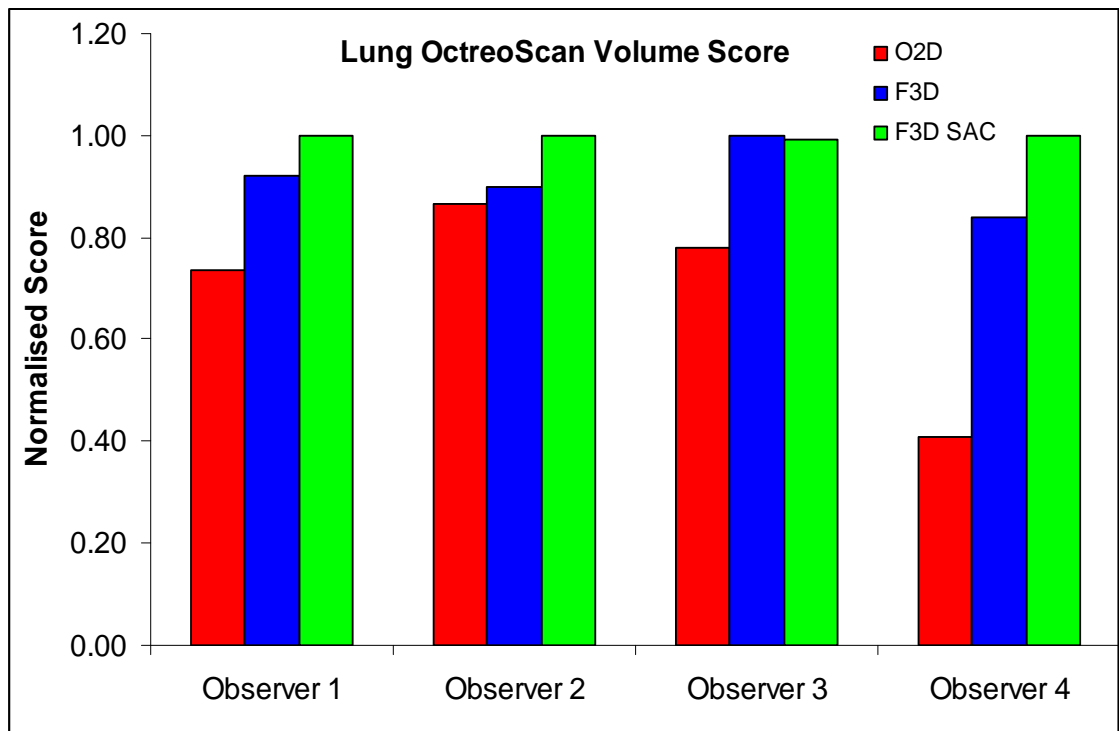


Figure 67 - Graph of Lung OctreoScan Volume Observer Score
Bar chart showing the scores allocated by each observer for each reconstruction technique over the lung fields. The red bars indicate the scores given for the OSEM reconstruction, the blue bars for the Flash 3D with no corrections and the green bars for Flash 3D with corrections.

As with the 'Entire' volume the results demonstrated that 3 out of the 4 observers allocated the F3D SAC the largest score, second to this was F3D and lastly all 4 observers allocated the O2D the lowest score. To assess for statistically significant differences between the scores allocated to each reconstruction technique a Friedman test was performed, see Table 44 for the results.

	Lung OctreoScan Volume Score (Including duplicates)						
	P-Score	O2D		F3D		F3D SAC	
		Est. Median	Sum of Ranks	Est. Median	Sum of Ranks	Est. Median	Sum of Ranks
Observer 1	0.206	1.33	73.5	1.67	83.0	2.00	89.5
Observer 2	0.866	2.00	62.5	2.00	67.0	3.00	67.5
Observer 3	0.021	3.00	67.5	4.00	88.0	4.00	90.0
Observer 4	0.00	1.00	47.0	3.00	72.0	3.00	81.5

Table 44 - 'Lung' Volume Friedman Test Results

For the lung volume set of data two of the four observers failed to provide scores that were statistically significantly different between reconstruction techniques (p-score greater than 0.05). Of the two observers who identified

statistically significant differences between the scores, they ranked the 'O2D' reconstruction with the lowest score and ranked 'F3D SAC' as the reconstruction with the highest score. Reproducibility between observers was also assessed. Individual observer score can be found **Appendix D** - Reproducibility results for each observer. A Wilcoxon Signed Ranks test was undertaken to assess for differences between the scores allocated, see **Table 45** and **Table 46** for the results.

	Entire Volume Score					
	O2D		F3D		F3D SAC	
	P-Score	Est. Median & 95 % CI	P-Score	Est. Median & 95% CI	P-Score	Est. Median & 95% CI
Observer 1	1.000	0.00 (-1.00, 0.50)	0.181	0.00 (0.00, 1.00)	0.108	0.50 (0.00, 1.00)
Observer 2	0.933	0.00 (-0.50, 0.50)	0.225	0.25 (0.00, 0.50)	0.602	0.00 (-0.50, 0.25)
Observer 3	0.107	-1.00 (-2.20, 0.00)	0.953	0.00 (-1.00, 1.00)	0.870	0.00 (-1.00, 1.00)
Observer 4	0.181	0.00, (-1.00, 0.00)	0.675	0.00, (-1.00, 0.50)	0.154	0.00, (-1.00,1.00)

Table 45 - 'Entire' Volume Wilcoxon Signed Ranks Test Results

	Entire Volume Score					
	O2D		F3D		F3D SAC	
	P-Score	Est. Median & 95 % CI	P-Score	Est. Median & 95% CI	P-Score	Est. Median & 95% CI
Observer 1	0.402	-0.5 (-2.00, 0.50)	0.499	-0.50 (-3.00, 1.00)	0.353	-0.5, (-2.00, 1.00)
Observer 2	0.059	0.50 (0.00, 0.76)	0.371	0.00 (0.00, 0.500)	1.000	0.00 (-0.25, 0.25)
Observer 3	0.401	-0.50 (-1.00, 1.00)	0.612	0.00 (-1.00, 1.50)	0.050	1.00 (0.00, 1.50)
Observer 4	1.00	0.00 (0.00, 0.50)	0.100	1.0 (0.00, 2.00)	1.00	0.00 (0.00, 1.00)

Table 46 - 'Lung' Volume Wilcoxon Signed Ranks Test

The Wilcoxon Signed Rank Test was undertaken to test that the median was not equal to zero. All the p-scores calculated in **Table 45** and **Table 46** were greater than 0.05 therefore reproducibility for each observer and technique was demonstrated.

4.3.3.2 Investigation 2: Semi-Quantitative Analysis Results

Profiles were created over solid organs present in the FoV which included the liver, spleen, kidneys. These profiles helped to determine which reconstruction method resulted in images where the distribution of radiopharmaceutical uptake within an organ (in the absence of known disease) was more uniform as would be expected. **Figure 68** is an example of the expected distribution of uptake within the liver. The reconstruction technique shown in this example is flash3d with attenuation and scatter correction.

The patient's CT was reviewed to determine which dimension of the patient would have the greatest impact on attenuation, that is, the width or depth of the patient. The width being the greatest factor would indicate the use of a horizontal profile, whilst the depth would indicate the use of a vertical profile. Profiles were drawn as shown in **Figure 68**, which demonstrates how the distribution of uptake within the liver could be assessed.

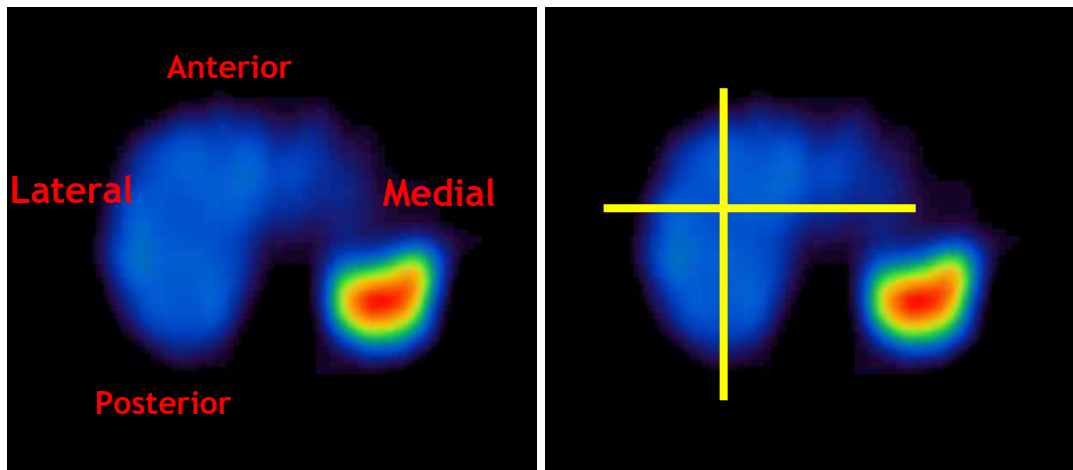


Figure 68 - SPET Liver (Flash3D SAC) with profiles

Images shown are of a transverse slice through the liver. These images were reconstructed with Flash 3D with SAC. The image on the left contains labels used to describe the orientation of the patient orientation. The yellow lines on the right show the position of the horizontal (horizontal line) and vertical (vertical line) profiles in relation to the labelled annotation.

The examples of relevant profiles are shown in **Figure 69** and **Figure 70**.

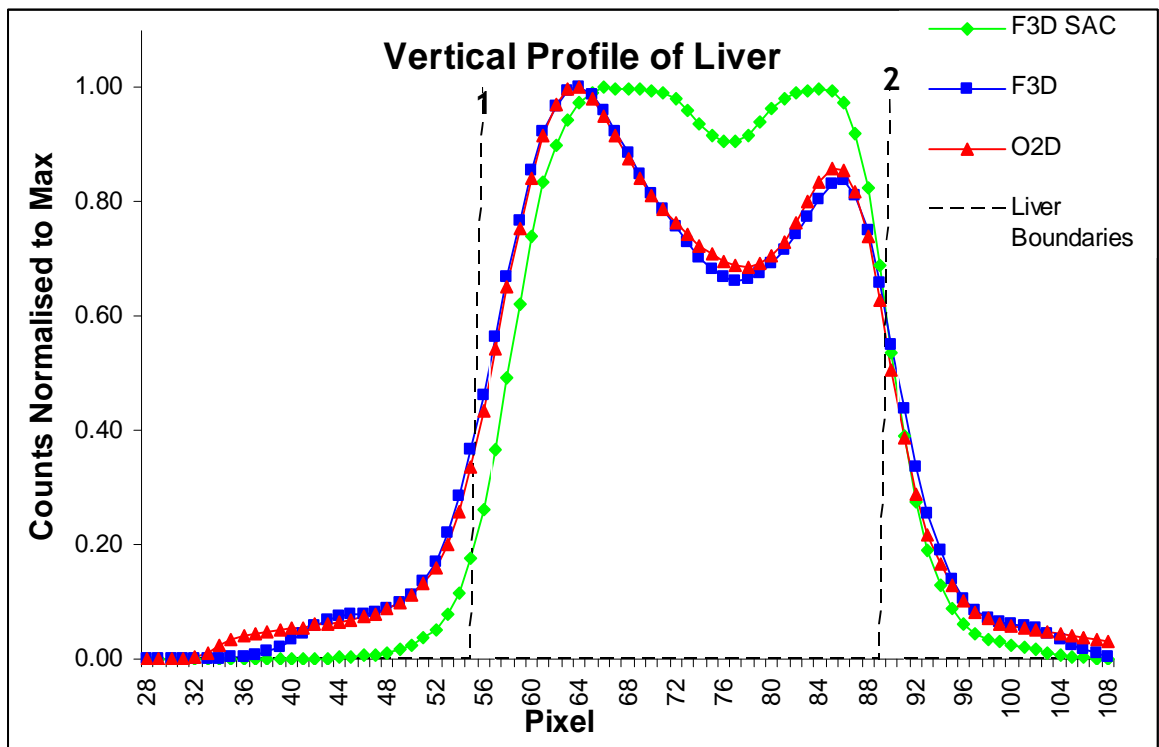


Figure 69 - Liver Vertical profile

Image shown is a plot of the pixel data obtained from vertical line profiles placed through the transaxial liver slice for each reconstruction technique. The dashed vertical lines are used to highlight the anatomical boundaries of the liver as defined by the CT.

Figure 69 shows the results of a vertical profile placed through a cross section of a patient's liver (transverse slice). The dashed vertical lines show the delineation of the patient's liver boundaries taken from the CT image. Line 1 corresponds to the posterior edge of the liver and line 2 is the anterior edge of the liver.

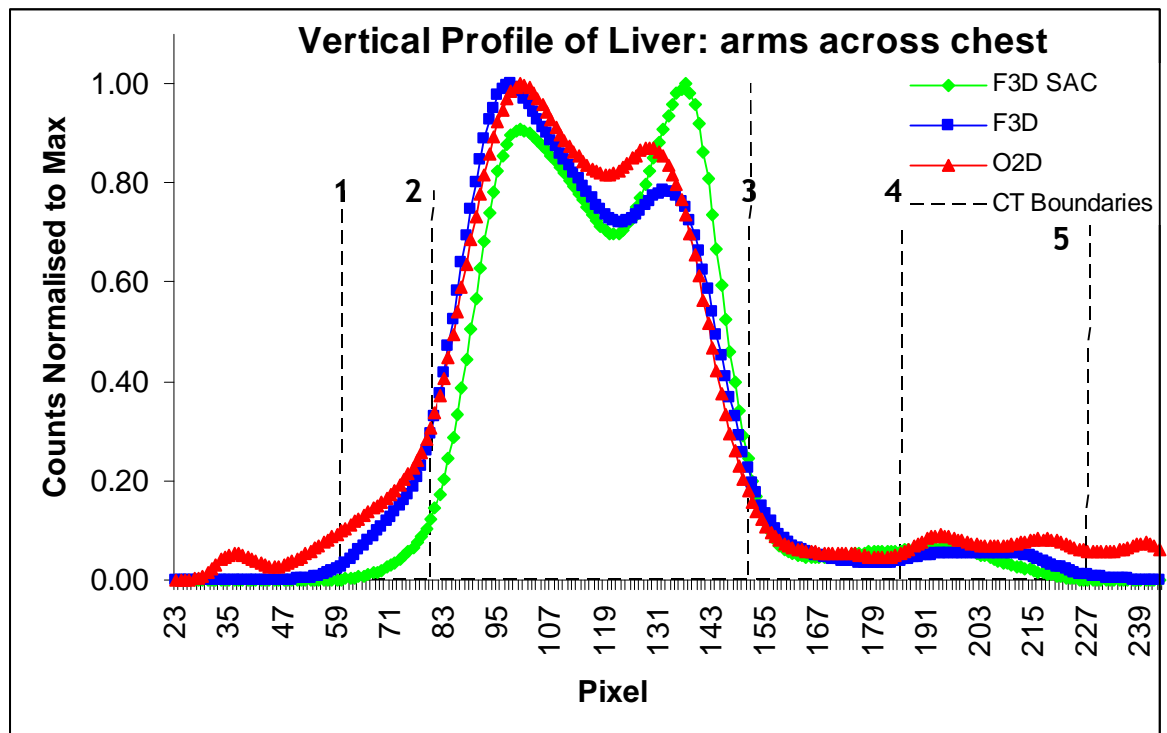


Figure 70 –Liver Vertical profile; patient arms across chest
Image shown is a plot of the pixel data obtained from vertical line profiles placed through the transverse liver slice for each reconstruction technique. The dashed vertical lines are used to highlight the anatomical boundaries of the various organs as defined by the CT.

Figure 70 shows the results of a vertical profile placed through a cross section of another patient's liver (transverse slice) where the patient had their arms placed over their chest in addition to the breast tissue in the FoV, as shown in **Figure 71**. The dashed vertical lines show the delineation of the patient's liver boundaries. Line 1 corresponds to the posterior edge of the patient, line 2 is the posterior edge of the liver, line 3 is anterior edge of liver, line 4 is the anterior edge of patient and finally line 5 is the anterior edge of the arms.

F3D and O2D profiles both demonstrate a rise in the counts at the posterior edge of the liver (line 2), followed by a dip a slight rise in counts at the anterior edge of liver (line 3). The F3D SAC, however, demonstrated almost equal rises in counts at both the posterior and anterior edge of liver. The reduction counts seen in the F3D and O2D reconstructions is clearly a direct result of the uncorrected attenuation cause by the arms being placed over the chest in addition to breast attenuation.

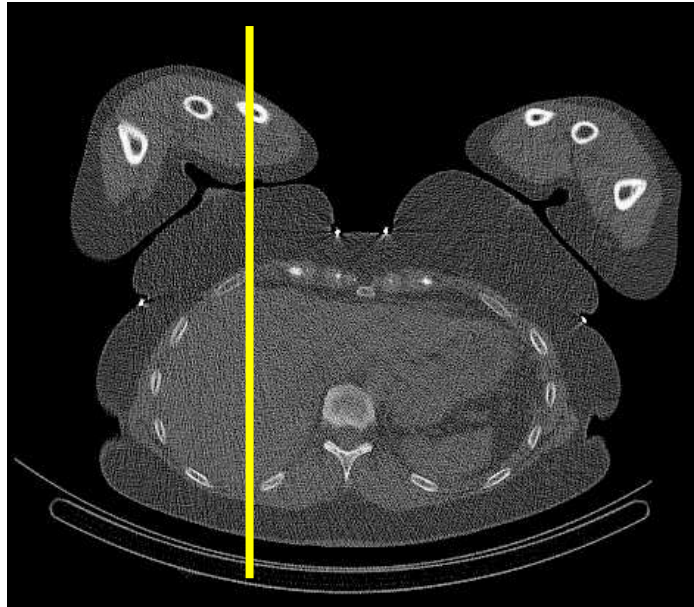


Figure 71 - CT of Liver Vertical Profile

Image shown is a CT transverse slice of a patient who had their arms placed over their chest during the SPET and CT acquisition. The yellow line is used to highlight the placement of the line profile which produced the plot shown in Figure 70.

Both examples of profiles demonstrate clear evidence that the profile across a solid organ (in this case the liver) is more uniform when using the F3D SAC reconstruction. Neither patient showed any definite evidence of liver disease on the CT therefore the expected profile would be relatively flat with the anterior and posterior edges of the liver being similar in counts. The solid organ profile results suggest the fully corrected reconstruction algorithm to be closer to the expected distribution than those from the other reconstructions.

One of the major difficulties with the NEOSPECT images in Chapter 2 was the significant apparent uptake within the lung volumes as a result of both physiological uptake and the effects of scatter and attenuation within the patient. This non-specific uptake hampered accurate quantification of tumour uptake as the background lung uptake was relatively high. Profile analysis was also performed over the lungs (when present in the volume) for all three reconstructions types. The profile analysis from the lung data was quite striking, an example of which is shown in **Figure 72**.

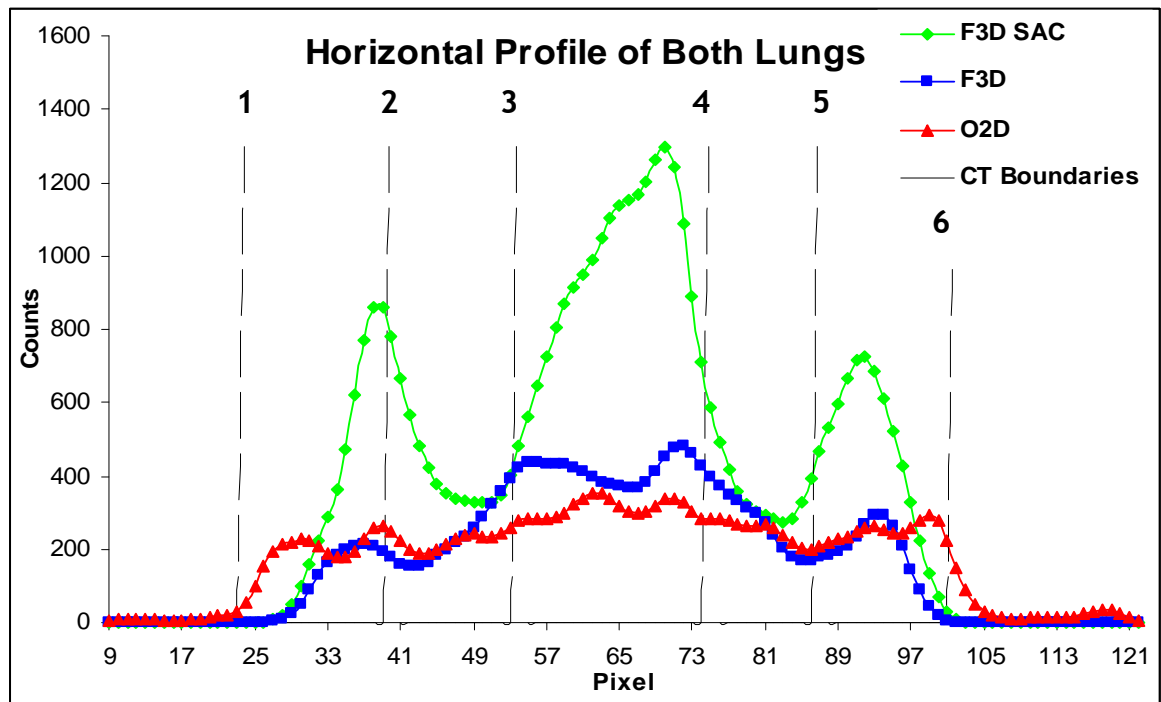


Figure 72 - Graph of Lung profiles

Image shown is a plot of the pixel data obtained from horizontal line profiles placed through the transaxial thorax slice for each reconstruction technique. The dashed vertical lines are used to highlight the anatomical boundaries of the various organs as defined by the CT.

Figure 72 are the results of a horizontal profile placed through a cross section of a patient's thorax (transverse slice). The dashed vertical lines show the delineation of the patient as determined by the CT image. Line 1 corresponds to the edge of the patient (right side), line 2 is the lateral edge of the right lung, line 3 the medial edge of the right lung, line 4 the medial edge of the left lung, line 5 the lateral edge of the left lung and finally line 6 the edge of the patient (left side).

Figure 72 clearly demonstrates differences in the reconstruction techniques. As can be seen, the OSEM reconstruction produces a fairly flat profile indicating very little difference in the distribution of counts across the thorax and subsequent lung. This is very similar to the images seen with NeoSPECT. Whilst both the F3D and F3D SAC reconstructions demonstrate a non-uniform distribution in the counts across the thorax, a dip in the number of counts over the lung volume and a corresponding rise over the cardiac cavity is present in both cases, with the F3D SAC reconstruction providing a more pronounced distribution relative to the F3D reconstruction.

Corresponding images are shown in **Figure 73** to highlight this issue. The middle row of images in **Figure 73** shows lung with the OSEM reconstruction showing that the lung areas contain a significant amount of non-specific physiological radiopharmaceutical uptake.

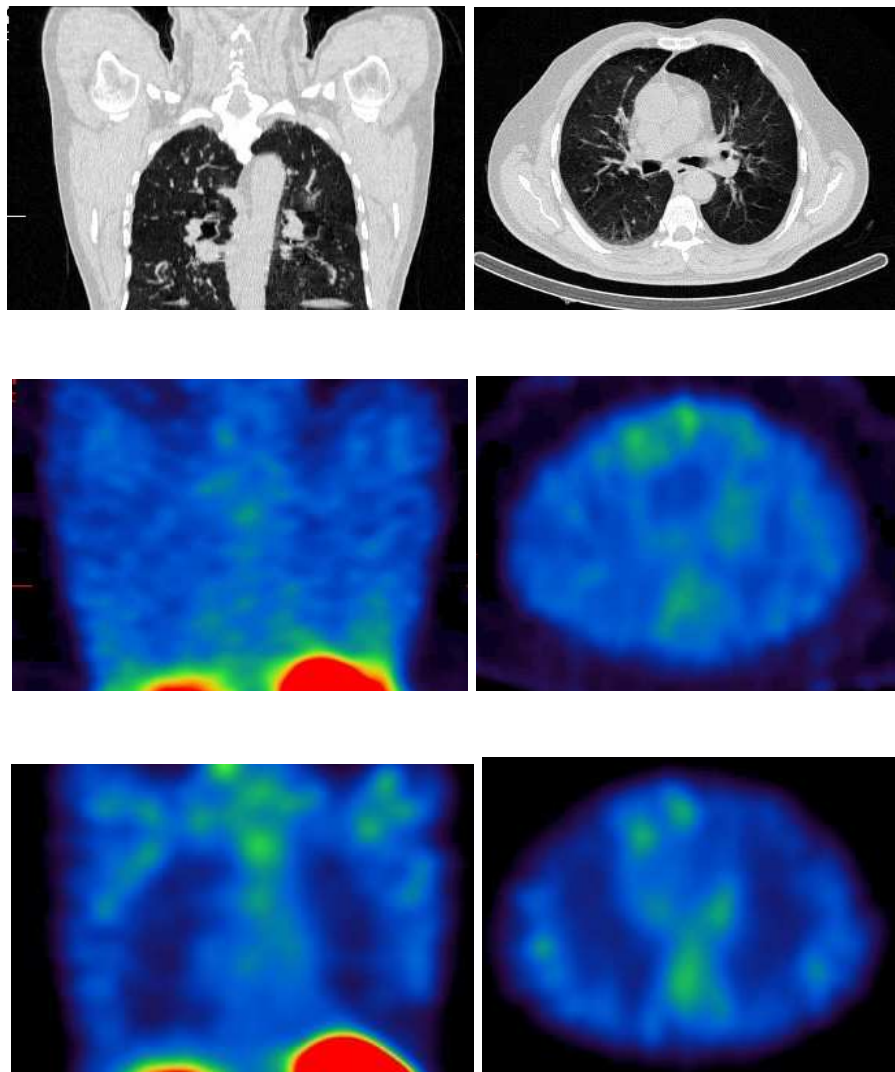


Figure 73 - SPET-CT Lung (CT, OSEM & F3D SAC).

Images showing coronal (on the left) and transverse (on the right) slices through the thorax of an OctreoScan patient. CT images appears on the top row whilst the middles and bottom row are the corresponding SPET data reconstructed with OSEM and Flash 3D SAC respectively.

Whilst the lower row in **Figure 73** shows lung with Flash 3D with both attenuation and scatter corrections. The F3D SAC clearly demonstrates a lack of non-specific physiological uptake of pharmaceutical within the lungs in keeping with the profile analysis.

The example profile analysis included in this section correlates with the findings from the qualitative analysis. That is, a marked improvement in image quality is demonstrated with the use of F3D in comparison with OSEM. In particular the additional use of attenuation and scatter correction with F3D produces a significant improvement in the quality of images which include the lungs in the FoV.

4.3.4 Discussion and Conclusion

The qualitative results demonstrated a clear trend in observer preference, in terms of image quality, as the F3D SAC reconstruction was scored the highest by 3 out of 4 observers, followed by the F3D and lastly the O2D. Despite this preference, statistically differences in scores were only significant between O2D and F3D, and O2D and F3D SAC. No significant statistical difference in the scores was demonstrated between F3D and F3D SAC.

Again when the lungs were scored in isolation of the remaining volume there was also a clear trend in preferences for 3 out of the 4 observers towards the F3D SAC, followed by the F3D and lastly the O2D. Statistically, however, the difference in scores between reconstruction techniques was only considered significant for 2 out of the 4 observer's scores.

Semi-quantitative profile analysis of solid organs demonstrated a significant improvement in image quality with the use of F3D SAC reconstruction. A clear differentiation between O2D and F3D SAC, and F3D and F3D SAC was demonstrated. Profiles through solid organs like the liver using F3D SAC demonstrated a more uniform distribution in uptake when compared with O2D and F3D.

The most striking improvement in image quality was demonstrated when the lungs were included in the FoV. Profile analysis of the lungs demonstrated F3D and F3D SAC to clearly delineate between lung and surrounding tissue within the body, whereas O2D produced a fairly flat profile across the thorax regardless of tissue type. Of the F3D and F3D SAC reconstructions, F3D SAC produced images and profiles which delineated the lung in such a way that in the absence of

disease there was minimal background activity present. This would likely have benefited the NEOSPECT data, as it would have delineated any abnormal tissue within the lung better and in particular allowed better visualization of small nodal disease within the lungs.

4.4 ^{111}In Phantom Acquisition Data

In addition to increasing the ability to localize the anatomical localization of functional abnormalities a great deal an emphasis has also been made on SPET CT's capabilities to correct for soft tissue attenuation. The previous section considered OSEM and Flash3D with and without corrections from an image quality perspective, however, there is a need to assess image reconstruction technique from a quantitative perspective which allows comparison to be made with the previous NeoSPET work.

The in-house built SPET-CT phantom, described in **Chapter 3**, was used in this section to investigate the following:

Investigation 1 Optimise post reconstruction filter setting for Flash 3D.

Investigation 2 Accuracy of hybrid imaging quantification techniques.

4.4.1 Investigation 1 - Optimisation of post reconstruction filter

Nuclear medicine is limited in terms of its resolution. This low resolution can be compounded further by the use of a post reconstruction smoothing filters and this can make the ability to distinguish between true uptake and scatter or extension of areas of increased uptake very difficult. The first use of the in-house built SPET-CT phantom, was to investigate the influence of various post reconstruction filter settings used for OctreoScan imaging. For all iterative reconstructions on the Symbia-T there is only one filter type available namely a Gaussian Filter. This is a low pass filter used to remove high frequency (noise) components from the image data.

4.4.1.1 Methods for Investigation 1 - Optimisation of post reconstruction filter

To establish an optimal setting for the post reconstruction filter the SPET-CT phantom was used, each of the components within the phantom was filled as shown in **Figure 74**.

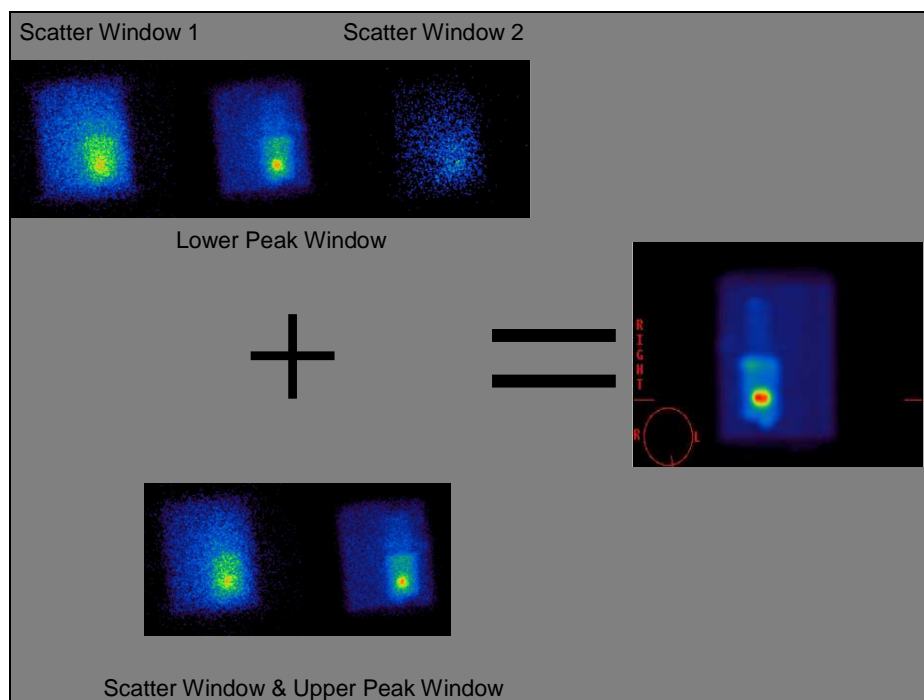


Figure 74 - In111 Filled Phantom

Image showing a screen capture of the various energy windows acquired of the phantom when filled with In111.

The phantom was acquired under the acquisition parameters described in **Table 47**. To minimise the effect of air bubbles gathering over areas of interest the phantom was tilted. The SPET acquisition was followed by a CT acquisition to allow a comparison of the true morphology of the internal structures of the phantom.

Collimator:	MELP
Orbit:	360 degrees
Frame time:	30 seconds
Interval:	3 degrees
Energy Windows (keV):	5 Windows; See Figure 74
Set Up @:	For the purpose of these acquisitions the heads were set round the circumference of the phantom.

Table 47 - OctreoScan Acquisition Parameters

The SPET raw images were reconstructed as described in **Table 48**, as a result there were 7 reconstructed data sets to compare. Using the Symbia software the reconstructed SPET volume was co-registered to the sharp CT volume.

Reconstruction Method:	Siemens OSEM – Ordered Subset Expectation Maximisation
Subsets:	4
Iterations:	8
Number of slices:	82
Low Pass Filter Setting:	Gaussian FWHM of 1.0mm, 3.7mm, 5.5mm, 8.4mm (default settings), 10.25mm, 17mm, 30mm
Zoom:	No Zoom

Table 48 - OctreoScan Reconstruction Parameters

The reconstruction parameters, including post reconstruction filters, were all derived for clinical use. The clinicians and physicists at GRI had originally selected filter settings for FBP prior to the SPET-CT unit installation. When the Symbia-T was installed advice was taken from Siemens as to their recommended parameters. These were compared with previously acquired data in order to maintain clinical reporting capability and the routinely used parameters were set using the remit of maintaining a consistent image quality as best possible.

Both the registered SPET and CT volume were simultaneously viewed on the Hermes system using the Multi-Modality function for display which allowed the SPET and CT volume to be displayed side by side along with allowing the SPET volume to be superimposed onto the CT volume and vice versa (image fusion).

To aid identification of the inside cavity of the tumour volume both images were manipulated in the transverse plane to identify the section of phantom of interest. The images were reoriented to correct for the off centre placement of the phantom on the bed (because the phantom was tilted to avoid air bubbles around the area of interest), and finally zoomed as described in **Table 49**:

Zoom		Reorientation		Pan	
X	150	XY	-15	X	0
XY	100	YZ	0	Y	-32
Y	150	XZ	2	Z	0

Table 49 - Optimised Display Parameters

Visualisation of the inside boundaries of the tumour cavity was achieved by adjusting the truncation of the CT image as there was little contrast between Perspex and the inside of the tumour cavity which was filled with the water.

To assess the influence each filter setting had on the overall spatial resolution of the SPET volume, ROI analysis was undertaken. ROIs were drawn on the transverse plane of the Sharp Registered CT images, ROI 1 (in red) is the ROI defined by the CT and ROI 2 (in yellow) is the ROI defined by the area of radioactivity on the SPET image- see **Figure 75**.

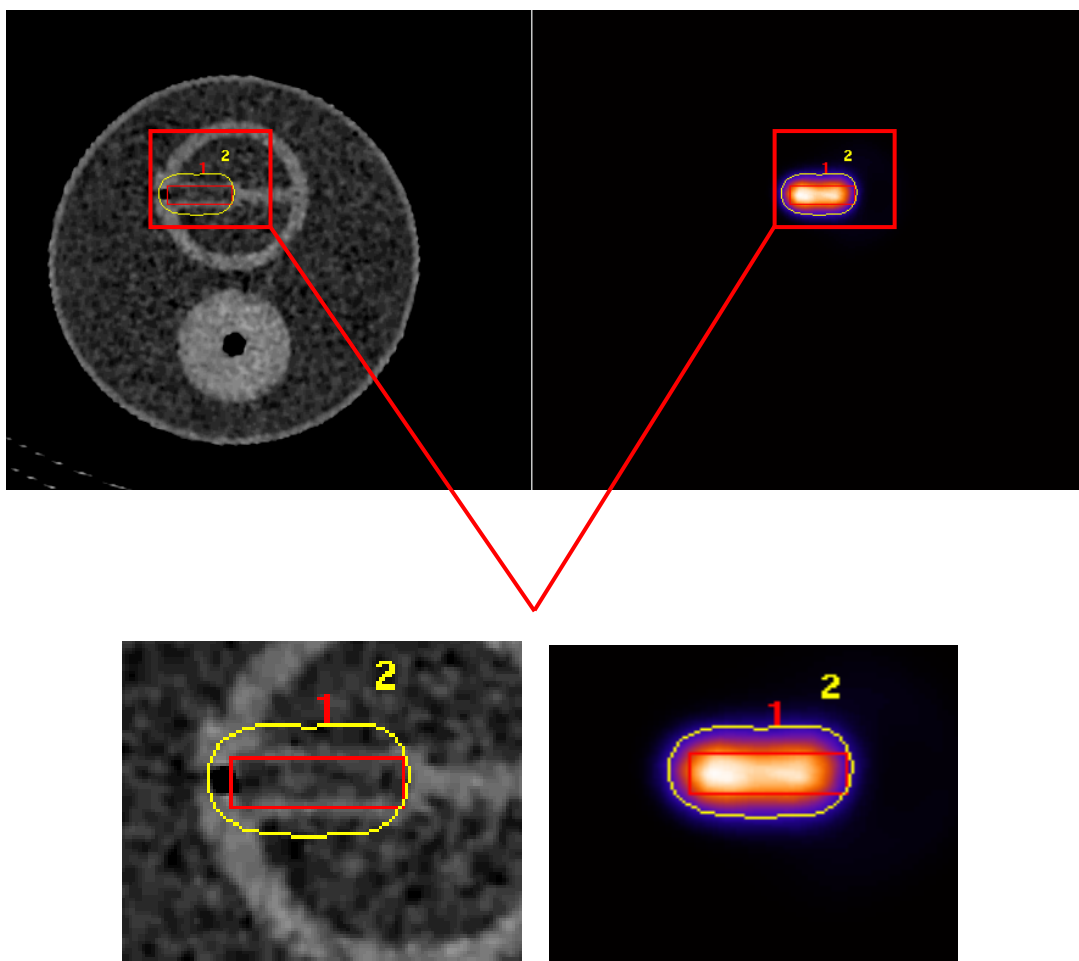


Figure 75 - ROI's defined by structure & radioactive contents
 Images showing transverse slices from the SPET-CT phantom and the associated ROIs drawn. Images on the bottom row are zoomed versions of the upper row to show more clearly the boundaries of the tumour compartment on the CT.

The 'tumour ROI' was drawn on the mid slice of the cavity visualized. For each filter setting the number of slices over which the 'tumour' area was visible was noted but the counts were only recorded and compared for slice 31 of each set as this represented the mid section of the phantom's tumour cavity.

The influence of the range of filter settings investigated are described in **Table 50**.

Low Pass type	Setting FWHM (mm)	Range CT	Range NM	REG ROI OK?
Gaussian	1.0	63-69	59-72	Y
Gaussian	3.7	63-69	59-72	Y
Gaussian	5.5	63-69	59-72	Y
Gaussian	8.4	63-69	59-72	Ref ROI
Gaussian	10.25	63-69	58-73	Y
Gaussian	17	63-69	57-74	N
Gaussian	30	63-69	57-74	N

Table 50 - Settings for In111 filled phantom

For comparison, this measurement was also undertaken using a Tc99m filled phantom, the results of which are detailed in **Table 51**.

Low Pass type	Setting FWHM (mm)	Range CT	Range NM	REG ROI OK?
Gaussian	1.0	24-37	21-44	Y
Gaussian	3.7	24-37	18-77	Y
Gaussian	5.5	24-37	19-44	Y
Gaussian	8.4	24-37	18-46	Ref ROI
Gaussian	10.25	24-37	18-46	Y
Gaussian	17	24-37	14-50	N
Gaussian	30	24-37	7-58	N

Table 51 - Setting for Tc99m filled phantom

Correct filter selection for image reconstruction is paramount as an incorrect filter setting has the potential to create or remove small areas of increased radioisotope uptake. The CT generated ROI was successfully correlated with all reconstructed data sets with the exception of Gaussian settings FWHM 17mm and 30mm. It was noticed that filter settings above FWHM of 10.25mm provided too much smoothing of the data and failed to accurately detect the edge as there was over blurring of the edges and expansion of the volume. This is significant as clinically this may lead to the overestimation of tumour volume especially where small tumour volumes are present. Despite the NM volume correlating with the CT volume on the remaining filter settings there was an increase in the noise component which led to decrease in the image quality. This reduction in image quality was more notable when using the Gaussian settings 1.0 and 3.7.

Summary of work

As with most nuclear medicine studies each individual patient should be assessed on an individual basis and optimized as appropriate, in terms of the order of the

post reconstruction filter used. Despite slight adjustments this work was successful in defining a useful range of filter settings for OctreoScan studies. The range of useful values of Gaussian settings identified was FWHM 5.5mm - 10.25mm. Since the default setting of 8.4mm lay within this range, it was deemed suitable to continue to use the default setting of 8.4mm for phantom reconstructions and therefore made for a more like for like comparison with the actual patient data.

4.4.2 Investigation 2 - Accuracy of hybrid imaging quantification techniques

Over the years there has been great a deal of consideration given to the use of some diagnostic radiopharmaceuticals as tumour-targeted radiation therapy agents. In determining the efficacy of these agents image quantification has been performed using planar diagnostic images. An example of such work which investigated the efficacy of OctreoScan described planar geometric mean methods to quantify uptake (Lener et al, 1996).

However, in recent years nuclear medicine imaging has moved away from planar imaging towards SPET hybrid imaging. In addition to the work undertaken previously quantitating NeoSPECT it was important to assess if SPET-CT could be used to accurately quantify tumour and organ uptake using other radiopharmaceuticals, in this case OctreoScan. This might also allow postulation as to whether the addition of CT data to the NeoSPECT group would have significantly affected accuracy.

Since the work undertaken in the **Section 4.3.3.1** demonstrated that the largest qualitative improvement in image quality between reconstruction techniques lay between OSEM and Flash3D with or without scatter and CT-attenuation corrections, it was decided to only assess differences in image quantification between Siemens Flash3D with and without scatter and CT-attenuation corrections.

4.4.2.1 Methods for Investigation 2 - Accuracy of hybrid imaging quantification techniques

The in-house manufactured phantom for SPET-CT was used in this work to determine the accuracy of the new techniques in image quantification of In-111 acquisitions. The phantom was filled with activities as described in **Table 52**.

Lung Phantom Details		
	Activity (MBq)	Time
Background	29	11.18
Lung	16	10.53
Liver	58	10.46
Tumour	5	10.39
SPET-CT Acquisition Details		
Acquisition Start Time	15.05	
Lung Phantom Details Corrected to Start of SPET-CT Acquisition		
Background	27.9	15.05
Lung	15.3	15.05
Liver	55.5	15.05
Tumour	4.77	15.05

Table 52 - SPET-CT Phantom Activities and Acquisition Times

Figure 76 demonstrates slices of the images acquired.

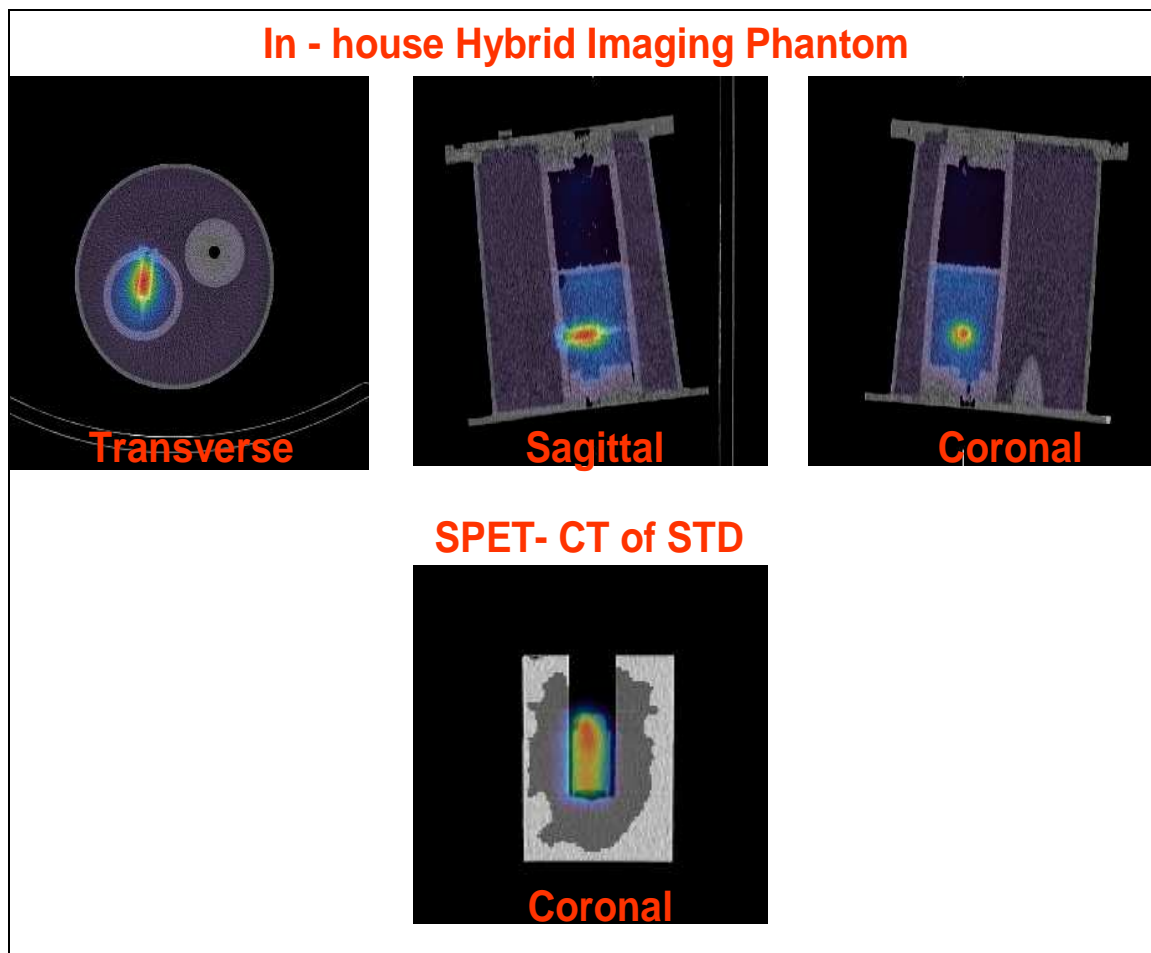


Figure 76 - SPET-CT Acquisition of Hybrid Phantom

Images showing transverse, sagittal and coronal slices of the SPET-CT phantom when filled with In111 on the top row. The bottom row is a fused SPET-CT coronal slice of the standard volume used to calculate sensitivity, also filled with In111.

As can be seen from **Figure 76** a standard acquisition was also acquired, this was acquired using the thyroid phantom which is a solid perspex cylinder with a small aperture for placement of a 5ml vial, refer to **Table 53** for details of activities used.

STD Details		
	Activity (MBq)	Time
STD	5.0	11.18
SPET-CT Acquisition Details		
Acquisition Start Time	15.49	
STD Details Corrected to Start of SPET-CT Acquisition		
STD	4.77	15.49

Table 53 - SPET-CT STD Activities and Acquisition Times

The acquisition protocol for the phantom and the STD were the same as those used for routine patient imaging, as described in **Table 37**, with the exception

of a reduced frame time for the STD acquisition (3 seconds was used as previously in Chapter 2).

Both the SPET-CT phantom and the STD were reconstructed as follows:

1. Siemens Flash 3D, F3D - No corrections.
2. Siemens Flash 3D Corrected, F3D SAC - with scatter and CT-attenuation based corrections.

Regardless of the application of corrections the reconstructions parameters used matched those described in **Table 38**, and are those routinely used for the patient data reconstruction. As in previous chapters, ROI analysis was performed, an example of which is shown in **Figure 77**.

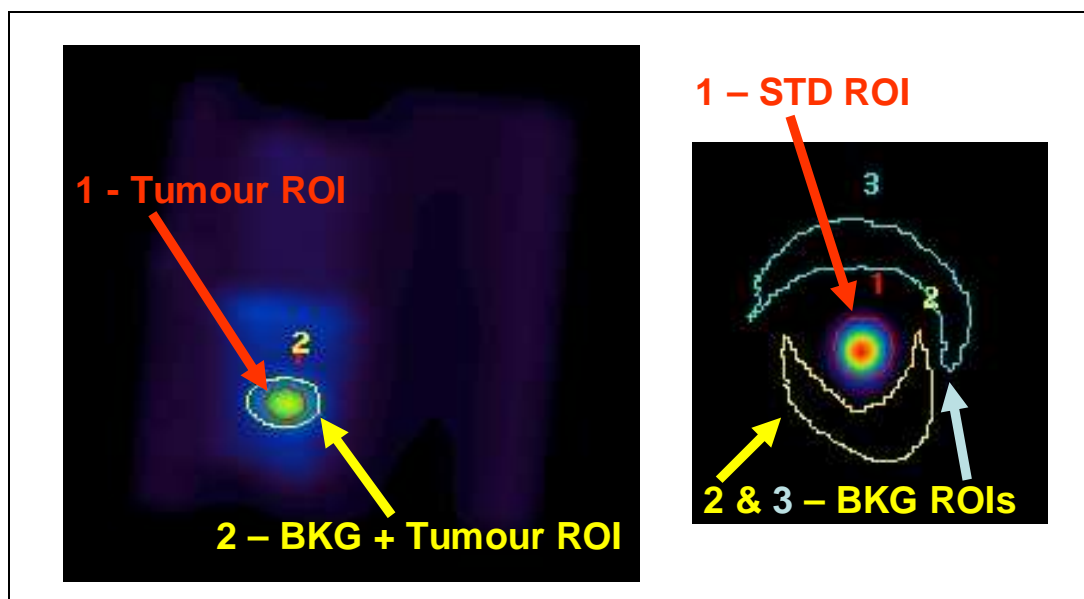


Figure 77 - In-111 SPET-CT ROIs

Images showing the different ROIs used to obtain data from the SPET-CT phantom on the left and the ROIs used to obtain data from the standard volume on the right.

From the ROIs, values of total counts along with the number of pixels (area) were extracted. This information was saved from all slices over which the tumour and STD vial were demonstrated. CT images were used to aid identification of the edges of each.

4.4.2.2 Results for Investigation 2 - Accuracy of hybrid imaging quantification techniques

To calculate absolute activity, a value of sensitivity for each reconstruction technique had to be determined. The sensitivity for each technique was calculated from the STD acquisition using Equation 6 in Chapter 2. Using the ROI data from each reconstruction, a value of total counts was obtained by summing the total counts in each slice over the entire volume of the standard vial. From Table 53 it can be seen that the activity in the standard vial at the time of imaging was 4.77 MBq. Each frame was 3 seconds long with 120 frames acquired in total, therefore, the total duration of the acquisition of was 360 seconds. Using these values the sensitivity (counts per second per MBq) was calculated - see Table 54.

	Symbia	
	No Corrections	Scatter & CT-attenuation Correction
Sensitivity No BKG Correction	5979 cps MBq ⁻¹	8158 cps MBq ⁻¹
Sensitivity BKG Correction	5961 cps MBq ⁻¹	8113 cps MBq ⁻¹

Table 54 - Sensitivities

For this work a different phantom was used for the STD acquisition and it was therefore important to investigate the effect of background correction.

From the ROIs of the SPET-CT phantom, values of counts and number of pixels were extracted. The ‘tumour’ counts were then corrected for background using the technique described by Equation 7 in section 2.3.2.3 of Chapter 2. The background corrected counts for each slice were summed over the entire volume of the ‘tumour’ or vial and are shown in Table 55 along with the uncorrected counts.

	Symbia	
	Phantom No Corrections	Phantom Corrected for Scatter & CT-attenuation Correction
Total Counts	64741349	110221777
Total Counts BKG Cor	49825602	85668873

Table 55 - Total Counts for Each Reconstruction Technique

The values in Table 55 were used along with the values of sensitivity in Table 54 to calculate a value of absolute activity for each reconstruction technique. The results are shown in Table 56.

		Activity	
		Phantom Total Counts (MBq)	Phantom Total Counts BKG Corrected (MBq)
STD & Phantom No A + SC	STD Total Counts	3.01	2.31
	STD Total Counts BKG Corrected	3.02	2.32
STD & Phantom with A + SC	STD Total Counts	3.75	2.92
	STD Total Counts BKG Corrected	3.77	2.93

Table 56 - Activities Calculated

Figure 78 provides a graphical comparison between the actual known activity and those calculated from the various reconstruction techniques.

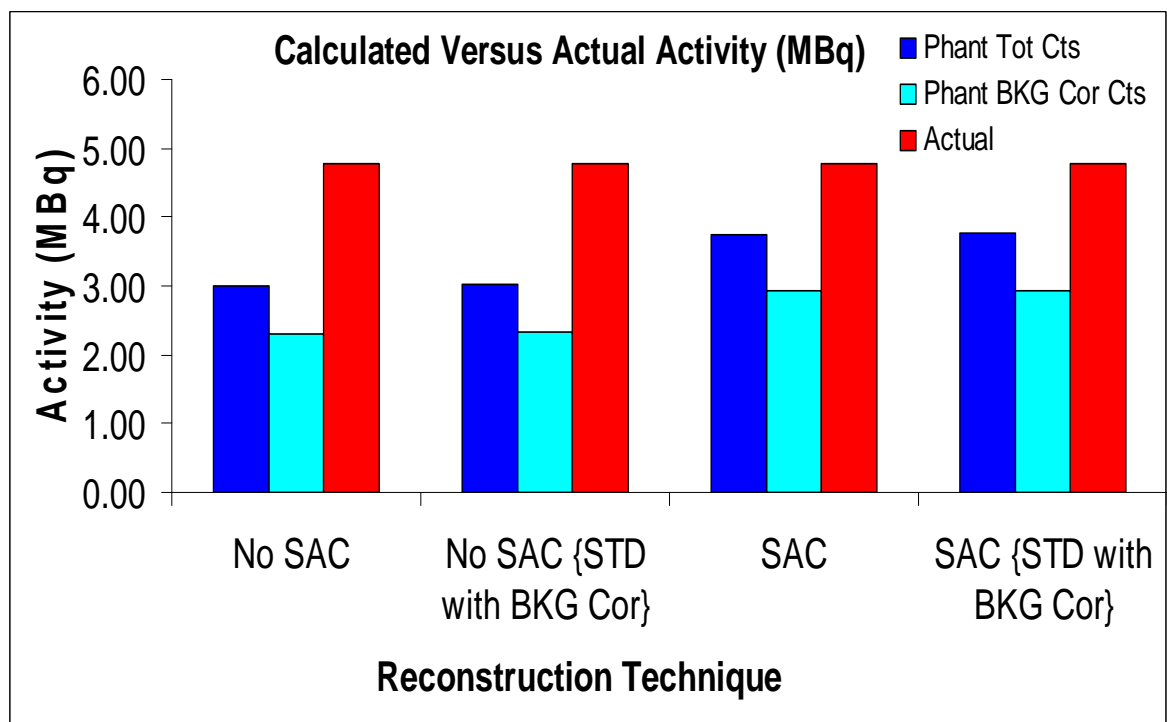


Figure 78 - Graph of Calculated Versus Actual Activity (MBq) In111 SPET-CT phantom Bar chart showing the calculated versus actual activity for each reconstruction technique. The blue bars correspond to values of activity calculated using total counts, the lighter blue bars are of values of activities calculated from background corrected total counts and finally the red bars are of the actual value of activity measured on the radionuclide calibrator.

Table 56 and **Figure 78** demonstrate a difference between the actual and calculated which is dependant upon the reconstruction technique used. The results clearly demonstrate that the use of a background correction on the STD reconstructions made very little difference.

Looking specifically at the results and at the difference between the actual and calculated activity the use of a scatter and CT - attenuation correction (SAC) provide the better estimate of activity. However, when a background correction is applied in conjunction with reconstruction implemented corrections the data significantly underestimated the activity within the volume

This is perhaps to be expected, when the data has been properly corrected for scatter and attenuation, the counts within the volume of interest should be correct and in SPET unlike planar data there is no overlying tissue so in principle no background corrections should be necessary. The data in **Figure 78** shows that where corrections are in place the activity measured is very close to the actual known activity when no background subtraction is employed.

Without proper correction for scatter and attenuation the counts within the volume are likely to be incorrect and there will be increased scatter in surrounding tissue and decreased and non uniform counts within the volume due to attenuation.

Summary of work

The percentage difference calculated between the image derived activity and the actual activity went from 37% for the uncorrected data to 21% for the corrected data, therefore work in this section clearly demonstrated that the addition of scatter and CT-attenuation correction helped improve the accuracy of calculating activity from SPET data using ^{111}In .

4.4.3 Discussion/Conclusion - ^{111}In Phantom Data Acquisition

Investigation of several post reconstruction filters showed a range of Gaussian cut-off values which gave reasonable image quality and definitive limits where image quality became unacceptable.

Assessment of the accuracy of image quantification from ^{111}In based SPET-CT studies demonstrated an underestimation in the value of activity calculated for both the corrected and uncorrected SPET volumes when compared with the

actual value. However, the corrected data did demonstrate a notable improvement in the accuracy of the image quantification.

Comparison to the original phantom work undertaken in Section 2.3.2.3 of Chapter 2 disappointingly failed to demonstrate a large improvement in the accuracy of the calculation of activity from the hybrid data. However, it is worth bearing in mind that a different isotope was used and therefore a direct comparison may not be appropriate as ^{99m}Tc (used in chapter 2) has only one photo peak whilst ^{111}In has two photo peaks.

Whilst quantification using hybrid imaging of ^{111}In based acquisitions may not provide the most accurate measure of activity within a specified volume the technique could be used to monitor disease response fairly accurately when data is reconstructed with F3D SAC.

4.5 ^{99m}Tc Phantom Acquisition Data

Both OctreoScan patient and phantom work indicated a clear improvement in the image quality and accuracy of the calculation of absolute activity when scatter and CT-attenuation corrections were applied. However, since ^{99m}Tc has a single photo peak and In111 has 2 photo peak it may not be appropriate to compare. It was important to validate these results using Tc99m data in order to comment on what impact the new techniques would have had on the NeoSPECT results.

4.5.1 Methods - ^{99m}Tc Phantom Acquisition Corrected Versus Uncorrected

The in-house designed lung phantom involved in the NeoSPECT phantom work in Chapter 2 was used. This phantom was filled with activity as described in Table 57 and acquired using the standard NeoSPECT acquisition protocol as described previously in Chapter 2.

Lung Phantom Details		
	Activity (MBq)	Time
Background	442	12.06
Lung (each lung)	110	11.18
Tumour	1.1	11.57
SPET-CT Acquisition Details		
Acquisition Start Time	18.15	
Lung Phantom Details Corrected to Start of SPET-CT Acquisition		
Background	217	18.15
Lung (each lung)	98	18.15
Tumour	0.53	18.15

Table 57 - Phantom Activities and Acquisition Times

In addition to the lung phantom a STD acquisition was also undertaken, refer to Table 58 for further details.

STD Details		
	Activity (MBq)	Time
STD	5.91	16.49
SPET-CT Acquisition Details		
Acquisition Start Time	16.53	
Lung Phantom Details Corrected to Start of SPET-CT Acquisition		
STD	5.86	16.53

Table 58 - STD Activity and Acquisition Times

As previously noted, one of the largest factors influencing the degradation of NeoSPECT or indeed any SPET imaging is attenuation and scatter as a result of body habitus and the presence and/or extent of breast tissue. The new technique aimed to remove this degradation, however, the phantom was fixed in its size with very little attenuating material which made assessment of these new techniques limited. In an attempt to introduce attenuating material two saline bags were placed over what would be considered as the anterior aspect of the phantom, these are highlighted by red arrows in **Figure 79**. These saline bags therefore could be considered as mimicking a breast component.

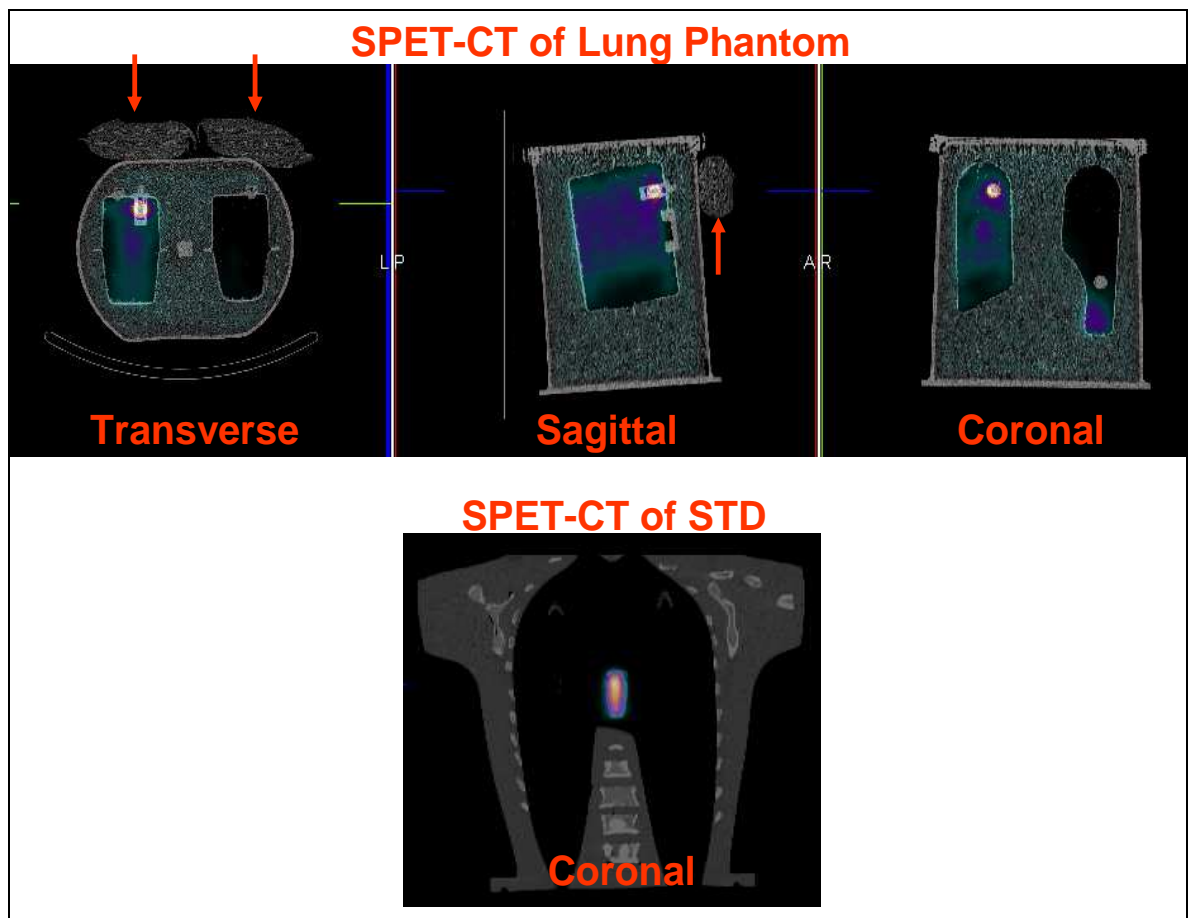


Figure 79 - SPET-CT Acquisition of Lung Phantom and STD
 Images showing fused SPET-CT transverse, sagittal and coronal slices of the lung phantom filled with Tc99m on the top row - red arrows indicate additional attenuating material placed on the phantom to simulate a breast component. The bottom row is a fused SPET-CT coronal slice of the standard volume used to calculate sensitivity, also filled with Tc99m.

To allow a comparison of the new techniques with those used in **Chapter 2**, reconstruction of the lung phantom data was undertaken as follows:

1. NeoSPECT Technique - Hermes OSEM with attenuation correction (HOSEM AC).
2. New Technique - Siemens Flash 3D with scatter and CT-attenuation based corrections (F3D SAC).

Previous results in **Chapter 2** demonstrated that the use of an attenuation correction in the reconstruction of the STD data resulted in a gross overestimation in the calculation of sensitivity and a subsequent underestimation in the value of absolute activity calculated. However, as this was a geometric attenuation correction it was important to assess if a CT-attenuation based correction would provide a more accurate measure of sensitivity from the STD reconstructed images.

The STD data was reconstructed as follows:

1. Hermes OSEM without attenuation correction (STD No Corr).
2. Siemens Flash 3D without scatter and CT-attenuation based corrections (STD No Corr).
3. Siemens Flash 3D with scatter and CT-attenuation based corrections (STD Corr).

As in previous chapters, ROI analysis was performed, an example of which is shown in **Figure 80**.

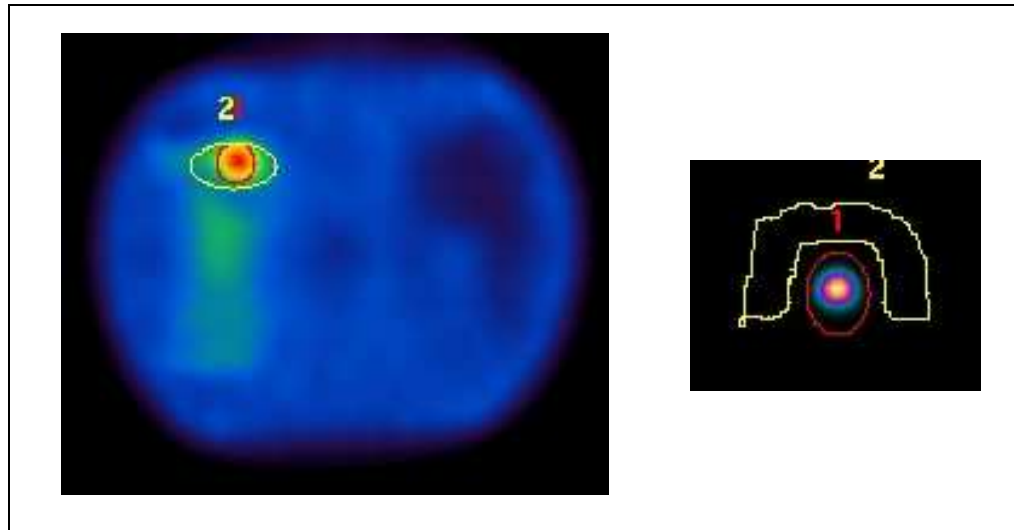


Figure 80 - Lung Phantom and STD ROIs

Images show a transverse slice of the lung phantom with ROI's on the left (ROI 1 - Tumour/abnormality and ROI 2 - Tumour/abnormality with background) and a transverse slice of the standard vial acquisition on the right (ROI 1 - standard vial and ROI 2- background).

To assess the accuracy of image quantification, in other words the value of absolute uptake, values of total counts along with the number of pixels (area) were extracted from the ROIs. Data were obtained from all transverse slices which demonstrated the tumour vial.

4.5.2 Results - ^{99m}Tc Phantom Acquisition Corrected Versus Uncorrected

To calculate absolute activity the first step was to calculate a value of sensitivity for each reconstruction technique. Sensitivity was calculated using **Equation 6** in **Chapter 2**. Values of total counts were obtained by summing the total counts over the entire volume of the standard vial. From **Table 58** it can be seen that the activity in the standard vial at the time of imaging was 5.86 MBq. Each frame was 3 seconds long with 120 frames acquired therefore the total duration of the acquisition of was 360 seconds. Using these values the sensitivity (counts per second per MBq) was calculated - see **Table 59**.

	Hermes	Symbia	
	No Attenuation Correction	No Attenuation Correction	Attenuation Correction
Sensitivity	34 cps MBq ⁻¹	4661 cps MBq ⁻¹	1860 cps MBq ⁻¹

Table 59 - Sensitivities

No background correction was undertaken since, as was demonstrated in **section 2.3.2.3 of Chapter 2** and **section 4.4.2.2** the background activity was essentially negligible relative to the STD volume activity.

Finally, from the ROIs of the lung phantom, values of counts and number of pixels were extracted. The tumour counts were then corrected for background using the technique described by **Equation 7 in section 2.3.2.3 of Chapter 2**. The background corrected counts for each slice were summed over the entire volume of the tumour/vial and are shown in **Table 60** along with the uncorrected counts.

	Hermes	Symbia
	Lung Phantom Corrected for AC	Lung Phantom Corrected for SAC
Total Counts	183421	8911814
Total Counts BKG Cor	108683	5629456

Table 60 - Total Counts and Sensitivity for Each Reconstruction Technique

The values in **Table 60** were used along with the values of sensitivity in **Table 59** to calculate a value of absolute activity for each reconstruction. The Hermes and Symbia results are shown in **Table 61**.

	Hermes	Symbia	
	Lung Phantom Corrected for AC STD NO AC (MBq)	Lung Phantom Corrected for SAC STD No SAC (MBq)	STD SAC (MBq)
Activity - Total Cts	1.51	1.33	0.53
Activity - Total Cts BKG	0.89	0.84	0.34

Table 61 - Activities Calculated

For the Hermes two values of activity were calculated from one reconstructed volume, namely, a value from total counts and from total counts corrected for background. This was also the case for the Symbia phantom volume, however, values of activity were calculated using values of sensitivity calculated from both the corrected and uncorrected standard volume. **Figure 81** provides a comparison between the actual and those calculated using the various techniques.

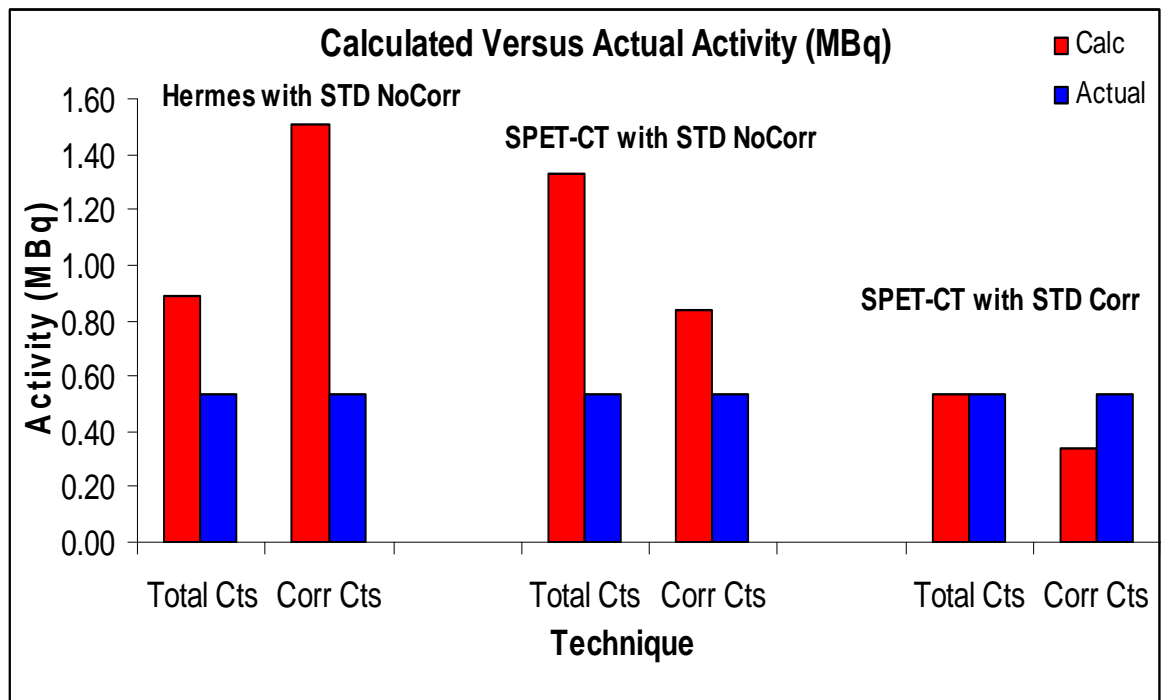


Figure 81 - Graph of Calculated Versus Actual Activity (MBq) Tc99m Lung Phantom
Bar chart showing the calculated versus actual activity for each reconstruction technique. The red bars correspond to values of activity calculated and the blue bars are of the actual value of activity measured on the radionuclide calibrator.

Where, “Total Cts” are the counts within the ROI of the abnormality. “Corr Cts” are the total counts within the ROI abnormality that have been corrected for background.

For both the phantom and STD SPET-CT’s the CT component was used to identify the number of slices over which the abnormality and the standard volume were demonstrated. Only counts from these slices were used in the calculation. From **Figure 81** it can be seen that the use of a scatter and CT-attenuation correction in the reconstruction of the standard volume reduced the difference demonstrated between the value of activity calculated and the actual value.

A negligible difference was demonstrated when the activity was calculated without correcting the phantom abnormality ROI counts for background. This increase in accuracy can therefore be attributed to the ability to identify and delineate the abnormality using CT in addition to the use of scatter and CT-attenuation.

In addition to differences demonstrated quantitatively, it was also important to review the images to determine if qualitative differences were also present. This was achieved by simple slice by slice visual comparison (- see **Figure 82**) and also via profile analysis (- see **Figure 83**).

From the transverse image slice it can be seen that there is a significant difference in the distribution of activity in the lung region. The slices chosen contain additional attenuating material added to the phantom to replicate breast as shown previously in **Figure 79**

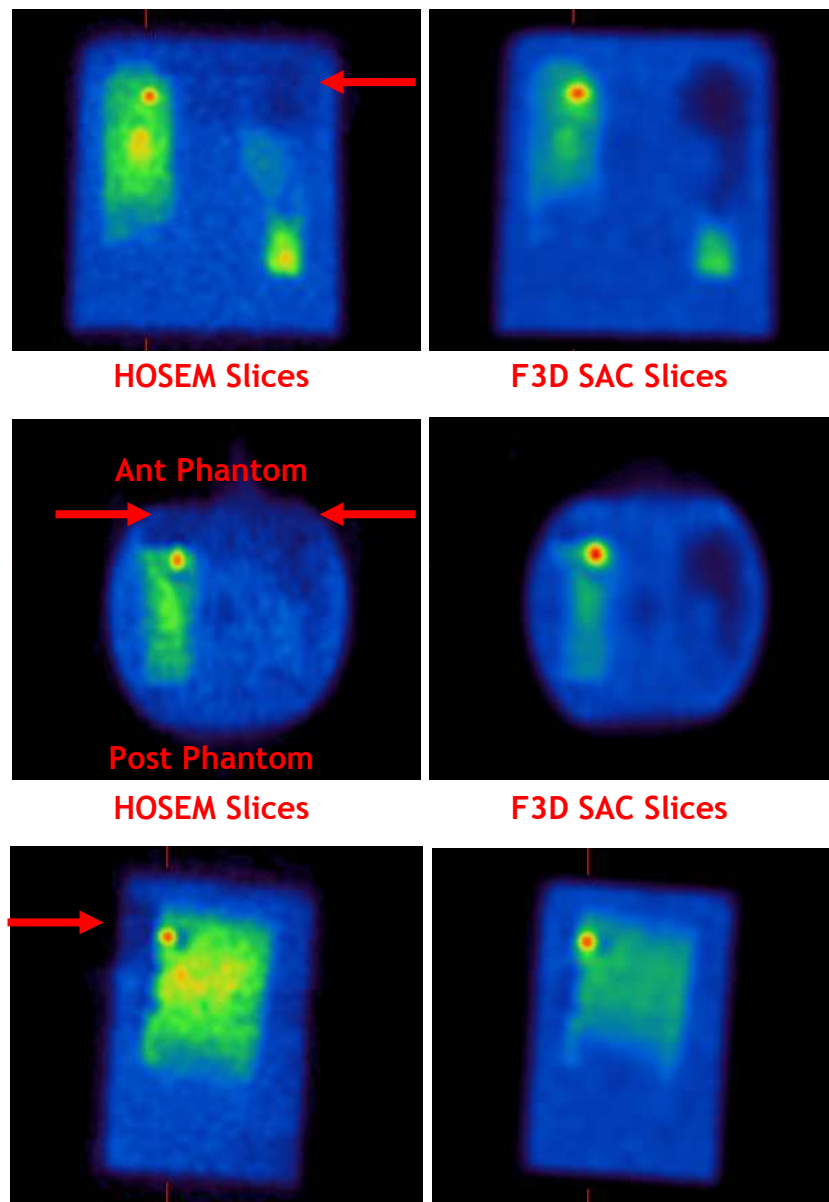


Figure 82 - Qualitative Differences Demonstrated
 Images showing SPET transverse, sagittal and coronal slices of the lung phantom filled with Tc99m. Images on the left have been reconstructed with HOSEM and images on the right with Flash 3D SAC. The red arrows on the images on the left indicate areas of low count density.

The red arrows on the HOSEM images highlight areas of reduced counts caused by the additional attenuation (the synthetic breast component). The HOSEM images also show quite marked background activity with the lungs in comparison to the corrected F3D SAC images.

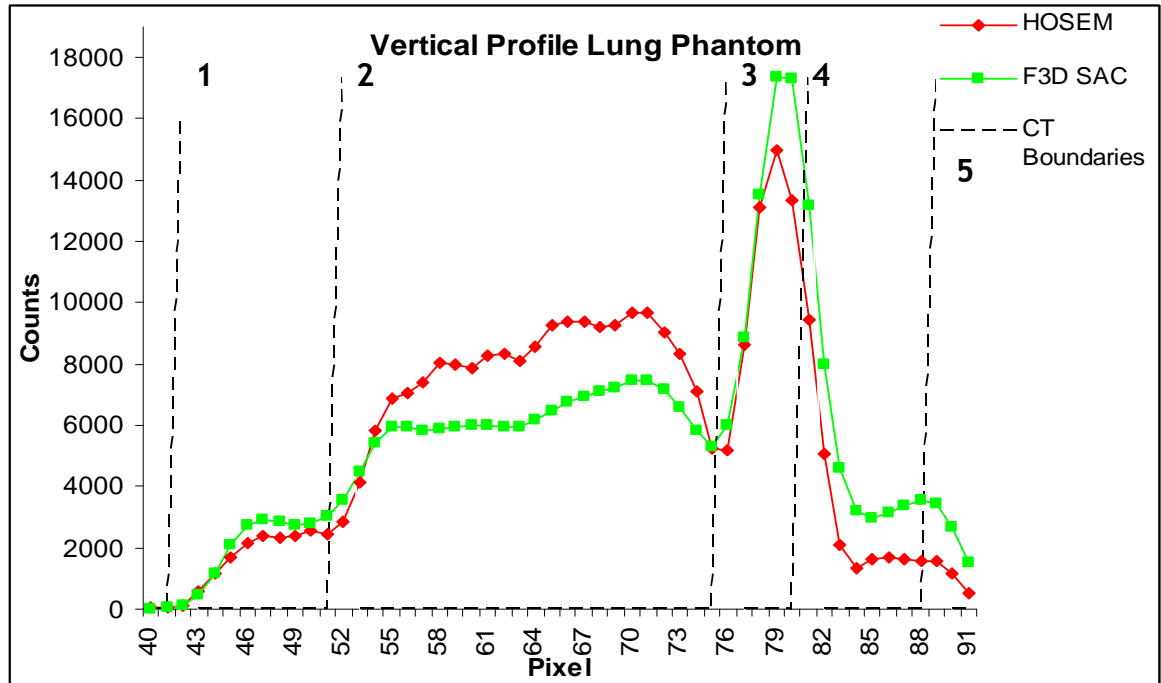


Figure 83 - Vertical Profiles; HOSEM Versus F3D SAC

Image shown is a plot of the pixel data obtained from vertical line profiles placed through transaxial slice of the main body of the phantom which contained the tumour compartment. The dashed vertical lines are used to highlight the physical boundaries of the various compartment and attenuating material as defined by the CT.

Figure 83 are the results of a vertical profile placed through a cross section of the in-house lung phantom (transverse slice). The dashed vertical lines show the delineation of the phantom as determined by the CT image. Line 1 corresponds to the posterior edge of the phantom, line 2 is the posterior edge of the right lung compartment, line 3 is the posterior edge of the tumour component, line 4 the anterior edge of the tumour and lung components and line 5 the anterior edge of the phantom.

Profile analysis has further highlighted the difference in the distribution of activity in the lung between the old and new technique (HOSEM and F3D SAC). In terms of the lung component the F3D SAC demonstrates a reduction in lung background activity but also an increase in tumour activity which is clearly

reduced in the HOSEM images as a result of the attenuating material. There is also a clear reduction in counts on the HOSEM images at the anterior edge of the phantom as a result of the attenuating material.

The change in distribution, that is the reduced tumour counts and higher background activity, would therefore have resulted in an underestimation of both values of T:B and values of % uptake.

4.5.3 Discussion and Conclusion - ^{99m}Tc Phantom Acquisition Corrected Versus Uncorrected

Quantitative analysis work performed in this chapter was undertaken using Hermes Volume Fusion Display. This program allowed 2 SPET volumes to be loaded simultaneously and ROI analysis to be undertaken. However, care should be exercised when performing comparative quantification work using the Hermes system or any other image display and analysis software, as the Hermes systems takes the first volume selected and matches the matrix of the second volume to that of the first. Work in this chapter was originally undertaken using this display and analysis protocol to compare the Hermes reconstruction technique (128x128 matrix) with the new technique, the Symbia (512x512). This led to the corrected volume from the Symbia being binned down into a 128x128 matrix and subsequently pixel data was lost. This loss in pixel data led to inaccurate values of activity calculated. This was corrected and the data presented here are accurate. The 'pixel loss' is a function of the display program rather than a real pixel loss, it is therefore important to use a registered volume SPET data with its target volume CT data on the Hermes system.

Work in this section demonstrated that the use of scatter and CT-attenuation corrections improved not only the overall image quality of the SPET volume but also the accuracy of the pixel data for the volume. The accuracy of the image quantification was greatly improved when using SPET-CT in comparison the SPET only quantification. The accuracy of this technique, however, also relied on the corrected SPET volume being viewed with the CT image component, as the CT

image component was essential in the identification and delineation of any abnormalities.

The semi-quantitative profile analysis demonstrated a change in the distribution and a reduction in the background activity using the new technique, which implied that values of T:B's calculated in Chapter 2 were underestimated. This could have masked differences between the groups although the data were so mixed that this is extremely unlikely.

4.6 Discussion and Conclusion

The work in this chapter was driven by questions raised in Chapter 2 over the impact hybrid imaging would have with regards to improvements in SPET image reconstruction from both a qualitative and quantitative perspective.

In an attempt to answer these questions both patient and phantom work were undertaken. Since NeoSPECT was no longer on the market the patient work was undertaken using a radiopharmaceutical which had a similar mechanism of uptake, OctreoSCAN. OctreoScan unlike NeoSPECT is not a ^{99m}Tc based radiopharmaceutical but is ^{111}In based. Phantom work was undertaken using both ^{99m}Tc and ^{111}In .

Hybrid imaging based reconstruction improvements were assessed firstly by reviewing patient data. Patient data were reconstructed using the existing OSEM2D technique and comparing this with newly available resolution recovery techniques (with and with scatter and CT based attenuation corrections, F3D and F3D SAC). Data were anonymised in terms of patient demographics and reconstruction details. Four observers experienced in OctreoSCAN image interpretation were asked to review the data and provide a score in terms of image quality. Each observer was asked to take into accounts factors such as delineation of patient habitus, delineation of the lungs as air, uniformity of uptake across solid organs and finally delineation of any abnormalities including loops of gut. Based of these factors a score was assigned between 1 and 5 (5 indicating a good quality and 1 indicating a poor quality).

The scores from the observers indicated a preference towards F3D SAC, followed by F3D and lastly O2D. One of the most notable features of F3D SAC in comparison to the other reconstruction techniques was the delineation of body outline and the bio-distribution of uptake within the lung fields.

The scores for each observer were assessed statistically. Of the 4 observers 3 were found to demonstrate a statistically significant difference between the existing technique and the improved image reconstruction as a result of hybrid imaging.

From the patient qualitative cohort semi-quantitative analysis was also performed. This was in the form of profile analysis which was able to assess the distribution of OctreoScan uptake across organs in the body. The findings from the semi-quantitative profile analysis results of solid organs demonstrated a significant improvement in image quality with the use of F3D SAC reconstruction. A clear differentiation between O2D and F3D SAC, and F3D and F3D SAC was demonstrated. Profiles through solid organs like the liver using F3D SAC demonstrated a more uniform distribution in uptake when compared with O2D and F3D. Whilst profile analysis through the thorax demonstrated a significant dip in counts across the lungs with both the F3D and F3D SAC, whereas O2D produced a fairly flat profile across the thorax regardless of tissue type indicating very little differentiation between the lungs and surrounding tissue within the body. As with the qualitative analysis, semi-quantitative analysis also demonstrated a clear improvement in SPET image quality as a result of hybrid imaging.

Finally quantitative analysis was undertaken, since the patient cohort was a retrospective review no standard image acquisition had been acquired that would allow image quantification to be performed. The accuracy of image quantification with hybrid imaging was therefore assessed using an in-house designed and manufactured SPET-CT phantom.

The first phantom work was undertaken using ^{111}In , results from this work concluded that regardless of reconstruction technique the image calculated value of activity failed to closely meet the value of actual activity. However, the hybrid imaging techniques with corrections reduced the difference between the calculated and actual value of activity from 37% for the uncorrected data to 21% for the corrected data. Although this work failed to accurately calculate the value of absolute activity there was a clear improvement demonstrated when scatter and CT-attenuation correction were corrected for as part of the reconstruction. This is in keeping with results reported by Assie et al (2010), however, whilst it is acknowledged that all phantom work is idealistic, the work undertaken by Assie et al (2010) involved a separate CT acquisition. The use of a separate CT is not desirable for quantifying OctreoSCAN, as co-registration of the SPET-CT may be subject to significant errors. Errors which would result from differences in patient set-up between the modalities i.e. arms up or down,

breath hold or simply because there is a spatial differences in the anatomical distribution of organs within the abdomen and pelvis as a result of variations in bowel, bladder and stomach content.

Unlike ^{111}In phantom work the $^{99\text{m}}\text{Tc}$ phantom work demonstrated hybrid imaging to provide a significant improvement in the overall accuracy of image quantification using $^{99\text{m}}\text{Tc}$ when compared with the existing reconstruction techniques used in the chapter 2 for the NeoSPECT work. It is also worthwhile noting that for both ^{111}In and $^{99\text{m}}\text{Tc}$ the closest match to the actual activity was calculated without a background correction for the counts, presumably as the activity was calculated from data from transverse slices and therefore there was no need to correct for overlying structures as would normally be the case with planar imaging.

The work in this chapter clearly indicates hybrid imaging's ability to improve SPET image quality. As a result there is no doubt that the accuracy of the quantitative and semi-quantitative NeoSPECT work in chapter 2 would have benefited. The use of the SPET-CT would have led to improved accuracy of tumour volume delineation and better identification of 'other' disease processes within the lungs. The improved reduction in non-physiological tracer distribution would also have allowed better visualization of small nodal disease within the lungs.

Incidentally, from reviewing the patient OctreoScan images in this chapter, as a result of hybrid imaging, new consideration should be given to the standard imaging protocol for OctreoScan studies. OctreoScan studies are normally performed at 24 and 48 hrs to help distinguish between physiological uptake and abnormal uptake in bowel. However, now that anatomical information is available and the quality of the SPET reconstruction has improved as a result of various corrections, it may be time to amend current protocols. If abnormal uptake at 24 hours can be characterised using the SPET-CT fused volume then there would be no need to perform additional 48 hour imaging. A recent editorial published in Nuclear Medicine Communications also recognised the improvements in OctreoScan as a result of hybrid imaging particularly when its role in distinguishing physiological from pathological uptake in the abdomen (Navalkissoor & Buscombe, 2011). Amendment to current standard OctreoScan

imaging protocols would increase the number of patients imaged in a department by freeing up camera time. This would also optimise the time spent by the patient within the department as the overall length of the current protocol from injection to final set of images, requires a certain level of tolerance and general fitness of patient. There would therefore be a number of patients who do not have this investigation because they were unable to comply fully.

Chapter 5 - Thesis Conclusion and Discussion

The main aim of this thesis was to investigate the use of SPET and SPET-CT image quantification and its role in tissue characterisation of somatostatin receptor imaging.

Work initially involved the ^{99m}Tc labeled somatostatin analogue, NeoSPECT. This radiopharmaceutical was licensed for use in Europe to image NSCLC solitary pulmonary nodules. The work in Chapter 2 aimed to determine if dual time imaging and quantification using iterative SPET reconstruction techniques could be used to differentiate between benign and malignant disease within the mediastinum. It was believed that the consequence of a positive finding would have great benefits in staging disease without the need for invasive methods such as mediastinoscopy and CT guided biopsy. Furthermore, accurate image quantification could also be considered as a useful tool in determining therapy efficacy. Two forms of image quantification were undertaken in Chapter 2. The first was simple ratio calculation between the tumour and the surrounding background tissue. The second was a calculation of percentage uptake from the tumour volume.

Differences between SPET volumes reconstructed with FBP and Iterative reconstruction techniques were assessed via T:B ratio's. Despite there being no statistically significant difference between the techniques quantitatively there was a noticeable improvement in image quality when using Iterative techniques. This difference was considered important as the lower quality FBP technique meant accurate delineation of the tumour volume was more difficult, this in turn, would have an impact on the accuracy of the percentage uptake value calculated.

In terms of tumour histology, neither the T:B ratio nor values of percentage uptake calculated from the 2 hours acquisition were able to differentiate between benign and malignant disease.

Leading on from this, the patients who had undergone dual time imaging at 2 and 4 hours were assessed to determine if there was any difference

demonstrated quantitatively in the malignant group between the 2 and 4 hour SPET volumes. Neither the T:B or the more sensitive measure of percentage uptake, were able to demonstrate any statistically significant change in the distribution of the NeoSPECT within the tumour volume and surrounding lung tissue between the images acquired at 2 and 4 hours. Separate analysis undertaken of the NSCLC group only, also failed to identify any quantitative differences in T:B or percentage uptake within the histological subtypes of NSCLC.

In terms of the mediastinum, direct correlation of quantification performed in the mediastinum with histology findings could not be undertaken due to a lack to anatomical information. Therefore nodes could only be characterized based on their size and shape and therefore nodal disease could not be definitively confirmed. Previous work by Waxman, 2002, claimed that NeoSPECT could be used to accurately stage disease within the mediastinum, however, the mechanism as to how node identified on SPET imaging were validated was omitted from this abstract. Work in this thesis failed to identify an accurate technique to do this with SPET imaging alone, directly as a result of lack of anatomical information.

Work in chapter 2 clearly demonstrated that quantification of NeoSPECT imaging was not a suitable technique to differentiate benign from malignant disease. In the past consideration had been given to the use of radio-labeled Depreotide as a radionuclide targeted therapy agent, however, the fact that significant uptake exists in benign disease makes the use of a therapy agent based on NeoSPECT of no value.

The NeoSPECT work undertaken identified a number of pitfalls in SPET image quantification. Firstly patient compliance, there were a number of physical difficulties which could not be overcome such as the patient's limited flexibility and general compliance to remain still throughout the duration of the study. These often led to large orbits of rotation and image degradation. Another similar problem encountered in the dual time imaging, but relevant to any repeated study, was the reproducibility of the patient set-up in patients with large BMIs. Body habitus greatly affected the orbit of rotation, this significantly affected the correction for attenuation using Chang's technique. This work also

highlighted a low confidence in the correct identification of anatomical features predominantly nodal disease within the mediastinum due to a lack of anatomical information.

Shortly after the NeoSPECT work was undertaken the department installed the latest in hybrid imaging, a Siemens Symbia T SPET-CT unit. In theory, not only was hybrid imaging able to provide anatomical information to the SPET volume but both CT and software components were able to correct for factors which degraded SPET images such as attenuation and scatter. All of these new features could have impacted on the quality of the data and on the qualitative and quantitative results. It was therefore important to re-evaluate the role of NeoSPECT image quantification in light of the availability of better reconstruction algorithms. Work was undertaken with another SSTR imaging agent, OctreoScan, to determine if hybrid imaging could have improved image quality and accuracy of SPET image quantification.

Little published work is available investigating the use of SPET-CT and in particular work looking at image quantification using new reconstruction techniques in patient data other than in the field of cardiology. The work within this thesis using OctreoScan allowed important analysis to be undertaken to determine whether these new techniques did improve image quality.

Firstly, a qualitative comparison was undertaken using patient data which looked for differences in image quality between images reconstructed as in Chapter 2 and using new techniques as a result of hybrid imaging. From the results it was clear that hybrid imaging reconstruction techniques provided a better quality SPET volume when compared with existing reconstruction technique.

Using the same patient cohort semi-qualitative analysis was also undertaken. Profile analysis of the main organs within the abdomen and thorax was undertaken to assess the distribution of OctreoScan uptake across the organs between the existing and new reconstruction techniques. Results demonstrated a significant improvement in image quality when using the hybrid based reconstruction techniques, the distribution of OctreoScan uptake in solid organs like the liver were more uniform and areas such as the thorax demonstrated

pronounced differentiation between lung with surrounding tissue when compared with the existing reconstruction techniques.

Finally, analysis was undertaken to assess the accuracy SPET image quantification using hybrid imaging techniques. Results from the ^{111}In based phantom demonstrated an improvement in the accuracy of the absolute activity calculation when using hybrid imaging, although the difference between the actual and calculated activity differed from the actual value by approximately 21%. $^{99\text{m}}\text{Tc}$ phantom work on the other hand demonstrated hybrid imaging to provide a significant improvement in the overall accuracy of image quantification using $^{99\text{m}}\text{Tc}$ in comparison to the reconstruction techniques used in the chapter 2 for the NeoSPECT work. This conclusion is in keeping with work undertaken by Zeintl *et al.* (2010) which involved both a patient cohort and phantoms.

The work in this thesis clearly demonstrated hybrid imaging's ability to improve SPET image quality for both ^{111}In and $^{99\text{m}}\text{Tc}$ based radiopharmaceuticals this is an important factor in image quantification. In particular a great improvement in the accuracy of the calculation of absolute uptake was demonstrated for $^{99\text{m}}\text{Tc}$ which would have benefited the work in chapter 2. It is unlikely that hybrid imaging would have added any additional value to NeoSPECT as a diagnostic imaging product for NSCLC. In fact despite its rebranding, NeoSPECT has recently been withdrawn from having a European license. This is as a direct of result of a decrease in demand for the product brought about by the increased availability of PET-CT imaging within mainland Europe and the UK. In Scotland one of the key roles of PET-CT imaging lies in the diagnosis and staging of NSCLC cancer. There has been work published recently which redefines the role of NeoSPECT in patients in SCLC, Gerasimou *et al.* (2010), it may be that NeoSPECT is made available again in the future.

In terms of further work, as mentioned in Chapter 4, the EANM has published new guidelines on OctreoScan imaging. The acquisition parameters in these new guidelines differ from the acquisition parameters currently used at Glasgow Royal Infirmary and probably many other centres across the UK. The guidelines indicate extended planar and SPET acquisition times. In terms of the SPET imaging there is no indication as to whether or not these new guidelines have

been drawn up with SPET resolution recovery in mind and whether there is a real need to extend the already lengthy SPET acquisition. Further work will be undertaken to investigate if SPET-CT acquisitions with resolution recovery could impact the SPET acquisition times advised by the EANM guidelines. In addition to this, the department will also seek to undertake an audit of the OctreoScan findings of 24 hour SPET-CT versus 48 hour imaging to determine how many patients continue to have indeterminate findings at 24 hours.

Currently, there are a number of research groups working with commercial partners looking to incorporate Monte Carlo based scatter corrections into their resolution recovery software. As SPET image reconstruction techniques continue to evolve, it may be that greater improvements are demonstrated in image quantification which could see a major role emerge for nuclear medicine SPET imaging techniques as accurate and effective quantitative tools for the measurement of therapy efficacy.

The work of this thesis has produced some novel work leading to a number of important conclusions in the field of somatostatin imaging in particular and in general for SPET-CT hybrid imaging reconstruction tools. These can be summarised as follows:

- No difference could be found between uptake in malignant and benign disease in NeoSPECT imaging using conventional image acquisition.
 - NeoSPECT should not be considered as a therapy agent.
- Using hybrid imaging (SPET-CT) significantly improves both image quality and quantification of images from somatostatin receptor radiopharmaceuticals. This work has not been previously published.
- The use of SPET-CT and SPET iterative reconstruction using resolution recovery, scatter and attenuation correction show clear improvements in both Tc^{99m} and In¹¹¹ images from a quantitative perspective.

Appendices

Appendix A - NeoSPECT LREC Approval

North Glasgow University Hospitals
NHS Trust

Research Ethics Committee (2)
Glasgow Royal Infirmary
4th floor, Walton Building
84 Castle Street
GLASGOW
G4 0SF
Tel: 0141 211 4020
Fax: 0141 232 0752



Date 11th March 2004

Dr A Stanton
Clinical Research Fellow
Department of Respiratory Medicine
Glasgow Royal Infirmary

Enquiries to Mrs Sharon Macgregor (Administrator)
Email: sharon.macgregor@northglasgow.scot.nhs.uk

Chairman: Dr M Booth

Dear Dr Stanton,

**Full title of study: The role of ^{99m}Tc labelled Depreotide scanning in the staging of lung cancer.
REC reference number: 03RE010 (REC/2)**

Thank you for your letter of 3rd December 03, responding to the Committee's request for further information on the above research and submitting revised documentation.

The further information was considered at the meeting of the Glasgow Royal Infirmary LREC (2) held on 19th December 03. However, favourable opinion was deferred until a copy of the ARSAC certificate was received on 3rd March 2004.

Confirmation of ethical opinion

On behalf of the Committee, I am pleased to confirm a favourable ethical opinion for the above research on the basis described in the application form and supporting documentation as revised.

The favourable opinion applies to the following research site:

Site: *North Glasgow University Hospitals NHS Trust*
Principal Investigator: *Dr A Stanton*

Conditions of approval

The favourable opinion is given provided that you comply with the conditions set out in the attached document. You are advised to study the conditions carefully.

Approved documents

The final list of documents reviewed and approved by the Committee is as follows:

Application Form (updated 2 December 2003)
Subject Information Sheets (version 2, dated December 2003)
Consent Form
Investigator CV
MHRA letter re DDX (dated 24 November 2003)
ARSAC letter (dated 12 February 2004)

Management approval

The study may not commence until final management approval has been confirmed by the organisation hosting the research.

of compliance (from 1 May 2004)

Committee is constituted in accordance with the Governance Arrangements for Research Ethics Committees (July 2001) and complies fully with the Standard Operating Procedures for Research Ethics Committees in the UK.

REC reference number: 03RE010

Please quote this number on all correspondence

Yours sincerely,

for Macgregor
Malcolm Booth
Chairman

Appendix B - NeoSPECT Imaging Proforma

NEOSPECT TRIAL	
Patient name _____	Weight(Kg): _____
Study code neo01 _____	Height(cm): _____
Technician imaging:	
Date _____	
Tc99m neospect injected:	
_____ MBq measured at _____	
Tc99m neospect residual:	
_____ MBq measured at _____	
Tc99m in standard:	
_____ MBq measured at _____	
Standard acquisition started _____	
2 Hour SPECT started _____ arms up down (circle)	
0° & 180°	90° & 270°
Detector 1 radius _____	Detector 1 radius _____
Detector 2 radius _____	Detector 2 radius _____
Table Height _____	
Static images started _____	
4 hour SPECT started _____ arms or 2 hour	
<u>N.B Ensure table and detector settings are identical to those defined at 2 hours.</u>	
Any difficulty/comments	

Appendix C - OctreoScan Observer Score Record

Oct	Vol ^m Score	Lung Score	Oct	Vol ^m Score	Lung Score	Oct	Vol ^m Score	Lung Score	Oct	Vol ^m Score	Lung Score	Oct	Vol ^m Score	Lung Score
1			31			61			91			121		
2			32			62			92			122		
3			33			63			93			123		
4			34			64			94			124		
5			35			65			95			125		
6			36			66			96			126		
7			37			67			97			127		
8			38			68			98			128		
9			39			69			99			129		
10			40			70			100			130		
11			41			71			101			131		
12			42			72			102			132		
13			43			73			103			133		
14			44			74			104			134		
15			45			75			105			135		
16			46			76			106			136		
17			47			77			107			137		
18			48			78			108			138		
19			49			79			109			139		
20			50			80			110			140		
21			51			81			111			141		
22			52			82			112			142		
23			53			83			113			143		
24			54			84			114			144		
25			55			85			115			145		
26			56			85			116			146		
27			57			87			117			147		
28			58			88			118					
29			59			89			119					
30			60			90			120					

Please score the volume 1-5 (1 poorest 5 best) & if the lungs have been included give them a separate score based on their appearance only.

Taking into account

- Delineation of the patient e.g. scatter outside where you would expect with CT
- Delineation of lungs as air
- Uniformity of uptake across solid organs e.g. liver, spleen, kidneys, bladder
- Delineation of any abnormalities and loops of gut

Use Hybrid viewer CT SPECT and you may need to adjust the scale of the SPECT for different areas.

Appendix D - Reproducibility results for each observer

Results - Observer 1

	Entire OctreoScan Volume Score							
	O2D			F3D			F3D SAC	
	Score 1	Score 2		Score 1	Score 2		Score 1	Score 2
Oct080 / 147	4	4	Oct062 / 118	5	4	Oct060 / 119	4	3
Oct027 / 135	2	2	Oct036 / 143	3	3	Oct077 / 139	3	2
Oct053 / 134	2	4	Oct070 / 132	4	2	Oct068 / 138	4	3
Oct030 / 121	3	3	Oct039 / 141	3	3	Oct042 / 125	3	2
Oct081 / 140	2	2	Oct101 / 126	2	2	Oct033 / 120	2	2
Oct094 / 130	3	3	Oct017 / 145	3	3	Oct084 / 137	2	2
Oct045 / 131	3	3	Oct005 / 142	4	4	Oct020 / 123	4	3
Oct051 / 144	3	3	Oct100 / 127	3	3	Oct079 / 129	3	4
Oct103 / 122	4	4	Oct108 / 124	4	3	Oct114 / 128	3	3
Oct112 / 136	4	3	Oct116 / 146	3	3	Oct109 / 133	3	2
Sum	30	31	Sum	34	30	Sum	31	26

	Lung OctreoScan Volume Score							
	O2D			F3D			F3D SAC	
	Score 1	Score 2		Score 1	Score 2		Score 1	Score 2
Oct080 / 147	0	4	Oct062 / 118	0	4	Oct060 / 119	0	3
Oct027 / 135	2	2	Oct036 / 143	0	3	Oct077 / 139	2	2
Oct053 / 134	0	0	Oct070 / 132	2	2	Oct068 / 138	2	3
Oct030 / 121	1	2	Oct039 / 141	2	1	Oct042 / 125	2	2
Oct081 / 140	2	1	Oct101 / 126	1	1	Oct033 / 120	3	1
Oct094 / 130	0	0	Oct017 / 145	0	3	Oct084 / 137	2	2
Oct045 / 131	0	2	Oct005 / 142	1	4	Oct020 / 123	1	2
Oct051 / 144	0	3	Oct100 / 127	2	0	Oct079 / 129	2	0
Oct103 / 122	3	0	Oct108 / 124	4	0	Oct114 / 128	0	3
Oct112 / 136	0	0	Oct116 / 146	0	0	Oct109 / 133	0	2
Sum	8	14	Sum	12	18	Sum	14	20

Results - Observer 2

	Entire OctreoScan Volume Score							
	O2D			F3D			F3D SAC	
	Score 1	Score 2		Score 1	Score 2		Score 1	Score 2
Oct080 / 147	2.5	2.5	Oct062 / 118	3	3.5	Oct060 / 119	3	4
Oct027 / 135	2	1	Oct036 / 143	3.5	2.5	Oct077 / 139	3.5	3
Oct053 / 134	2	1.5	Oct070 / 132	3	3	Oct068 / 138	3	3
Oct030 / 121	3	3.5	Oct039 / 141	3	3	Oct042 / 125	4	4
Oct081 / 140	2	2.5	Oct101 / 126	3	3	Oct033 / 120	3	4
Oct094 / 130	2.5	2.5	Oct017 / 145	3.5	3	Oct084 / 137	3.5	3
Oct045 / 131	2	2.5	Oct005 / 142	3.5	3	Oct020 / 123	3	3.5
Oct051 / 144	2	2	Oct100 / 127	3	3	Oct079 / 129	3.5	3.5
Oct103 / 122	2	3	Oct108 / 124	3	2.5	Oct114 / 128	3	3
Oct112 / 136	2.5	1	Oct116 / 146	2.5	2.5	Oct109 / 133	2.5	2
Sum	22.5	22	Sum	31	29	Sum	32	33

	Lung OctreoScan Volume Score							
	O2D			F3D			F3D SAC	
	Score 1	Score 2		Score 1	Score 2		Score 1	Score 2
Oct080 / 147	1.5	1	Oct062 / 118	2.5	2	Oct060 / 119	3.5	4
Oct027 / 135	1	0.5	Oct036 / 143	1	1	Oct077 / 139	0	0
Oct053 / 134	1	1	Oct070 / 132	1	1	Oct068 / 138	1	1
Oct030 / 121	4	4	Oct039 / 141	3.5	3.5	Oct042 / 125	4	4
Oct081 / 140	3	1.5	Oct101 / 126	3.5	2.5	Oct033 / 120	3.5	4
Oct094 / 130	0	0	Oct017 / 145	0	0	Oct084 / 137	0	0
Oct045 / 131	2	1	Oct005 / 142	0	0	Oct020 / 123	1	0
Oct051 / 144	1	0	Oct100 / 127	0	0	Oct079 / 129	0	0
Oct103 / 122	0	0	Oct108 / 124	0	0	Oct114 / 128	0	0
Oct112 / 136	0	0	Oct116 / 146	0	0	Oct109 / 133	0	0
Sum	13.5	9	Sum	11.5	10	Sum	13	13

Results - Observer 3

	Entire OctreoScan Volume Score							
	O2D			F3D			F3D SAC	
	Score 1	Score 2		Score 1	Score 2		Score 1	Score 2
Oct080 / 147	4	3	Oct062 / 118	3	2	Oct060 / 119	3	4
Oct027 / 135	2	4	Oct036 / 143	5	2	Oct077 / 139	4	4
Oct053 / 134	1	4	Oct070 / 132	4	3	Oct068 / 138	4	3
Oct030 / 121	1	4	Oct039 / 141	4	4	Oct042 / 125	4	5
Oct081 / 140	4	4	Oct101 / 126	2	3	Oct033 / 120	4	4
Oct094 / 130	3	4	Oct017 / 145	4	5	Oct084 / 137	4	3
Oct045 / 131	1	3	Oct005 / 142	5	3	Oct020 / 123	5	3
Oct051 / 144	2	4	Oct100 / 127	3	5	Oct079 / 129	5	4
Oct103 / 122	2	2	Oct108 / 124	2	3	Oct114 / 128	3	3
Oct112 / 136	3	1	Oct116 / 146	3	4	Oct109 / 133	2	4
Sum	23	33	Sum	35	34	Sum	38	37

	Lung OctreoScan Volume Score							
	O2D			F3D			F3D SAC	
	Score 1	Score 2		Score 1	Score 2		Score 1	Score 2
Oct080 / 147	3	2	Oct062 / 118	3	4	Oct060 / 119	4	3
Oct027 / 135	2	2	Oct036 / 143	3	2	Oct077 / 139	4	3
Oct053 / 134	2	3	Oct070 / 132	3	3	Oct068 / 138	4	2
Oct030 / 121	3	4	Oct039 / 141	3	4	Oct042 / 125	4	5
Oct081 / 140	3	4	Oct101 / 126	2	1	Oct033 / 120	5	3
Oct094 / 130	3	4	Oct017 / 145	2	4	Oct084 / 137	4	3
Oct045 / 131	1	2	Oct005 / 142	5	3	Oct020 / 123	4	3
Oct051 / 144	1	3	Oct100 / 127	4	4	Oct079 / 129	4	3
Oct103 / 122	0	0	Oct108 / 124	0	0	Oct114 / 128	0	0
Oct112 / 136	3	0	Oct116 / 146	3	0	Oct109 / 133	0	0
Sum	21	24	Sum	28	25	Sum	33	25

Results - Observer 4

	Entire OctreoScan Volume Score							
	O2D			F3D			F3D SAC	
	Score 1	Score 2		Score 1	Score 2		Score 1	Score 2
Oct080 / 147	1	2	Oct062 / 118	4	3	Oct060 / 119	4	5
Oct027 / 135	1	1	Oct036 / 143	3	4	Oct077 / 139	3	3
Oct053 / 134	1	1	Oct070 / 132	3	3	Oct068 / 138	3	4
Oct030 / 121	3	3	Oct039 / 141	5	3	Oct042 / 125	5	5
Oct081 / 140	1	1	Oct101 / 126	3	4	Oct033 / 120	4	5
Oct094 / 130	1	1	Oct017 / 145	4	5	Oct084 / 137	4	5
Oct045 / 131	1	1	Oct005 / 142	4	4	Oct020 / 123	5	3
Oct051 / 144	1	1	Oct100 / 127	1	3	Oct079 / 129	3	3
Oct103 / 122	1	3	Oct108 / 124	3	3	Oct114 / 128	5	3
Oct112 / 136	1	3	Oct116 / 146	1	1	Oct109 / 133	3	1
Sum	12	17	Sum	31	33	Sum	39	37

	Lung OctreoScan Volume Score							
	O2D			F3D			F3D SAC	
	Score 1	Score 2		Score 1	Score 2		Score 1	Score 2
Oct080 / 147	1	1	Oct062 / 118	5	3	Oct060 / 119	5	5
Oct027 / 135	1	1	Oct036 / 143	3	3	Oct077 / 139	3	3
Oct053 / 134	1	1	Oct070 / 132	3	3	Oct068 / 138	3	3
Oct030 / 121	5	4	Oct039 / 141	5	3	Oct042 / 125	5	5
Oct081 / 140	1	1	Oct101 / 126	3	3	Oct033 / 120	5	5
Oct094 / 130	1	1	Oct017 / 145	4	0	Oct084 / 137	4	4
Oct045 / 131	1	1	Oct005 / 142	4	3	Oct020 / 123	5	3
Oct051 / 144	1	1	Oct100 / 127	0	0	Oct079 / 129	3	3
Oct103 / 122	0	0	Oct108 / 124	0	0	Oct114 / 128	0	0
Oct112 / 136	0	0	Oct116 / 146	0	0	Oct109 / 133	0	0
Sum	12	11	Sum	27	18	Sum	33	31

References

ARSAC

ARSAC, 2006. Notes for Guidance on the Clinical Administration of Radiopharmaceuticals and Use of Sealed Radioactive Sources. Produced by the Health Protection Agency for ARSAC, Rev. 20th April.

Assie,

Assie, K, Dieudonne, A, Gardin, I, Vera, P and Buvat, I 2010: A Preliminary Study of Quantitative Protocols in Indium 111 SPECT Using Computational Simulations and Phantoms. IEEE Trans Nucl Sci, 57(3), pp 1096 - 1104.

Baert and Sartor,

Baert, AL and Sartor, K 2006. Diagnostic Nuclear Medicine. pp. 153-184. Springer.

Berkowitz,

Berkowitz, M and Waxman, AD 2001: The utility of NeoTect in the evaluation of pulmonary malignancy. Journal of Nuclear Medicine, 42(5), p 28P.

Blum,

Blum, J, Handmaker, H, Lister-James, J 2000: A multicenter trial with a somatostatin analogue ^{99m}Tc Depreotide in the evaluation of solitary pulmonary nodules. Chest, 117, pp 1232-38.

Bombardieri,

Bombardieri, E, Ambrosini, V, Aktolun, C, Baum, RP, Bishof-Delaloye, A, Del Vecchio, S, Maffioli, L, Oyen, W, Pepe, G and Chiti, A 2010: ¹¹¹In-pentetreotide scintigraphy: procedure guidelines for tumour imaging. Eur J Nucl Med and Mol Imaging, 37 (7), pp 1441 - 1448.

Brown,

Brown, S, Bailey, DL, Willowson, K and Baldock, C 2008: Investigation of the relationship between linear attenuation coefficients and CT Hounsfield units using radionuclides for SPECT. *Appl Radiat Isotop*, 66 (9), pp 1206 - 1212.

Bruyant,

Bruyant, PP 2002: Analytic and Iterative Reconstruction Algorithms in SPECT. *Journal of Nuclear Medicine*, 43(10), pp 1343-1358.

CancerResearchUK-Lung,

Cancer Research UK 2011: Types of Lung Cancer.

<http://www.cancerhelp.org.uk/type/lung-cancer/about/types-of-lung-cancer>:

accessed on 10/05/2011.

CancerResearchUK-NET,

Cancer Research UK 2011: What are carcinoid tumours?

<http://www.cancerhelp.org.uk/type/carcinoid/about/what-are-carcinoid-tumours>: accessed on 10/05/2011.

Carrieshealth,

Carries Health 2009: Pancreas.

<http://www.carrieshealth.com/images/pancreas.jpg>: accessed on 21/01/2009.

Cremonesi,

Cremonesi, M, Ferrari, M, Bodei, L, Tossi, G, Pagnelli, G 2006: Dosimetry in peptide radionuclide receptor therapy; a review. *Journal of Nuclear Medicine*, 47, pp 1467-1475.

de Herder,

de Herder, WW, Hofland, LJ, van der Lely, AJ and Lamberts, SWJ 2003: Somatostatin receptors in gastroentero-pancreatic neuroendocrine tumours. *Endocrine-Related Cancer*, 10, pp 451-458.

DaSilva,

DaSilva, AJ, Tang, HR, Wong, KH, Wu, MC, Dae, MW and Hasegawa, BH 2001: Absolute quantification of regional myocardial uptake of ^{99m}Tc-Sestamibi with SPECT; experimental validation in a porcine model. *Journal of Nuclear Medicine*, 42(5), pp 772-779.

Delebeke & Israel

Delbeke, D and Israel, O 2010. Hybrid PET/CT and SPECT/CT Imaging; A Teaching File. pp. 3-31. Springer.

Dwamena,

Dwamena, BA, Sonnad, SS, Angobaldo, JO and Wahl, RL 1999: Metastases from non-small cell lung cancer: mediastinal staging in the 1990's - meta-analytic comparison of PET and CT. *Radiology*, 213, pp 530-536.

Farr & Allisy-Roberts

Farr, RF and Allisy-Roberts, PJ 1998. *Physics for Medical Imaging*. WB Saunders.

GE Healthcare,

GE Healthcare 2009: Infinia Hawkeye.

http://www.gehealthcare.com/euen/fun_img/products/nuclear_medicine/products/infinia_hawkeye4.html: accessed on 17/11/2009.

Gemmel,

Gemmel, HG 2008. Benchmarking in Nuclear Medicine in Scotland. Report compiled by NHS Grampian for Audit Scotland.

Gerasimou

Gerasimou, GP, et al 2010: Functional Imaging with Tc-99m-Depreotide (NeoSPECT) in Small Cell Lung Carcinoma. Eur J Nucl Med Mol Imaging, 37 (S2), S33-S481, p 421(P440).

Guerrero,

M Guerrero 2009: Pancoast Tumour Imaging. 2009.

<http://emedicine.medscape.com/article/359881-overview> : accessed on 09/08/2010.

Han,

Han, S, Colville, D, Ainslie-McLaren, G, Lang, J, and Watt, E 2010: Clinical impact of SPECT/CT bone scan in the assessment of bone metastases in breast cancer a somatostatin analogue 99mTc Depreotide in the evaluation of solitary pulmonary nodules. Journal of Nuclear Medicine, 51 (S2), p 541.

Hayat,

Hayat, MA 2008. Cancer Imaging: Instrumentation and Applications. p314. Elsevier Academic Press.

Hermes,

Hermes Medical Solutions, AB 2008. Hermes Data Analysis Applications - Iterative Recobstruction (HOSEM™). Version 3.6, CD 300.2-P7V3.6.

Hesse,

Hesse, B, Tagil, K, Cuocolo, A, Anagnostopoulos, C, Bardies, M, Bax, J, Bengal, F, Busemann Sokole, E, Davies, G, Dondi, M, Edenbrandt, L, Frabken, P, Kjaer, A, Knuiti, J, Lassmann, M, Ljungberg, M, Marcassa, C, Marie, PY, McKiddie, F, O'Connor, M, Prvulovich, E, Underwood, R and van Eck-Smit, B 2005: EANM/ESC procedural guidelines for myocardial perfusion imaging in nuclear cardiology. Eur J Nucl Med Mol Imaging, 32 (7), pp 855-897.

Hindie,

Hindie, E, Ugur, O, Fuster, D, O'Docherty, M, Grassetto, G, Urena, P, Kettle, A, Gulex, SA, Pons, F, and Rubello, D 2009: 2009 EANM parathyroid guidelines. *Eur J Nucl Med Mol Imaging*, 36 (7), pp 1201-1216.

Hosie,

Hosie, CJ 1993: Measurement of trabecular bone mineral density in the distal radius of two gamma-ray computed tomography scanners. *Journal of Physiological Measurement*, 14, pp 269-276.

Hudson,

Hudson, HM, Larkin, RS 1994: Accelerated Image Reconstruction using Ordered Subsets of Projection Data. *IEEE Transactions on Medical Imaging*, 20, pp 100-108.

Hutton,

Hutton, BF 2002: Correction for Attenuation and Scatter in SPECT. *Alasbimn Journal*, 5(18), Article: AJ18-5.

ICRP Task Group,

ICRP 1994. Report by ICRP: Report of the Task Group on Reference Man. Oxford: Pergammon Press Ltd.

ICRU,

ICRU, 1989. ICRU Report 44: Tissue Substitutes in Radiation Dosimetry and Measurement. Bethesda, MD: ICRU

Kernstein,

Kernstein, KH, Kahn, D, Menda, Y, Bushnell, D, McLaughlin, K, Miller, S and Rossi, N 2001: A new technique for staging potentially resectable lung cancer: NeoTect SPECT Tc-99m compared with F-18 FDG. *American society of Clinical Oncology*, 20, Abstr 1352.

Lawson,

Lawson, R 2011. Principles of iterative reconstruction. Lecture presented at a course organised by IPEM, Iterative Reconstruction in Nuclear Medicine: towards a “clearer” picture.

Lener,

Lener, N, Jamar, F, Fiasse, R, Ferrant, A, and Pauwels, S 1996: Indium-111-Pentetreotide Uptake in Endocrine Tumours and Lymphoma. *Journal of Nuclear Medicine*, 37(6), pp 916-922.

Leslie,

Leslie, WD, Dupont, JO, Bybel, B and Riese, KT 2002: Parathyroid 99mTc-sestamibi scintigraphy; dual-tracer subtraction is superior to double-phase washout. *Eur J Nucl Med Mol Imaging*, 29 (12), pp 1566-1570.

MacMillan - Lung,

Macmillan Cancer Support 2011: Lung Cancer

<http://www.macmillan.org.uk/Cancerinformation/Cancertypes/Lung/Lungcancer.aspx>: accessed on 10/05/2011.

MacMillan - NET,

Macmillan Cancer Support 2011: Carcinoid tumour.

<http://www.macmillan.org.uk/Cancerinformation/Cancertypes/Neuroendocrine/Carcinoidtumours.aspx>: accessed on 10/05/2011.

Mariani,

Mariani, G, Bruselli, L, Kuwert, T, Kim, EE, Flotats, A, Israel, O, Dondi, M and Watanabe, N 2010: A Review on the clinical uses of SPECT/CT. *Eur J Nucl Med Mol Imaging*, 37 (10), pp 1959-1985.

McKillop and Fogelman,

McKillop, J H and Fogelman, I 1991. Benign and Malignant Bone Disease. Churchill Livingstone. London.

NeoSPECT™,

Nycomed Imaging, AS 2001. Bound to see more, NeoSPECT™ Depreotide kit for radiopharmaceutical preparation. Amersham plc product information sheet.

NICE,

National Institute for Health and Clinical Excellence 2009: Clinical Guidelines.

http://www.nice.org.uk/search/guidancesearchresults.jsp?keywords=cancer%20isotope%20bone%20scan&searchType=guidance_finder&includeCG=on: accessed on 21/01/2009.

Navalkisoor & Buscombe

Navalkissoorm, S and Buscombe, JR 2011: The continuing evolution of somatostatin receptor imaging in neuroendocrine tumours. Nuclear Medicine Communications, 32, pp 163-167.

OctreoScan®,

Mallinckrodt. OctreoScan® *kit for the preparation of Indium In-111 Pentetreotide*. Tyco Healthcare product information sheet, 050.

OSEM Technology,

OSEM - Nuclear Medicine Imaging, OSEM Technology 2006: Iterative Reconstruction.

<http://osem.s-pla.net/>: accessed on 08/12/2009

Perri,

Perri, M, Erba, P, Volteranni, D, Lazzeri, E, Boni, G, Grosso, M and Mariani, G 2008: Octreo-SPECT/CT imaging for accurate detection and localisation of suspected neuroendocrine tumours. *Q J Nucl Med Mol Imaging*, 52(4), pp 323-333.

Prekeges,

Prekeges, J 2011. *Nuclear Medicine Instrumentation*. Pp 162-163. Jones and Barlett.

RSD Phantoms

Radiology Support Devices, RSD 2011: *Anthropomorphic Phantoms for Nuclear Medicine*.

<http://www.rsdphantoms.com>: accessed on 17/05/2010

Reubi

Reubi, JC, Laissue, J, Krenning, E and Lamberts, SW 1992: Somatostatin receptors in human cancer: incidence, characteristics, functional correlates and clinical implications. *Journal of Steroid Biochemistry and Molecular Biology*, 43, pp 27-35.

Ritt,

Ritt, P, Vija, H, Hornegger, J and Kuwert, T 2011: Absolute quantification in SPECT. *Eur J Nucl Med Mol Imaging*, 38 (Suppl1), pp S69-77.

Shapiro

Shapiro, LG and Stockman, GC 2001. *Computer Vision*. p 137, 150. Prentence Hall.

Shcherbinin,

Shcherbinin, S, Cellar, A, Belhocine, T, Vanderwerf, R and Driedger, A 2008: Accuracy of quantitative reconstructions in SPECT/CT Imaging. *Phys Med Biol*, 53, pp 4595-4604.

Siemens, 2005

Siemens Medical Solutions, 2005. Symbia™ TruePoint SPECT-CT: System Specifications. Siemens Medical, 2005.

Siemens, 2006

Kalra, MK and Bradym, TJ 2006. Care Dose4D: New Techniques for Radiation Dose Reduction. Siemens Medical, article from the customer magazine SOMATOM Sessions, 19, November 2006.

Srikant,

Srikant, CB 2004. Somatostatin. p. 146. Kluwer Academic Publishers.

Stalheim-Smith

Stalheim-Smith, A and Fitch, GK 1993. Understanding Human Anatomy and Physiology. pp 148 - 151. WEST.

UKRG,

UK Radiopharmacy Group, UKRG 2002. UKRG Radiopharmacy Handbook, Section 4 - Radiopharmaceuticals available with marketing authorisations (OCTOBER 2001).

<http://www.ukrg.org.uk/> : accessed September 2008.

Vandenbergh,

Vandenbergh, S, Asseler, YD, Van de Walle, R, Kauppinen, T, Koole, M, Bouwens, L, Van Laere, K, Lemahieu, I and Dierckx, RA 2001: Iterative

reconstruction algorithms in nuclear medicine. *Computerised Medical Imaging and Graphics*, 25, pp 105-111.

Vandervoort,

Vandervoort, E, Cellar, A and Harrop, R 2007: Implementation of an iterative scatter correction, the influence of attenuation map quality and their affect on absolute quantitation in SPECT. *Phys Med Biol*, 52, pp 1527 - 1545.

Waxman,

Waxman, AD, Tcherniantchouk, O, Williams, CM, Marchevsky, A, McKenna, R, Fuller, C and D'Agnolo, A 2002: ^{99m}Tc Depreotide in the staging of lung cancer: Mapping of tumour lymphatic drainage. *Journal of Nuclear Medicine*, 43 (5), Abstr 407.

W-Healthy,

W-Healthy 2009: Healthy Lungs.

<http://www.w-healthy.com/healthy-lungs/>: accessed on 12/05/2011.

Wiki-CT,

Wikipedia 2011: X-ray computed tomography; History.

http://en.wikipedia.org/wiki/X-ray_computed_tomography#History: accessed May 2011

Wiki-Hounsfield,

Wikipedia 2011: Hounsfield scale; The HU of common substances.

http://en.wikipedia.org/wiki/Hounsfield_scale: accessed May 2011

Willowson,

Willowson, K, Bailey, DL, and Baldock, D 2008: Quantitative SPECT reconstruction using CT-derived corrections. *Phys Med Biol*, 53, pp 3099-3112.

Zeintl,

Zeintl, J, Vija, AH, Yahil, A, Hornegger, J and Kuwert, T 2010: Quantitative Accuracy of Clinical ^{99m}Tc SPECT/CT Using Ordered-Subset Expectation Maximization with 3-Dimensional Resolution Recovery, Attenuation And Scatter Correction. *Journal of Nuclear Medicine*, 51 (6), pp 921-928.